Measurement of Neutrino Oscillations with IceCube-DeepCore

Von der Fakultät für Mathematik, Informatik und Naturwissenschaften der RWTH Aachen University zur Erlangung des akademischen Grades eines Doktors der Naturwissenschaften genehmigte Dissertation

vorgelegt von

Diplom-Physiker Markus Vehring

aus Haren (Ems).

Berichter:

Universitätsprofessor Dr. Christopher Wiebusch
Universitätsprofessor Dr. Thomas Hebbeker

Tag der mündlichen Prüfung: 06.03.2017

Diese Dissertation ist auf den Internetseiten der Universitätsbibliothek online verfügbar.

Abstract

Neutrino oscillations are an active topic of research with several yet unresolved issues. Neutrino oscillations occur due to a mixing of flavor- and mass-states which results in a varying probability to measure a distinct neutrino flavor. This effect is dependent on the propagation length and energy of the neutrino. For a detector measuring muon neutrinos produced in the Earth's atmosphere, the oscillation is visible as an energy and zenith dependent deficit in muon-neutrino events compared to the hypothesis of no neutrino oscillation.

The IceCube Neutrino Observatory is a neutrino detector located at the geographical South Pole. Its extension DeepCore enables the detection of muon neutrinos of low-energy. With an energy threshold as low as 10 GeV DeepCore triggers to about 150 000 atmospheric muon neutrino events each year. This enables the measurement of the oscillation of muon neutrinos into other flavors.

In a recent analysis using three years of IceCube data from 2011 to 2014, a sensitivity comparable to dedicated neutrino oscillation experiments was achieved. This work extends that analysis by including another year of data that was measured between 2010 and 2011. The live time of the analysis is increased from 953 to 1266 days. This permits an improvement in sensitivity. Also it is explored, how the analysis can be improved further.

Zusammenfassung

Neutrinooszillationen sind ein aktives Thema der Forschung mit mehreren noch ungelösten Problemen. Die Oszillationen treten aufgrund einer Vermischung von Flavor- und Massenzustände auf, welche zu einer wechselnden Messwahrscheinlichkeit für einen bestimmten Flavor-Zustand führen. Dieser Effekt ist abhängig von der zurückgelegten Wegstrecke und der Energie des Neutrinos. Bei Myonneutrinos welche in der Erdatmosphäre erzeugt wurden und mit einem Detektor in der Erdoberfläche gemessen werden, ist der Oszillationseffekt sichtbar als energie- und zenitwinkelabhängiges Defizit der Myonneutrinoereignisse im Vergleich zur 0-Hypothese.

Das IceCube Neutrino-Observatorium ist ein Hochenergie-Neutrinodetektor am geographischen Südpol. Durch die Erweiterung DeepCore ist es auch möglich niederenergetische Myonneutrinos mit IceCube zu detektieren. DeepCore senkt die Energieschwelle für den Neutrinonachweis auf etwa 10 GeV und registriert 150000 Ereignisse von atmosphärischen Myonneutrinos pro Jahr. Dies ermöglicht die Messung der Oszillation von Myonneutrinos in andere Flavor-Zustände.

In einer Analyse von IceCube-Daten aus den Jahren 2011 bis 2014 wurde eine Sensitivität erreicht, welche vergleichbar mit der von dedizierten Neutrinooszillationsexperimenten ist. Die vorliegende Arbeit ergänzt die Dreijahresanalyse um ein weiteres Jahr an Daten, welches zwischen 2010 und 2011 gemessen wurde. Dies erhöht die Gesamtmesszeit von 953 auf 1266 Tage und führt zu einer Verbesserung der Messsensitivität. Nachfolgend wird untersucht wie die Analyse weiter verbessert werden kann.

Contents

List of Figures

List of Tables

Chapter 1

Neutrinos

This chapter covers the physics of neutrinos in the standard model and gives a brief historic background. It covers the different neutrino interactions as well as the theoretic origin of the neutrino mass. Furthermore, cosmic-ray induced air showers are briefly explained as decaying pions, kaons and muons from the air showers are the source of athmospheric muon neutrinos.

1.1 Introduction

"Today I did something a theorist should never do in his life. I tried to explain something that one cannot understand by something one cannot detect."

Original:
"Heute habe ich etwas getan, was ein Theoretiker nie in seinem Leben tun sollte. Ich habe nämlich etwas, was man nicht verstehen kann, durch etwas zu erklären versucht, was man nicht beobachten kann."

Wolfgang Pauli [1]

In a letter addressed to the "Radioactive Mrs and Sirs" Wolfgang Pauli postulated the neutrino[1] (ν) to explain the the continuous energy spectrum of electrons from β-decays. The postulated low interaction probability then led to his famous quote.

Neutrinos (νs) were first discovered in an experiment by Frederick Reines et al. in 1956 [2]. In the experiment νs produced in a nuclear reactor of the Savannah River power plant interacted with protons in two water tanks and produced neutrons and positrons. By observing the photons produced in the annihilation of the positrons and photons produced when a neutron was catched by cadmium nuclei, the ν interaction could be identified. Since the neutrinos interacted with electron flavor fermions, they are called (ν_es). Six years later in 1962 a group around Leon Lederman, Melvin Schwartz and Jack Steinberger at the Brookhaven National Laboratory [3] used a beam of $\pi^{\pm}$ to create a neutrino beam. Spark chambers were used to discover the neutrino interactions. The observed leptons from the neutrino interaction were identified as μs and thus the neutrinos as muon neutrinos (ν_μs). Both of the discoveries were awarded with the Nobel Prize in Physics in 1988 for Leon Lederman, Melvin Schwartz and Jack Steinberger and in 1995 for Frederick Reines. Finally a neutrino interacting with tau leptons, the tau neutrino (ν_τ), was detected by the DONUT collaboration in 2001 [4]. ν_τs were produced in interactions between a strong proton beam and a tungsten target. A 15 m thick shielding was used to filter all particles except neutrinos. The neutrinos itself were detected in an emulsion cloud chamber[2] through the produced τ lepton.

Today neutrino physics is a very active field in experimental physics and most parameters of neutrinos are measured with a high precision.

1.2 Neutrinos

In the Standard Model (SM) of particle physics (see figure 1.1) neutrinos are defined as massless, left-handed spin-1/2 leptons [6]. They interact only via the weak force and do not carry electromagnetic charge or color. Due to their low cross-section, neutrinos interact only very sparsely with matter. A huge neutrino flux and large interaction volume is needed to detect neutrinos in sufficient numbers.

[1] he called it a neutron

[2] An emulsion cloud camber (ECC) is a detector of stacked nuclear emulsion film modules. The modules are separated by plates of for example steel or lead [4, 5].

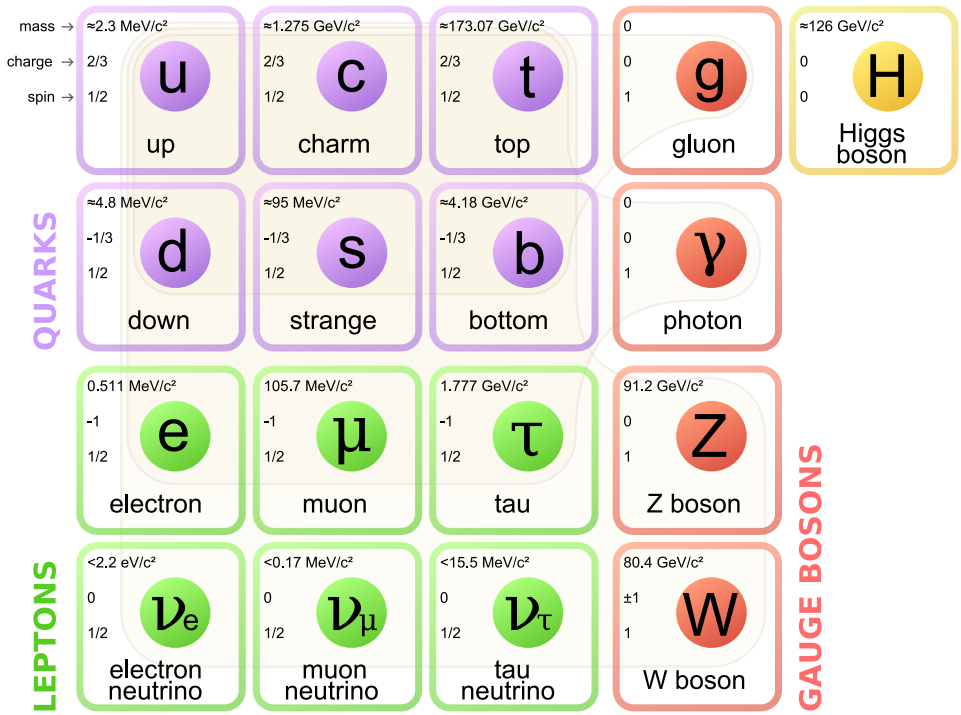

Figure 1.1: The standard model of particle physics. The picture was taken from [7].

Today three different kinds of neutrinos are known. In a precision measurement at the Z resonance done with the LEP collider it was confirmed, that exactly three kinds of neutrinos exist with a mass below $M_Z/2$ [8]. The result of this measurement is shown in figure 1.2.

As described above the SM assumes that neutrinos are massless particles. However, the measurement of neutrino oscillations (see section 2.1) requires non-zero mass differences between the different physical neutrinos. Up to today there is no absolute measurement of the neutrino mass but only limits. One experiment aimed at the measurement of the ν_e mass is the KATRIN experiment [9]. The neutrino mass is measured with the continuous spectrum of electrons from the beta decay of tritium

$$H^3 \rightarrow {}^3He + e^- + \nu_e \quad . \tag{1.1}$$

The difference between the measured end of the spectrum and the theoretical end without a ν_e mass is then the value for the ν_e mass (see figure 1.3). The sensitivity for the measurement is aimed to be around 0.2 eV.

Depending on the energy of the neutrino and its interaction partner, there are different types of interactions. [10] defines five different energy regions of interest that are shown in table 1.1. As the analysis described in this thesis uses charged-current (CC) interactions from muon neutrinos as signal, energy regions below the muon rest-mass of ∼100 MeV are not relevant.

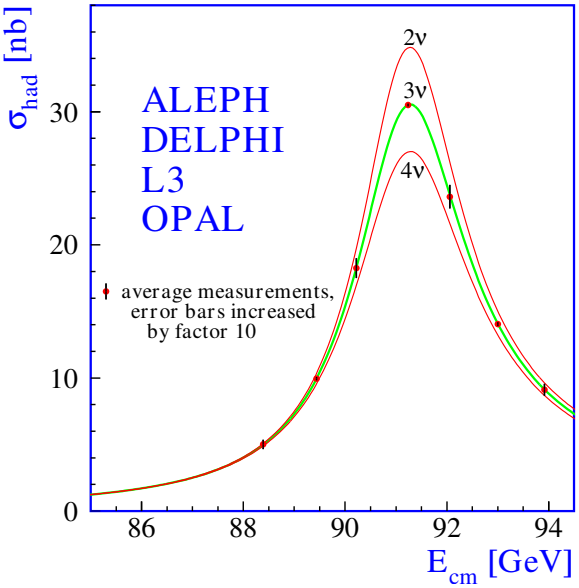

Figure 1.2: Theoretical curves of the hadron production cross-section for two, three and four different kinds of neutrinos and a measurement done with LEP at the Z resonance [8]. It is assumed, that the neutrino mass can be neglected. Neutrinos with a mass above $M_Z/2$ do not couple to the Z boson and thus do not contribute to the predicted curves.

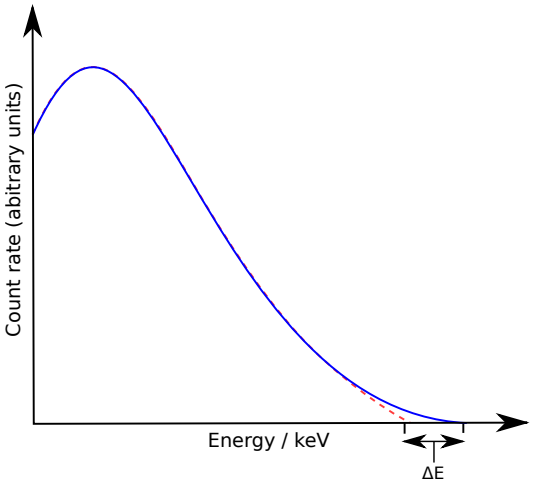

Figure 1.3: Sketch how the mass of the ν_e can be measured from an energy spectrum of electrons produced in a β-decay. The blue line would be the energy spectrum of the electrons if ν_e are massless, whereas the red-dashed line is for a mass of $m_{\nu_e} = \Delta E$.

Table 1.1: Different energy regions of neutrino interactions as defined in [10]

$0 - 1\,\mathrm{MeV}$	Threshold-less
$1 - 100\,\mathrm{MeV}$	Low Energy Nuclear
$0.1 - 20\,\mathrm{GeV}$	Intermediate Energy
$20 - 500\,\mathrm{GeV}$	High Energy
$0.5\,\mathrm{TeV} - 1\,\mathrm{EeV}$	Ultra High Energy

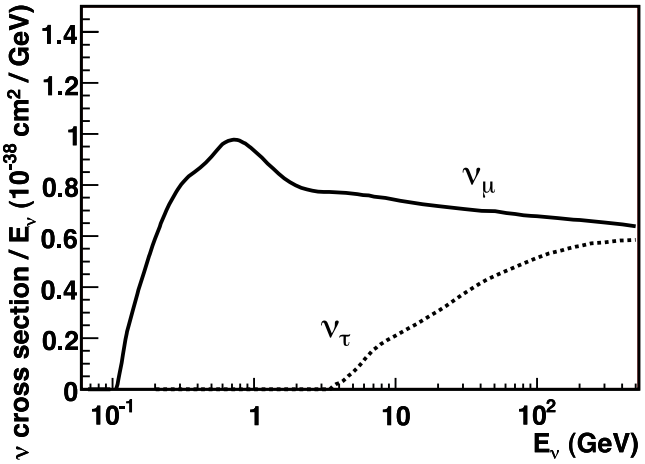

Figure 1.4: Total charged-current neutrino interaction cross-section per nucleon for ν_μ and ν_τ divided by neutrino energy [10]. Due to the high mass m_τ of the τ lepton the cross-section is reduced for energies below some 100 GeV. Below $2m_\tau$ the cross-section is reduced to zero. The peak in cross-section for ν_μ is due to baryonic resonance production becoming relevant (see figure 1.5).

1.2.1 Neutrino Interactions

All neutrino interactions discussed in this section are between (anti-)muon neutrinos and nucleons, as these are the most relevant for this work. However, the interactions between neutrinos and electrons become relevant in chapter 2.3.2 and are discussed there. The interactions between the other neutrino flavors and nucleons are the same, but the cross-sections vary for charged-current interactions. In CC interactions a part of the neutrinos energy is needed for the production of the lepton, this is shown in figure 1.4. The cross-section for CC interactions between ν_τ and nucleons is altered due to the high rest-mass of the τ with $m_\tau = 1777\,\text{MeV}$ [11].

The relevant energy range for this thesis starts at a few 1 GeV and ends at some hundred GeV in neutrino energy. Relevant neutrino interaction processes in this energy range are elastic (ES) and quasi-elastic (QES) neutrino-nucleon scattering, resonance production (RES) and deep inelastic scattering (DIS) [10].

Elastic and Quasi-Elastic Scattering (QE)

Figure 1.5 shows the charged-current cross-sections for ν_μ and $\bar{\nu}_\mu$. In the low-energy range between 0.1 and a few GeV quasi-elastic scattering between neutrinos and nucleons is dominant. In this interaction the neutrino liberates a nucleon of the target nucleus by

$$\nu_\mu + \text{n} \rightarrow \mu^- + \text{p} \quad \text{or} \quad \bar{\nu}_\mu + \text{p} \rightarrow \mu^+ + \text{n} \tag{1.2}$$

by exchanging $W^\pm$ with the nucleon [10]. The end state of this interaction is a $\mu^\mp$ and a nucleon of opposite charge. Since in the charged-current interaction a muon has to be produced, this

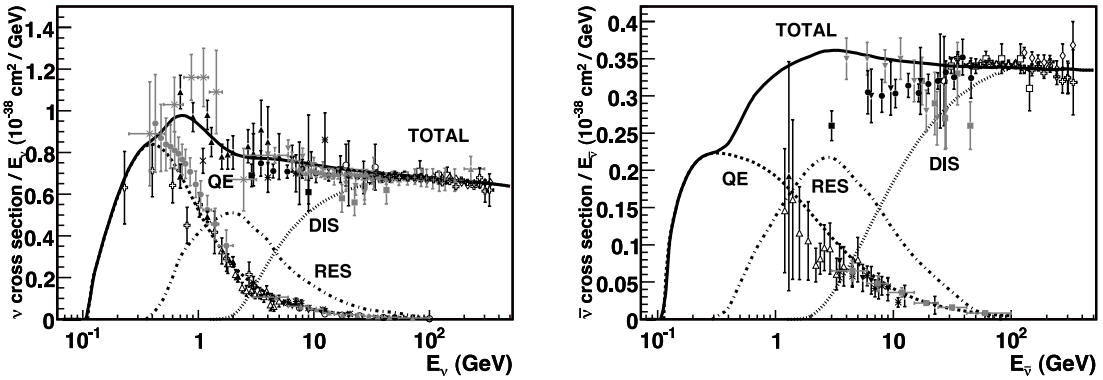

(a) Neutrinos (b) Anti-Neutrinos

Figure 1.5: CC interaction cross-sections against neutrino energy for ν_μ and $\bar{\nu}_\mu$. The cross-section value is per nucleon and divided by the neutrino energy. The markers are measurements from various experiments. The lines are predictions generated with the NUANCE generator [12]. The cross-sections for quasi-elastic scattering (QE), resonance production (RES), deep inelastic scattering (DIS) and the total cross-section (TOTAL) are labeled (from [10]).

interaction is called quasi-elastic. A neutral-current interaction between the neutrino and the nucleon also can liberate the nucleon over

$$\nu_\mu + \mathrm{X} \rightarrow \nu_\mu + \mathrm{X} \quad \text{or} \quad \bar{\nu}_\mu + \mathrm{X} \rightarrow \bar{\nu}_\mu + \mathrm{X} \quad . \tag{1.3}$$

The X can be either a proton or a neutron. Since no lepton is produced from the neutrino it retains its kinetic energy, this interaction is called elastic.

Resonance and Coherent Pion Production (RES)

Around 1 GeV up to a few ten GeV resonance production is a relevant part of the total neutrino interaction cross-section, as can be seen in figure 1.5. Here the neutrino and nucleon inelastically scatter. This also excites the nucleon while liberating it from the nucleus and produces a baryonic resonance [10]. After $\hbar/\Gamma \approx 10^{-25}$ s the baryonic resonance decays. The final state with a branching ratio of nearly 100 % consists of a nucleon and a single pion [11]. Apart from single pions the exited baryon can also decay into kaons, photons or multiple pions.

There are also inelastic neutrino-nucleon interactions without the intermediate baryonic resonance [10]. In this coherent pion production the pion is forward scattered while the nucleon only receives a very small amount of the neutrinos energy. Charged pions are produced together with charged leptons, while for π^0 the neutrino is conserved. Like for the resonance production, the production of kaons instead of pions is also possible, but suppressed.

Deep Inelastic Scattering (DIS)

Above ∼10 GeV DIS is the dominating part of the total neutrino interaction cross-section [10]. In this interaction the neutrino scatters off a quark inside the nucleon, destroying it in the process. The final state is a hadronic shower and a lepton for the CC interaction or a shower and the neutrino for the NC interaction.

In deep inelastic scattering a part of the neutrino's energy ends up in the hadronic system. The ratio between the energy of the hadronic shower E_{had} and the initial energy of the neutrinos E_ν is called the inelasticity parameter or Bjorken-y [13] with

$$y = E_{\text{had}}/E_\nu \quad . \tag{1.4}$$

Together with the kinematic four-momentum transfer

$$Q^2 = -m_\mu^2 + 2E_\nu(E_\mu - p_\mu \cos\theta_\mu) \tag{1.5}$$

and the Bjorken scaling variable

$$x = \frac{Q^2}{2m_N \cdot E_{\text{had}}} \tag{1.6}$$

the DIS interactions can be completely described [10]. Here m_μ and m_N are the muon and nucleon mass, E_μ and p_μ are the energy and momentum of the resulting muon and θ_μ is the outgoing scattering angle of the muon.

Figure 1.6 shows the CC cross-section divided by the neutrino energy, which becomes constant above some ten GeV. Here the the cross-section increases linearly with energy up to about 10 TeV. At these high energies the dominance of the W-Z boson in the interaction is reduced [10]. The energy dependent cross-sections between neutrinos and nucleons transition from a linear to a power-law dependence with

$$\sigma \propto E^{0.363} \quad . \tag{1.7}$$

Very high energy electron neutrinos that interact with electrons have a resonant increase in cross-section at $\frac{M_W^2}{2m_e} \approx 6.3\,\text{PeV}$ caused by the intermediate production of a W boson. This resonance was first described by Sheldon L. Glashow in 1960 [14].

Du to their increase in cross-section, neutrinos of very high energy, i.e. cosmic neutrinos, can have energies high enough that Earth becomes opaque to them.

1.2.2 Massive Neutrinos

The Standard Model of particle physics is defined by symmetry groups [15]. The electro weak interactions can be described by the gauge group $SU(2)_L \times U(1)_Y$. Here we omit the $SU(3)_c$ part that describes strong interactions, because neutrinos do not carry color. Experimental observations showed, that only left-handed neutrinos and right-handed anti-neutrinos are found in particle interactions [6]. Furthermore, experimental measurements of the neutrino mass only provided upper limits. Thus, in the Standard Model neutrinos are artificially defined as purely left-handed, massless particles without charge.

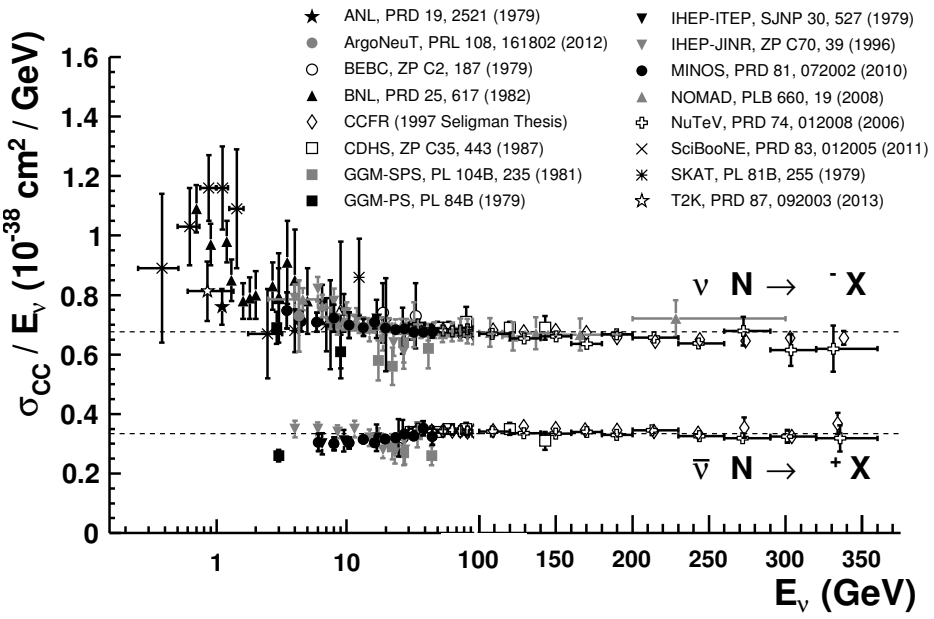

Figure 1.6: Inclusive charged-current scattering cross-section divided by neutrino energy for ν_μ (above) and $\bar{\nu}_\mu$ (below) measured with various experiments [11]. At energies above some ten GeV deep inelastic scattering is the dominant contributing factor. At 100 GeV the scale transitions from logarithmic to linear.

Today we know that neutrinos do have a non-vanishing rest-mass due to the observed effects of neutrino oscillations (see chapter 2), which forces non-zero neutrino mass differences. This requires a modification of the Standard Model to account for the neutrino mass.

Fermions in the Standard Model are defined as Dirac particles [15]. They are represented by complex four element Dirac spinors and obey the Dirac equation. The elements of the Dirac spinor for electrons are for example the left and right handed electron and the left and right handed particle with inverted charge, the positron. All charged fermions have to be Dirac particles so electric charge is conserved.

Neutrinos are defined as massless, left-handed particles and do not carry any electric charge and thus they can be described by only two elements of the Dirac spinor. This complex two element spinor of left-handed particle and right-handed anti-particle is called a Weyl spinor [6]. Since in reality neutrinos have a non-vanishing rest-mass, the helicity of the neutrino can be changed with a Lorentz boost and the Weyl spinor representation is not a valid one for neutrinos.

Massive neutrinos can be described in two different ways. They can be Dirac or Majorana particles. For a massless particle one cannot distinguished between both descriptions. Since the rest-mass of neutrinos is very small, so is the experimental difference between Dirac and Majorana particles. The correct case still has to be confirmed. Both variants are discussed below.

Dirac Masses

As stated above, Dirac particles are represented by a complex four-element spinor. A massive left-helicital particle can be boosted to get a right-helicital particle with the same charge. Thus, a massive neutrino has to have the left- and right-helicital fields $\boldsymbol{\psi}^0_{\mathrm{L}}$ and $\boldsymbol{\psi}^0_{\mathrm{R}}$. The mass term of the particle is generated by the Higgs mechanism over Yukawa coupling as

$$\mathscr{L}_D = m_{\mathrm{D}}\bar{\boldsymbol{\psi}}\boldsymbol{\psi} = m_{\mathrm{D}}(\bar{\boldsymbol{\psi}}_{\mathrm{L}}\boldsymbol{\psi}_{\mathrm{R}} + \bar{\boldsymbol{\psi}}_{\mathrm{R}}\boldsymbol{\psi}_{\mathrm{L}}) \quad \text{with} \quad \bar{\boldsymbol{\psi}}_{\mathrm{R}}\boldsymbol{\psi}_{\mathrm{L}} = (\bar{\boldsymbol{\psi}}_{\mathrm{L}}\boldsymbol{\psi}_{\mathrm{R}})^\dagger \quad [6]. \tag{1.8}$$

Here m_{D} is the Dirac-mass of the particle and $\bar{\boldsymbol{\psi}} = \boldsymbol{\psi}^\dagger\gamma^0$ is the Dirac adjoint of $\boldsymbol{\psi}$. From equation 1.8 it is obvious that for a Dirac particle the mass term vanishes if only $\boldsymbol{\psi}_{\mathrm{L}}$ and $\bar{\boldsymbol{\psi}}_{\mathrm{R}}$ are present.

A charge transformation turns a Dirac particle into an anti-particle [16]. For a charged particle like an electron the sign of the charge changes to the opposite. However, the neutrino does not carry charge, so neutrino and anti-neutrino cannot be identified by charge. Even so, if neutrinos are Dirac particles, the neutrino and the anti-neutrino are different particles. They are defined by their interaction with other leptons, in such a way that the Lepton number is conserved.

Since neutrinos do not carry charge one would think, that neutrinos do not possess charge related properties, viz. a magnetic moment, an electric dipole moment or a mean charge radius. However due to radiative loop corrections for Dirac neutrinos these properties are possible [16, 6].

Majorana Masses

First ideas about the Majorana formalism were introduced by Ettore Majorana in 1937 [17]. In contrast to massive Dirac fermions, Majorana fermions are represented by a real spinor with two elements. Majorana neutrinos are their own anti-particles, thus violating Lepton number conservation. The two elements of the spinor are the two different helicity states (left and right) of the particle. A CPT transformation only changes the helicity of the Majorana particle. Since massive neutrinos are slower than the speed of light, the same is possible with a Lorentz boost. This forces that Majorana particles to not have an electric charge, otherwise the Lorentz boost would violate charge conservation [16].

The Majorana mass term can be obtained additionally to the Dirac mass term by including the CPT conjugated spinor field $\bar{\boldsymbol{\psi}}^c$ [6]. This gives

$$\mathscr{L}^L = \frac{1}{2} m_{\mathrm{L}} (\bar{\boldsymbol{\psi}}_{\mathrm{L}} \boldsymbol{\psi}^c_{\mathrm{R}} + \bar{\boldsymbol{\psi}}^c_{\mathrm{R}} \boldsymbol{\psi}_{\mathrm{L}}) \tag{1.9}$$

$$\mathscr{L}^R = \frac{1}{2} m_{\mathrm{R}} (\bar{\boldsymbol{\psi}}^c_{\mathrm{L}} \boldsymbol{\psi}_{\mathrm{R}} + \bar{\boldsymbol{\psi}}_{\mathrm{R}} \boldsymbol{\psi}^c_{\mathrm{L}}) \tag{1.10}$$

as the left- and right-handed Majorana mass terms. m_{L} and m_{R} are the real Majorana masses. Due to the CPT invariance pure Majorana fermions do not have a magnetic moment, electric dipole moment or charge radius.

As Majorana neutrinos are their own anti-particles, the Majorana case allows a neutrinoless double beta decay [6]. Observing such a decay would solve if neutrinos are Dirac or Majorana particles.

The See-saw Mechanism

Apart from the mechanism behind the neutrino mass, one puzzle is also the difference in mass with respect to the other leptons [18]. Neutrinos have a very small rest-mass that is orders of magnitude lower than even the electron mass. In comparison, in the quark sector the rest-mass of quarks within one generation is more or less the same order of magnitude. The very low neutrino mass can be explained with a mix between Dirac and Majorana mass terms that is naturally obtained with the Majorana formalism. The case that $m_{\mathrm{D}} \ll m_{\mathrm{R}}$ and $m_{\mathrm{L}} = 0$ is called the "See-saw mechanism". This case has two solutions for particle masses

$$m_\nu = m_1 = \frac{m_{\mathrm{D}}^2}{m_{\mathrm{R}}} \quad \text{and} \quad m_{\mathrm{N}} = m_2 = m_{\mathrm{R}} \left(1 + \frac{m_{\mathrm{D}}^2}{m_{\mathrm{R}}^2}\right) \approx m_{\mathrm{R}} \quad [6]. \tag{1.11}$$

The Dirac-mass of the neutrinos is in the same order of magnitude like the associated charged leptons. For very high m_{R} the masses of the neutrinos are very small. The heavy twin particles of the neutrinos in this case have a mass equal $m_{\mathrm{R}} \gg m_{\mathrm{Z}}$ and thus cannot be created in W or Z decays.

The See-saw mechanism is an elegant explanation for the smallness of the neutrino masses and forces the neutrinos to be Majorana particles.

1.3 Atmospheric Neutrinos

Atmospheric neutrinos are produced in particle interactions in the atmosphere induced by cosmic rays. Naturally these neutrinos follow the spectrum of the primary cosmic ray modified by the energy dependent production efficiency. The neutrinos traverse the atmosphere unhindered and hit the Earth. Typical atmospheric neutrinos recorded by IceCube have kinetic energies of some $10 - 100\,\mathrm{GeV}$. These low energy neutrinos can also cross the Earth. The following sections will cover cosmic rays and the production of neutrinos in the atmosphere.

1.3.1 Cosmic Rays

Cosmic rays are particles from outside the Earth that interact with the Earth's atmosphere [11]. The spectrum of cosmic rays as shown in figure 1.7 follows a power-law with few features that covers several orders in magnitude in particle flux and energy. For lower energies E the spectrum is proportional to about $E^{-2.7}$ [18]. At the so called *knee* the spectrum steepens to $E^{-3.0}$ and even further to $E^{-3.3}$ at the *second knee*. The spectrum then flattens back to $E^{-2.7}$ at the *ankle*. For the low-energy region of this work $E^{-2.65}$ is assumed to be consisten with measurements by the Fréjus experiment in the same energy range [19].

Most of the cosmic rays that hit the atmosphere possess energies up to some TeV and are free protons with around $\sim$79 % followed by helium nuclei with $\sim$15 %. The remaining $\sim$6 % are more massive nuclei [11]. Particles with low energies below some ten GeV are affected by the solar wind and show a modulation dependent on the solar activity. Nuclei that are directly produced in in the source of cosmic rays are called cosmic primaries, whereas particles that are produced in interactions on the path to the Earth are called cosmic secondaries.

Particles with energies of some GeV are accelerated for the most part outside the solar system [21]. Here two acceleration mechanisms are important, viz. the Fermi acceleration of first and second order [22]. In the acceleration of second order the magnetic fields of moving plasma clouds act as "mirrors" for charged particles [23]. The particles are accelerated in stochastic processes. The average energy gain of these processes is proportional to the quadratic speed of the clouds and is thus of second order. The process leads to a power spectrum as it is observed for cosmic rays but is very inefficient. The Fermi process of first order is also called the "Shock Acceleration". Here charged particles are accelerated in astrophysical shock fronts, for example from supernovae explosions. The average energy gain for this process is $\Delta E/E = 4/3 \cdot (v_1 - v_2)$ [23]. Here $-v_1$ is the speed of the shock front and v_2 is the speed of the shocked gas relative to it. The obtained energy dependence follows a power-law with an index of $\sim$2.1 which is near the observed value. This process can accelerate charged particles in supernova remnants (SNRs) to energies of around $10^{15}\,\mathrm{eV}$. However, the accelerators for higher particle energies are still unclear.

1.3.2 Cosmic Ray Induced Extensive Air Showers

When a high energy cosmic ray hits the Earth's atmosphere, it interacts with the nuclei of the atmospheric gas [24]. The first interaction starts an interaction avalanche that is propagating through the atmosphere, an extensive air shower. There are different parts of an air shower.

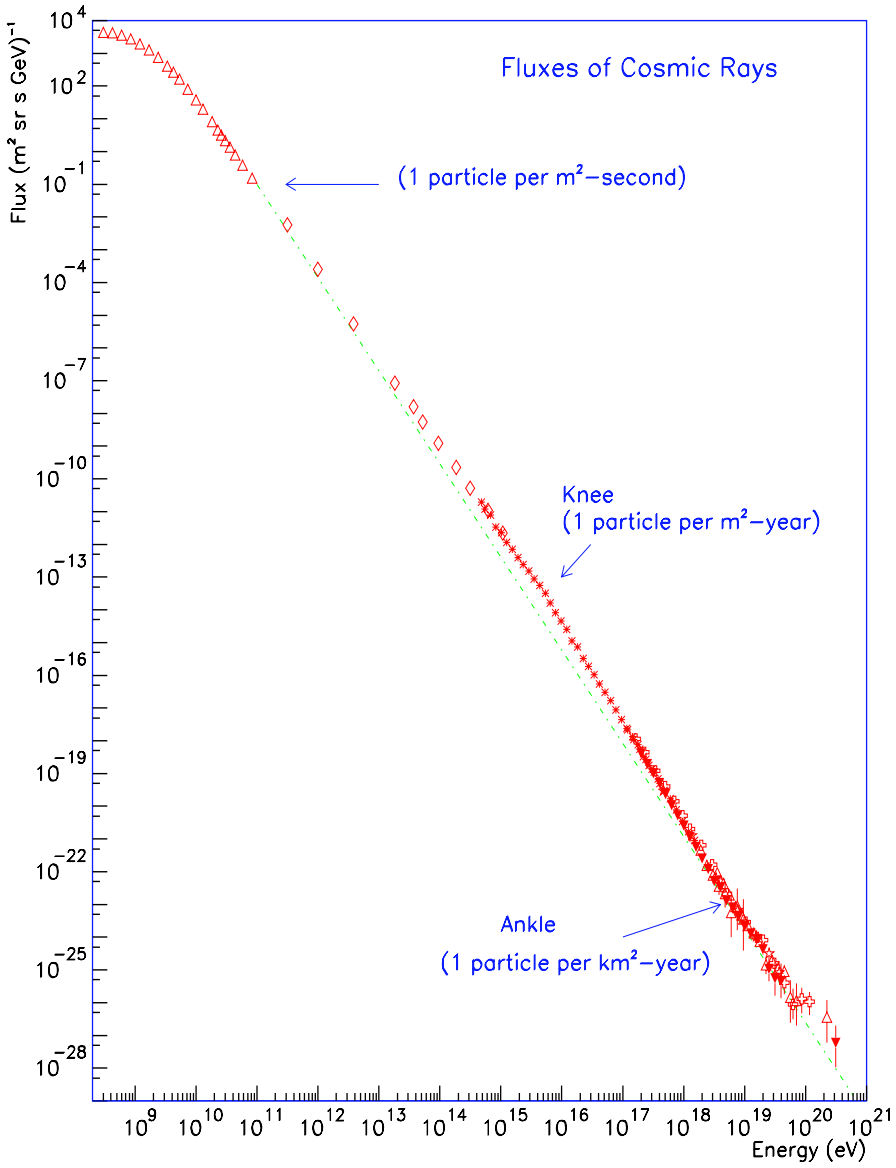

Figure 1.7: Flux of cosmic rays against their kinetic energy. The plot is a compilation of different measurements (taken from [18]; originally in [20]). The green, dotted line represents a power-law $\propto E^{-3}$.

The hadronic part is the core of the shower and feeds the other parts. Above 25 GeV primary particle energy it mostly consists of pions ($\pi^0, \pi^\pm$) with 90 % and kaons ($K^0_\mathrm{L}, K^0_\mathrm{S}, K^\pm$) with 10 % [25]. For the most part the kaons decay quickly into pions, muons and neutrinos, whereas the charged pions decay into muons and neutrinos. The muons from the muonic part of the shower decay into electrons and neutrinos. The electrons form the last part of the shower, the electromagnetic part. The uncharged π^0 nearly always decays into two photons (∼99 %) or one proton and an electron-positron pair (∼1 %) [11].

1.3.3 Production of Atmospheric Neutrinos

Neutrinos are produced in every part of the air shower in the flavors ν_e, $\bar{\nu}_\mathrm{e}$, ν_μ and $\bar{\nu}_\mu$. Since the neutrino production is directly coupled to the production of pions and kaons, the number of produced neutrinos can be estimated from the number of available pions and kaons in the shower. ν_τ and $\bar{\nu}_\tau$ are only produced in rare processes through charm-meson decay and form a flux that is negligible [6].

Since pions are very abundant in the hadronic part of the shower, their decays produce a dominant part of the atmospheric neutrino flux with

$$\pi^+ \to \mu^+ + \nu_\mu \quad \text{and} \quad \pi^- \to \mu^- + \bar{\nu}_\mu \quad . \tag{1.12}$$

This decay has a branching ration of nearly 100 % [11] since the similar decay into electrons or positrons is suppressed. If the resulting muons are not high energetic enough, they can decay in the atmosphere by

$$\mu^+ \to e^+ + \nu_\mathrm{e} + \bar{\nu}_\mu \quad \text{and} \quad \mu^- \to e^- + \bar{\nu}_\mathrm{e} + \nu_\mu \quad . \tag{1.13}$$

This also feeds the neutrino part of the shower. As stated in section 1.3.2, a relevant part of the hadronic shower also consists of kaons. The decays of these also produce neutrinos, muons and pions. Here the most relevant decays and their branching ratios are [11]

$$K^0_\mathrm{L} \to \pi^\pm + e^\mp + \nu_\mathrm{e}(\bar{\nu}_\mathrm{e}) \quad (\sim 41\,\%) \quad , \quad K^0_\mathrm{L} \to \pi^\pm + \mu^\mp + \nu_\mu(\bar{\nu}_\mu) \quad (\sim 27\,\%) \quad , \tag{1.14}$$

$$K^0_\mathrm{S} \to \pi^+ + \pi^- \quad (\sim 69\,\%) \quad , \tag{1.15}$$

$$K^\pm \to \mu^\pm + \nu_\mu(\bar{\nu}_\mu) \quad (\sim 64\,\%) \quad , \tag{1.16}$$

$$K^\pm \to \pi^0 + \pi^\pm \quad (\sim 21\,\%) \quad , \quad K^\pm \to \pi^\pm + \pi^\pm + \pi^\mp \quad (\sim 6\,\%) \quad , \tag{1.17}$$

$$K^\pm \to \pi^0 + e^\pm + \nu_\mathrm{e}(\bar{\nu}_\mathrm{e}) \quad (\sim 5\,\%) \quad \text{and} \quad K^\pm \to \pi^0 + \mu^\pm + \nu_\mu(\bar{\nu}_\mu) \quad (\sim 4\,\%) \quad . \tag{1.18}$$

1.3.4 Neutrino Flux at the South Pole

Since the data for this analysis was taken with a detector located at the South Pole, it is important to know the neutrino flux at this place. Figure 1.8 shows the neutrino flux at South Pole against the cosine of the zenith angle for four different neutrino energies [26, 27]. Since for the South Pole the geomagnetic field only has a minor impact on the azimuthal dependence of the neutrino flux, only the zenith and energy dependence is discussed. At low energies up to

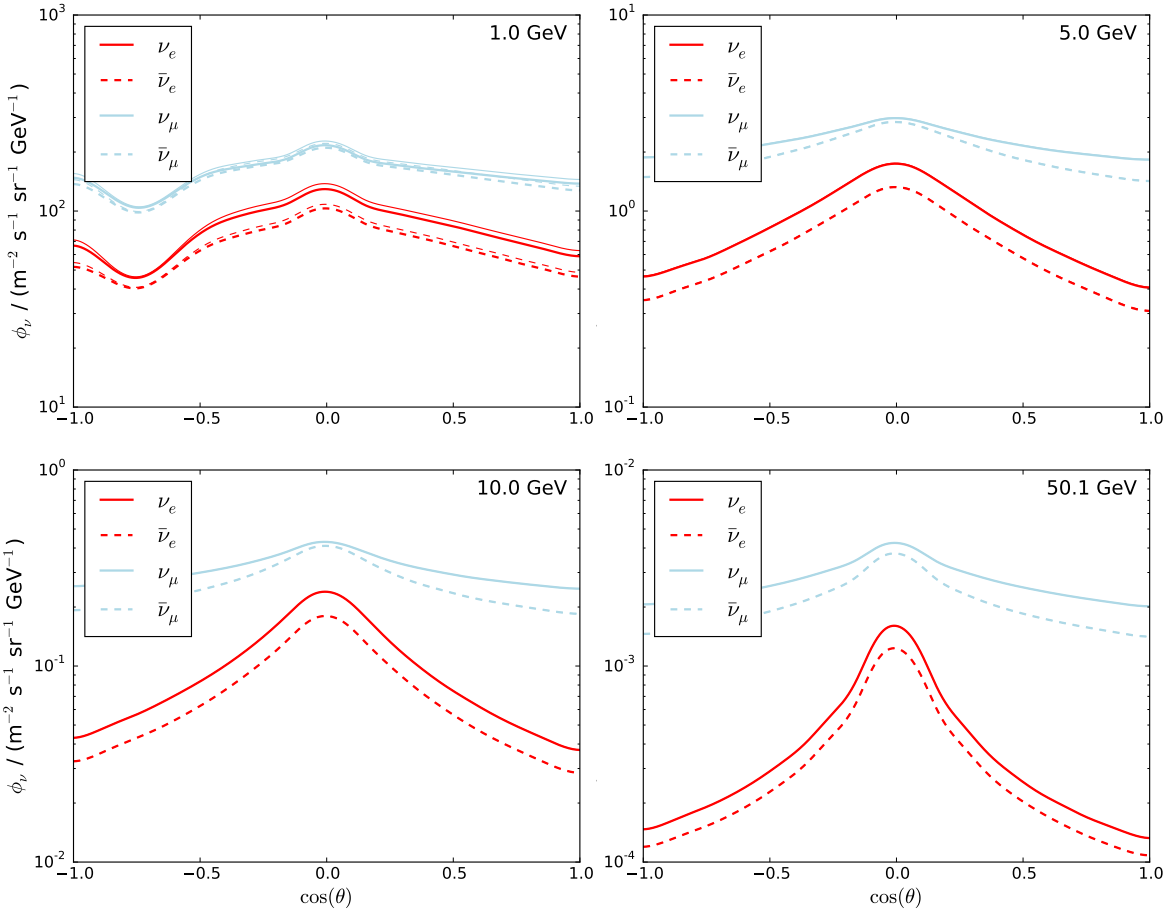

Figure 1.8: Calculated zenith angle dependent neutrino flux at the South Pole for different energies without neutrino oscillations taken into account. The flux is averaged over the azimuth angle and one year. The thin lines represent values for the solar minimum, the thick lines for the solar maximum. At energies above 5 GeV both are identical. Please note the changing scale of the y-axis for each plot. Shown are spline interpolated values from [26, 27].

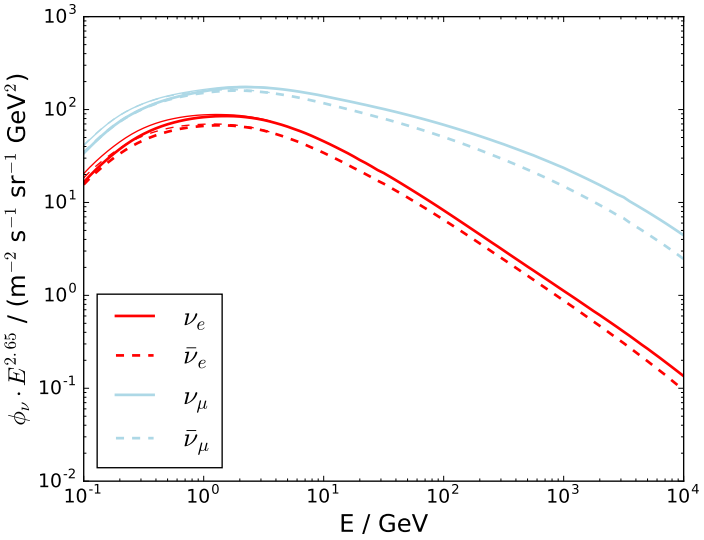

Figure 1.9: Simulated energy dependent neutrino flux at the South Pole without neutrino oscillations taken into account. The flux is averaged over the incident direction and one year. The thin lines represent values for the solar minimum, the thick lines for the solar maximum. At energies above 5 GeV both are identical. The flux was multiplied by $E^{2.65}$. Shown are spline interpolated values from [26, 27].

1 GeV there are flux variations for changing zenith angles. With rising energy the flux becomes more up-down-symmetric. For the analysis the relevant neutrino energies are above some GeV and the complex zenith dependent flux pattern can be ignored. The same is true for a differing flux due to changing solar activity, as this minor effect vanishes in the relevant energy range.

One major neutrino source is the decay of atmospheric muons in the atmosphere (see section 1.3.3). Muons of sufficient energy can reach the Earth's surface before they decay [11]. Since horizontal muons have a longer path inside the atmosphere, their probability to decay inside the atmosphere is higher than for vertical muons. This causes a rise in the neutrino flux for horizontal directions in relation to more vertical directions and results in a peak in the neutrino flux for horizontal neutrinos above ∼1 GeV.

Figure 1.9 shows the energy dependent neutrino flux for the South Pole. Apart from the primary cosmic-ray flux the neutrino flux is governed by the production due to the decay of other particles viz. pions, kaons and muons. In the data provided by [26] the electron-neutrino flux is falling with a steep power law $\propto E^{-3.55}$ above ∼10 GeV while the $\nu_\mu/\bar{\nu}_\mu$ flux is more stable reaching the same power-law index at about 10 TeV. The neutrino flux is dependent on the muon production and decay mechanism. As stated above, at higher energies muons reach the ground before decaying, thus removing a balanced source of $\nu_e/\bar{\nu}_e$ and $\nu_\mu/\bar{\nu}_\mu$. However, $\nu_\mu/\bar{\nu}_\mu$ production still remains due to pion and kaon decay. The mixture of pions and kaons is influencing the spectrum of ν_μ and $\bar{\nu}_\mu$.

The next chapter deals with the theory of neutrino oscillations and experiments designed to measure this effect.

Chapter 2

Neutrino Oscillations

This chapter covers neutrinos oscillations in vacuum and matter. A historic context is presented, followed by the derivation of neutrino oscillations in vacuum. Additional oscillation effects by neutrino interactions with matter are discussed for a simple two flavor approximation. In the end relevant experiments are presented.

2.1 Introduction

"Despite the fact that what we have just said is at best very roughly true, at worst completely false, I shall continue to speculate about neutrino oscillations."

Bruno Pontocorvo [28]

With the discovery of the Higgs boson as a signal in CMS [29] and ATLAS [30] data, the Standard Model is completed. The Standard Model is very successful in particle physics, but there are indications that there is physics beyond that model. As stated in chapter 1.2.2 neutrinos in the Standard Model are massless particles. The measurement of Neutrino Oscillations implies a non-vanishing neutrino rest-mass, thus implying that the Standard Model has to be extended.

Neutrino Oscillation exists due to different flavor and mass eigenstates, which force non-zero mass differences between the different mass states [18]. Since neutrinos in the standard model do not couple to the Higgs, the existence of the Higgs boson itself does not solve this.

2.2 History

First hypothesized about by Bruno Pontocorvo in his work about leptonic charge conservation [28], neutrino oscillations are now a measured fact. The indicative measurement was performed by the Super-Kamiokande Collaboration in 1998 [31] for atmospheric and the SNO Collaboration in 2001 [32] for solar neutrino oscillations. The later one also solved the long standing solar neutrino problem (see section 2.2.1), explaining the observed deficit in neutrino rates in comparison to the theoretical values from solar fusion reactions. Both experiments were awarded the Nobel Prize in Physics in 2015 [33].

2.2.1 The Solar Neutrino Problem

The energy production in the sun is driven by fusion reactions [21]. The processes and their energy production are very well known, as is the emitted energy of the sun. In the fusion processes neutrinos are produced in great abundance. Due to the precise knowledge of the energy production mechanism, the number of produced neutrinos and their energy spectrum can be predicted very well and is shown in figure 2.1.

One first experiment to measure the neutrino flux of the sun was the Homestake Solar Neutrino Detector [35] as proposed by Raymond Davis Jr. in 1964 [36]. The detector is located in the Homestake Gold Mine, in South Dakota (USA) and used 615 t tetrachloroethylene as an interaction target for the solar electron neutrinos with the reaction

$$\nu_\mathrm{e} + {}^{37}_{17}\mathrm{Cl} \longrightarrow {}^{37}_{18}\mathrm{Ar} + \mathrm{e}^- \quad . \tag{2.1}$$

${}^{37}_{18}\mathrm{Ar}$ is an unstable isotope with a half-life of $t_{1/2} = 35.04\,\mathrm{d}$. Thus, the number of catched neutrinos can be measured from the recorded argon decays. The result of this measurement

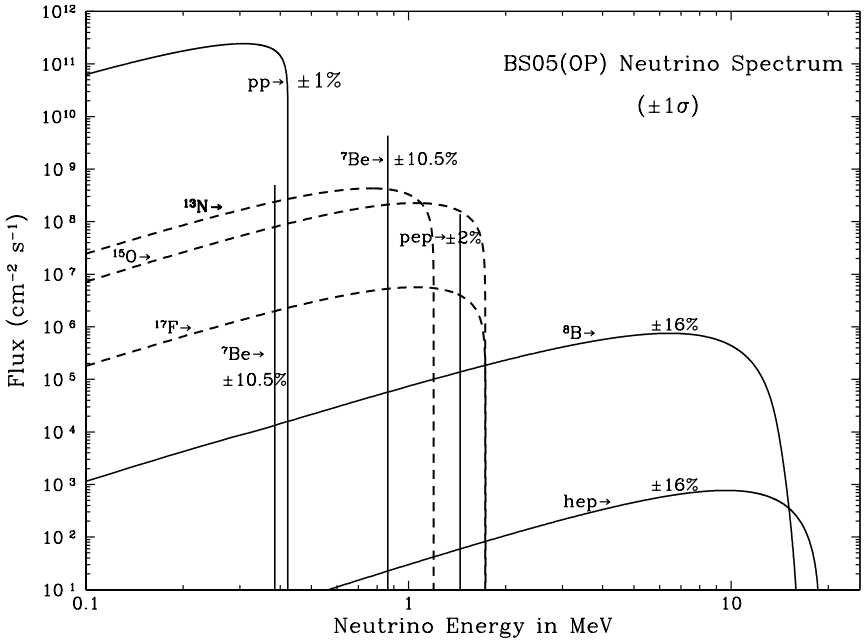

Figure 2.1: The energy dependent solar electron neutrino flux for different production channels [34].

was a neutrino flux that is, depending on the used solar model, only 27-40 % of the predicted flux and not explainable with systematic or model uncertainties.

To solve the solar neutrino riddle supplemental detectors have been build. Since the energetic threshold for the chlorine-argon transmutation is 814 keV [35] an important part of the neutrino energy spectrum (see figure 2.1) could not be explored with the Homestake experiment. The Gallium-Experiment (GALLEX) [37, 38] and its successor the Gallium Neutrino Observatory (GNO) [39] at the Laboratori Nazionali del Gran Sasso (LNGS) in Italy as well as the Soviet-American Gallium Experiment (SAGE) [40] at the Baksan Neutrino Observatory in Russia lower the detection threshold to about 233 keV [38]. In these detectors gallium is used as a target for the solar neutrinos. The resulting reaction is

$$\nu_e + {}^{71}_{31}\mathrm{Ga} \longrightarrow {}^{71}_{32}\mathrm{Ge} + e^- \quad . \tag{2.2}$$

All the gallium based experiments confirm the results from the Homestake experiment.

Another experiment that was used to verify the Homestake result is the Super Kamiokande experiment [41] (see section 2.4.2). The electron neutrino flux that was measured with this detector is also only ∼40 % of the expected flux [42, 43, 44, 34], thus confirming the Homestake result.

The Sudbury Neutrino Observatory

To solve the solar neutrino problem, the Sudbury Neutrino Observatory (SNO) was built [45]. It utilizes a spherical volume of one kiloton of D_2O for the detector and is located in the Creighton mine near Sudbury, Canada in a depth of ∼2040 m. SNO can detect the elastic scattering (ES) of electron neutrinos on electrons

$$\nu_e + e^- \longrightarrow \nu_e + e^- \tag{2.3}$$

through the light emission due to the Čerenkov effect. Charged particles like electrons that move faster than the speed of light in this medium generate a light emission that can be detected by light detectors. This effect is discussed in more detail in section 3.2.2. The scattered electron follows the direction of the neutrino, thus this interaction can be used for pointing.

However, the usage of heavy water also permits the following interactions

$$\nu_e + d \longrightarrow e^- + p + p \quad , \tag{2.4}$$

$$\nu + d \longrightarrow \nu + p + n \quad . \tag{2.5}$$

With the interaction of equation 2.4 the electron neutrino flux can be probed. The charged current interaction has an energy threshold of 1.442 MeV [6]. The other neutrino flavors can be neglected. The detection is performed via the produced electron which has an energy that is highly correlated with the electron energy [45].

The interaction of equation 2.5 is a neutral current interaction with a threshold of 2.225 MeV and thus all three neutrino flavors can interact this way [6]. The resulting neutron can be cought by the deuterium of the heavy water or ^{35}Cl which was added to the water [45]. The catched neutron produces a characteristic γ with an energy of 6.25 MeV for the deuterium and 8.6 MeV for the ^{35}Cl.

The energy threshold of SNO permits the probing of the ^{8}B neutrino flux. The different detection mechanisms permit the measurement of the electron neutrino and the total neutrino flux. The result of the electron neutrino flux measurement was compatible with the measurements of the previous experiments with the flux being lower than expected from the solar models [32]. The measurement of the total neutrino flux, however, is in very good agreement with the flux from the models. This means, that the neutrinos are not disappearing, but they have not the expected flavor. This result solves the solar neutrino problem and proves that neutrino oscillation does exist.

2.2.2 LSND

The Liquid Scintillator Neutrino Detector (LSND) [46] was a short baseline neutrino oscillation experiment at the Los Alamos National Laboratory from 1993 to 1998 [47]. A 798 MeV proton beam from a linear accelerator was first shot into a water target to produce pions. Later a high-Z target was used as a target. Muon neutrinos result from decaying π^+ and μ^+ in rest, while most π^- and μ^- are captured by a Fe shield or the beam stop. The neutrino flux behind the shielding should be mostly of $\bar{\nu}_\mu$ with the expected $\bar{\nu}_e$ flux being only $\sim 8 \cdot 10^{-4}$ of the $\bar{\nu}_\mu$

flux. The detector consisted of 167 t of scintillator in form of mineral oil and photomultiplier tubes (PMTs). It was distanced 30 m from the target. Neutrinos interacting in the scintillator produced light that was detected by the PMTs.

In 1995 LSND reported an excess of electron neutrinos above the expected background level in the energy range of 36 MeV to 60 MeV [48]. This excess was confirmed in subsequent measurements of LSND [49, 50, 51, 47] in an energy range of 20 MeV to 200 MeV.

From oscillations between the three known neutrino flavors one would not expect to detect an excess for these energies and baselines. This was seen as one indication for more then three neutrino flavors, the extra flavors being sterile to weak interactions. This is further discussed in section 2.3.4.

Additional measures by the KARMEN[1] experiment could not confirm measurements of LSND, but also could not disprove it [52]. In 2013 the MiniBooNE[2] experiment found a 2.8σ excess in the energy range of 200 MeV to 1250 MeV [53]. This gives an allowed region for $\bar{\nu}_\mu \to \bar{\nu}_\mathrm{e}$ that has some overlap with the result from LSND.

2.3 Theory of Neutrino Oscillations

In the following sections the theory behind the neutrino oscillations is derived. This derivation closely follows that given in chapter 7.1 of [18]. The focus is on the quasi-standard plane-wave approximation that was suggested as an analogon to the $K^0 - \bar{K}^0$ mixing in the quark sector by Pontocorvo [28]. He described a mixing between the ν_e and another, supposedly sterile ν. This ansatz was then refined by Eliezer and Swift in 1975 [54] and Fritzsch and Minkowski in 1976 [55] to solve the solar neutrino puzzle (see section 2.2.1). The completed theory was then reviewed by Bilenky and Pontecorvo in 1977 [56].

A differing ansatz with fewer assumptions is the wave packet treatment as first suggested by S. Nussinov in 1976 [57]. B. Kayser showed 1981 in a refined version, that this alternative yields the same result as the standard treatment [58]. A newer theory is the space-time approach from J. Rich that avoids the two defined neutrino states of the other theories and instead treats the emission, propagation and absorption of the neutrino as a single coherent quantum-mechanical process [59].

2.3.1 Neutrino Oscillations in Vacuum

Neutrino oscillations are an intrinsic feature of neutrinos. Most of the time neutrinos are separated into three particles by their flavor, that is the flavor of the lepton with which they are interacting. The physical particle, however, is not bound to one flavor, but one mass. If mass and flavor eigenstate would be the same, no neutrino oscillation would be visible. The existence of neutrino oscillation means that flavor eigenstates ν_α are a mixture of different mass eigenstates ν_k and vice versa. The different eigenstates are linked via a rotation matrix U called the PMNS matrix in honor to the theorists behind the neutrino oscillation theory

[1] KArlsruhe Rutherford Medium Energy Neutrino Experiment
[2] BooNE is short for “Booster Neutrino Experiment”

(Pontocorvo, Maki, Nakagawa, Sakata). The matrix U fulfills the unitarity relation

$$U^\dagger U = UU^\dagger = 1 \quad . \tag{2.6}$$

This means also that

$$\sum_\alpha U^*_{\alpha k} U_{\alpha j} = \delta_{jk} \quad \text{and} \quad \sum_k U_{\alpha k} U^*_{\beta k} = \delta_{\alpha\beta} \quad . \tag{2.7}$$

In the following flavor states are marked by Greek letters, where as mass states are marked by roman letters. The flavor states are linear combinations between the matrix U^* and the mass states $|\nu_k\rangle$

$$|\nu_\alpha\rangle = \sum_k U^*_{\alpha k} |\nu_k\rangle \quad , \quad \alpha = e, \mu, \tau \quad . \tag{2.8}$$

In the same way the mass states can be expressed as linear combinations of the matrix U and the flavor states $|\nu_\alpha\rangle$

$$|\nu_k\rangle = \sum_\alpha U_{\alpha k} |\nu_\alpha\rangle \quad , \quad k = 1, 2, 3 \quad . \tag{2.9}$$

The mass states are orthogonal to each other, as are the flavor states

$$\langle \nu_k | \nu_j \rangle = \delta_{kj} \quad , \quad \langle \nu_\alpha | \nu_\beta \rangle = \delta_{\alpha\beta} \quad . \tag{2.10}$$

The mass states represent the physical neutrino particle, are eigenvectors to the Hamilton operator in vacuum and yield the energy of the neutrino as the eigenvalue.

$$\mathscr{H} |\nu_k\rangle = E_k |\nu_k\rangle \tag{2.11}$$

It can be assumed that the neutrino is traveling close to the speed of light and thus its momentum $\mathbf{p}$ is very high. Also the rest-mass m_k of the neutrino is very small. With this in mind the energy eigenvalue E_k of the neutrino can be approximated to

$$E_k = \sqrt{\mathbf{p}^2 + m_k^2} \simeq E + \frac{m_k^2}{2E} \quad . \tag{2.12}$$

Here E is the kinetic energy of the neutrino. The time evolution of $|\nu_k\rangle$ is given by the Schrödinger equation

$$i \frac{\mathrm{d}}{\mathrm{d}t} |\nu_k(t)\rangle = \mathscr{H} |\nu_k(t)\rangle \quad . \tag{2.13}$$

A solution of this differential equation is a plane wave with

$$|\nu_k(t)\rangle = e^{-iE_k t} |\nu_k(0)\rangle \quad . \tag{2.14}$$

Since the flavor states are a linear combination of the mass states, we can substitute $|\nu_k(t)\rangle$ with equation 2.8 and get

$$|\nu_\alpha(t)\rangle = \sum_k U^*_{\alpha k} e^{-iE_k t} |\nu_k(0)\rangle \quad . \tag{2.15}$$

The neutrino is produced in a weak interaction with a lepton, thus at the time $t = 0$ the flavor state of the neutrino is equal to the lepton flavor α with $|\nu_\alpha(t=0)\rangle = |\nu_\alpha\rangle$.

To get the time evolution of the flavor state we can combine the equations 2.15 and 2.9 to

$$|\nu_\alpha(t)\rangle = \sum_{\zeta=\alpha,\beta,\gamma} \left(\sum_k U^*_{\alpha k} e^{-iE_k t} U_{\zeta k} \right) |\nu_\zeta\rangle \quad . \tag{2.16}$$

A neutrino of flavor α with an energy E_k can thus be expressed as a superposition of different flavors ζ. The transition amplitude between a flavor α and a flavor β is given by the scalar product of the two flavor states as

$$\psi_{\nu_\alpha \to \nu_\beta} = \langle \nu_\beta | \nu_\alpha(t) \rangle = \sum_k U^*_{\alpha k} U_{\beta k} e^{-iE_k t} \quad . \tag{2.17}$$

Since different flavor states are orthogonal to each other, the sum over the flavor states vanishes. The transition probability from α to β is now

$$P_{\nu_\alpha \to \nu_\beta}(t) = |\psi_{\nu_\alpha \to \nu_\beta}(t)|^2 = \sum_{k,j} U^*_{\alpha k} U_{\beta k} U_{\alpha j} U^*_{\beta j} e^{-i(E_k - E_j)t} \quad . \tag{2.18}$$

Using equation 2.12 the difference of the energy eigenvalues can be approximated to

$$E_k - E_j \simeq \frac{\Delta m^2_{kj}}{2E} \quad \text{with} \quad \Delta m^2_{kj} \equiv m^2_k - m^2_j \quad , \tag{2.19}$$

with the squared mass differences Δm^2_{kj} between the mass states of the neutrino. The phase of the neutrino oscillation probability is sensitive to the difference of the neutrino mass states, but not to the absolute mass value itself with

$$P_{\nu_\alpha \to \nu_\beta}(t) = \sum_{k,j} U^*_{\alpha k} U_{\beta k} U_{\alpha j} U^*_{\beta j} \exp\left(-i \frac{\Delta m^2_{kj} t}{2E} \right) \quad . \tag{2.20}$$

If the mass states were equal, the phase term would always be 1 and there would be no time dependence and with this no neutrino oscillations. Since the neutrino is traveling near the speed of light, we can substitute the propagation time t with the traveled distance of the neutrino L due to $L = c \cdot t = t$ and get

$$P_{\nu_\alpha \to \nu_\beta}(L, E) = \sum_{k,j} U^*_{\alpha k} U_{\beta k} U_{\alpha j} U^*_{\beta j} \exp\left(-i \frac{\Delta m^2_{kj} L}{2E} \right) \quad . \tag{2.21}$$

It is more common to separate the equation into a constant term and an interference term by exploiting the unitarity of U. We can also separate the quartic product of U into a real and an imaginary part which leads to

$$\begin{aligned} P_{\nu_\alpha \to \nu_\beta}(L, E) = \delta_{\alpha\beta} &- 2 \sum_{k>j} \Re[U^*_{\alpha k} U_{\beta k} U_{\alpha j} U^*_{\beta j}] \left[1 - \cos\left(\frac{\Delta m^2_{kj} L}{2E} \right) \right] \\ &+ 2 \sum_{k>j} \Im[U^*_{\alpha k} U_{\beta k} U_{\alpha j} U^*_{\beta j}] \left[\sin\left(\frac{\Delta m^2_{kj} L}{2E} \right) \right] \quad . \end{aligned} \tag{2.22}$$

In this step the expression

$$\sum_k |U_{\alpha k}|^2 |U_{\beta k}|^2 = \delta_{\alpha\beta} - 2\sum_{k>j} \Re[U^*_{\alpha k} U_{\beta k} U_{\alpha j} U^*_{\beta j}] \tag{2.23}$$

is used. For a derivation see section A in the appendix. This probability was derived for neutrinos. In the case of anti-neutrinos we have to use the conjugated version of U for the derivation. For equation 2.22 this would mean that the imaginary part of the quartic product of U would flip its sign. The rest of the probability is identical.

The case $P_{\nu_\alpha \to \nu_\beta}$ for $\alpha \neq \beta$ is called the "transition probability". For $\alpha = \beta$ we see that $U^*_{\alpha k} U_{\beta k} U_{\alpha j} U^*_{\beta j}$ simplifies to $|U_{\alpha k}|^2 |U_{\alpha j}|^2$ and the imaginary part of equation 2.22 is zero. By using the identity $\sin^2(x) = \frac{1-\cos(2x)}{2}$ we can write

$$P_{\nu_\alpha \to \nu_\alpha}(L, E) = 1 - 4\sum_{k>j} |U_{\alpha k}|^2 |U_{\alpha j}|^2 \sin^2\left(\frac{\Delta m^2_{kj} L}{4E}\right) \tag{2.24}$$

which is called the "survival probability".

The PMNS matrix for the full three flavor case is[18]

$$U_{\text{PMNS}} = \begin{pmatrix} 1 & 0 & 0 \\ 0 & c_{23} & s_{23} \\ 0 & -s_{23} & c_{23} \end{pmatrix} \begin{pmatrix} c_{13} & 0 & s_{13} \\ 0 & 1 & 0 \\ -s_{13} & 0 & c_{13} \end{pmatrix} \begin{pmatrix} c_{12} & s_{12} e^{i\delta} & 0 \\ -s_{12} e^{i\delta} & c_{12} & 0 \\ 0 & 0 & 1 \end{pmatrix} \quad . \tag{2.25}$$

We see that this 3×3 mixing matrix depends only on a few different parameters. c_{ij} and s_{ij} are short for $\cos\theta_{ij}$ and $\sin\theta_{ij}$ where θ_{ij} are the different mixing angles. There are three different mixing angles that can be determined by measuring neutrino oscillations. Also there is a phase term $e^{i\delta}$. The phase δ impacts the probability difference between the neutrino and anti-neutrino case and thus is coupled to CP violation. With the matrix the oscillations of three different flavors into each other can be described.

Since it is relatively complex to calculate the probabilities for a full three flavor case, the following example is reduced to only two flavors of neutrinos. In this "two flavor case" we can explicitly calculate the transition and survival probability. In general the two flavor case is a good approximation as can be seen in figure 2.3. The PMNS matrix for two flavors simplifies to

$$U_{\text{PMNS}} = \begin{pmatrix} \cos\theta & \sin\theta \\ -\sin\theta & \cos\theta \end{pmatrix} \quad . \tag{2.26}$$

If the two flavor matrix is combined with equation 2.24, we get

$$P_{\nu_\alpha \to \nu_\alpha}(L, E) = 1 - \sin^2(2\theta) \sin^2\left(\frac{\Delta m^2 L}{4E}\right) \quad . \tag{2.27}$$

Here the identity $\sin(2x) = 2\sin(x)\cos(x)$ was used. Since we only have two flavors and the sum over the possible flavor states has to be 1, we can easily get the transition probability $P_{\nu_\alpha \to \nu_\beta} = 1 - P_{\nu_\alpha \to \nu_\alpha}$. For the application in experiments with a very long baseline and neutrino

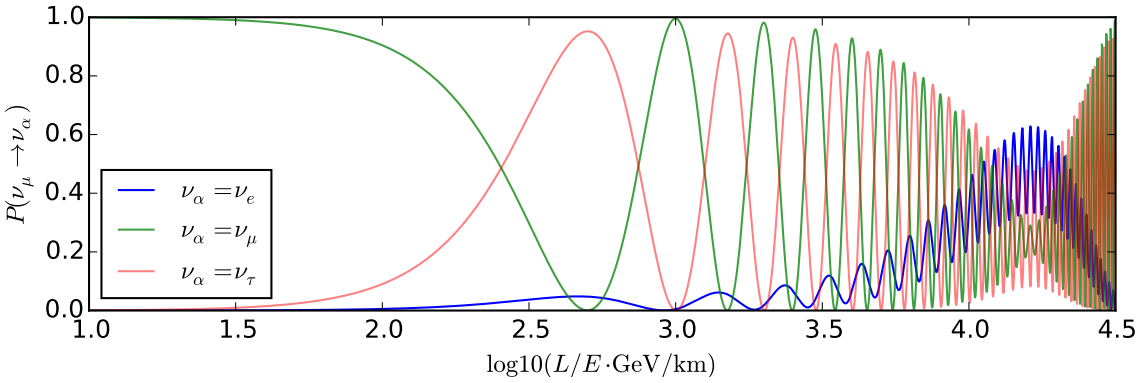

Figure 2.2: Transition probabilities and survival probability in vacuum for a muon neutrino in dependence of $\log_{10}(\frac{L/\mathrm{km}}{E/\mathrm{GeV}})$.

Table 2.1: Current values for neutrino parameters

Current values for neutrino parameters [11]	
mass m_ν from tritium decay	$< 2\,\mathrm{eV}$
Number N (LEP)	2.984 ± 0.008
$\sin^2(\theta_{12})$	0.304 ± 0.014
$\sin^2(\theta_{23})$ for normal mass hierarchy	$0.514^{+0.55}_{-0.56}$
$\sin^2(\theta_{23})$ for inverted mass hierarchy	$0.511 \pm +0.55$
$\sin^2(\theta_{13})$	$(2.19 \pm 0.12) \times 10^{-2}$
Δm^2_{21}	$(7.53 \pm 0.18) \times 10^{-5}\,\mathrm{eV}^2$
Δm^2_{32} for normal mass hierarchy	$(2.44 \pm 0.06) \times 10^{-3}\,\mathrm{eV}^2$
Δm^2_{32} for inverted mass hierarchy	$(2.49 \pm 0.06) \times 10^{-3}\,\mathrm{eV}^2$

energies above 1 GeV it is more convenient to use SI units ($\hbar c = 1.973 \cdot 10^{-16}\,\mathrm{GeV} \cdot \mathrm{m}$). We then get for the two flavor survival probability of muon neutrinos

$$P_{\nu_\mu \to \nu_\mu}(L, E) = 1 - \sin^2(2\theta) \cdot \sin^2\left(1.27 \cdot \Delta m^2/\mathrm{eV}^2 \frac{L/\mathrm{km}}{E_\nu/\mathrm{GeV}}\right) \quad . \tag{2.28}$$

Table 2.1 shows the actual World's best values for the neutrino mass, number and oscillation parameters.

2.3.2 Matter Effects

In section 2.3.1 we discussed neutrino oscillations in vacuum. However, if the neutrino transverses matter it can interact with it which alters the neutrino oscillation probability. All neutrino flavors can interact with a matter using as a neutral current (NC) interaction, while ν_e can also interact in a charged current (CC) interaction with the electrons in the matter (see figure 2.4). This section again uses the derivation found in [18] as a base.

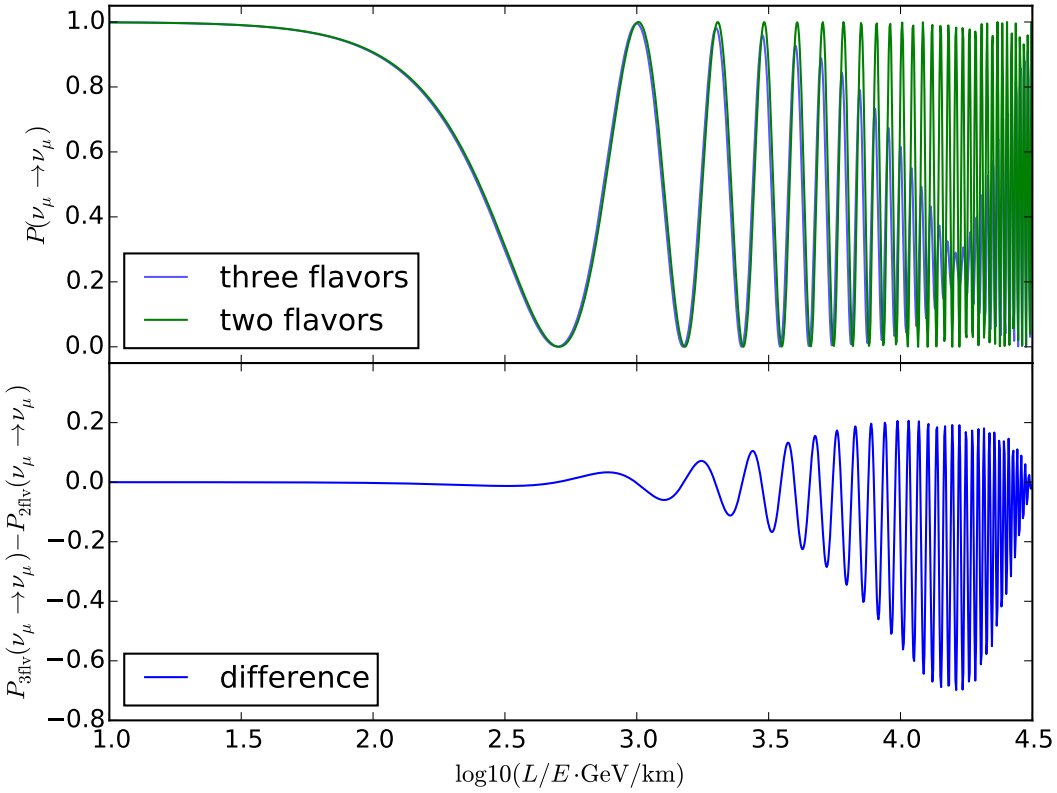

Figure 2.3: Top: Survival probabilities in vacuum for a muon neutrino for the three flavor and the two flavor case in dependence of $\log_{10}(\frac{L/\mathrm{km}}{E/\mathrm{GeV}})$. Bottom: Difference between three and two flavor case.

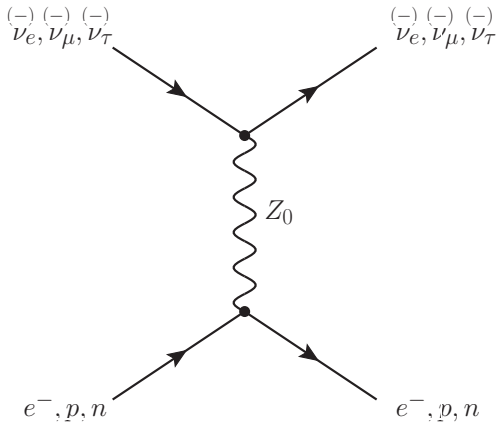

(a) Neutral current interaction between all ν flavors and all matter particles.

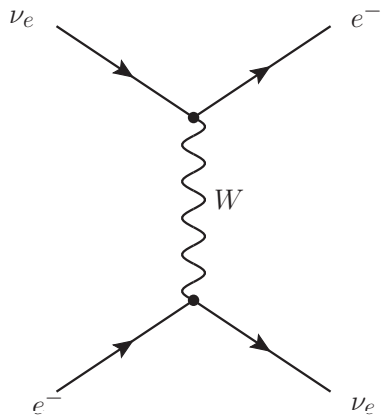

(b) Charged current interaction between a ν_e and an electron.

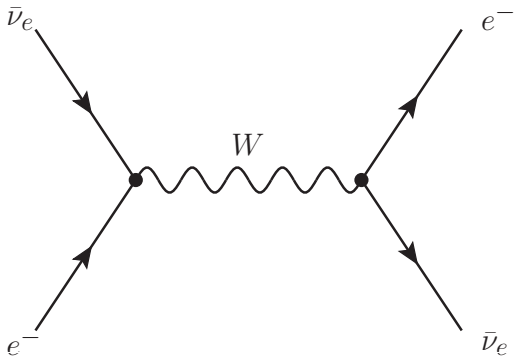

(c) Charged current interaction between a $\bar{\nu}_e$ and an electron.

Figure 2.4: Different interaction types between νs and matter.

The interaction with matter induces a potential due to coherent forward elastic scattering. This was first discovered by L. Wolfenstein in 1978 [60]. The effect of incoherent scattering is very small and can be neglected for low neutrino energies [18].

The possible interactions lead to extra matter potentials

$$V_{\mathrm{CC}} = \sqrt{2} G_{\mathrm{F}} N_e \quad \text{and} \quad V_{\mathrm{NC}} = -\frac{1}{2}\sqrt{2} G_{\mathrm{F}} N_n \tag{2.29}$$

the neutrino is subjected to [15, 61]. Here N_e is the electron density of the matter and G_{F} is the Fermi constant. Like in the previous section for the vacuum case, the flavor states are a linear combination of the mass states and elements of the PMNS matrix and vice versa with

$$|\nu_\alpha\rangle = \sum_k U^*_{\alpha k} |\nu_k\rangle \quad \text{and} \quad |\nu_k\rangle = \sum_\alpha U_{\alpha k} |\nu_\alpha\rangle \quad . \tag{2.30}$$

The mass states are eigenvectors to the Hamilton operator in vacuum with

$$\mathscr{H}|\nu_k\rangle = E_k |\nu_k\rangle \quad . \tag{2.31}$$

As in the previous section $E_k = \sqrt{\mathbf{p}^2 + m_k^2}$ is the total energy of the neutrino. The mass potentials that are impacting the neutrino modify the Hamilton operator and we get the Hamilton operator for a neutrino in matter as

$$\mathscr{H} = \mathscr{H}_0 + \mathscr{H}_1 \quad \text{with} \quad \mathscr{H}_1 |\nu_\alpha\rangle = V_\alpha |\nu_\alpha\rangle \quad . \tag{2.32}$$

At the time of production the neutrino has a definitive flavor α. The time evolution of the flavor state is expressed by the Schrödinger equation

$$i\frac{\mathrm{d}}{\mathrm{d}t} |\nu_\alpha(t)\rangle = \mathscr{H} |\nu_\alpha(t)\rangle \quad \text{with} \quad |\nu_\alpha(0)\rangle = |\nu_\alpha\rangle \quad . \tag{2.33}$$

From the time evolved flavor state we can derive the transition amplitude between the flavors α and β with $\psi_{\alpha\beta}(t) = \langle\nu_\beta|\nu_\alpha(t)\rangle$. At the time of production the neutrino has a definitive flavor and thus we have $\psi_{\alpha\beta}(0) = \delta_{\alpha\beta}$. The transition probability is now

$$P_{\nu_\alpha \to \nu_\beta}(t) = |\psi_{\alpha\beta}(t)|^2 \quad . \tag{2.34}$$

As for the vacuum case the Schrödinger equation together with the linear combinations of equation 2.30 give the time evolution of the transition amplitude in dependence of the energy eigenvalue and the new matter potential as

$$i\frac{\mathrm{d}}{\mathrm{d}t}\psi_{\alpha\beta}(t) = \sum_\eta \left(\sum_k U_{\beta k} E_k U^*_{\eta k} + \delta_{\beta\eta} V_\beta \right) \psi_{\alpha\eta}(t) \quad . \tag{2.35}$$

The transition amplitudes are orthogonal to each other and thus satisfy the relation $\sum_\eta \psi_{\alpha\eta}(t)\psi^*_{\beta\eta}(t) = \delta_{\alpha\beta}$ [18].

Like for the vacuum case, we can again use an approximation for the energy of the neutrino $E_k =\simeq E + \frac{m_k^2}{2E}$ as the rest-mass of the neutrino is assumed to be much smaller than the kinetic energy of the neutrino with $p \simeq E$. Since the neutrino is traveling near the speed of light this also means that $t \simeq x$.

Since the neutral-current potential affects all neutrino flavors the same way, it has no impact on the oscillation probability. It can be separated from the rest to get the equation

$$\begin{aligned} i\frac{\mathrm{d}}{\mathrm{d}x}\psi_{\alpha\beta}(x) = &\left(p + \frac{m_1^2}{2E} + V_{\mathrm{NC}} \right) \psi_{\alpha\beta}(x) \\ &+ \sum_\eta \left(\sum_k U_{\beta k} \frac{\Delta m^2_{k1}}{2E} U^*_{\eta k} + \delta_{\beta e}\delta_{\eta e} V_{\mathrm{CC}} \right) \psi_{\alpha\eta}(x) \quad . \end{aligned} \tag{2.36}$$

With a phase shift

$$\psi_{\alpha\beta}(x) \to \psi_{\alpha\beta}(x) e^{-i(p + m_1^2/2E)x - i\int_0^x V_{\mathrm{NC}}(x')\mathrm{d}x'} \tag{2.37}$$

that is not affecting the oscillation probability the expression $p + m_1^2/2E + V_{\mathrm{NC}}$ can be removed. The resulting Schrödinger equation

$$i\frac{\mathrm{d}}{\mathrm{d}x}\psi_{\alpha\beta}(x) = \sum_\eta \left(\sum_k U_{\beta k} \frac{\Delta m^2_{k1}}{2E} U^*_{\eta k} + \delta_{\beta e}\delta_{\eta e} V_{\mathrm{CC}} \right) \psi_{\alpha\eta}(x) \tag{2.38}$$

now describes the space evolution of the neutrino flavors in matter. Since only interactions between electrons and electron neutrinos are relevant, the impact of matter on the oscillation probability is strongly coupled to the electron density of the matter and not the matter density itself. Also, as for the vacuum case, the transition is dependent on the squared mass differences and not the mass of the neutrino eigenstates. The equation can be written as

$$i\frac{\mathrm{d}}{\mathrm{d}x}\boldsymbol{\psi}_\alpha = \mathscr{H}_\mathrm{F}\boldsymbol{\psi}_\alpha \quad . \tag{2.39}$$

Where $\mathscr{H}_\mathrm{F}$ is the effective Hamiltonian of the Schrödinger equation which can be separated into a part governed by the mass differences $\mathbb{M}$ and a part

$$A_\mathrm{CC} \equiv 2EV_\mathrm{CC} = 2\sqrt{2}EG_\mathrm{F}N_e \tag{2.40}$$

that is dependent on the matter potential.

$$\mathscr{H}_\mathrm{F} = \frac{1}{2E}(U\mathbb{M}^2U^\dagger + \mathbb{A}) \tag{2.41}$$

For the three flavor description of neutrino oscillations in matter one gets [18]

$$\boldsymbol{\psi}_\alpha = \begin{pmatrix}\psi_{\alpha e}\\ \psi_{\alpha\mu}\\ \psi_{\alpha\tau}\end{pmatrix} \quad , \quad \mathbb{M}^2 = \begin{pmatrix}0 & 0 & 0\\ 0 & \Delta m^2_{21} & 0\\ 0 & 0 & \Delta m^2_{31}\end{pmatrix} \quad , \quad \mathbb{A} = \begin{pmatrix}A_\mathrm{CC} & 0 & 0\\ 0 & 0 & 0\\ 0 & 0 & 0\end{pmatrix} \quad . \tag{2.42}$$

MSW Effect

As showed in the previous section, the oscillation probabilities in matter are modified due to the CC interaction between electron neutrinos and the electrons of the said matter. Under certain conditions (electron density and neutrino energy) the oscillation probability can reach maximal mixing, even if in vacuum this is not the case. This resonant amplification condition was discovered by Mikheev and Smirnov in 1985 [64, 65] and is called the MSW effect after Mikheev, Smirnov and Wolfenstein.

For simplicity we are now switching to a "two flavor case" between ν_e and ν_μ, thus the squared mass difference $\Delta m^2 = \Delta m^2_{21}$ and the mixing angle $\theta = \theta_{12}$. The case for $\nu_\mathrm{e} \to \nu_\tau$ mixing is equivalent. For a two flavor mixing between ν_μ and ν_τ the interactions between ν_e and electrons have no impact and we get the vacuum case. Again the derivation borrows from [18]. The full three flavor calculations for the MSW effect can be found in [66].

The matrix U for the two flavor case was defined in equation 2.26. With

$$\begin{aligned} 2\sin^2(x) &= 1 - \cos(2x) \quad ,\\ 2\cos^2(x) &= 1 + \cos(2x) \quad \text{and}\\ 2\sin(x)\cos(x) &= \sin(2x) \end{aligned}$$

we can write the Schrödinger equation 2.39 explicitly as

$$i\frac{\mathrm{d}}{\mathrm{d}x}\begin{pmatrix}\psi_{ee}\\ \psi_{e\mu}\end{pmatrix} = \left(\frac{\Delta m^2}{4E}\begin{pmatrix}1-\cos(2\theta) & \sin(2\theta)\\ \sin(2\theta) & 1+\cos(2\theta)\end{pmatrix} + \begin{pmatrix}V_\mathrm{CC} & 0\\ 0 & 0\end{pmatrix}\right)\begin{pmatrix}\psi_{ee}\\ \psi_{e\mu}\end{pmatrix} \quad . \tag{2.43}$$

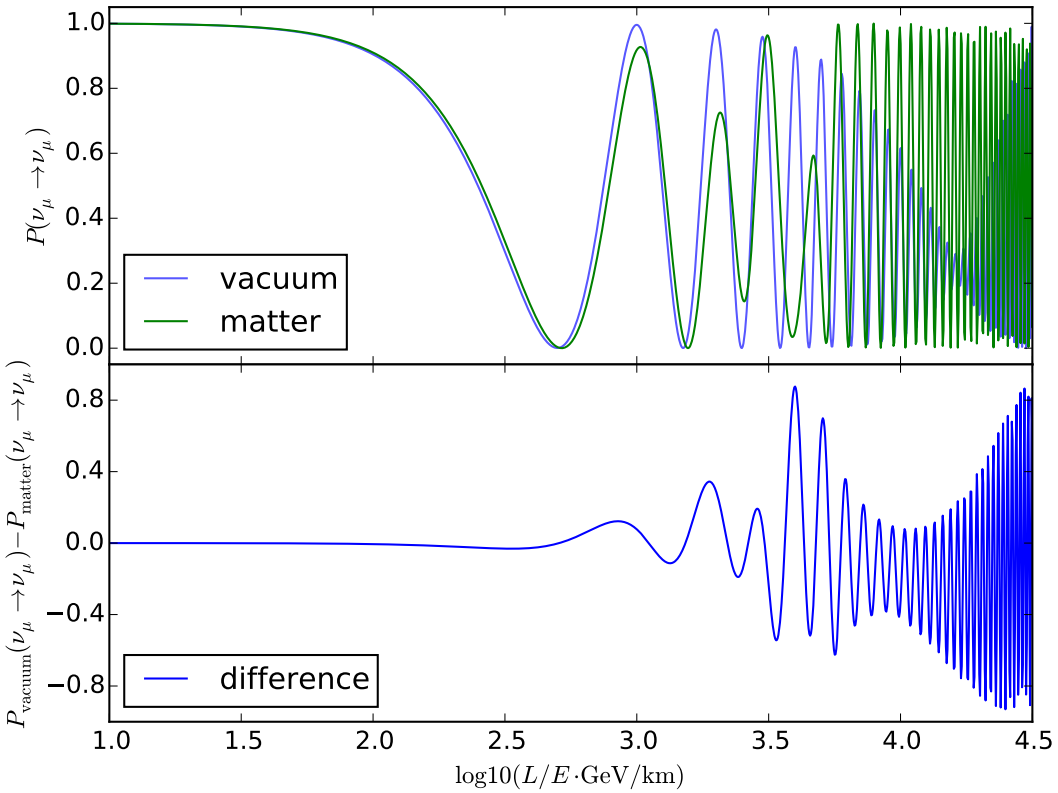

Figure 2.5: Top: Survival probability of muon neutrinos in vacuum (blue) and matter (green) in dependence of $\log_{10}(\frac{L/\text{km}}{E/\text{GeV}})$.
Bottom: Difference between the vacuum and the matter case. The survival probability in matter was calculated with NuCraft [62] using the Preliminary Reference Earth Model (PREM) [63] for the calculation of matter effects and Earth's diameter as the baseline L. The used neutrino oscillation parameters are taken from [11].

The common phase can be removed by shifting the phase of the wave function

$$\psi(x) \to \psi(x) e^{-i\Delta m^2 x/4E - i/2 \int_0^x V_{\mathrm{CC}}(x')\mathrm{d}x'} \quad . \tag{2.44}$$

This gives the evolution equation in matter for the two flavor case as

$$i\frac{\mathrm{d}}{\mathrm{d}x}\begin{pmatrix}\psi_{ee}\\ \psi_{e\mu}\end{pmatrix} = \frac{1}{4E}\begin{pmatrix}-\Delta m^2\cos(2\theta)+A_{\mathrm{CC}} & \Delta m^2\sin(2\theta)\\ \Delta m^2\sin(2\theta) & \Delta m^2\cos(2\theta)-A_{\mathrm{CC}}\end{pmatrix}\begin{pmatrix}\psi_{ee}\\ \psi_{e\mu}\end{pmatrix} \quad . \tag{2.45}$$

This equation describes the time evolution of the flavor states. Hence, the matrix

$$\mathscr{H}_{\mathrm{F}} = \frac{1}{4E}\begin{pmatrix}-\Delta m^2\cos(2\theta)+A_{\mathrm{CC}} & \Delta m^2\sin(2\theta)\\ \Delta m^2\sin(2\theta) & \Delta m^2\cos(2\theta)-A_{\mathrm{CC}}\end{pmatrix} \tag{2.46}$$

is the Hamiltonian matrix of the flavor base. The eigenvalues of the Hamiltonian matrix are the effective squared mass differences in matter m^2_{M} and can be obtained with the characteristic polynomial

$$\chi = \frac{1}{(4E)^2}[(\Delta m^2_{\mathrm{M}})^2 - (\Delta m^2\cos(2\theta) - A_{\mathrm{CC}})^2 - (\Delta m^2\sin(2\theta))^2] \tag{2.47}$$

as

$$\Delta m^2_{\mathrm{M}} = \pm\sqrt{(\Delta m^2\cos(2\theta) - A_{\mathrm{CC}})^2 + (\Delta m^2\sin(2\theta))^2} \quad . \tag{2.48}$$

Thus, the matrix $\mathscr{H}_{\mathrm{F}}$ can be diagonalized with

$$U_{\mathrm{M}}^T \mathscr{H}_{\mathrm{F}} U_{\mathrm{M}} = \mathscr{H}_{\mathrm{M}} = \frac{1}{4E}\mathrm{diag}(-\Delta m^2_{\mathrm{M}}, \Delta m^2_{\mathrm{M}}) \quad . \tag{2.49}$$

Here the unitarian matrix

$$U_{\mathrm{M}} = \begin{pmatrix}\cos(\theta_{\mathrm{M}}) & \sin(\theta_{\mathrm{M}})\\ -\sin(\theta_{\mathrm{M}}) & \cos(\theta_{\mathrm{M}})\end{pmatrix} \quad \text{with} \quad U_{\mathrm{M}}^{\mathrm{T}}U_{\mathrm{M}} = U_{\mathrm{M}}U_{\mathrm{M}}^{\mathrm{T}} = \mathbf{1} \tag{2.50}$$

has the shape of the two flavor mixing matrix from section 2.3.1 and connects the flavor and the effective matter amplitudes to each other with

$$\begin{pmatrix}\psi_{ee}\\ \psi_{e\mu}\end{pmatrix} = U_{\mathrm{M}}\begin{pmatrix}\phi_{e1}\\ \phi_{e2}\end{pmatrix} \quad . \tag{2.51}$$

The angle θ_{M} of U is the effective mixing angle in matter. The resulting diagonal elements of the Hamiltonian matrix in the matter basis $\mathscr{H}_{\mathrm{M}}$ are the effective squared mass differences in matter. From equation 2.49 one obtains the relation

$$\tan(2\theta_{\mathrm{M}}) = \frac{\tan(2\theta)}{1 - \frac{A_{\mathrm{CC}}}{\Delta m^2\cos(2\theta)}} \tag{2.52}$$

which defines the mixing angle θ_{M}. One can see, that the denominator of the equation can get to zero for specific

$$A^{\mathrm{R}}_{\mathrm{CC}} = \Delta m^2\cos(2\theta) \quad . \tag{2.53}$$

At this resonance the mixing gets maximal even if it is only small in vacuum. At the resonance the effective mass difference has its minimum and equals $\Delta m^2 \sin(2\theta)$. With equation 2.40 we can get the electron density for the resonance condition as

$$N_e^{\mathrm{R}} = \frac{\Delta m^2 \cos(2\theta)}{2\sqrt{2} E G_{\mathrm{F}}} \quad . \tag{2.54}$$

The resonance can occur for any initial value of θ below $\pi/4$. For greater values than $\pi/4$ the resonance is shifted to anti-neutrinos as the sign of the matter potential is swapped with $A \to -A$ [66].

With the definition 2.46 we can write the evolution equation 2.45 as

$$i\frac{\mathrm{d}}{\mathrm{d}x}\begin{pmatrix}\psi_{ee}\\ \psi_{e\mu}\end{pmatrix} = \mathscr{H}_{\mathrm{F}}\begin{pmatrix}\psi_{ee}\\ \psi_{e\mu}\end{pmatrix} \quad . \tag{2.55}$$

We can now substitute the flavor amplitudes with the effective matter amplitudes by using the relation 2.51 and get

$$i\frac{\mathrm{d}}{\mathrm{d}x}\left(U_{\mathrm{M}}\begin{pmatrix}\phi_{e1}\\ \phi_{e2}\end{pmatrix}\right) = \mathscr{H}_{\mathrm{F}} U_{\mathrm{M}}\begin{pmatrix}\phi_{e1}\\ \phi_{e2}\end{pmatrix} \quad . \tag{2.56}$$

If the transpose of effective mixing matrix in matter is multiplied to the left, the matrix $\mathcal{H}_{\mathrm{F}}$ is diagonalized to $\mathcal{H}_{\mathrm{M}}$ (see equation 2.49). This gives us the effective evolution equation in matter as

$$i\frac{\mathrm{d}}{\mathrm{d}x}\begin{pmatrix}\phi_{e1}\\ \phi_{e2}\end{pmatrix} = \left(\mathcal{H}_{\mathrm{M}} - iU_{\mathrm{M}}^T\left(\frac{\mathrm{d}}{\mathrm{d}x}U_{\mathrm{M}}\right)\right)\begin{pmatrix}\phi_{e1}\\ \phi_{e2}\end{pmatrix} = \frac{1}{4E}\begin{pmatrix}-\Delta m^2_{\mathrm{M}} & -i4E\frac{\mathrm{d}\theta_{\mathrm{M}}}{\mathrm{d}x}\\ i4E\frac{\mathrm{d}\theta_{\mathrm{M}}}{\mathrm{d}x} & \Delta m^2_{\mathrm{M}}\end{pmatrix}\begin{pmatrix}\phi_{e1}\\ \phi_{e2}\end{pmatrix} \quad . \tag{2.57}$$

Here we used that U_{M} is unitary. From equation 2.57 we see, that the evolution of the neutrino amplitudes is dependent on the change of electron density along the path of the neutrino. To get the transition and survival probability one has to know the electron density profile of the matter the neutrino is crossing and has to integrate along the path. In general this is not trivial. Figure 2.5 shows the impact of matter effects for neutrinos that cross the Earth through the Earth's core. The first oscillation minimum is only slightly shifted, whereas for later minima the differences become larger. In the following sections some simple cases that are relevant for neutrinos crossing the Earth are discussed.

Oscillation for Neutrinos Crossing the Earth

The most widely used model of the Earth's interior is the Preliminary Reference Earth Model (PREM)[63] from 1981 [67]. In contrast to other models like the newer IASP91 model [68] from 1991 PREM does not only give the speed of seismic waves but also the density profile. It was created by using measurements of the speed of seismic waves from earthquakes.

The Earth's density profile as shown in figure 2.6 can be roughly segmented into three bigger regions. The inner and outer core and the mantle and crust. The Earth's core is mainly composed of iron (∼80 %), sulfur (∼9 %) and nickel (∼7 %) [67]. Thus the electron to nucleon ratio in this region can be estimated to $\frac{N_{\mathrm{e,core}}}{N_{\mathrm{p,core}}+N_{\mathrm{n,core}}} \approx 0.47$. The matter density of the inner

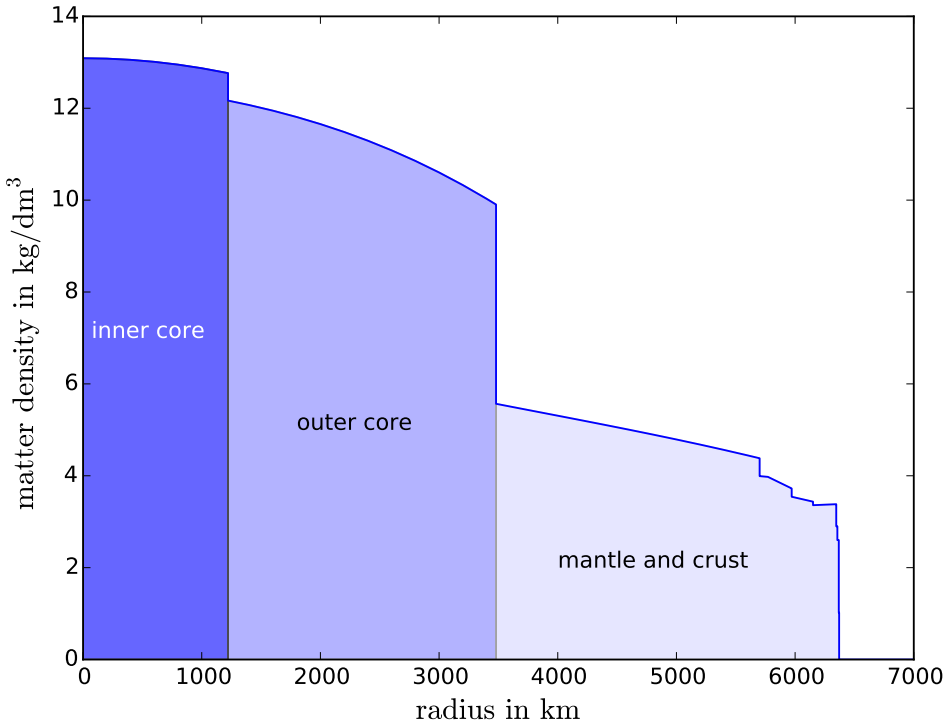

Figure 2.6: The matter density profile of the Earth as specified in the Preliminary Reference Earth Model (PREM)[63].

core is nearly constant while the density of the outer core is changing with bigger radius by about 20%. The boundary between the solid inner and the liquid outer core is marked by a discontinuity in the density profile.

The rapid chance in matter density at a radius of about 3480 km marks the core-mantle boundary (CMB) which is caused by the change in composition from the liquid metal outer core to a solid lower mantle of silicate [67]. The mantle mainly consists of oxygen (∼44 %), magnesium (∼23 %) and silicon (∼21 %). The electron to nucleon ratio of the mantle can be estimated to $\frac{N_{\mathrm{e,mantle}}}{N_{\mathrm{p,mantle}}+N_{\mathrm{n,mantle}}} \approx 0.50$. The outer layers of the mantle-crust region is characterized by several discontinuities in the density profile. These are the boundaries between the lower mantle, the transition zone, the upper mantle and the crust. There are also smaller discontinuities inside the upper mantle and the crust.

Inside the inner layers of the Earth, the matter composition is stable and the density is nearly constant (inner core) or only increasing moderately in a continuous way (outer core, lower mantle).

Matter of Constant Electron Density

If the electron density is constant the off-diagonal therms in equation 2.57 become zero. This means the mixing matrix U_{M} is not affected by a spacial differentiation. In this case the amplitude evolution looks like the one for the vacuum case with the mixing parameters θ and Δm^2 substituted by the effective parameters in matter θ_{M} and Δm^2_{M}. For the solution of the differential equation we can use a plane wave ansatz like in section 2.3.1.

Thus the transition probability of the neutrino looks similar to the vacuum case of equation 2.27 with

$$P_{\nu_{\mathrm{e}}\to\nu_{\mu},\mathrm{M}}(x,E) = \sin^2(2\theta_{\mathrm{M}})\sin^2\left(\frac{\Delta m^2_{\mathrm{M}} x}{4E}\right) \quad . \tag{2.58}$$

Because the sum over all probabilities is $P_{\nu_{\mathrm{e}}\to\nu_{\mathrm{e}},\mathrm{M}} + P_{\nu_{\mathrm{e}}\to\nu_{\mu},\mathrm{M}} = 1$ we can easily get the survival probability as

$$P_{\nu_{\mathrm{e}}\to\nu_{\mathrm{e}},\mathrm{M}}(x,E) = 1 - \sin^2(2\theta_{\mathrm{M}})\sin^2\left(\frac{\Delta m^2_{\mathrm{M}} x}{4E}\right) \quad . \tag{2.59}$$

Slab Approximation

In the previous section the case of constant electron density was discussed. However, from figure 2.6 we can conclude, that apart from the inner core region, the matter and electron density cannot be seen as constant. As an approximation the different layers of the Earth can, however, be segmented into smaller slaps of constant electron density. An example of this is shown in figure 2.7. Inside the slab the electron density is constant and the off-diagonal terms of equation 2.57 vanish. The solution for the evolution equation inside the slab is a plane wave with the width of the slap $\Delta x = x_1 - x_0$ as propagation length. Since the mixing matrix is not affected by the spatial differentiation, the solutions to the evolution equation are

$$\boldsymbol{\phi}_e(x_0+\Delta x) = K_{\mathrm{M}}\boldsymbol{\phi}_e(x_0) \quad \text{and} \quad \boldsymbol{\psi}_e(x_0+\Delta x) = U K_{\mathrm{M}} U^{\mathrm{T}} \boldsymbol{\psi}_e(x_0) \quad . \tag{2.60}$$

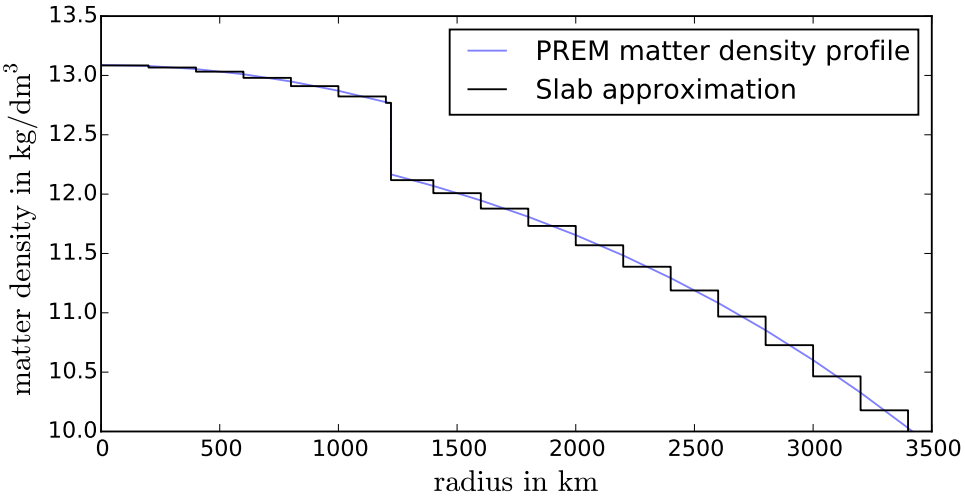

Figure 2.7: Part of the matter density profile of the PREM and its slab approximation.

Here

$$\boldsymbol{\phi}_e = \begin{pmatrix} \phi_{e1} \\ \phi_{e2} \end{pmatrix} \tag{2.61}$$

is the wave function in the effective matter base and

$$\boldsymbol{\psi}_e = \begin{pmatrix} \psi_{ee} \\ \psi_{e\mu} \end{pmatrix} \tag{2.62}$$

is the wave function in the flavor base. The evolution operator

$$K_{\mathrm{M}} = \begin{pmatrix} \exp(i\Delta m^2_{\mathrm{M}} \Delta x/4E) & 0 \\ 0 & \exp(-i\Delta m^2_{\mathrm{M}} \Delta x/4E) \end{pmatrix} \tag{2.63}$$

expresses the spatial evolution of the different components of the effective matter wave function. At the beginning of each slab the initial flavor state is given by the end state of the previous slab. Thus, the evolution in the slab approximation for n slabs and a complete propagation length X is

$$\boldsymbol{\psi}_e(x_n) = \left[\prod_{i=1}^{n} K_i \right] \boldsymbol{\psi}_e(x_0) \quad . \tag{2.64}$$

$K_i = U_i K_{\mathrm{M,i}} U_i^{\mathrm{T}}$ is then the evolution operator in the flavor base for the ith slab with the width $(\Delta x)_i = x_i - x_{i-1}$.

Parametric Resonance

Due to the MSW effect the flavor transition of neutrinos is boosted. The mixing amplitude can get maximal for a neutrino in matter even if the mixing amplitude in vacuum is small. Another

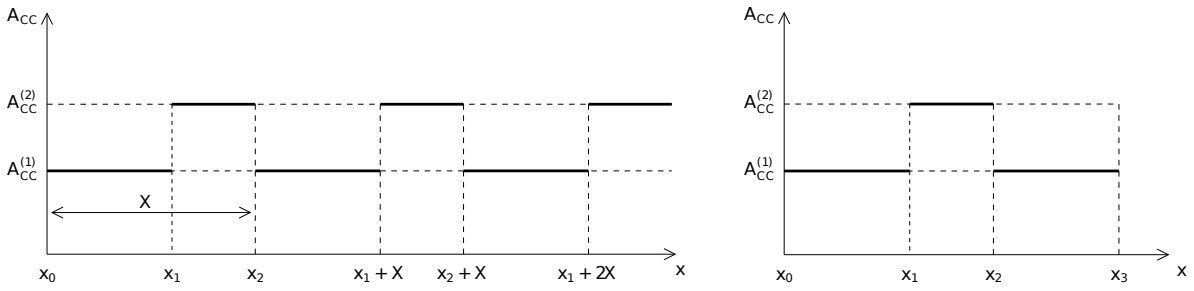

(a) Castle wall profile

(b) One and a half periods

Figure 2.8: The castle wall matter density profiles (from [18]).

effect to increase the transition probability is the "parametric resonance" [69, 70]. Apart from the oscillation amplitude the oscillation phase of a neutrino is changed in matter of varying electron density. If the density profile is periodic (see figure 2.8), this change in phase can accumulate and greatly influence the transition probability between neutrino flavors. This happens, for example, if a neutrino is crossing the Earth through the Earth's core [71].

The core-transition can be approximated with a "caste wall" matter density profile with one and a half periods [18]. For simplification the matter density of the core and the mantle is assumed to be constant. If we see this as a simple slab approximation, the density profile the neutrino has to transverse thus consists of three slabs and

$$\boldsymbol{\psi}_e(x_3) = K_1 K_2 K_3 \boldsymbol{\psi}_e(x_0) \quad . \tag{2.65}$$

It can be found [18], that in this case the transition probability in a two flavor representation is

$$P_{\nu_e \to \nu_\mu} = [2 s_1 \sin(2\theta_{\mathrm{M1}})(c_1 c_2 - s_1 s_2 \cos(2(\theta_{\mathrm{M1}} - \theta_{\mathrm{M2}}))) + s_2 \sin(2\theta_{\mathrm{M2}})]^2 \tag{2.66}$$

with

$$s_i = \sin\left(\frac{\Delta m^2_{\mathrm{Mi}}(x_i - x_{i-1})}{4E}\right) \quad \text{and} \quad c_i = \cos\left(\frac{\Delta m^2_{\mathrm{Mi}}(x_i - x_{i-1})}{4E}\right) \quad . \tag{2.67}$$

2.3.3 Neutrino Mass Hierarchy

From table 2.1 one can see, that the squared mass differences between the different massive neutrino states to this date are relatively good known. However, what is not known in the mass ordering also known as mass hierarchy between the third mass state and the other ones. For these, the second mass state is heavier than the first mass state [45]. Figure 2.9 shows the two different possible orderings for the mass state. The ordering where the two similar masses states 1 and 2 are also the lightest neutrino states or the inverse ordering where these two mass states are the heaviest ones.

The sign of Δm^2_{32} has jet to be determined. Several experiments planed to solve this question.

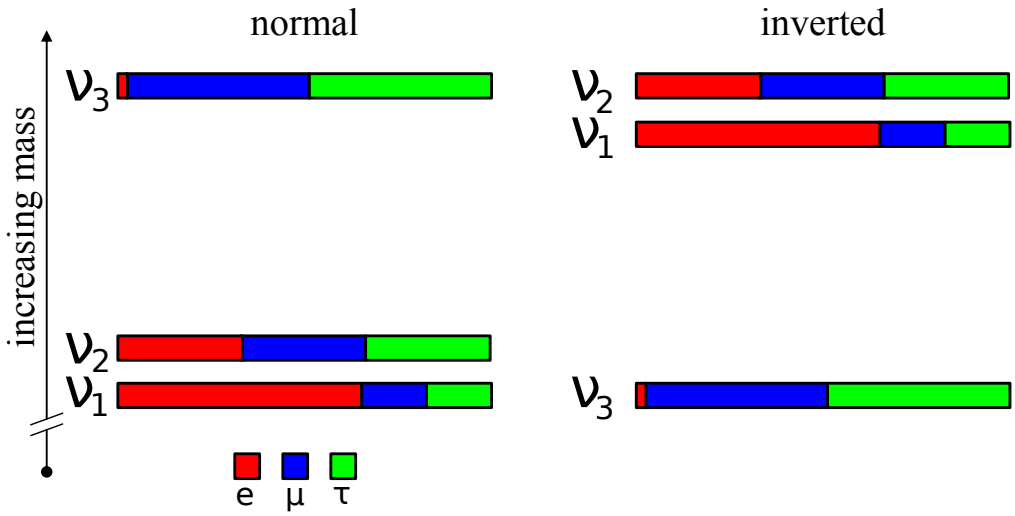

Figure 2.9: Different possible orderings for the neutrino mass states. Each mass state is a linear combination of the three possible flavor states e, μ, τ. In the normal mass-hierarchy ordering the lightest mass state is the one with the largest fraction of electron flavor and the heaviest mass state is the one with the smallest fraction of electron flavor. In the inverse mass hierarchy the state that has the smallest fraction of electron flavor is the lightest one. The other two states keep their ordering. The picture was taken from [72] and slightly modified.

2.3.4 Sterile Neutrinos

Like was discussed in section 1.2 only three kinds of neutrinos are known as up to today. However, experiments like LSND indicate an oscillation of more than three flavors of neutrinos. As discussed in section 1.2.2 in the standard model neutrinos are defined as massless left-handed particles. Only left-handed neutrinos are observed in particle interactions. However, neutrino oscillations force non-zero squared mass differences and with this also neutrinos masses. Thus, right-helicital neutrinos can be generated by Lorentz boosting. In contrast to helicity, chirality is not bound to mass and only left-chiral neutrinos or right-chiral anti-neutrinos have been observed in particle interactions. If right-chiral neutrinos exist, they do not interact in weak, electromagnetic or strong interactions and are thus labeled as "sterile".

Sterile neutrinos only interact over gravitational force. The most popular models are the "minimal" models 3+1 and 3+2 [11]. As the name implies, the models include one or two right-handed sterile neutrino fields to the three "normal" left-handed neutrino fields. Since sterile neutrinos do not participate in weak interactions, they cannot be detected easily. However, if sterile neutrinos mix with the "normal" neurinos, they can be detected over the modification of the neutrino oscillation pattern. For this the mixing matrix has to be extended to a 4×4 or 5×5 matrix.

2.4 Atmospheric Neutrino Oscillation & Experiments

Several ongoing neutrino oscillation experiments utilize cosmic-ray interactions in the atmosphere as a neutrino source. Due to the size of the Earth, these experiments have very long baselines and operate at much higher neutrino energies than reactor or accelerator based experiments.

2.4.1 Atmospheric Neutrino Oscillations

Figure 2.10 depicts the principle of the measurement of atmospheric neutrino oscillations. Atmospheric neutrinos are produced in a height of about 20 km above ground. These neutrinos can then transverse the Earth mostly unhindered due to their low cross-section. If signals from interactions of these neutrinos are recorded in a ground-based neutrino detector like IceCube, the propagation length of the neutrino can be approximated from its measured zenith angle to a very good degree. A good general approximation for the propagation length is

$$L \approx D \cdot \cos(180^\circ - \vartheta) \quad \text{if} \quad \vartheta \gg 90^\circ. \tag{2.68}$$

Here $D \approx 12700\,\text{km}$ is the Earth's diameter and ϑ is the measured zenith angle. From a matter density profile like PREM [63] the electron density variations the neutrino is affected by can be extrapolated. Due to the very long baseline up to Earth's diameter and energies in the GeV regime, experiments dedicated to atmospheric neutrino oscillations are most sensitive to Δm^2_{32} and θ_{23} by measuring the disappearance of atmospheric muon neutrinos.

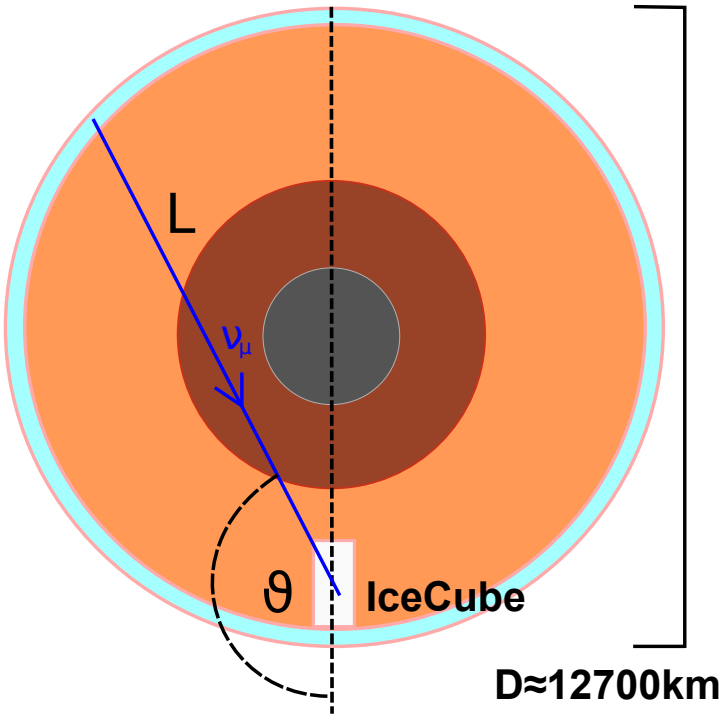

Figure 2.10: Sketch of an experimental setup to measure atmospheric muon neutrinos with IceCube. The ν_μ are produced in the atmosphere and transverse the Earth until they reach the IceCube detector. As a good approximation the propagation distance is only dependent on the Earth's diameter with $D \approx 12700\,\text{km}$ and the measured zenith angle ϑ of the neutrino inside the detector.

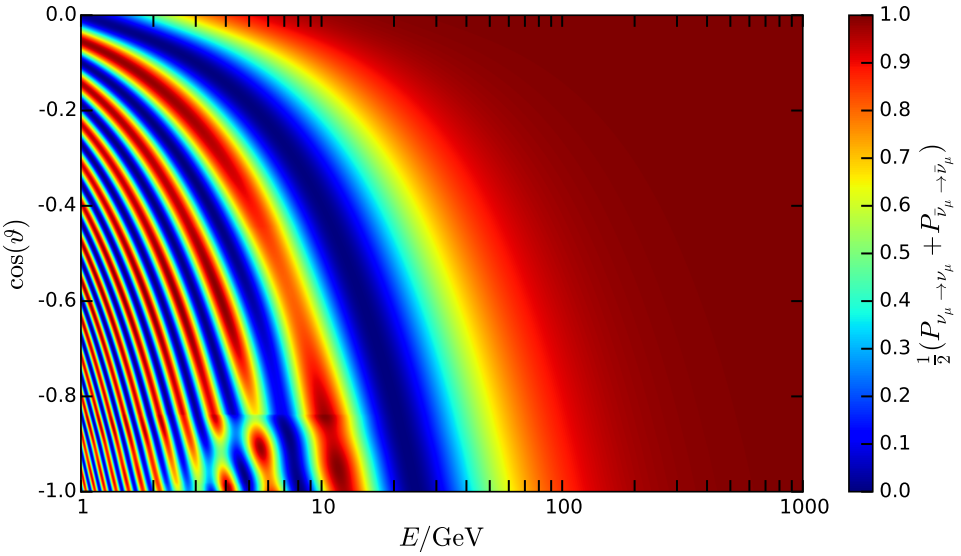

Figure 2.11: Survival probability of muon neutrinos reaching the IceCube detector in dependence to the energy and the zenith angle of the neutrino. The oscillogram was calculated with NuCraft [62] using the Preliminary Reference Earth Model (PREM) [63] for the calculation of matter effects. The used neutrino oscillation parameters are taken from [11].

2.4.2 Current Experiments

Several different neutrino experiments with the goal of measuring neutrino oscillations by measuring atmospheric neutrinos exist. The experiments running today are briefly discussed in the following sections.

IceCube/DeepCore

IceCube/DeepCore is a detector at the geographic South Pole [73]. For the measurement of neutrinos the natural grown glacial ice is used as a medium. Light sensors detect the faint light from fast charged particles inside the ice, that are produced in neutrino interactions. The detector is explained in more detail in chapter 3.

Figure 2.11 shows the survival probability for a 1:1 mix of ν_μ and $\bar{\nu}_\mu$. The survival probability was calculated by taking matter effects into account. Atmospheric neutrinos with a zenith angle of 180° have a minimal surviving probability at around 25 GeV. For lower inclinations the survival minimum is shifted to lower neutrino energies. Below about 15 GeV the oscillation pattern shows a distortion in the pattern due to matter effects becoming relevant. To fully resolve these effects, the detector has to be capable to measure below 10 GeV, though.

Several measurements of neutrino oscillations have been published by the IceCube collaboration [74, 75]. The sensitivity has reached a degree comparable to other, dedicated oscillation experiments.

ANTARES

The Astronomy with a Neutrino Telescope and Abyss environmental RESearch project (ANTARES) is a neutrino detector located in the Mediterranean sea of the coast of Toulon (France) in a depth of 2475 m [76]. The detection principle is identical to the one from IceCube. Instead of glacial ice, ANTARES uses the water of the Mediterranean see. This gives the advantage of a homogeneous medium without strong light scattering effects. The detector itself consists of 12 cables (lines) that are attached to the seabed. Each line then supports 75 optical sensors. The ANTARES collaboration published results from a neutrino oscillation analysis in 2012 [77].

Super-Kamiokande

The Super-Kamioka Neutrino Detection Experiment (Super-K) [41] consists of a large tank filled with 50.000 tons of pure water located in a depth of 1000 m in the Mozumi mine in Japan. The inner walls of the detector vessel are equipped with around 11100 photomultiplier tubes (PMTs). Neutrinos that enter the Super-K detector can interact in multiple ways with the detector medium. Low-energy neutrinos of solar origin (see 2.2.1) can interact over elastic scattering on electrons. The scattered electron produces Čerenkov light inside the detector and can be detected by the PMTs. This process has an energetic threshold of 4.5 MeV.

Atmospheric neutrinos and neutrinos from accelerators have higher energies in the range of GeV. At these energies muon neutrinos and electron neutrinos can interact in charged and neutral current interactions. Resulting muons and electrons can be distinguished by differing Čerenkov patterns in the detector [78]. An electron will produce a fuzzy ring of light on the PMTs, while a muon produces a ring with a sharp edge.

The Super-K experiment was the first experiment to measure the oscillation of atmospheric neutrinos [31].

2.4.3 Future Experiments

Several future experiments measuring atmospheric neutrinos are planed. These experiments are designed to give an answer to the question of the neutrino mass ordering and also will measure the atmospheric oscillation parameters Δm^2_{32} and θ_{23} with more precision than today.

PINGU

The Precision IceCube Next Generation Upgrade (PINGU) is a planed low-energy extension of the IceCube detector [79]. Its planed to build upon the successful low-energy extension DeepCore by raising the amount of sensors in the deep and clear ice even more. The sensors are planed to be installed on cables and deployed into boreholes that are driven into the glacial ice. About 4000 new sensors would bring the energy threshold of IceCube down from the 10 GeV of DeepCore and simultaneously raise the statistics of low-energy muon neutrino events by a factor of three. The detector is designed to be fully efficient at 8 GeV and ∼50 % efficient at 3 GeV.

ORCA

The successor of ANTARES will be the Cubic Kilometer Neutrino Telescope (KM3NeT) with its dedicated low-energy extension ORCA[3] [80]. ORCA will be a detector array in the Mediterranean sea. It is planed to consist of about 2000 glass spheres housing optical sensors. The glass spheres are attached to cables that are placed vertical up-going from the seabed. Each glass sphere houses 31 single photomultiplier tubes. The spacing between the cables and the glass spheres will be dense enough to measure muon neutrino events of 3 GeV with ∼50 % efficiency.

2.5 Other Experiments

In the following other current neutrino oscillation experiments are discussed. The experiments are split into reactor based and accelerator based experiments.

2.5.1 Reactor Experiments

Reactor based experiments utilize the electron anti-neutrino flux from nuclear fission reactors to measure the mixing angle θ_{13}. Since the energy output of these reactors is monitored all the time, the quantity of the fission reactions is known to a high degree. To gain a high level of precision, the experiments typically imply two detectors. A near and a far detector. While the near detector should be as near at the reactor as possible to measure the unoscillated electron anti-neutrino flux, the far detector should be placed in a location where one is able to measure an oscillation maximum. Since the power plants were normally built without neutrino experiments in mind, the site for the far detector is not always optimal.

Ongoing reactor experiments are the DayaBay Experiment in China [81], the DoubleChooz experiment in France [82] and the Reactor Experiment for Neutrino Oscillation (RENO) in South Korea [83].

Another reactor based experiment is the Kamioka Liquid Scintillator Anti-neutrino Detector (KamLAND) in Japan [84]. The detector was build in a region with 55 nuclear power reactors and detects electron anti-neutrinos over the inverse beta decay. The direction and energy of the neutrino is then extrapolated from the measured positron that is produced in the interaction. KamLAND is sensitive to the mass splitting Δm_{21} and the mixing angle θ_{12}.

A future reactor experiment is the Jiangmen Underground Neutrino Observatory (JUNO) [85, 86] which is a successor to the DayaBay experiment. One goal of JUNO is to solve the ongoing question of the neutrino mass hierarchy.

2.5.2 Accelerator Experiments

Accelerator based neutrino experiments utilize particle accelerators to produce a neutrino beam [87, 78]. A particle beam (e.g. electrons) is pointed to a target to produce charged mesons, mostly pions and kaons. A good target for this is a block of graphite. The charged mesons

[3] Oscillations Research with Cosmics in the Abyss

are focused with magnetic fields and enter a decay tunnel where they decay into muons and muon neutrinos. Particles other than neutrinos are then blocked by rock, whereas the neutrino beam can reach the detectors. As for the reactor experiments, the experiments utilize a near and a far detector. The near detector is used to measure the unoscillated neutrino flux and is normally some hundred meters away from the neutrino source. The far detector has the purpose to measure the oscillated neutrino signal and is some hundred kilometers away from the source. Ongoing experiments are the Tokai to Kamioka (T2K) experiment [78] in Japan, the Main Injector Neutrino Oscillation Search (MINOS) experiment [88] in the United States and its follow up the NuMI Off-Axis ν_e Appearance (NOνA) experiment [89].

If the disappearance of muon neutrinos is measured, accelerator experiments are sensitive to the mass splitting Δm_{23} and the mixing angles θ_{23} (MINOS, T2K, NOνA). If also the appearance of electron neutrinos is measured, the experiments are also sensitive to θ_{13} and the CP violating phase δ (T2K, NOνA). Since the neutrino beam has to cross several hundred kilometers of rock, mass effects have to be reconsidered for the measurement. The T2K experiment uses the Super-Kamiokande as its far detector. This detector is discussed further in section 2.4.2.

A new experiment is the NuMI Off-Axis ν_e Appearance (NOνA) experiment [89] which full operation began in 2014. Its primary goal is the measurement of θ_{13} and the determination of the neutrino mass hierarchy.

Chapter 3

Detector

The following chapter describes the IceCube experiment and the simulation of the detector.
First the general detection principle is explained, followed by a description of the individual detector components. One component of the IceCube experiment is natural grown glacial ice. Thus, its properties are also explained. The last section covers the complete simulation chain for the simulation of neutrino events in IceCube.

3.1 Introduction

For this work data measured by the IceCube experiment is used. IceCube is a neutrino detector in Antarctica [73]. It is located at the geographic South Pole inside the glacial ice of the Antarctic ice sheet and was constructed between 2005 and 2010. In a depth between 1450 m and 2450 m $\sim$1 km^3 of ice is instrumented with light sensors to detect the faint light produced in particle interactions. A sketch of the IceCube detector is shown in figure 3.1.

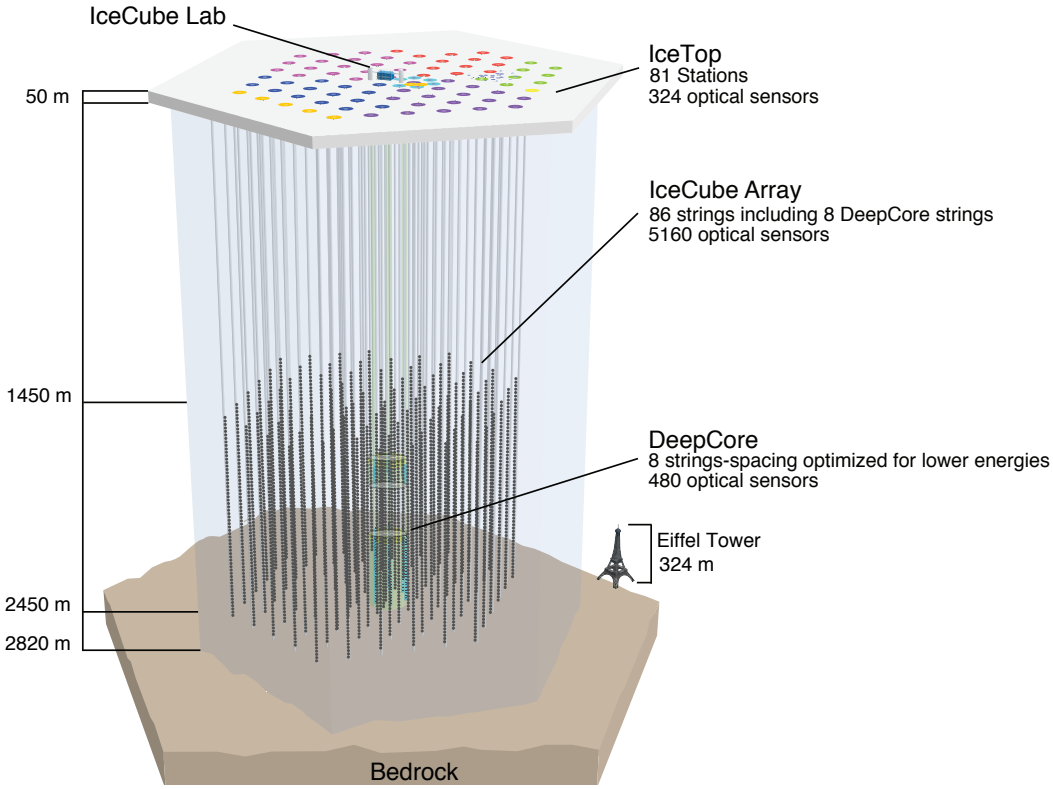

Figure 3.1: Sketch of the complete IceCube detector. [90]

3.2 Detection Principle

As stated above, the IceCube detector records the light of particle interactions inside the glacial ice. This light is produced by different charged particles, like electrons, hadrons and especially muons. An underlying background is the light produced in the decay of radioactive isotopes. This is further explained in section 3.4.5.

3.2.1 Energy Loss in Ice

Fast charged particles can loose energy in the ice in different ways. Figure 3.2 shows the energy dependent differential energy loss of muons in ice.

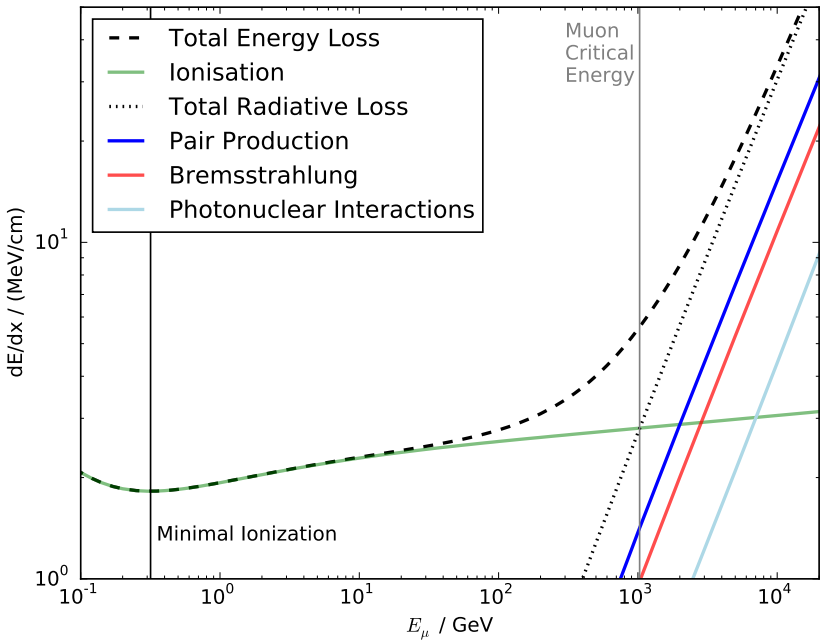

Figure 3.2: Muon energy loss in ice. The total energy loss is the sum of losses from ionization and radiation. The total radiative loss is the sum of losses due to pair production, bremsstrahlung and photo-nuclear interactions. Values taken from [91].

At low energies below ∼100 GeV the energy loss is dominated by ionization [91]. At ∼0.31 GeV the total energy loss is minimal with ∼0.18 GeV/m. Muons with this kinetic energy are labeled as *minimum ionizing particles* (MIPs). In the energy region interesting for this work of 1-100 GeV, the loss is 0.19-0.23 GeV/m with a linear rise in-between. Since muons have a mean life-time of about 2 μs [11], they can travel long distances in the ice while only loosing energy due to ionization. This causes a more or less constant energy deposition along their path. If the traveled distance L_μ of the muon inside the ice can be estimated, a rough energy proxy for the muon is

$$E_\mu \approx 0.2\,\mathrm{GeV/m} \cdot L_\mu \quad . \tag{3.1}$$

Starting at ∼100 GeV the energy loss due to radiative processes raises. Above the critical energy of about 1030 GeV the radiative losses begin to dominate over ionization losses.

Due to their low mass the domination of radiative losses starts for electrons at much lower energies than for muons. Thus, in the energy range relevant for this work electrons only produce electromagnetic cascades in the ice. High-energy neutrino interactions with nuclei also can produce hadronic cascades. These cascades show a similar signature as the electromagnetic cascades produced by electrons [92]. The difference is in average an energy dependent factor for the energy deposited in the ice. The light output of the cascade depends on the involved hadronic particles in the shower. Since the shower development can differ quite strongly, the

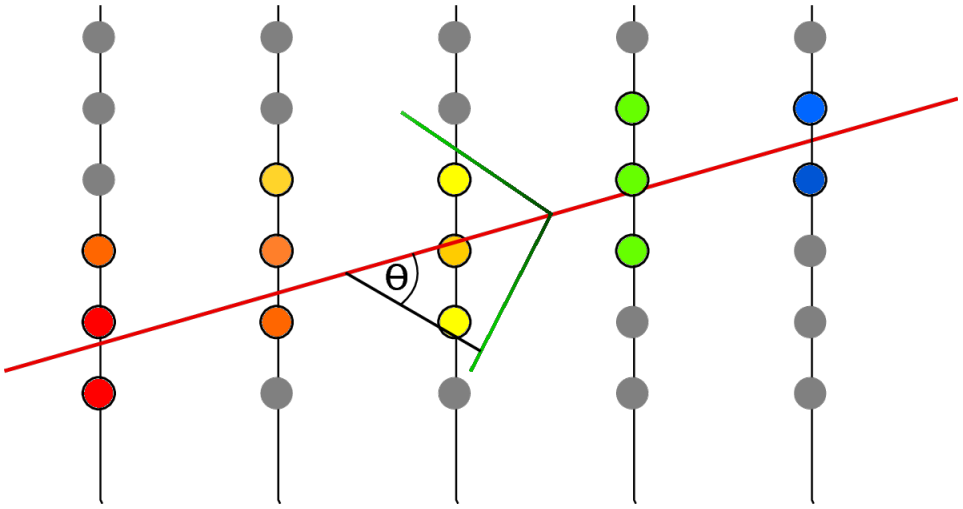

Figure 3.3: Sketch of the Čerenkov effect of a charged particle (red line) traveling through the IceCube detector. The Čerenkov light is detected by light sensors. Red marked sensors are hit early and blue are hit late. The Čerenkov photons are emitted under the Čerenkov angle θ away from the track of the particle.

visible energy is fluctuating. In general the light yield by hadronic cascades is lower than for electromagnetic cascades of the same total energy. This is causes by energy being bound in electric neutral neutrons and in nuclear bindings. Furthermore, due to the higher rest-mass of hadrons, the Čerenkov threshold is higher.

If a ν_τ interacts in a charged current interaction with a nucleus, it produces a tau lepton. The tau has a high mass of 1.8 GeV [11] and a mean life-time of only 29 ps. This means that the tau will decay more or less instantaneously and in ∼83 % produce a cascade. In the remaining ∼17 % a muon is produced. At very high energies a ν_τ interaction could be detected inside IceCube, if two separate cascades are detected in close proximity and in the same event. For the energy range relevant for this work, however, these two cascades cannot be resolved with the detector.

3.2.2 Čerenkov Light

Charged particles in matter polarize their surrounding atoms. If the particle is traveling with a speed higher than the phase velocity $v_\mathrm{p} = c/n$ of the light in the medium, the polarizing effect adds up and leads to the emittance of electromagnetic radiation, Čerenkov photons [24].

The photons are emitted on a cone along the track of the particle with a Čerenkov angle of

$$\cos(\theta_\mathrm{c}) \approx \frac{1}{\beta n} \quad . \tag{3.2}$$

This is also depicted in figure 3.3. The angle is dependent on the velocity of the particle and the index of refraction n of the medium. If the particle is traveling with very high energies near the speed of light $\beta = 1$ and the cosine of the angle is equal to n^{-1}. With an index of

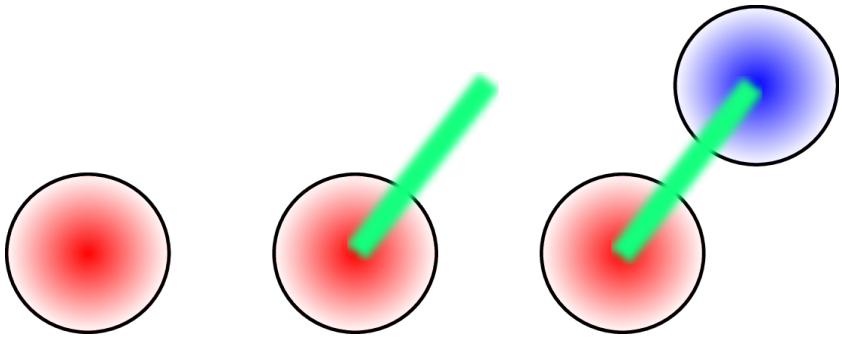

Figure 3.4: Light signatures due to neutrino interactions. CC electron neutrino interactions as well as all NC interactions produce cascades, which have a more or less spherical light distribution (left). CC muon neutrino interactions produce a hadronic cascade and a muon track (middle). A CC ν_τ interaction produces a hadronic cascade, a τ track and a cascade due to the decaying τ (right).

refraction for ice at $\lambda = 532\,\text{nm}$ of $n_{\text{ice}} = 1.32$ [93] this leads to a Čerenkov angle of about $\theta_c \approx 41°$.

3.2.3 Interaction Signatures

As stated above, charged relativistic particle in the ice produce light. The different neutrino interactions lead to different interaction signatures which are depicted in figure 3.4.

Electrons, Hadrons and NC Interactions

Electromagnetic or hadronic cascades as shown on the left side of the figure, emit photons in every direction. In regard to the detector cascades are small with a typical length below ten meters [92] which leads to a spherical light signature. Cascades are produced in neutral-current interactions of neutrinos or in charged-current electron neutrino interactions.

Muons

High energy muons below 100 GeV can travel long distances through the ice. Due to the Čerenkov effect they produce light along their track. In the middle of figure 3.4 the signature of a charged current muon neutrino interaction is shown. At the interaction vertex a hadronic cascade and a muon is produced. The amount of energy that ends up in the muon or cascade is dependent on the inelasticity of the interaction (see section 1.2.1). The signature is the spherical photon emission due to the cascade and a track-like signature due to the ionizing muon.

Taus

As described in section 3.2.1 CC tau neutrino interactions can produce two cascades connected by a track signature. This is also shown in figure 3.4 on the right. The detection of this signature is very difficult since the track is very short and the cascades will most likely overlap. If the tau lepton decays into a muon, another track is produced. This is also very hard to differentiate from a normal muon neutrino signature.

3.3 The Detector

In the following section, the different parts of IceCube are discussed.

3.3.1 The Digital Optical Module

The light sensors of the detector are called *digital optical modules* (DOMs) (see sketch in figure 3.5). The sensor part of a DOM consists of a R7081-02 type photomultiplier tube (PMT) from Hamamatsu Photonics K.K. [94, 95]. The PMT is a 10-stage hemispherical design with a bialkali photocathode. It resides inside a pressure sphere of glass to shield the PMT from the high pressure in the depth of the glacial ice. The glass sphere is assembled from two half spheres that are filled with dry nitrogen of about 0.5 atmospheres so the half spheres are pressed together. The PMTs are coupled to the glass via an optical gel to reduce light loss due to refraction on the glass-medium boundary. The PMT readout and the digitalization is performed directly inside the DOM on a "DOM mainboard". Signals from the PMT are transported to a discriminator and over a delay line to a waveform digitizer. If the PMT outputs a pulse that is higher than $\sim$0.25 of a single photo electron (SPE) pulse height, the DOM is triggered and the waveform digitization is started. This is done by using 128 Wilkinson 10-bit common-ramp analog to digital converters (ADCs) of a custom application-specific integrated circuit (ASIC) which is also called the *Analog Transient Waveform Digitizer* (ATWD) [96, 95]. The analog waveform is sampled by three individual channels with different gain to 128 capacitors. A forth bank is used to read out different signal sources from the DOM mainboard and is thus used for calibration and validation. When a DOM is triggered it sends signals to the two DOMs above and below and listens for any incoming signal. If the DOM receives a signal under 1 μs after the initial DOM trigger or received a signal under 1 μs before, a "local coincidence" (LC) flag is set inside the DOM and the hit is set to be of *hard local coincidence* (HLC). To reduce dead time every DOM mainboard features two ATWDs. Thus, if one ATWD is still digitalizing a captured waveform, the DOM can trigger.

Apart from the waveform capture by the ATWD the PMT output is sampled in a continuous way by a 10-bit high speed ADC with 40 mega samples per second (MSPS) [95]. The output of this fast ADC (fADC) is recorded by the DOM mainboard, if the DOM is triggered. The length of the capture is set to 6.4 μs.

Not every DOM will have a set LC flag when the detector is red out. Triggered DOMs that do not fulfill the needed requirement will only send a "charge stamp". The charge stamp consists of the highest sample in the first 16 fADC samples after the DOM trigger and its two

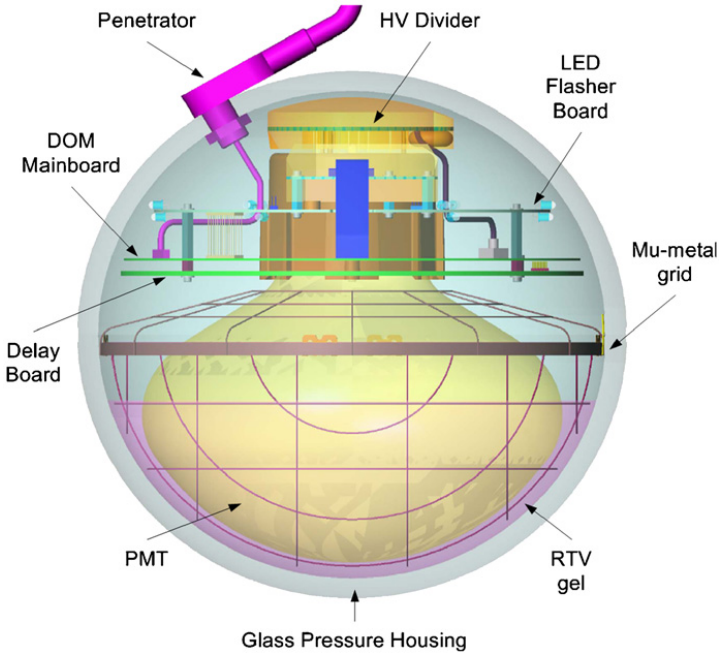

Figure 3.5: Sketch of an IceCube DOM [95].

direct neighbor samples. These single, isolated hits are called *soft local coincidence* (SLC).

3.3.2 IceCube

Sixty DOMs are connected to a supporting cable for power delivery and data transfer with an inter-DOM spacing of about 17 m [97]. These cables are called *strings*. The full IceCube detector consists of 86 strings in a hexagonal pattern deployed in the clear glacial ice at South Pole in a depth between 1450 m and 2450 m. The mean inter string distance for normal IceCube-strings is around 125 m. The complete instrumented volume is about 1 km^3. At the surface the strings are connected to computers (string hubs) for read-out.

3.3.3 IceTop

On top of IceCube there is also a ground based air-shower detector called "IceTop". It consists of water tanks on top of each string and is constructed to veto incoming muons from air showers that produce one kind of background in high-energy neutrino measurements.

3.3.4 DeepCore

The center of IceCube is more densely instrumented to lower the detection threshold to around 10 GeV [97]. This part of IceCube is called DeepCore (see figure 3.6 for a sketch). DeepCore utilizes the seven normal IceCube-strings in the center, consisting of the center string, six shell strings and eight special DeepCore strings. Six of these strings are instrumented with

DOMs that have a higher optical efficiency (HQE) than the normal IceCube-DOMs. The efficiency is raised by around 35 %. Each of these strings is located in the middle of a polygon formed by two neighboring shell strings and the center string. The mean inter-string distance between one DeepCore-string and the next three IceCube-strings is ca. 72 m. The other two DeepCore-strings were added after the initial planing phase and consist of a mix of IceCube- and DeepCore-DOMs. They are located near the center string and lower the inter-string distance in the middle even more to about 42 m. These strings are also called *infill strings*.

On each of the special DeepCore-strings the inter-DOM spacing is also changed to lower the detection threshold. The lower 50 DOMs are placed in the clearest ice in a depth between 2100 m and 2450 m. For these DOMs the inter-DOM spacing is 7 m. The remaining ten DOMs have an inter-DOM spacing of 10 m and are placed in a depth of 1900 m to 2000 m. They are not part of the DeepCore fiducial volume, but form an extra layer to veto incoming muons, a veto cap. Between the two instrumented regions, there is a gap of ∼100 m, the *dust layer*. No DOMs were placed here, because the scattering length is very small due to enclosed dust inside the ice [98].

3.3.5 The Ice at South Pole

Since the IceCube detector uses natural grown ice as a detection medium, several measurements were performed in the past to produce a complete description of the ice [98, 99, 100, 101]. Figure 3.7 shows the depth and wavelength dependent scattering and absorption in the ice at South Pole. Below a depth of 1300 m bubbles in the ice cause a higher scattering of light. Photons from particle interactions loose their timing information in this region. A first minimum of the effective scattering and absorption coefficient is reached at a depth of about ∼1450 m. Thus, IceCube-DOMs are deployed between 1450 m and 2450 m. There are four peaks in this range where the scattering and absorption is raised. This is caused by dust accumulations inside the ice [99]. The forth peak in a depth of $2000 - 2100$ m is higher then the other three and marks a layer of dust in which the optical performance of the detector is reduced significantly, the dust layer. Due to this raised scattering and absorption the DeepCore sub-detector was built in a depth between 2100 m and 2450 m [97].

3.3.6 Triggering

There are several trigger conditions defined for IceCube. The trigger relevant for this analysis is the DeepCore trigger. It is a simple majority trigger and requires three HLC hits in a 2.5 μs time window in the DeepCore fiducial volume for a read-out of the complete detector [97]. This is more relaxed condition than the standard IceCube trigger which requires eight HLC hits in 5 μs (SMT8). The DeepCore trigger has a lower energy threshold due to the reduced number of required hits, but is more prone to trigger noise driven events.

If a trigger condition is met, the detector is read out in a $\pm 10\,\mu$s time window. If multiple trigger conditions are met, the read-out window is extended accordingly.

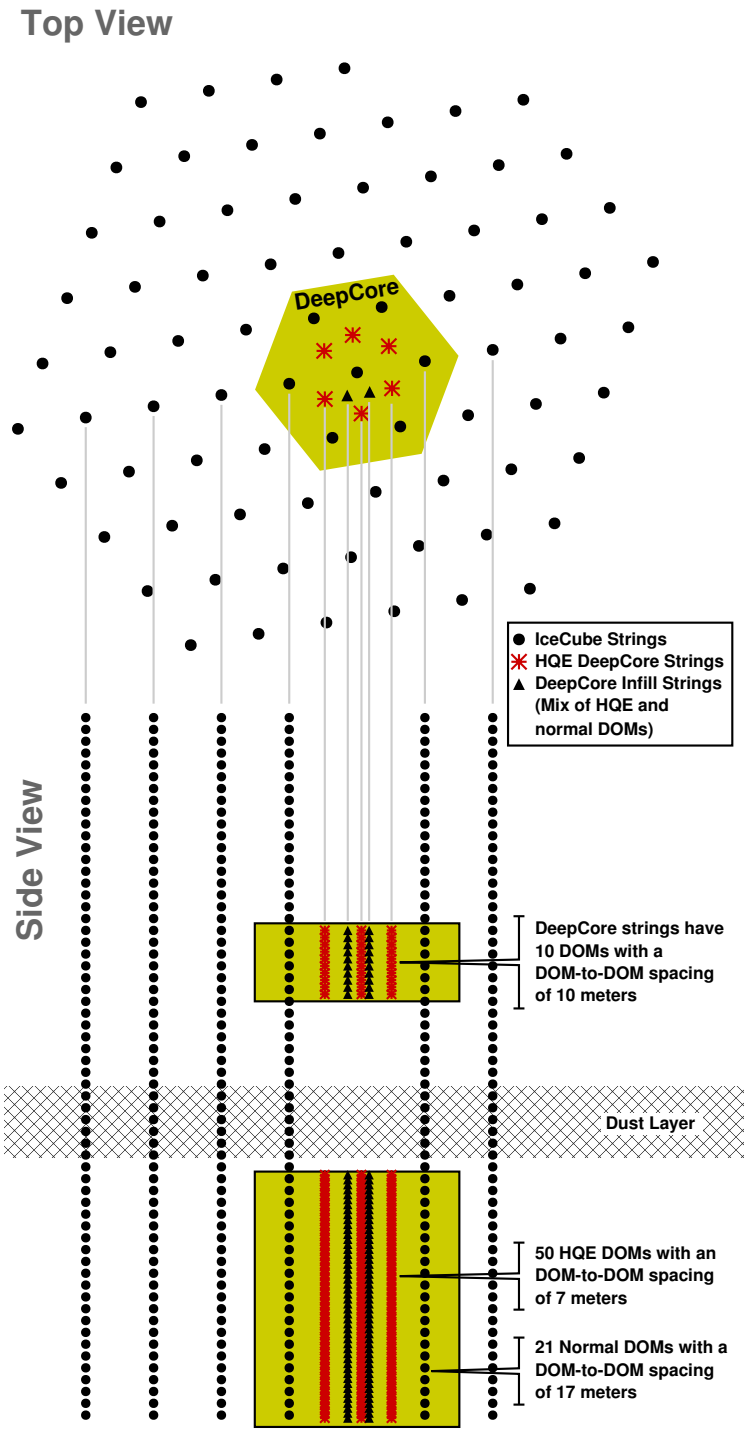

Figure 3.6: A sketch of the DeepCore sub-detector (yellow area below the dust layer) and the veto cap (yellow area above the dust layer) [97].

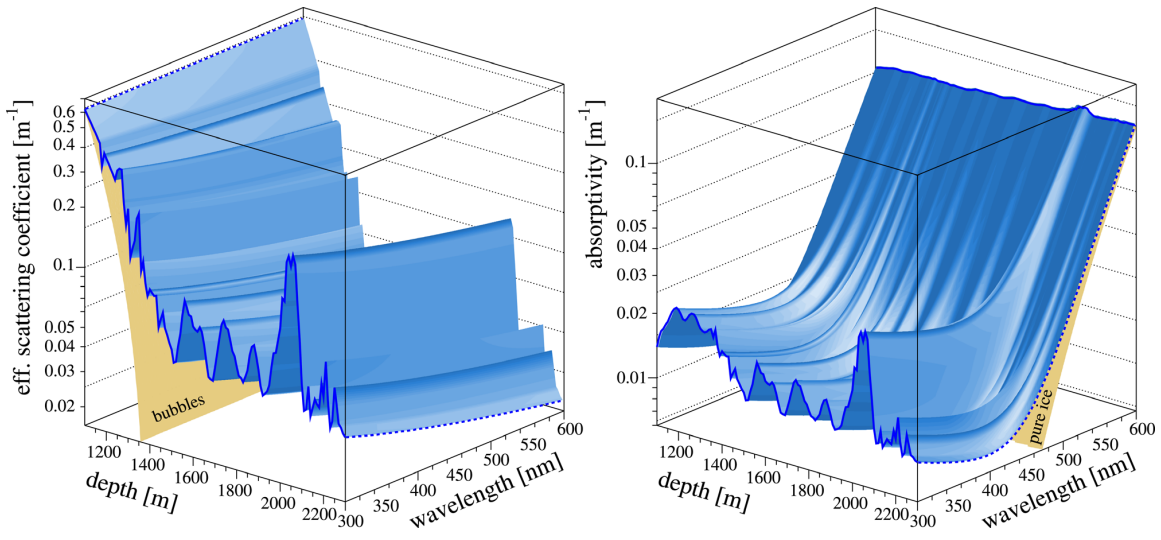

Figure 3.7: The effective scattering and absorption coefficient in dependence to the depth of the ice and the wavelength of the photon [98]. Clearly visible is the raised scattering due to air bubbles below 1300 m and the four peaks in scattering and absorption due to dust.

3.3.7 Detector Configuration

The IceCube detector was completed in December 2010 with 86 deployed string including the eight strings of DeepCore. This configuration is also called IC86. As data was also taken with the incomplete detector, several different other configurations exist. The main part of this work centers around the IC79 configuration. Data from this configuration was recorded from end of May 2010 to May 2011 when the detector read-out was switched to IC86. IC79 consists of 79 strings including six DeepCore strings (IC79/DC6). The difference between IC86 and IC79 is visualized in figure 3.8.

3.4 Simulation

An integral part of the oscillation analysis is the usage of events from simulations. Also the event selection was tuned with simulated events from atmospheric muons and neutrinos. The event simulation consists of four different steps:

1. event generation
2. secondary particle propagation
3. photon propagation
4. detector simulation

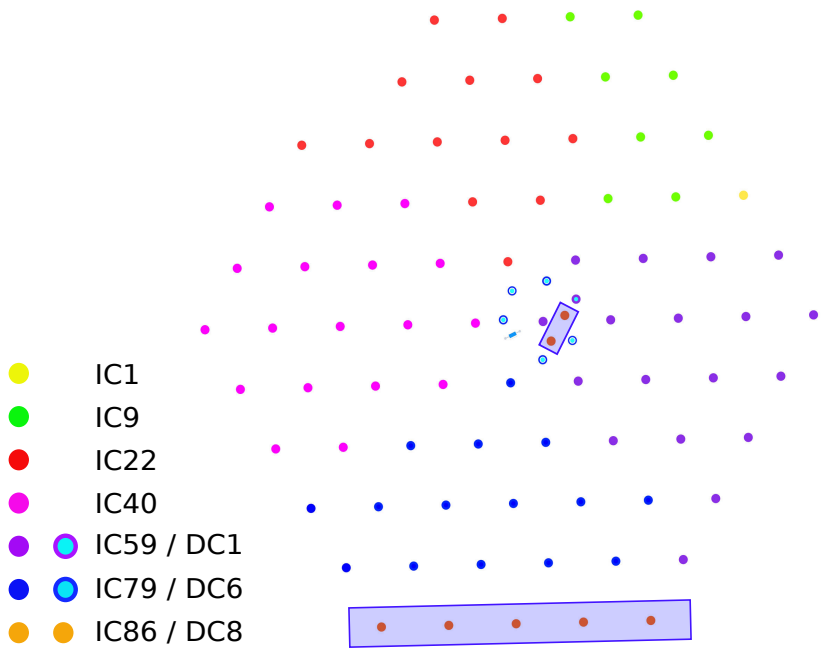

Figure 3.8: Top view of the IceCube detector (modified from [90]). The circles represent the deployed strings. Different colors indicate the different seasons of the detector construction. Strings in blue shaded area were deployed last for the transition from IC79 to IC86.

5. on-line filtering

In the following sections these steps are discussed closer.

3.4.1 Neutrino Event Generation

For the particle propagation of low-energy neutrinos the *GENIE Neutrino Monte Carlo*[1] framework is used [102]. Implemented into GENIE are cross-sections for several different interaction types. These include the ones relevant for energies above 1 GeV that are elastic and quasi-elastic scattering (QE), resonance production (RES) and deep inelastic scattering (DIS) (compare section 1.2.1). The implemented cross-section for DIS is valid to several hundred GeV depending on the used version. The neutrino particle of flavor n and type t is generated on the surface of a disk with radius r. The disk is the front of a cylinder that defines the generation volume defined by r and the cylinder length L. The cylinder is randomly rotated around the center in azimuth ϕ and zenith angle ϑ. From a randomly chosen position $\{\rho, \psi\}$ on the disk the neutrino is shot into the generation volume[2] with a kinetic energy drawn from a power law distribution. The direction of the neutrino is aligned to the axis of symmetry of the cylinder. Along the path of the neutrino GENIE than simulates the interaction with water that is drawn from a cross-section spline. At the interaction point the particle interaction with the medium

[1] Generator, Comparisons, Tuning
[2] that is into the cylinder volume

is further simulated by the PYTHIA framework [103] which is closely linked to the GENIE framework. The stable end-state particles of the interaction are then written to an output map and saved to an event interaction frame.

Another neutrino event-generator is the *Neutrino-Generator* (NuGen). NuGen is the default neutrino event generator in IceCube and is based on the ANIS framework[3] [104]. NuGen is developed for higher energies starting at several ten GeV in neutrino energy. Thus, only DIS is implemented. Furthermore, NuGen cannot give the output of all end-state particles. Hadronic particles are summed up to a virtual particle, a "hadron blob". Since the simulation error of low-energy events below some ten GeV rises, NuGen is only suitable for neutrino oscillations to a limited degree and the usage of GENIE is advised. On the other hand GENIE is only valid to several hundred GeV, so events generated by NuGen can be used to model the high-energy neutrino component of the total neutrino flux.

3.4.2 Background Simulation

For the event selection the background of atmospheric muons is given by simulated events. The used simulation dataset was generated with the CORSIKA[4] Monte Carlo code [105]. CORSIKA simulates the interaction of cosmic ray primaries and the resulting extensive air shower. The muons produced in the particle cascade are propagated down to the detector and generate atmospheric muon events in the ice. Due to the huge particle cascades, the computational demand for this simulation is very high. Furthermore, the resulting amount of data on filter level is very high. Thus typically only a small fraction of a year is simulated.

3.4.3 Particle and Photon Propagation

To get the appropriate photon yield inside the detector, one has to propagate the end-state particles. Muons are propagated through the ice with the *Muon Monte Carlo* code (MMC) [106]. The length of the muon track and the lost energy is then written into the event frame, together with possible particles from the muon decay. All end-state particles from low-energy neutrino interactions are propagated in the same step with the CLSim [107] code. CLSim can utilize the GEANT4[5] framework [108] to correctly simulate the single particle interactions in the medium. Otherwise the photon yield of the particles is drawn from parameterizations, except for muon and tau leptons. Photons from the individual particles are then propagated through the ice one by one. If a photon hits a DOM inside the simulation, it is stopped and together with the hit-time and DOM added to a list of recorded photons. In the propagation step the ice model and the angular reception of the DOMs is taken into account.

CLSim uses OpenCL [109] to speed up the simulation process by utilizing graphic processing units (GPU). Using GEANT4 for particle propagation is very CPU intensive and negates the gain from using GPUs for the photon propagation. On the other hand the parameterizations are not valid for very low-energy particles and GEANT4 has to be used to correctly simulate

[3] All Neutrino Interaction Simulation
[4] COsmic Ray SImulations for KAscade
[5] Geometry and Tracking - Version 4

the light yield for these particles. Thus, to get a correct and fast simulation GEANT4 is only used for electromagnetic particles below 100 MeV and hadronic particles below 30 GeV.

Another tool for photon propagation is the *Photon Propagation Code* (PPC) [110]. Photons of simulations of atmospheric muons and high energy neutrino simulations generated with NuGen were propagated with this code. PPC can also utilize GPUs to speed up the propagation. In contrast to CLSim it cannot perform an individual propagation of end-state particles. Also it always uses parameterizations to get the photon yield, thus it is not as suitable for low-energy neutrino events as CLSim. The results of PPC and CLSim are compatible if only parameterizations are used in CLSim.

3.4.4 Ice Model

CLSim and PPC both simulate the light propagation through the glacial ice inside the detector. The used model of the ice used in in this work is called *SpiceMie* [100]. It consists of a depth dependent table of parameters related to scattering and absorption for a wavelength of 400 nm as well as six global parameters. The parameters were obtained through fits to in-situ measurements at single DOMs. These were done by flashing LEDs installed on the DOMs and measuring the resulting light and time delay at other DOMs. Furthermore the measurements from dust-loggers were used. SpiceMie correctly covers Mie scattering of photons on dust as well as a shift of the different layers of the ice. A newer ice model that improves on SpiceMie is called *SpiceLea* [111]. It also covers the azimuthal anisotropy of the ice. This ice model was used for newer simulations.

3.4.5 Detector Simulation

The first step of the detector simulation is the simulation of the PMT response to the recorded photons. The simulated PMT waveform is then fed into the simulation of the DOM electronics. The resulting output is a "DOM launch map" with the digitized waveforms, hit-time, charge-stamp and number of the DOM.

Apart from particle interactions of muons and neutrinos in the ice, light is also produced in radioactive decays of unstable isotopes in the ice and the glass of the DOMs pressure sphere. The latter contribution is mostly due to ^{40}K. The photons from different decaying nuclei are uncorrelated and can be simulated as a poissonian noise contribution to the physical photon hits. However, apart from the pure poissonian, uncorrelated noise contribution there is also a light contribution due to scintillation which causes correlated photon hits. To get a realistic simulation of the detector, DOM launches from detector noise have to be added to the existing DOM launch map.

For events from NuGen and CORSIKA based simulations, only the poissonian noise distribution has been simulated. For GENIE based simulations a newer software called *Vuvuzela* [112] that more correctly simulates correlated noise photons due to scintillation was used.

In the next step the DOM launch map with added noise is run through the simulation of the different trigger systems in IceCube. The trigger simulation marks for each simulated event which triggers flags were set and also, if the global trigger requirement was fulfilled. Events

that do not fulfill the trigger requirement are discarded.

3.4.6 Feature Extraction and On-line Filter

Now the simulation has to be run through the same processing steps as real data. From the recorded waveforms of the DOM-launches features from photo electrons have to be extracted. These then can be used in reconstructions and filters. Also in this step the DeepCore-filter flag is set, if an event fulfills the specific requirement. This is described more in the following chapter.

Chapter 4

Event Selection and Reconstructions

In this chapter the event selection for the one year IC79 dataset is described. At the first level of this event selection the background of atmospheric muons is several orders of magnitude higher than the signal of ν_μ events. The selection is used to reduce the background to about $5 - 10\,\%$ of the final dataset. The chapter covers the used tools and reconstructions. One integral step in the event selection is the usage of a machine learning algorithm. This part of the selection is covered in more details. The individual selection levels are then discussed afterwards.
For the reconstructions that are also used in the final analysis the reconstruction performance together with the expected resolution is discussed.

4.1 Introduction

The event selection presented here is based on the event selection of a previous analysis by Sebastian Euler [113]. Several steps in the event selection were revised and changed due to optimizations. The integral components of the selection are explained followed by the actual selection steps. In the event selection several different definitions for hits are used. For clarification these are listed in the appendix in section B.

4.2 Tools and Reconstructions

The following sections will discuss the different tools and reconstructions used in the event selection.

4.2.1 On-line-Filter

Due to bandwidth limitations for satellite transmissions, the recorded data at the South Pole has to be reduced before it can be transmitted north. For this, there are different on-line filters in place that reduce the amount of data by selecting only interesting events. This oscillation analysis uses the DeepCore filter stream [97]. A sketch of the filter is depicted in figure 4.1. It starts with events that trigger the DeepCore sub-detector (see section 3.3.6). The "center of gravity" (COG) of the HLC hits inside the DeepCore fiducial volume is used next. The COG is first estimated by calculating the mean position of the hits. Also a mean hit time is calculated as an estimate for the event time. In a further step the position is refined by using only the hits that have a time stamp in one standard deviation around the mean hit time. For these hits the average position is calculated again. It represents the new COG position $\mathbf{r}$. The hit time of the COG is also refined. This is done by calculating "corrected" times t, that is the time of the hit subtracted by the time an unscattered photon needs to travel the distance between the hit DOM and the refined COG. The refined values $\mathbf{r}$ and t are used to calculate the speed of a virtual particle from every hit DOM to the COG by using

$$v = \frac{|\mathbf{r} - \mathbf{r_{DOM}}|}{t - t_{\mathrm{DOM}}} \quad . \tag{4.1}$$

Positive speeds indicate a particle entering the DeepCore sub-detector and are usable to distinguish between atmospheric μ and neutrinos. This is visible in figure 4.2, where the bulk of hits from neutrinos have a negative speed. Thus, events are discarded if they have at least one hit that is in a window between 0.25 m/ns and 0.4 m/ns.

4.2.2 Hit Cleaning

Not every recorded hit in IceCube data is caused by photons from particle interactions. Decay of radioactive isotopes inside the ice or the glass of the pressure sphere, as well as self induced pulses of the PMT produce hits as well. These "noise hits" inside a recorded event frame are not connected to the particle and reduce the veto efficiency and reconstruction quality.

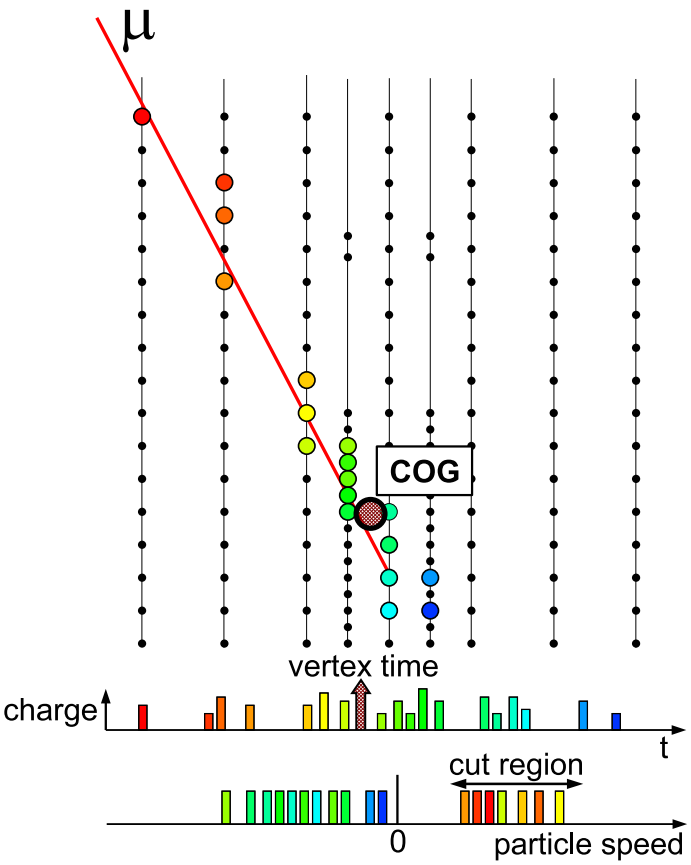

Figure 4.1: Sketch of the scheme behind the DeepCore on-line filter. [97]

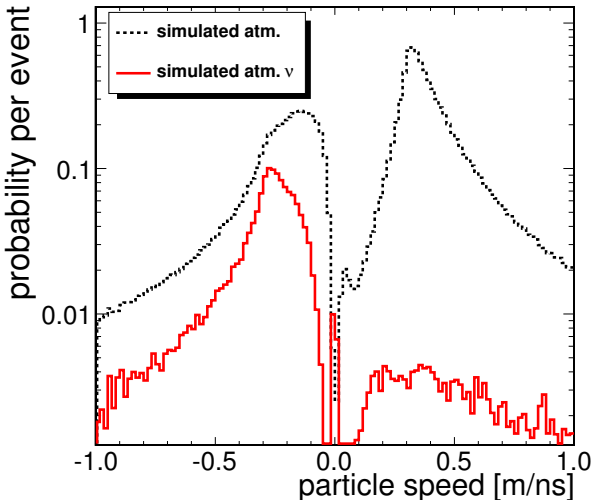

Figure 4.2: Particle speed distributions for atmospheric μ and neutrinos. [97]

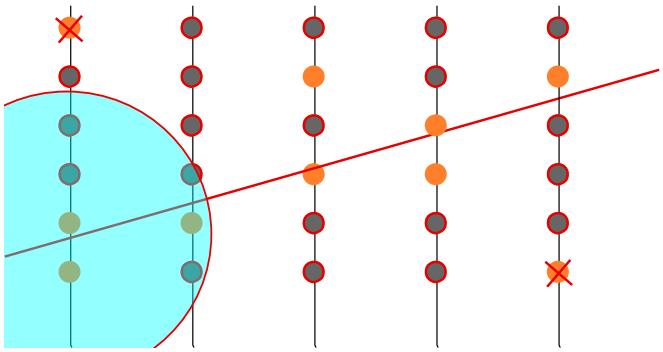

Figure 4.3: The RT cleaning algorithm removes hits (red crossed) that have no neighbor below given spatial or temporal radius R and T (blue area).

Especially for low-energy events inside the detector noise contributes a significant portion of the recorded hits. To reduce the amount of noise hits, dedicated cleaning algorithms are used.

Static Time Window Cleaning

The timespan of an event frame can be of several ten μs. Most part of this will be governed by noise events, since the typical event length of a muon track should be around 5 μs if the muon has to travel 1500 m. To reduce the noise hits around the event, a static time window (TW) is used. Only hits in a time window of $-4\,\mu$s and $+6\,\mu$s around the DeepCore-trigger time are used. Every hit map used in this analysis is TW cleaned.

CRT Cleaning

A simple noise cleaning algorithm as depicted in figure 4.3 utilizes the spatial r and temporal t distance between hits. For every given hit i at position $\mathbf{x_i}$ inside the recorded hit map, the spatial and temporal distances $r_{\mathrm{ik}} = |\mathbf{x_i} - \mathbf{x_k}|$ and $t_{\mathrm{ik}} = |t_{\mathrm{i}} - t_{\mathrm{k}}|$ to the other hits are calculated. The hit is added to a new hit map, if it has at least one neighbor hit below a given R and T. Typical values are $R = 150\,\mathrm{m}$ and $T = 1000\,\mathrm{ns}$. This algorithm is called the *Classic-RT* (CRT) cleaning.

Improved CRT Cleaning Optimized for DeepCore

The spacing between strings and DOMs is different, as is the spacing between DeepCore and the rest of IceCube. To consider this different spacings, the CRT cleaning was modified to include separate parameters for IceCube $(R_{\mathrm{IC}}, T_{\mathrm{IC}})$ and DeepCore $(R_{\mathrm{DC}}, T_{\mathrm{DC}})$. Also a spherical and a cylindrical topology is implemented. The later one adds a Z parameter for the height of the cylinder for both, IceCube and DeepCore. The cleaning parameters were optimized to perform optimally with the CRT-Veto algorithm (see section 4.2.3 and figure C.1 in the appendix). The optimized values are listed in table 4.1.

Table 4.1: CRT values used in the event selection

$$R_{\mathrm{IC}} = 200\,\mathrm{m} \quad T_{\mathrm{IC}} = 700\,\mathrm{ns} \quad R_{\mathrm{DC}} = 100\,\mathrm{m} \quad T_{\mathrm{DC}} = 400\,\mathrm{ns}$$

Seeded-RT Cleaning

There can be a significant amount of noise hits even after the CRT cleaning. This cleaning does not consider the event itself, but only keeps hits that have a neighbor inside the range defined by the parameters. If there are two noise hits isolated in one part of the detector, they will survive the cleaning. To prevent this, one can use the *Seeded-RT* cleaning algorithm. One starts with a given hit map as a seed, which are all recorded HLC hits by default. For each seed hit the general hit map is checked, if there is another hit in the RT parameter space around the seed hit. If hits are found these are added to an output hit map together with the seed hits. If wanted, one can iterate several times by using the output hit map as a new seed.

4.2.3 Veto-Algorithms

Even after passing the DeepCore filter, the rate of recorded atmospheric muons is four orders of magnitude higher than the rate of muon neutrinos. To suppress atmospheric muons dedicated veto algorithms have been developed for analyses utilizing DeepCore. The veto algorithms used in this work are presented in the following sections.

CRT-Veto

This algorithm is closely coupled to the noise-hit cleaning algorithm described in section 4.2.2. It starts with an uncleaned hit map. Then an optimized noise hit cleaning is performed. An incoming atmospheric muon will first travel through the outer layers of IceCube before it enters the DeepCore sub-detector. Thus, hits outside DeepCore that happen before the DeepCore trigger and survive the noise hit cleaning are most likely from an atmospheric muon. These hits are are counted as "veto hits". Hits inside DeepCore after the noise hit cleaning are considered to be good "signal hits" and are also counted. An event is discarded, if it has at least one veto hit, since it is very likely that it is from an atmospheric muon. Also an event is discarded if it has less than five signal hits. Below this threshold the event quality is very bad and reconstructions will fail to deliver meaningful results.

Top-Bottom-Layer Veto

As stated in section 3.3.4 above DeepCore the ice is diluted by dust. An atmospheric muon that enter the detector through this "dust layer" will not produce much detectable light here and can remain undetected until it enters the region of more clear ice that is also the DeepCore fiducial volume. This event will probably trigger DeepCore in the upper most layer. Also, neutrinos can interact with the bedrock below the detector and produce muons that enter DeepCore from below. These events will probably trigger DeepCore in the lowest layer.

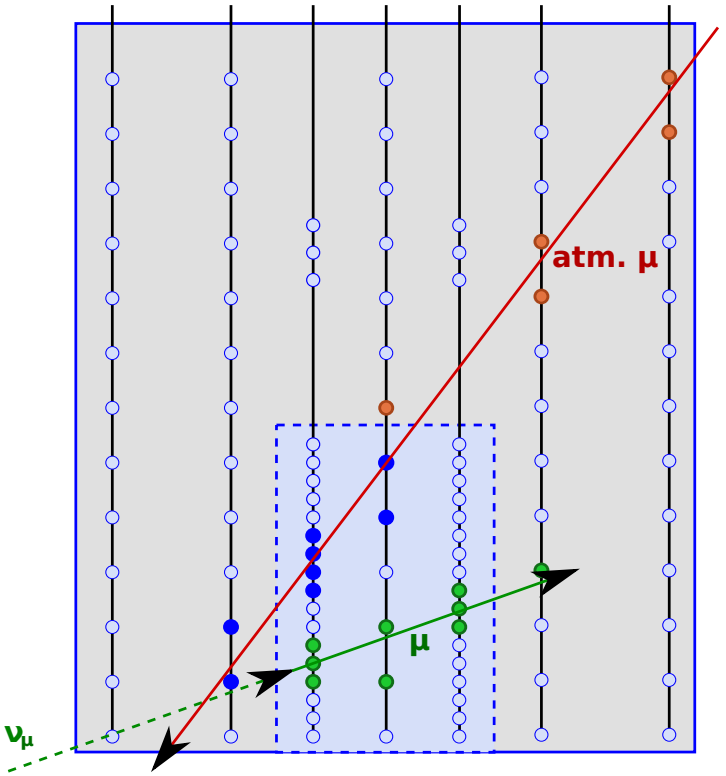

Figure 4.4: A sketch of the CRT-Veto algorithm. An atmospheric muon (red) first produces hits inside the veto volume (gray area) before it reaches DeepCore (blue area). A neutrino (green, dashed) enters IceCube undetected and interacts in the ice. The muon from this interaction (green, solid) produces its first hits inside the fiducial volume of DeepCore.

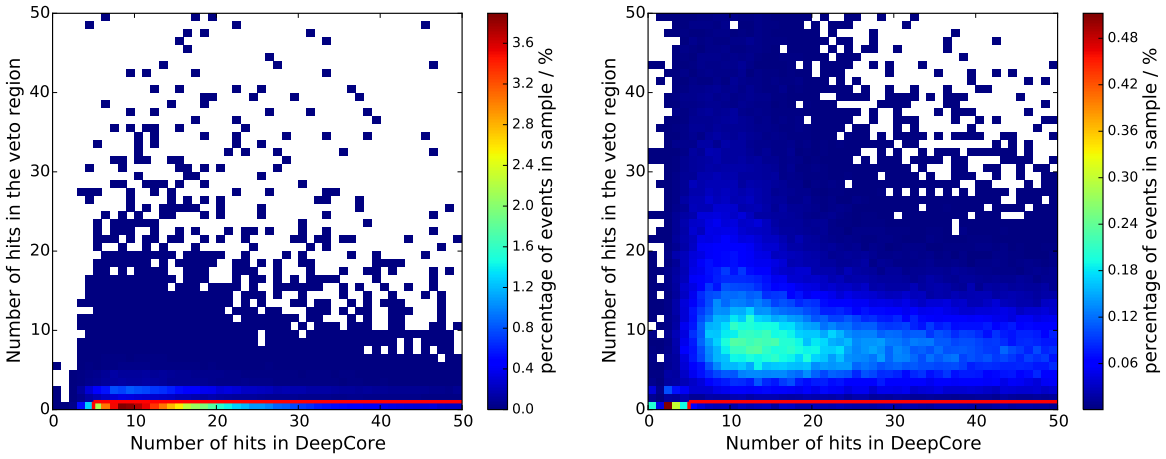

(a) signal events (b) background events

Figure 4.5: Hits in the DeepCore fiducial volume against veto hits in the surrounding veto volume. For the veto only hits are counted if they were recorded before the DeepCore trigger. The selection region of the CRT-Veto is the red surrounded area. Most signal events (left) have no veto-hits and more than four hits inside DeepCore. Many events from atmospheric muons (right) have veto hits.

The energy of the primary neutrino for these events cannot be reconstructed reliably. Thus, events that have their trigger hit in the top or bottom layer of DeepCore are discarded.

Removal of Events Dominated by Detector Noise (NoiseEngine)

As described in section 3.4.5 scintillation processes inside the ice and the glass of the DOMs produce a contribution of correlated noise photons. The DeepCore trigger has a relatively loose triggering requirement (see section 3.3.6) that can be met by some events dominated by correlated noise hits. This produces an excess of events with a low number of hits in contrast to pure poissonian noise.

Early simulation datasets used for development of the event selection lacked the contribution of correlated noise photons. Also, noise dominated events cannot be reconstructed very well. Thus, these events are removed from the sample.

The used algorithm first uses a sliding time window of 750 ns around the largest number of hits [114]. The remaining hits are then connected to each other. Every hit is connected to one other hit in all possible combinations. Everyone of these “hit-pairs“ has an azimuth and a zenith direction pointing from the earlier to the later hit. The directions of the hit-pairs are then binned into a HEALPix map[1] of 48 bins. If no bin has more than three pairs, the event treated as a noise dominated event and removed from the sample.

[1]Hierarchical Equal Area isoLatitude Pixelation

Hits from Muons Traveling Between Strings (CorridorCut)

This cut discards events that are most likely produced by atmospheric muons that travel on the corridors between strings. A more thorough discussion of this algorithm can be found in [115]. These muons will not produce many hits inside IceCube, but most likely inside DeepCore. With this, they survive other veto algorithms and look like events starting inside of DeepCore. All possible corridors in azimuthal direction are scanned. The zenith direction is scanned in steps. If it is likely that a hit inside DeepCore was generated by a muon entering from the corridor it is counted for this corridor. Events are discarded if a corridor with more than one hit is found.

Removal of Coincident Events (Topological Splitter)

Not every recorded event in IceCube is caused by a single incident particle. If two or more atmospheric muons cross the detector in the scope of one triggered event this can cause misreconstructions since the reconstruction algorithms expect single particles. To separate the individual particles of such coincident events a cluster detection algorithm called *Topological Splitter* is used. This algorithm is a newer implementation of the *Topological Trigger* (TTrigger) algorithm that is presented in [116]. The algorithm searches for hits that form causally connected clusters. Two hits are treated as causally connected if they have a horizontal distance below 150 m to each other or they are recorded on the same string and not more than 15 DOMs apart from each other. Also, the hits have to have a causal time $t_c = \Delta t - \frac{\Delta r}{c}$ below 450 ns, where Δr is the spatial distance between the two hits. The values were chosen to reflect the smaller distances in the DeepCore sub-detector and the low energies of the neutrinos. These values are identical to the ones used in [113]. Five or more causally connected hits in a timespan of 4 μs form a cluster. Only the two biggest clusters are kept.

Causality Veto

The causality veto exploits the spatial and temporal distance of hits in the detector to the initial hit that triggered DeepCore. The algorithm is depicted in figure 4.6 and is more closely discussed in [113]. First the hit-time difference $\Delta t = t_{\text{Trigger}} - t_{\text{i}}$ and the distance $r = |\mathbf{x_{Trigger}} - \mathbf{x_i}|$ between the trigger hit and all other hits is calculated. Positive Δt indicate hits before and negative Δt hits after the trigger hit. The yellow dashed line in the left picture of figure 4.6 represents the distance and time difference consistent with the speed of light in regard to the trigger hit.

If an atmospheric muon enters the IceCube detector, it produces hits t_{i} before it can trigger the DeepCore sub-detector at t_{Trigger}, thus these hits have a positive hit-time difference. The hits will be consistent with lower speeds than the speed of light, due to light scattering in the ice and also the time the photons need to travel to the DOMs. Thus, these hits will be below the yellow dashed line for positive Δt (line 1) and indicate an atmospheric muon. These hits are called "veto hits". After the detector is triggered a muon may also leave the detector, e.g. a muon produced in a neutrino interaction. The leaving muon can produce hits inside the detector which happen after t_{Trigger}. The Δt for these hits is negative and because of light

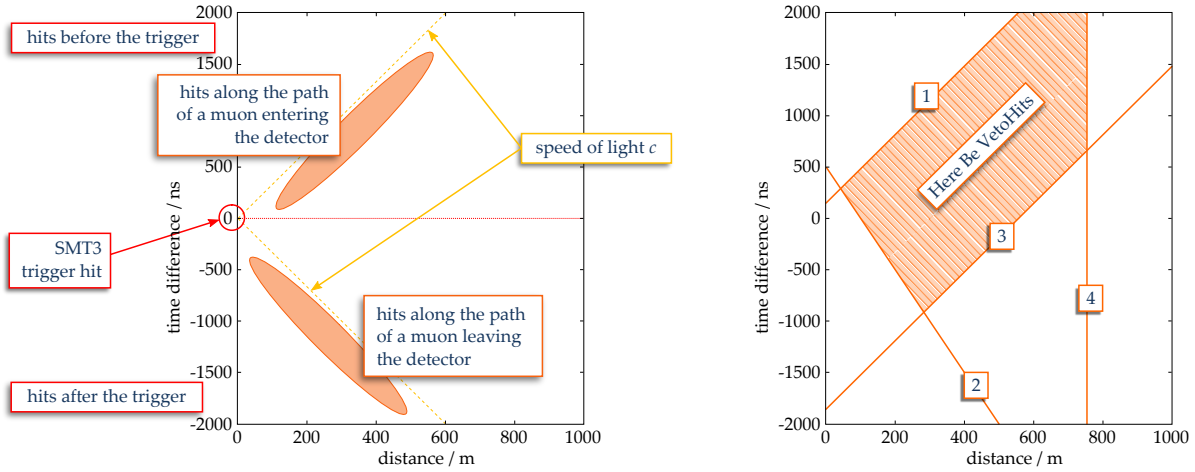

Figure 4.6: Sketch of the algorithm of the causality veto (taken from [113]). Events with a certain number of hits in the parameter space between line 1-4 are discarded, as these hits are likely from incoming atmospheric muons. Hits below line 2 are most likely from outgoing muons. Hits with a bigger distance then 750 m (line 4) are ignored.

scattering the hits populate the parameter space below the yellow dashed line for negative Δt (line 2). Thus hits below the lower line for the speed of light indicate an outgoing muon. These two described possible hit populations now indicate if an event is from an atmospheric muon or a muon neutrino event. An atmospheric muon event will consist of both hit populations, whereas a muon neutrino event only consists of hits below the lower speed of light boundary.

Apart from hits from incoming muons, also noise hits can populate the parameter space between the lines defined by the speed of light. To avoid discarding neutrino events because of noise hits, hits that are below a line parallel to the upper speed of light boundary but shifted to negative Δt (line 3), are not counted as veto hits. The same is true for hits with a high distance to the initial trigger hit (line 4).

The four described lines surround a parameter space for hits that are most likely from incoming muons. If an event has more than a certain number of veto hits or the summed charge of these hits is above a certain limit (see section 4.5), it is considered to be an event from an atmospheric muon and is discarded.

4.2.4 General Directional Reconstructions

Several directional reconstruction algorithms are used in different parts of the event selection, depending on the computational intensity of the algorithm and the amount of data that has to be processed.

First Guess Algorithm (Line-Fit)

As a first guess directional reconstruction the *Line-Fit* is used. This algorithm is a simple directional reconstruction without high computational demand [117]. It is often used as a seed for the more sophisticated reconstructions. The Line-Fit ignores the characteristics of the Čerenkov emission and optical properties of the ice. From the time t_i and position $\mathbf{r_i}$ of each hit a track hypothesis is created. The hypothesis is light that travels with speed v along a 1-dimensional track. The starting point of the track is $\{\mathbf{r_0}, t_0\}$ and is the reconstructed vertex of the track. The track itself is obtained by minimizing equation 4.2. The overall algorithm is a least squared ansatz, this means outliers from e.g. noise will have a quadratic impact on the result and thus will have a strong pull on the resulting fit.

$$\chi^2 = \sum_{i=1}^{N_{\text{hit}}} \phi_i \quad ; \quad \phi_i = \rho_i^2 \quad ; \quad \rho_i = ||\mathbf{r_i} - \mathbf{r_0} - \mathbf{v} \cdot (t_i - t_0)|| \tag{4.2}$$

A newer, improved version of Line-Fit addresses the problem of outliers [118]. This is done by reducing the amount of hits from scattered light. For each hit h_i the neighboring hits h_j inside a sphere of radius r are looked at. If the timestamp difference $\Delta t = t_i - t_j$ is greater than τ, h_i is considered to be from scattered light and not used in the improved Line-Fit reconstruction. Values for r and τ were tuned to simulated muon events. Another improvement is the replacement of the least squared fit by a Huber fit. For this a parameter μ is defined with:

$$\begin{aligned} \phi_i &= \rho_i^2 && \text{if} \quad \rho_i < \mu \\ & \text{and} && \\ \phi_i &= \mu(2\rho_i - \mu) && \text{if} \quad \rho_i >= \mu. \end{aligned} \tag{4.3}$$

This way outliers that have a distance of more than μ away from the track only go linear into the fit and not squared.

Likelihood Based Fit

Using the vertex and track from the first guess algorithm as a seed, a likelihood based approach is used for the general reconstruction [117]. A general likelihood approach is shown in equation 4.4. $p(x_i|\mathbf{a})$ is the probability density function (PDF) for the measurement and gives the probability to measure the parameter x_i given a selection of parameters $\mathbf{a}$. The parameters $\mathbf{a}$ can be obtained by maximizing the likelihood function.

$$\mathcal{L}(\mathbf{x}|\mathbf{a}) = \prod_{i=1}^{N_{\text{Hit}}} p(x_i|\mathbf{a}) \tag{4.4}$$

For a track reconstruction the track parameters and time residuals $t_{\text{res},i}$ of the hits with

$$t_{\text{res},i} = t_{\text{hit},i} - t_{\text{geo}} = t_{\text{hit},i} - \left(t_0 + \frac{\hat{\mathbf{p}} \cdot (\mathbf{r_i} - \mathbf{r_0}) + d_i \tan(\theta_c)}{c_{\text{vac}}} \right) \tag{4.5}$$

can be used as respective $\mathbf{a}$ and x_i. t_{geo} is the hit time that is expected for unscattered photons with the distance d_i between track and hit and the Čerenkov angle θ_c. In a perfect detector

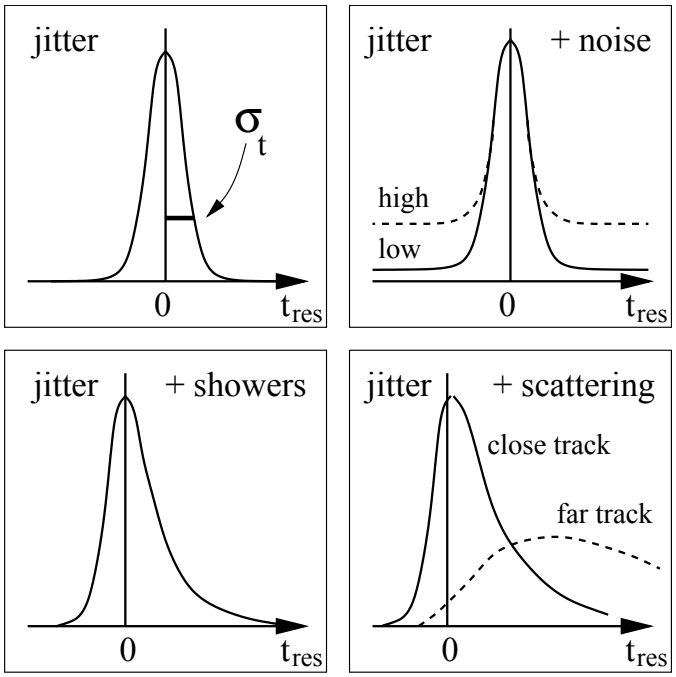

Figure 4.7: Modification of the time residuals of Čerenkov photons for different detector effects (figure from [117]). The ideal case without any detector effects and only Čerenkov photons would be a delta peak at t_{res}. Realistic PMTs have a jitter that dilute the temporal resolution and the time risiduals are convoluted with the normal distribution of the jitter (top left). Random noise hits in the detector are not connected to the physical particle and induce a positive bias to the distribution (top right). Secondary cascades produce photons that are delayed in regard to photons from Čerenkov emission and produce a tail to positive times (lower left). Scattering randomly delays the Čerenkov photons. This leads to a wider distribution that is shifted to positive time risiduals (lower right).

the time risiduals are delta functions. However, in a realistic detector like IceCube several effects like scattering in the ice, PMT jitter and detector noise affect the time risiduals (see figure 4.7). The PDF used for directional reconstructions in IceCube is the so called "Pandel function" [119, 117]

$$p_{\text{Pandel}}(t_{\text{res},i}) = \frac{1}{N(d_i)} \frac{\tau^{-(d_i/\lambda)} \cdot t_{\text{res},i}^{d_i/\lambda - 1}}{\Gamma(d_i/\lambda)} \cdot e^{-\left(t_{\text{res},i} \cdot \left(\frac{1}{\tau} + \frac{c_{\text{ice}}}{\lambda_{\text{ice}}}\right) + \frac{d_i}{\lambda_{\text{ice}}}\right)} \quad . \tag{4.6}$$

Here λ_{ice} is the absorption length of light in ice, Γ the gamma function, c_{ice} the speed of light in ice and d_i the distance of the hit to the track. The normalization factor $N(d_i)$ results to

$$N(d_i) = e^{-\frac{d_i}{\lambda_{\text{ice}}}} \cdot \left(1 + \frac{\tau \cdot c_{\text{ice}}}{\lambda_{\text{ice}}}\right)^{-\frac{d_i}{\lambda}} . \tag{4.7}$$

The "Pandel function" is a parametrization of the time risiduals for registered single-photons-electrons (SPE) of a series. The advantage of this simple model is that one can easily integrate over the time risiduals to create a multi-photon (MPE) PDF of the time distribution. Other advantages are the normalization and the computational simplicity. The "Pandel function" depends on the parameters functions τ and λ which are functions of the distance d_i and other parameters. τ and λ are obtained through fits against distributions of delay times from precise photon-propagation Monte Carlo simulations in AMANDA. A refined version of the likelihood convolutes the "Pandel function" with a Gaussian so negative time risiduals can also be obtained. Furthermore, a term for detector noise is added.

The SPE likelihood is a very simple definition, as it assumes that the PMTs and DAQ can resolve individual photon hits. However, if more than one photon hits a PMT in series often the timing information of only the first photon can be measured accurately. In this case a multi-photo-electron (MPE) likelihood can be used with the PDF

$$p_N^1(t_{\text{res}}) = N \cdot p_1(t_{\text{res}}) \cdot \left(\int_{t_{\text{res}}}^{\infty} p_1(t)\text{dt}\right)^{N-1} = N \cdot p_1(t_{\text{res}}) \cdot (1 - P_1(t_{\text{res}}))^{N-k} \quad . \tag{4.8}$$

In the case of N arriving photons p_N^1 gives the arrival time distribution of the first hit. p_1 is the single photon distribution of a single photon and P_1 is the cumulative distribution of the single photon PDF.

Figure 4.8a shows the cosine of the true neutrino direction from simulations against the cosine of the direction obtained with MPEFit. There is a good correlation for more horizontal reconstructed angles. Vertical reconstructed angles show a larger spread. This is due to low energy events that only produce hits on one string and more often reconstruct as directly vertical events. In NC interactions or interactions with a large Bjorken-y the light is produced by spherical cascades. No real direction is reconstructable for these events. Due to the smaller vertical then horizontal spacing of DOMs low-energy cascades are more often reconstructed as vertical events.

For very low-energy interactions with outgoing muons around and below 1 GeV the boosting of the muon is reduced. This means, that the muon direction does not necessarily align with

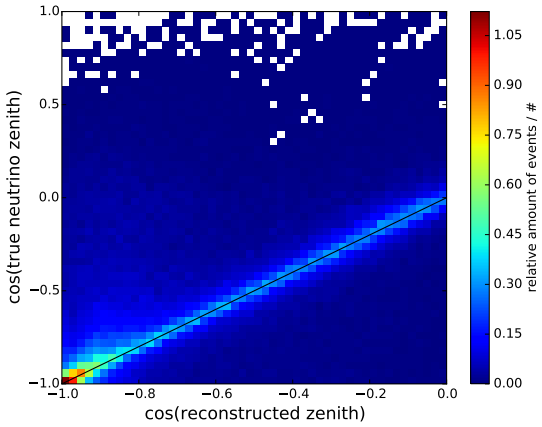

(a) Scatter plot of the cosine of the true zenith angle against the cosine of the zenith reconstructed with MPEFit. The spread for vertical events is mostly due to low-energy events.

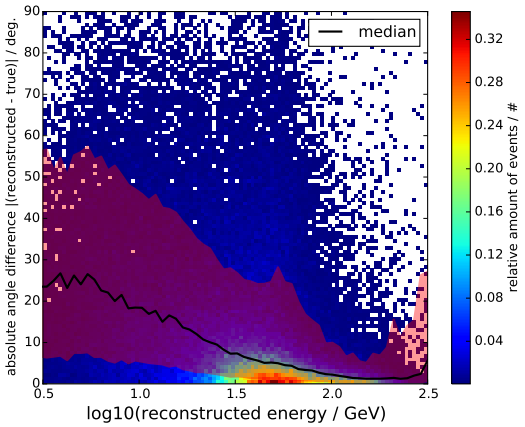

(b) Zenith reconstruction performance for a given reconstructed neutrino energy (see section 4.2.7). The black line marks the median of the events, while the lower and upper edge of the red band mark 16 % and 84 % quantile.

Figure 4.8: Performance of the likelihood based reconstruction using the multi-photon PDF (MPEFit) for muon neutrino events from a GENIE simulation at the final level of the event selection described in section 4.5. Events with $\cos(\theta_{\mathrm{MPEFit}}) > 0$ were removed from the sample.

the direction of the incident neutrino, reducing the resolution of directional reconstructions. With rising neutrino energy, this effect is reduced.

Figure 4.8b shows the median of the reconstructed zenith-angle resolution against the reconstructed energy. This shows how trustworthy the reconstructed angle is for a given reconstructed energy. The red band indicates the 68 % percentile around the median. For low reconstructed energies the angular resolution is reduced with $25° - 30°$ due to the low energy effects discussed above. At the energy critical for neutrino oscillation measurements, the resolution is ca. 10° and reaching a resolution of ∼2° for higher energies, which is typical for IceCube. The resolution gets worse for energies above 200 GeV due to effects of the energy reconstruction.

4.2.5 Reconstructions for Low Energy Events

Neutrinos with energies below some 100 GeV produce muons which loose their energy mostly due to ionization (see section 3.2.1). Muon events of these energies can produce tracks that are contained inside the detector. A rough estimate for the muon energy loss is $\frac{\mathrm{dE}}{\mathrm{dx}} \approx 0.2\,\mathrm{GeV/m}$. Thus a 40 GeV muon from a neutrino interaction inside the detector will produce a 200 m long track.

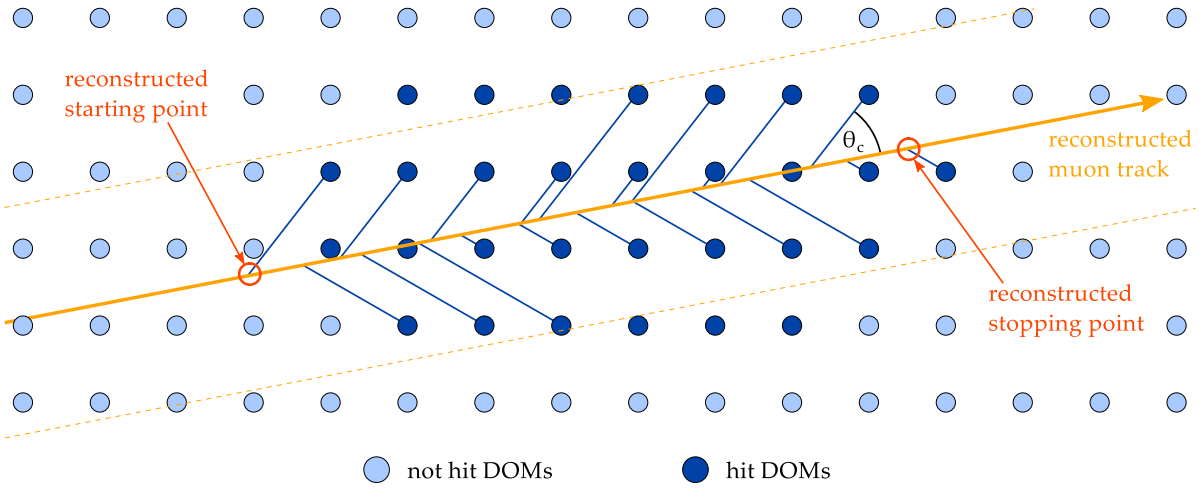

Figure 4.9: Sketch of the finiteReco algorithm from [113]. Hits are projected on a given track reconstruction under the hypothesis of Čerenkov emittance. A first guess for the start and stop point of the track are the both outermost projected hits.

Track Length Reconstruction (finiteReco)

As stated above, the length of a measured contained muon track can be used as an observable for the muon energy. For charged-current muon neutrino interactions this also gives a handle on the initial neutrino energy, if the inelasticity of the interaction is not high (see section 1.2.1).

The length reconstruction of tracks is done with the finiteReco algorithm as sketched in figure 4.9. The algorithm is described in more detail in [113] and [120]. It uses the directional reconstruction described in section 4.2.4 as a seed. Hits that are in a corridor 200 m around this track are selected. The selected hits are then projected onto the track using the Čerenkov-emittance hypothesis with the track as the center of the Čerenkov cone. The first-guess starting point of the track is then the first and the ending point the last projected hit.

For refinement a no-hit likelihood is used. Here the DOMs without hits that lay before (starting point) or after (ending point) the first guess points are selected. For any of these DOMs the likelihood for no hit is calculated, once for the hypothesis of an infinite track and once for a track with the given start- and end-point. The most probable start- and end-points for the track are then obtained by variation of the two points and a minimization of the likelihood ratio.

As the track needs to have a viable start- or stop-point, this reconstruction does not give correct results for muons with higher energies so the track extends into the uninstrumented ice. Thus, the best reconstruction results are obtained with contained events.

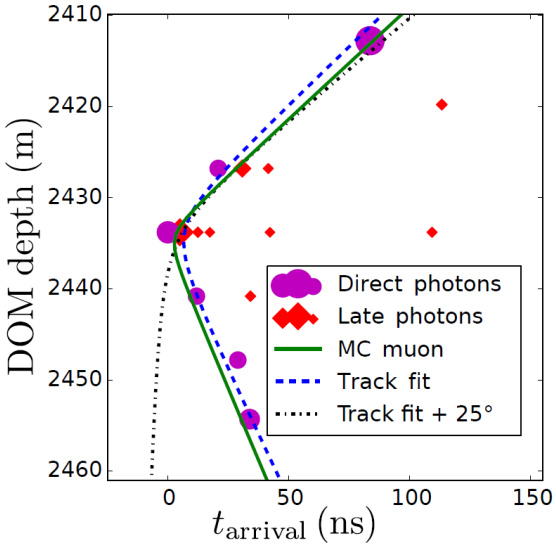

Figure 4.10: Sketch of the algorithm for the selection of direct hits [75].

Selection and Reconstruction Based on Direct Photons (SANTA)

A special directional reconstruction tuned to low-energy events was created for the IceCube neutrino-oscillation analysis covering three years of data [75]. The different parameters obtained in that reconstruction are also used for a step in the event selection described here.

Photons traveling through the ice can scatter before they reach a DOM to be detected. Strongly scattered photons loose their timing and directional information and are thus a factor limiting reconstructions. The algorithm (SANTA) as shown in figure 4.10 is aimed to select only direct hits from Čerenkov emission, thus reducing the diminishing effect of scattering. A complete and detailed description of the algorithm that is based on [121] can be found in [115] and [75].

The algorithm is a cleaning algorithm to generate pulse-maps populated with unscattered pulses. It works on a string by string base. A string is selected if it is populated by at least three hit DOMs [115]. The algorithm starts at the DOM with the highest recorded total charge in a $-1\,\mu$s to $+2\,\mu$s time window around the median arrival time of the first recorded pulse of each DOM on the string. This is the "Seed-DOM" for the selected string. As a first time, the recorded time of the first pulse of the Seed-DOM is used. Starting from the Seed-DOM pulses of DOMs above or below are added to the new pulse-map if their time of arrival relative to the Seed-DOM is consistent with photons emitted on a Čerenkov cone. This is shown in figure 4.10. Photons from a Čerenkov emission produce a hyperbolic hit pattern in the parameter space of DOM depth and arrival time. Every time a pulse is added to the new pulse-map, the Čerenkov hypothesis is updated and the added pulses are tested if they are still consistent with the hypothesis. The expected delay due to scattering in the ice is expected to be lower than 20 ns.

The result for all strings is a cleaned pulse-map. This pulse-map is now used for directional fits using all available strings and a χ^2-approach where no scattering is assumed [75]. Čerenkov photons emitted from a muon-track produce a hyperbolic pattern. Another hypothesis that is tested is the photon emission from hadronic or electromagnetic showers. These photons are emitted spherical and thus they will produce a more parabolic pattern. The χ^2 is modified to account for the angular acceptance and the size of the DOM. The resulting modified χ^2 for each hypothesis of the fit are later used for a final step in the event selection.

4.2.6 Common used Variables in IceCube-Analyses

In the following several variables are discussed that are commonly used in analyses of the IceCube collaboration [122]. These variables are used for a selection in a multivariate approach.

Zenith Weighted (Bayesian) Likelihood

Section 4.2.4 describes the reconstruction of tracks using a likelihood approach. This reconstruction can be extended by exploiting information of the zenith distribution of the muon flux by using the Bayes' Theorem [117].

The flux of atmospheric muons has a strong zenith dependence. Most of the resulting tracks from atmospheric muons are of down-going nature. By using this strong disparity between the directional probabilities of muons as a prior in the reconstruction, some tracks that would otherwise be reconstructed as up-going are reconstructed as down-going. In the event selection the difference of the logarithmic likelihoods for the normal reconstruction and the Bayesian reconstruction is used as an extra parameter and is called "bayesDiff". A bigger value indicates an event with small reconstruction preference between up- or down-going. Thus, a smaller value is preferred.

Number of Direct Hits (NDir)

One commonly used variable in analyses is the number of direct hits. For a given track hypothesis the time a Čerenkov photon would take to reach a hit DOM t_c is calculated. The difference between t_c and the recorded hit times then gives the time risidual. If the time residual is inside a time window of $[-15\,\text{ns}, +75\,\text{ns}]$ it is considered a direct hit[2]. NDir is then defined as the number of DOMs that have a direct hit.

Direct Charge (QDir)

The direct charge is the recorded charge of all found direct hits added together.

Direct Length (LDir)

The direct length represents the length of a track segment that is defined by the direct hits along the track of a given track hypothesis. The first and the last hit DOM perpendicular to

[2] for other analyses different time windows are used

the track direction mark the start- and endpoint for this segment.

Number of Direct Strings (NDirStrings)

The number of direct stings is the number of stings of the detector that have a direct hit.

Depth Direction (ZTravel)

Given a hit map with $N \geqq 4$ recorded hit DOMs, each DOM has a depth defining coordinate Z_i. The DOMs are sorted ascending in time, where the time of the first hit is taken as time of the DOM. The average depth coordinate of the first quartile of hits is given by

$$\langle Z_{\mathrm{FQ}} \rangle = \frac{1}{M} \sum_{j=1}^{M} Z_j \quad \text{with} \quad M = N/4 \quad . \tag{4.9}$$

ZTravel defined as

$$\mathrm{ZTravel} = \frac{1}{N} \sum_{i=1}^{N} Z_i - \langle Z_{\mathrm{FQ}} \rangle \tag{4.10}$$

then gives the cumulative direction in depth of all the hits. A down-going atmospheric muon will most likely produce a negative ZTravel, whereas an up-going neutrino event will produce a positive ZTravel.

Charge Weighted Average Distance (AvgDomDistQTotDom)

This parameter is the weighted mean of the distance d_i of hit DOMs to a given track hypothesis. For the weights of the mean the total charge q_i of the hit DOM is used.

$$\mathrm{AvgDomDistQTotDom} = \frac{\sum_i d_i \cdot q_i}{\sum_i q_i} \tag{4.11}$$

4.2.7 Energy Reconstruction

One observable in the measurement is the reconstructed neutrino energy. To get an accurate energy estimate tracks from the resulting muons of the CC ν_μ interaction as well as starting cascades have to be reconsidered. At energies below $\sim$100 GeV the muon can be considered a minimal ionizing particle and its energy can be estimated from the reconstructed track length (see section 3.2.1) with

$$E_{\mathrm{Muon}} = 0.2\,\mathrm{GeV/m} \cdot L_{\mathrm{Track}} \quad . \tag{4.12}$$

The track length can be reconstructed with finiteReco (see section 4.2.5) and gives a good estimate for events that are contained inside the IceCube detector. For energies above $\sim$100 GeV muons will leave the detector and the uncertainty of the reconstructed end-point rises.

The cascade energy is estimated with a dedicated cascade reconstruction. The complete procedure is explained in more detail in [123]. Since hits from the muon track would lead to overestimating the cascade energy, an algorithm that searches for hits that are likely from the muon track is used to remove these. The hits that remain in the hit map are likely to be

from the starting cascade. The possible cascade hits are then fed into the dedicated cascade reconstruction. The cascades energy is obtained in a likelihood based reconstruction [124, 123] by minimizing the equation

$$\text{nLLH} = -\sum_{i=1}^{n} \ln \mathcal{L}_i = \sum_{i=1}^{n} (B_i \cdot E_{\text{Cascade}} - N_i \ln(B_i \cdot E_{\text{Cascade}} + \rho_i)) \tag{4.13}$$

with respect to E_{Cascade}. Here B_i is the light expectation from a 1 GeV cascade for the i-th DOM, N_i is the recorded signal at said DOM, ρ_i is a noise contribution for the i-th DOM and E_{Cascade} is the wanted cascades energy.

The reconstructed total energy of the neutrino is then

$$E_{\text{reco}} = E_{\text{Muon}} + E_{\text{Cascade}} \quad . \tag{4.14}$$

Figure 4.11a shows the result of the energy reconstruction. The reconstructed value shows a strong correlation with the true neutrino energy of the simulation. However, the relation is not purely linear and a bias exists, indicating that the reconstructed energy is lower than the true one. Several effects lead to this:

- The detected light is dependent on the simulated optical efficiency. A lower efficiency leads to lower values for the reconstructed energy.
- The cascade reconstruction returns the expected energy of an electromagnetic cascade. Since hadronic cascades of the same energy are dimmer (see section 3.2.1), this leads to an underestimation for the cascade energy.
- In NC interactions the invisible outgoing neutrino carries some energy out of the detector.
- Muon tracks leaving the detector will not be reconstructed correctly and thus return a lower muon energy.

Figure 4.11b shows the relative difference between reconstructed and true energy. The difference is plotted against the reconstructed energy. This shows how trustworthy a given reconstructed energy value is. The relevant energy range of this analysis is $0.8 \leqq \log_{10}(E_{\text{reco}}) < 1.75$. In this region the distribution is mostly flat with a bias of around -0.5, indicating, that the true neutrino energy is $\sim$50 % higher. The spread of the values is visualized with the red band. The relative energy spread is around 50 %.

Since the actual reconstructed energy value is not very important, as long as there is a good correlation to the true energy of the neutrino, the reconstruction bias is not problematic. The reconstructed value is helpful for defining a correct range for the histograms of the analysis and for comparison between datasets. The effects of neutrino oscillations have to reside in the defined range.

4.3 Machine Learning

Manual tuned cuts on strong variables that separate signal and background events are fast and intuitive. These cuts are the pristine tool for big data masses on early selection levels. On later

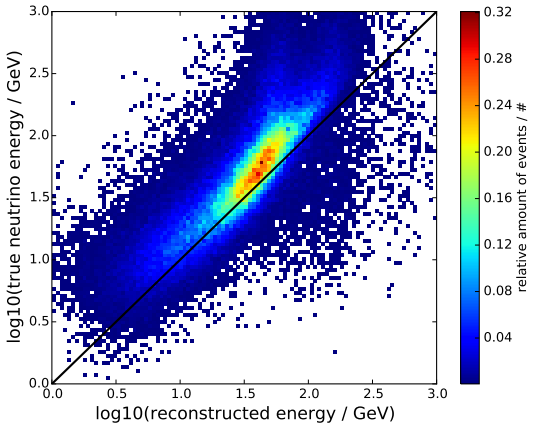

(a) Scatter plot between true neutrino energy of the simulation against reconstructed neutrino energy. there is a clear correlation between reconstructed and true neutrino energy.

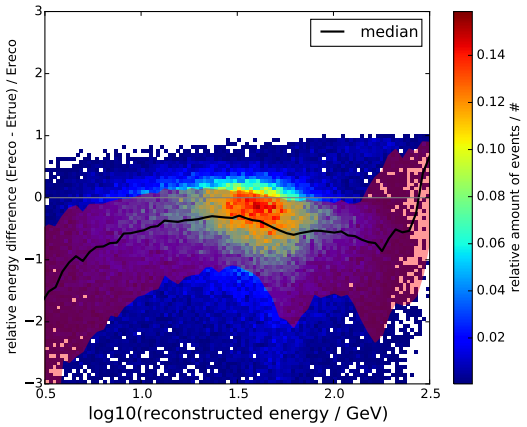

(b) Relative difference between reconstructed and true energy against the reconstructed energy. The black line marks the median of the events, while the lower and upper edge of the red band mark 16 % and 84 % quantile.

Figure 4.11: Performance of the energy reconstruction used for the IC79 dataset of the analysis. The events are from a muon neutrino dataset simulated with GENIE at the final level of the event selection described in section 4.5.

levels the data masses are reduced, so more sophisticated tools can be used. Also the strong variables were already used to separate signal and background. The remaining variables are sometimes weak and cannot be used for an easy manual separation.

In the last few decades machine learning algorithms have been developed to automatize the process of event classification [125]. Especially in the field of particle physics the growth of data has led to an early adoption of machine learning paradigms like artificial neural networks and decision trees. In the event selection used for this analysis decision trees were used to separate the atmospheric muon background from neutrino signal events. For this the tool *pybdt* [126] is used.

4.3.1 Decision Trees

Decision trees (DT) can be used for classification or regression [125]. They operate on continuous or discrete data alike. The DT itself is a binary tree. For an event a variable is checked at a node against a given threshold. If the value of the variable is lower than the threshold, the event is put into the left branch of the tree. For a higher value, the event is put into the right branch. This is repeated for every subsequent node. In the end the event will reach a leaf of the binary tree and is classified. For a simple case the event is classified into -1 or 1. In the given DT the event class is coupled to the purity of the leaf for the training dataset and can have values between -1 and 1. Instead of checking only against a single variable in the tree, an arbitrary number of known variables can be used.

With growing depth and number of variables the separation strength of the tree regarding the training dataset grows. In the end an optimal separation for the training dataset is reached. However, if this tree is used to classify a new test dataset, the separation may be worse than a classification for a more simple tree. This effect is called overtraining or overfitting. One way to reduce the overtraining is a limited growth of the tree itself. However, if the tree is too shallow its performance will also be limited. Other mechanisms to avoid overtraining are bootstrap aggregation (bagging) or tree complexity reduction (pruning).

4.3.2 Pruning

Pruning is a mechanism to reduce the complexity of a grown decision tree [125]. Branches that do not have a large impact on the classification error are removed from the tree. For this the cross validated error on every possible sub-tree is calculated. Typically branches are cut, if the increase in error is below one standard deviation with respect to the minimal classification error. Due to the reduction in complexity, the resulting tree is more stable regarding overfitting.

4.3.3 Boosting with AdaBoost

A strong impact on decision tree based learning had the introduction of boosting by R. Schapire in 1990 [127]. In boosting, several weak learners are coupled to increase the separation strength of a learning algorithm. The algorithm used in pybdt for boosting is AdaBoost[3] [128] as defined in [129] and [130].

Given there are N events for training, each with a set of variables $\mathbf{x}_i$ with $i = 1, 2, ..., N$. y_i is defined as 1 if the ith event is a signal event and as -1 if it is a background event. For a classifier trained with these events the weight for the ith event is $w_i = 1/N$. The classifier will output $T(\mathbf{x}_j) = 1$ if an event j with a set of variables $\mathbf{x}_j$ is classified as signal and -1 if it is classified as background. If the variables are only usable for separation to a very limited degree, the resulting classifier will not perform very good. This is called a weak learner.

For M trained classifiers we can now define $I(y_i) = 1$ if $y_i \neq T_m(\mathbf{x}_i)$ else $I(y_i)$ will be 0. Here m marks the index of the classifier with $m = 1, 2, ..., M$. Now we can calculate the classification error for the mth learner

$$err_m = \frac{\sum_{i=1}^{N} w_i \cdot I(y_i \neq T_m(\mathbf{x}_i))}{\sum_{i=1}^{N} w_i} \tag{4.15}$$

and define the boosting parameter

$$\alpha_m = \beta \cdot \ln((1 - err_m)/err_m) \quad . \tag{4.16}$$

Here β defines the boosting strength. The original AdaBoost algorithm uses $\beta = 1$, while in this event selection $\beta = 0.7$ is used. For the training of the next learner T_{m+1} the weights are now redefined with respect to their classification error of the actual learner

$$w_i \to w_i \cdot \exp(\alpha_m I(y_i \neq T_m(\mathbf{x}_i))) \quad . \tag{4.17}$$

[3] Adaptive Boosting

The sum of the weights has to be 1, thus the weights have to be renormalized

$$w_i \rightarrow \frac{w_i}{\sum_{i=1}^{N} w_i} \quad . \tag{4.18}$$

In this way M classifiers are trained. The boosting has a cumulative impact on the weights as the weights from the previous learner are used to reweight them for the actual learner.
For a new event with variables $\mathbf{k}$ that is classified with the M trained classifiers the final score is calculated as

$$T(\mathbf{k}) = \sum_{m=1}^{M} \alpha_m T_m(\mathbf{k}) \quad . \tag{4.19}$$

The score is a new parameter for the event build from the weak variables and can be used to separate signal and background. It was shown in [127] and [128] that boosting always can be used to improve the classification for weak variables, given the variables provide a better separation then pure chance. Boosting also reduces the importance of very weak variables in the BDT. This way the "curse of dimensions", where each added variable also increases the computational demand, can be negated.

4.3.4 Randomization

Another way to increase the robustness of the classifier is the usage of randomization. If for example N classifiers are trained each with a random drawn subset of the training data, the resulting classifiers will behave differently. The final result can then be drawn from the simple majority vote of all classifiers. This ansatz is widely called a "bagging"[4] algorithm [125]. The used randomness leads to a robust classification for the complete set of classifiers. Another way to induce randomness into the learning algorithm to reduce the variability of the classifier is the usage of "random forests". Here the variables at each node are a random drawn subset of the total set of variables. Random forests yield stronger decorrelated predictors as is possible with bagging and are thus widely used.

Pruning and "randomization" both are used to raise the robustness and are normally used independent of each other. In this event selection both are used in combination.

4.4 Datasets

The different simulation datasets used for the development of the event selection depicted in section 4.5 are listed in table 4.2. GENIE and NuGen datasets are "stitched" by using a linear reweighting in the crossover region as used in [113]. Given are the simulated and used energy range, the designated number of the dataset, the simulated optical efficiency and the scattering length of the refrozen ice columns surrounding the strings. All datasets used for the creation of the event selection were generated with the *SpiceMie* ice model as described in section 3.4.4.

These datasets differ from the datasets used in the actual analysis. The most striking difference is the noise model. Whereas the datasets used for the creation of the event selection

[4] bootstrap aggregating

Table 4.2: Datasets used for the test of the event selection and training of the BDT

Particle	Generator	$E_{\text{sim.}}$ [GeV]	E_{used} [GeV]	Number	Opt.Eff.	$\lambda_{\text{HoleIce}}[\text{cm}^{-1}]$
ν_e	GENIE	$1 - 100$	$1 - 99$	80003	0.90	1/50
ν_e	GENIE	$1 - 100$	$1 - 99$	80006	0.90	1/50
ν_μ	GENIE	$3 - 150$	$3 - 145$	80009	0.90	1/50
ν_e	NuGen	$10 - 10^9$	$50 - 10^9$	7785	0.90	1/50
ν_μ	NuGen	$10 - 10^9$	$50 - 10^9$	6467	0.90	1/50
atm. μ	CORSIKA	prime:	$600 - 10^{11}$	6939	0.90	1/50

only have a poissonian noise component, the datasets used for the analysis incorporate an extended noise model with simulated correlated noise pulses from scintillation. The reason is the lack of background simulation with the updated noise model. To not tune the event selection to differences in noise models, older neutrino simulations comparable to the background simulation have been used.

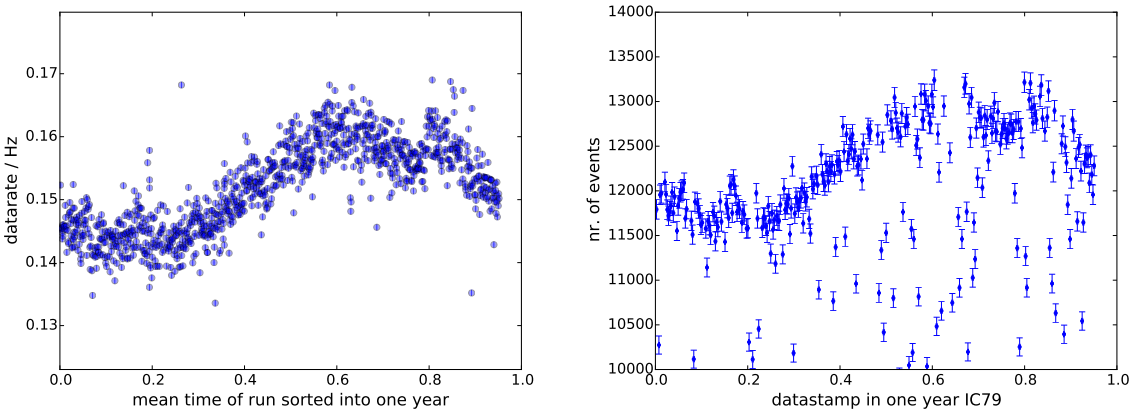

(a) Rate per individual run of data taking.

(b) Number of events for a given timespan.

Figure 4.12: Rate and number of events for IceCube data taken in the IC79 detector configuration in "fraction of year". The blue shaded area indicates a scheduled detector downtime for the preparation of the first IC86 run.

The described event selection is aimed for data taken in the 79 string configuration (IC79) of the IceCube detector. Figure 4.12 shows the event rate per individual run and number of events of the IC79 data over the course of one year. The data was taken between May 31th of 2010 and May 13th of 2011. In the last days of the year the detector was prepared for the IC86 detector configuration and no usable data was recorded (blue shaded area). Visible is the sinusoidal atmospheric variation of the muon flux over the year. The visibility of the seasonal variations indicates the dominance of events by atmospheric muons.

There is a jump in event rate at the 80 % point of the year in figure 4.12a. This is caused

by a change of the run configuration resulting in higher trigger rates. Figure 4.12b shows the number of events binned for each day of the year. Some days have a reduced number of events due to unphysical test runs reducing the overall live time for this day. This is especially visible at the 60 % mark of the year. Here a lot of test runs for the upcoming new detector configuration were performed.

4.5 Event Selection

In the previous sections the individual steps used in the event selection and the used datasets were discussed. In this section the individual selection steps and their impact on the datasets are presented.

The rates against recorded total charge per event in photo electrons is shown in figure 4.13. Due to the unsimulated noise contribution of coincident photons from scintillation light, the atmospheric muon background is affected differently than data for most of the veto-cuts. Since the simulated background is used solely for the development and review of the event selection but not in the actual fit, the fit itself is not impacted by this. For the plots in figure 4.13 the neutrino simulation with coincident noise as used in the actual fit is used.

Filter Level (Level 2)

The event selection starts at the *filter level* which is the second level in the event selection of on-line filters. From the existing level 2 data only events that passed the DeepCore filter (see section 4.2.1) are used. At this selection level the overwhelming part of the data consists of atmospheric muon events. The subsequent levels of the event selection are aimed to reduce the amount of these events while keeping the loss of actual neutrino events to a minimum.

Visible is a data-MC discrepancy for a total charge below 10 p.e. which is caused by events triggered by coincident noise. The rate between simulation and data matches well above 10 photo-electrons.

Level 3

In the next step the CRT-Veto is used together with the optimized CRT cleaning. This reduces the amount of atmospheric muons by ∼98 % while ∼70 % of the muon neutrinos remain. Due to the unsimulated coincident noise component data is reduced stronger by the veto than simulated atmospheric muon background.

Level 4

Now several tools like the NoiseEngine, Top-Bottom-Layer veto and CorridorCut[5] are combined. The amount of data is reduced to ∼30 %. A dominant part of this is due to the removal of noise triggered events by NoiseEngine. The amount of atmospheric muon background is reduced by about 50 %, while 70 % of the ν_μ signal events remain. There is still a considerably mismatch between data and total simulation.

[5] these were discussed in section 4.2.3

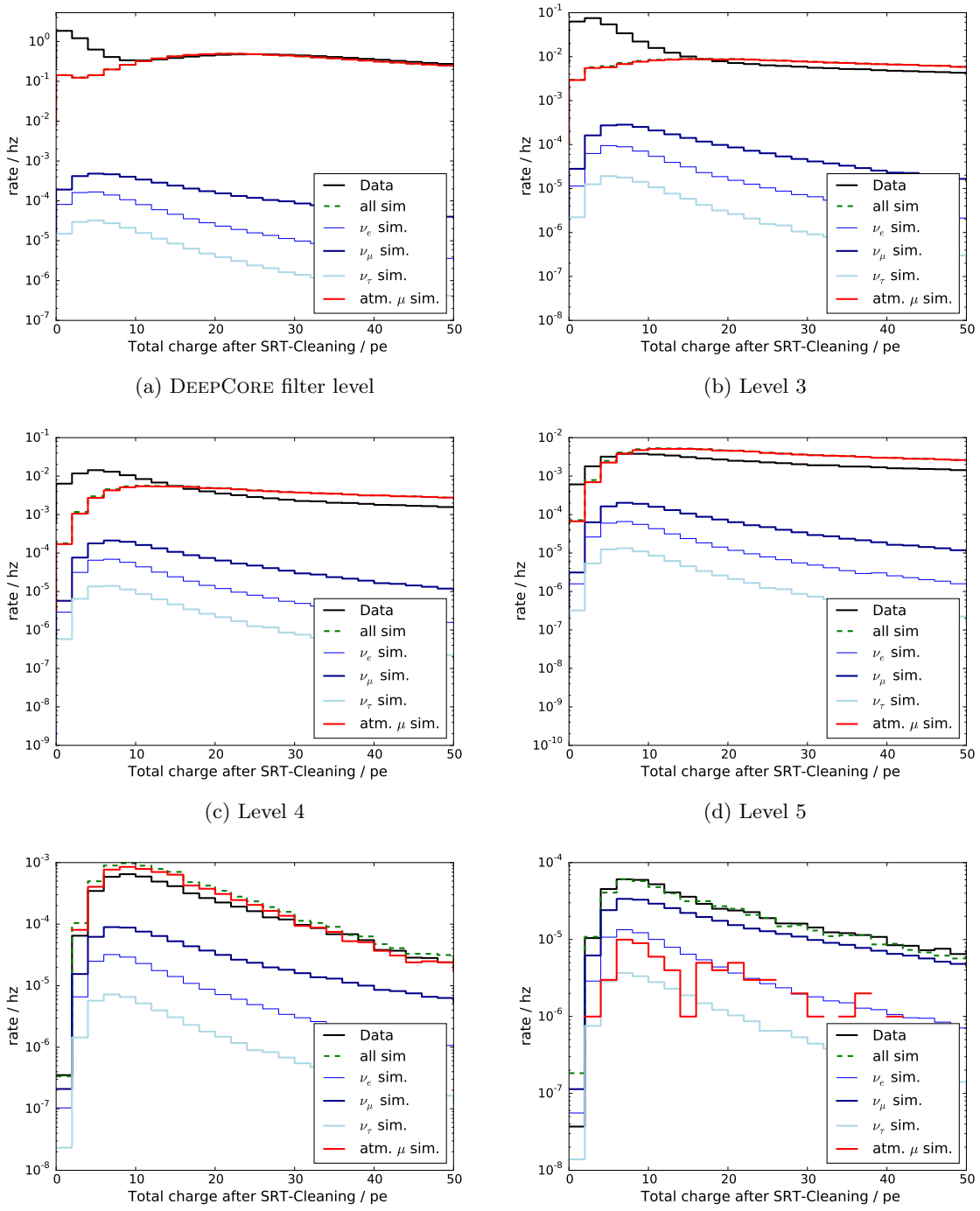

(a) DeepCore filter level

(b) Level 3

(c) Level 4

(d) Level 5

(e) PreBDT level

(f) after BDT

Figure 4.13: Rates of data and simulation datasets against the number of recorded photo-electrons per event at the different levels of the event selection, that is after the described selection of that level. The pulse map was processed with the SeededRT cleaning to remove pulses by detector noise. Two flavor neutrino oscillation is assumed with $\Delta m^2_{32} = 2.39 \cdot 10^{-3}$ and $\sin^2(2\theta_{23}) = 0.948$. The low energy GENIE simulations of ν_e and ν_μ are extended with high energy simulations generated with NuGen.

Table 4.3: Events removed before training of the BDT

Variables	$\cos(\theta_{\text{MPEFit}})$	VetoHitLaunches	VetoHit Charge [p.e.]		
remove if higher	0	10	10		
remove if lower	-	-	-		
Variables	recoZ [m]	recoR [m]	LDir [m]	QDir [p.e.]	bayesDiff
remove if higher	-170	270	350	100	5
remove if lower	-700	-	-	-	-

Level 5

One part of the mismatch between simulation and data is the unsimulated contribution of coincident muon hits. Thus, the fifth selection level incorporates the Topological Splitter (section 4.2.3). If more than one cluster is found, the event may have been caused by more than one muon. Thus, events are discarded if more than one cluster is found or if not even one cluster can be identified. The data rate is reduced to about 55 % while ∼94 % of the simulated atmospheric muon events and and ∼97% of the simulated muon neutrinos remain.

preBDT Level

At this stage the data rate is reduced sufficiently to perform time consuming reconstructions. These reconstructions are then used in the final selection steps.

The improved version of the Line-Fit as described in section 4.2.4 is run on the found cluster from level 5 and used as a first guess algorithm for a likelihood based fit with a single photo-electron (SPE) hypothesis. The reconstruction result is called *iSPEFit*. The result is then used as a first guess for a SPE fit with 32 iterations (*iSPEFit32*) which itself is fed into a likelihood based fit with a multi photo-electron (MPE) hypothesis called *MPEFit*. This is the final directional reconstruction. The SANTA reconstruction based on direct photons from section 4.2.5 also returns a track direction for some events. The zenith angle difference between this reconstruction and the MPEFit is saved as *SANTADiff*. If no SANTA fit is available, the parameter is set to -2. Also the parameter *hasSANTA* is created to indicate if the SANTA reconstruction has provided a direction or not.

Next the Causality-Veto algorithm as described in section 4.2.3 is run. The number of hits and the total charge inside the veto region defines the parameters *VetoHitLaunches* and *VetoHitCharge*.

In the last two steps, the common variables NDirString, NDir, LDir, QDir, ZTravel, AvgDomDistQTotDom and bayesDiff (section 4.2.6) are calculated and the track length reconstruction finiteReco (section 4.2.5) is run on a CRT cleaned pulse map. For the CRT cleaning the parameters $R = 150\,\text{m}$ and $T = 1000\,\text{ns}$ are used. Variables derived from finiteReco are Z position of the vertex (*recoZ*) and radial distance of the vertex to string 36 (*recoR*).

Before a machine learning algorithm can be trained for the next level of the event selection some events have to be discarded. Since in the analysis only up-going events are of interest and the final zenith reconstruction is based on the MPEFit, every event reconstructed by MPEFit

as down-going is dropped from the event stream. The statistics of simulated atmospheric muons from CORSIKA is very low, thus the tails of some variable distributions have to be removed from the sample to stabilize the BDT. For example there are virtually no CORSIKA events with VetoHitLaunches > 10, even though events with high values are most likely from atmospheric muons. Since the statistics of signal simulation is very high, there are, however, several neutrino events with VetoHitLaunches > 10. This would bias the BDT and cause a higher background of atmospheric muon events in the final sample. Table 4.3 shows the used values for the removal of these events.

Since most of the atmospheric muon background is reconstructed as down-going, the removal of these events strongly reduces the data rate. In relation to level 5 about 6.7 % of the data remains. The atmospheric muon background is reduced to 5.7 %. In contrast the muon neutrino rate remains at ∼47 %, which is only slightly below the optimum of 50 %.

BDT Selection

At this stage the rate of the atmospheric muon background is still one order of magnitude above the rate of muon neutrino events. The next step in the event selection utilizes a "forest" of boosted decision trees as described in section 4.3 to bring the background rate down further. The set of individual decision trees is simply called *BDT* in the following.

For this the simulation datasets are split into a training and a testing dataset each. Both sub-datasets consist of 50 % of the events. This is done to test the BDT with an independent set of events that are of the same quality as the training events. The test events are used to estimate the efficiency of the BDT. The BDT is used to classify events into "background" or "signal". For background the atmospheric muon dataset simulated with the CORSIKA Monte Carlo software is used. Signal events are from GENIE and NuGen simulations of muon neutrino events. The used GENIE dataset covers the energy range from 3 GeV to 150 GeV and was generated with an E^{-2} spectrum. Thus, the statistic for events of higher energies is sparse. Since at these energies simulations generated with NuGen are valid, a NuGen dataset is used to extend the muon neutrino dataset to higher energies. In the energy range of 50-145 GeV the GENIE events are linearly weighted down, whereas the NuGen events are linearly weighted up. From this dataset the special "signal dataset" used for the BDT training is drawn. The signal dataset only consists of events from CC muon neutrino interactions. The true energy from the simulation of these neutrinos has to be lower than 200 GeV. For the testing dataset all events are used without a special selection.

For the training of the BDT the software package "pyBDT" [126] is used with 14 different parameters drawn from the events of the training datasets. These parameters are NDirString, NDir, LDir, QDir, ZTravel, AvgDomDistQTotDom, bayesDiff, VetoHitLaunches, $\cos(\theta_{\mathrm{iSPEFit32}})$, $\cos(\theta_{\mathrm{MPEFit}})$, recoR, recoZ, SANTADiff and hasSANTA.

Correlation matrices of parameters used for the BDT are shown in figure 4.14. There is a distinct difference between the matrices for signal and background. For signal the event quality parameters LDir, NDir, NDirStrings and QDir are strongly correlated to each other, like one would expect. Also the santaDiff parameter has correlations with these parameters, since the used SANTA reconstruction itself is strongly connected to the event quality. The

bayesDiff parameter shows an anti-correlation for these quality driven parameters. Since events are more easily to reconstruct if they are of good quality, this anti-correlation is expected. For the background datasets this (anti)-correlation is much toned down. Most events are of poor quality and consist of hits from scattered photons with a loss in directionality. The data shows the same pattern as the background simulation, indicating the dominance of background over signal events.

For the training of the BDT 300 trees with a depth of three levels each are trained. The boosting parameter for AdaBoost is set to $\beta = 0.7$. The pruning strength was configured to 20 %. This means only 20 % of the pruning sequence is performed. Furthermore at every node of the trees four parameters of the total of 14 parameters are randomly chosen.

Like described in section 4.3, the output of the BDT is a score value. Small values are more background like and high values are more signal like. The split-value was chosen in such a way, that the rate of the background is identical to the analysis in [113]. The resulting rate of muon neutrino events is ∼50 % higher as for that analysis, if the same datasets are used. This gives a direct indication of the improvement of the event selection. One effect of the background removal is the improvement in agreement between simulation and data. As is visible in the signal dominated regions.

Figure 4.16 shows the efficiency of the BDT selection. At the threshold value around 50 % of the neutrino datasets remain, while the background is reduced to about 1 %. The remaining background simulation only consists of 63 events which is very sparse. The data is reduced to ∼12 % and is neutrino dominated. As shown in figure 4.17 the atmospheric muon background dropped below the background from electron neutrino events with the muon neutrino rate being one order of magnitude higher than both of the others.

final Level

At this stage the IC79 data is on neutrino level. To bring the datasets in sync with the existing IC86 datasets from [115], the final selection of that analysis is also performed as a final selection step. The fit results of the SANTA algorithm (see 4.2.5) are used to select track-like events with hits from unscattered photons. First events are discarded if less than five direct hits are found by the SANTA algorithm. In the following events are only used, if they have a reduced χ^2 below 20 for single-string or 60 for multi-string fits. The reduced χ^2 of the SANTA track and cascade fits are now used to calculate the overall fit quality

$$Q_{\text{fit}} = \frac{\chi^2_{\text{cascade}}/\text{ndof}}{\chi^2_{\text{track}}/\text{ndof}} \tag{4.20}$$

to select good track-like events [115]. The degrees of freedom (ndof) being the number of DOMs hit by direct photons reduced by the free parameters of the fits. Events are discarded if they have a Q_{fit} smaller than 0.8 for multi-string fits, or 0.6 for single-string fits. The last selection step uses the directional reconstruction of SANTA. Some events are reconstructed up-going by MPEFit, which is used as a directional proxy for the IC79 analysis, but down-going by the SANTA reconstruction. These events are discarded as they do not give a reliable directional fit.

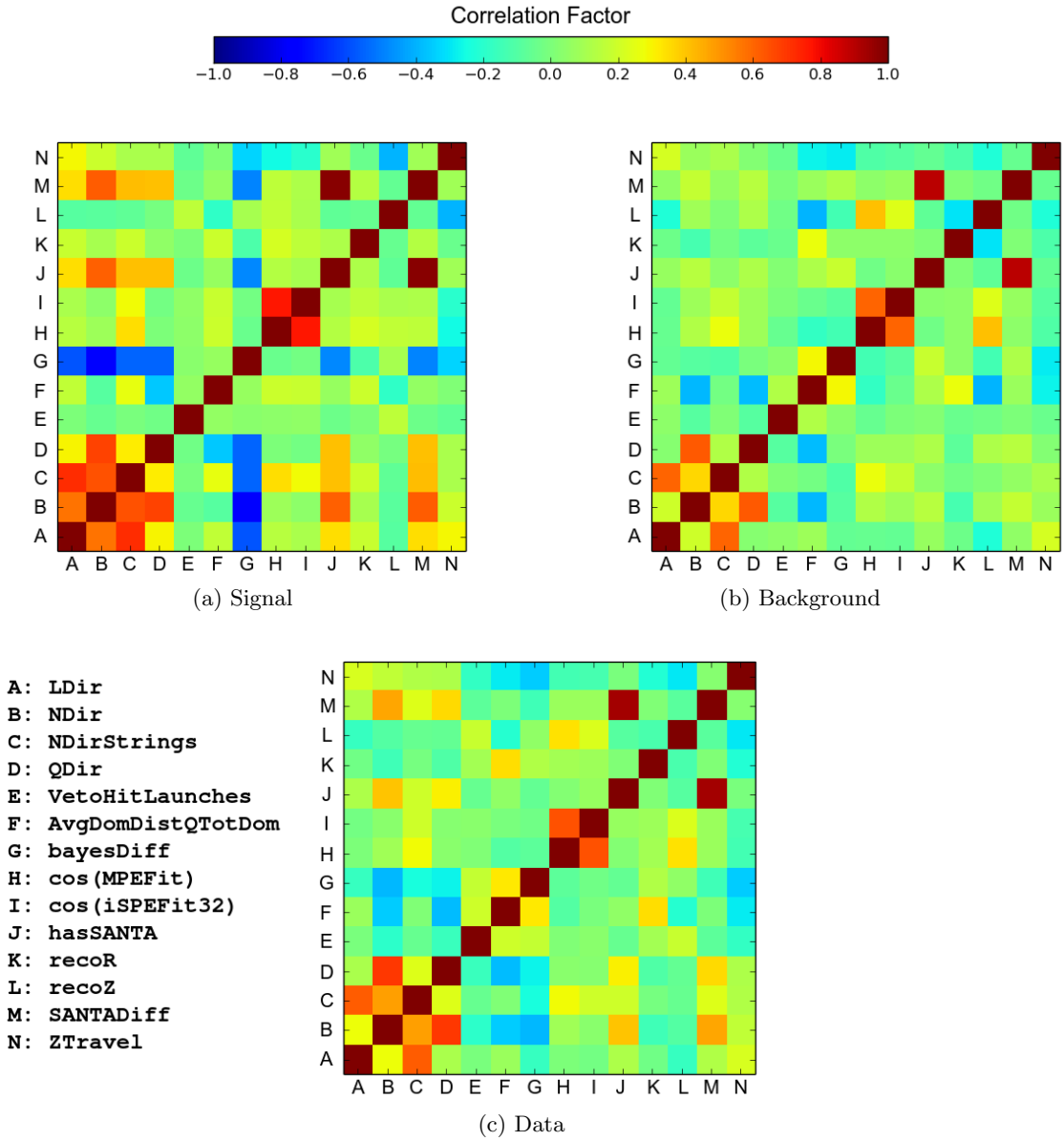

(a) Signal

(b) Background

(c) Data

Figure 4.14: The correlation matrix for signal, background and data with the parameters used for the training of the BDT.

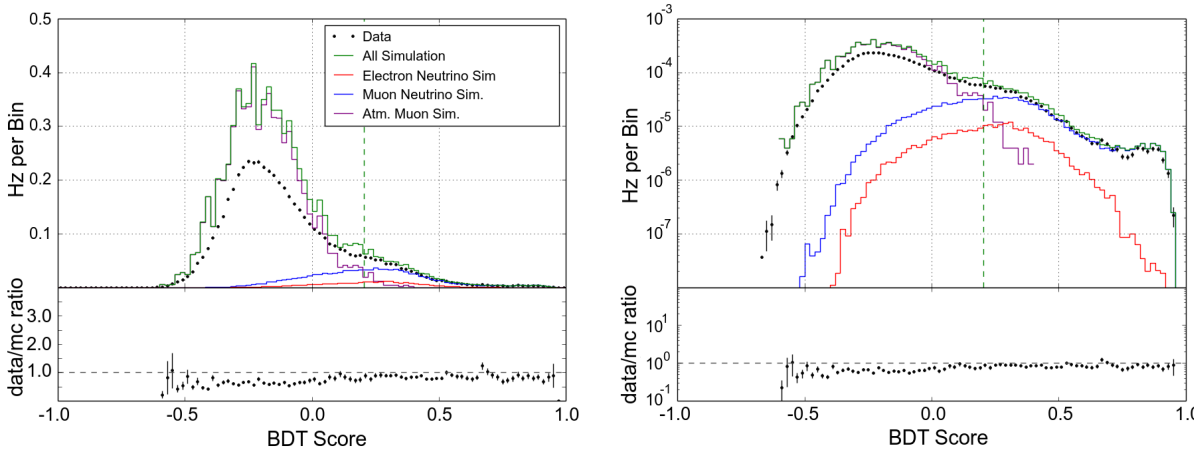

Figure 4.15: The event rate of the testing datasets and data against the BDT score in linear (left) and logarithmic scale (right). The dashed line indicates the threshold for the classification. Events with a higher score are classified as possible signal events, whereas events with a lower score are classified as background. For testing the full muon neutrino dataset is plotted. Neutrino oscillations are not taken into account.

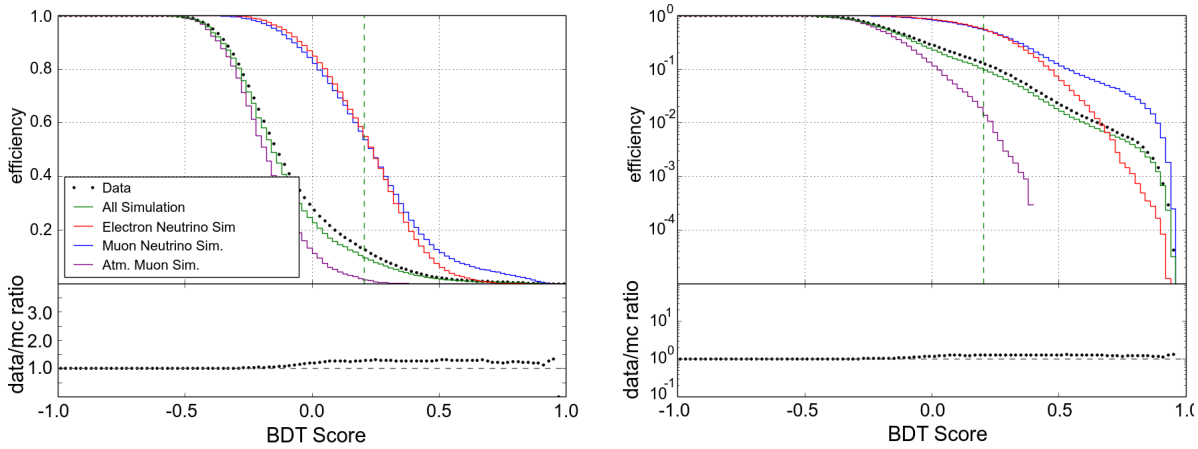

Figure 4.16: The selection efficiency of the BDT against the BDT score for the testing datasets and data in linear (left) and logarithmic scale (right). The dashed line indicates the threshold for the classification. For testing the full muon neutrino dataset is plotted. Neutrino oscillations are not taken into account.

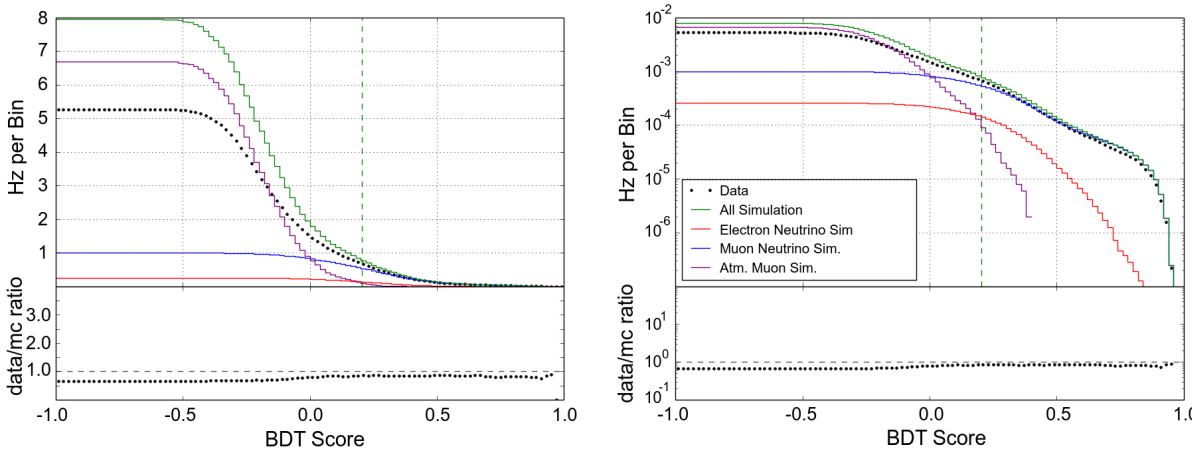

Figure 4.17: The cumulative rate for the testing datasets and data against the BDT score in linear (left) and logarithmic scale (right). The dashed line indicates the threshold for the classification. For testing the full muon neutrino dataset is plotted. Neutrino oscillations are not taken into account.

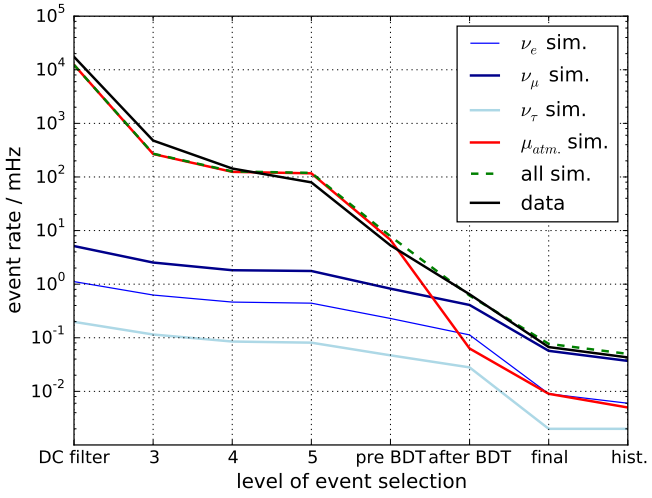

Figure 4.18: Event rates at different levels of the event selection. Two flavor neutrino oscillation is assumed with $\Delta m^2_{32} = 2.39 \cdot 10^{-3}$ and $\sin^2(2\theta_{23}) = 0.948$. The last step labeled "hist." is the content of the histogram used for the fit.

The last selection step reduces the sample by about 90 %, since only good quality events are used. Only 9 events remain of the atmospheric muon simulation. This number is reduced further to only 5 events for the relevant energy range, which is too low to be used in the analysis. Thus, a background extraction from data has been performed. This is discussed in section 5.4 of the following chapter.

The different rates of all datasets over the course of the event selection are plotted in figure 4.18 for a two flavor oscillation between ν_μ and ν_τ with $\Delta m^2_{32} = 2.39 \cdot 10^{-3}$ and $\sin^2(2\theta_{23}) = 0.948$. The whole event selection covers seven orders of magnitude and the atmospheric background is reduced by six orders of magnitude to below the irreducible background of electron neutrinos. The rates of each step can be found in table B.1 in the appendix.

Chapter 5

Data Analysis

In this chapter the treatment of the simulations and data at the analysis level and tools for the background estimation are discussed. Furthermore, the analysis framework and the systematics of the fit are presented. The result of several tests performed with the analysis framework and simulated data is covered in the second half of the chapter.

5.1 Introduction

The analysis presented in this work is an extension of a published analysis [75]. The published result is based on three years of IceCube data in the 86 string configuration. The previous chapter covered the event selection for IceCube data in the 79 string configuration. This analysis combines the four years giving an updated result.

The presented analysis aims to determine the oscillation parameters Δm^2_{32} and θ_{23}. For this the deficit of atmospheric muon neutrinos in regard to the case without oscillations is used.

In the following the datasets used for the analysis are discussed followed by a description of the combined fit procedure.

5.2 Datasets Used for the Analysis

For the IC79 part of this analysis several different datasets have to be used. Neutrino events have been generated with GENIE based Monte Carlo simulations (see section 3.4.1). Every neutrino flavor has its own set of simulations. To cover systematic effects due to uncertainties of the optical efficiency, datasets have been generated with a different global sensitivity of the optical modules. Another systematic that has to be covered is the angular acceptance of the DOMs. Due to bubbles in the refrozen ice that fills the holes of the deployed strings the average distance between two scattering processes of a photon, the scattering length s, is different than for the surrounding medium. This modifies the angular acceptance in regard to a DOM in water or clear ice. The difference between the individual datasets for the hole ice is shown in figure 5.1. The detector noise model used for all simulation datasets of the analysis covers poissonian noise contributions as well as correlated noise photons due to scintillation. The used SpiceMie ice model is the same as was used for the result from [75].

Apart from the main GENIE based Monte Carlo that covers energies up to 190 GeV and different detector systematics, two high-energy GENIE datasets exist. These datasets are used to extend the main GENIE datasets to higher energies starting at 190 GeV. The effects due to detector systematics are only obtained from the low-energy datasets, though. The high-energy extension only covers electron and muon neutrinos. However, the high energy flux of tau neutrinos is negligible since they are only produced by neutrino oscillations in the low-energy regime. A CORSIKA based dataset of atmospheric muons was used to optimize the event selection. Due to low statistics of simulated events in the final sample, a data driven approach for the atmospheric muon background was chosen. All datasets used in the analysis are shown in table 5.1. For the baseline an optical efficiency of 0.99 and a hole ice scattering length of 50 cm is used for the simulation.

Since this work is an extension of the three year IC86 neutrino oscillation analysis, the datasets used for the IC86 part are identical to the ones from [115, 75]. The IC79 simulation is generated from the same initial datasets. This means the low-energy neutrino simulations of the IC86 part differ only in the detector configuration. The parameters are thus the same as in table 5.1. However, the high-energy part is covered by NuGen based simulations. The description of the datasets used for the IC86 part is covered in more detail in [115].

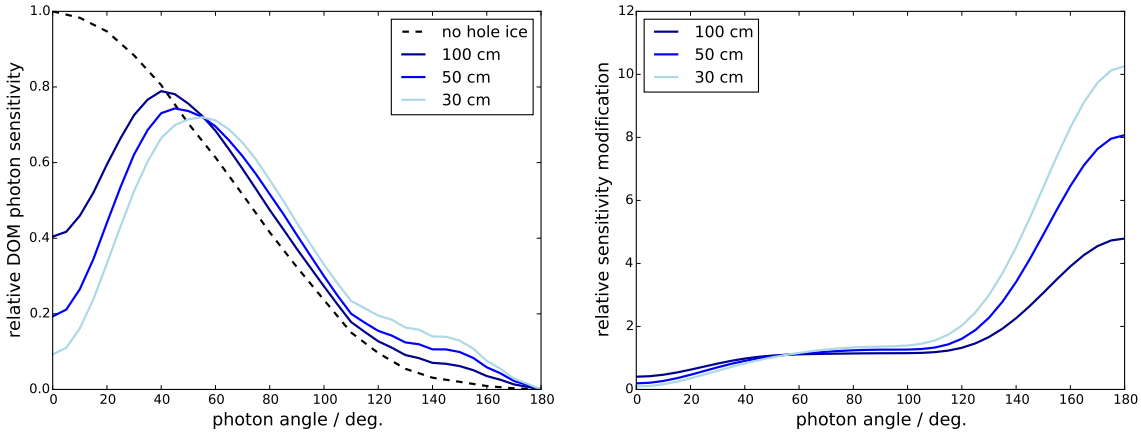

(a) Relative DOM Photon Sensitivity.

(b) Sensitivity modification to the "bulk ice" case.

Figure 5.1: Angular photon acceptance curves for "hole ice" models with different scattering lengths used in the data simulation (right). For no hole ice the acceptance is maximal on the bottom of the DOM (photon angle of 0°), since it directly enters the PMT. The modification to the bulk ice is shown on the right. Values taken from [131].

Table 5.1: Datasets used in the analysis to generate the expected event distribution for the one year of IC79

Particle	Generator	Energy Range	Number	Optical Efficiencies	s_{HoleIce} [cm]
ν_{e}	GENIE	$3 - 190\,\mathrm{GeV}$	1250	0.81, 0.90, 0.99, 1.08	30, 50, 100, inf
ν_{μ}	GENIE	$3 - 190\,\mathrm{GeV}$	1450	0.81, 0.90, 0.99, 1.08	30, 50, 100, inf
ν_{τ}	GENIE	$3 - 190\,\mathrm{GeV}$	1650	0.81, 0.90, 0.99, 1.08	30, 50, 100, inf
ν_{e}	GENIE	$3 - 1000\,\mathrm{GeV}$	12052	0.99	50
ν_{μ}	GENIE	$3 - 1000\,\mathrm{GeV}$	14052	0.99	50
atm. μ	Data	all	-	-	-

The final histograms consist of events with $\cos(\theta_{\text{reco}}) < 0$ and a reconstructed neutrino energy of $\log_{10}(E_{\text{reco}}) \in [0.8, 1.75)$. In these zenith and energy range 1172 events were measured in the IC79 configuration on the final level of the event selection. The combined three years of data in the IC86 configuration consist of 5174 events. Thus, the the total event count for the combined four year analysis is 6346 events.

5.2.1 Inclusion of High-Energy Events

As described in section 5.2, the low-energy GENIE datasets used for the analysis only cover an energy range up to 190 GeV. This is due to limitations of the used generator at the time of simulation. To extend this range simulations based on a patched version of GENIE are available, that cover the energy range up to 1000 GeV. However, not all needed simulation sets were available at the time this analysis was performed. Furthermore the new datasets were not approved by the collaboration, so the older datasets had to be used for the analysis. To account for the high energy events while still using the older and approved datasets, only the high energy part of the new datasets is used. For the baseline datasets, the low-energy and the high-energy sample are matched in rate in the energy range between $150 - 190$ GeV by scaling the high-energy sample. The low-energy simulation then supplies the events up to 190 GeV, while the high-energy simulation supplies the events starting from 190 GeV. Systematics like the optical efficiency and the hole-ice scattering are drawn from the available sets in the low-energy regime and then applied to the full-range sample in the end. This ist further explained in section 5.7.1.

5.3 Kernel Density Estimation

At the final level some datasets are drastically reduced in statistics. The reduced statistics results in very sparse histograms, especially if the events are binned in more than one dimension. To get smooth distributions and use the available events as effective as possible, a kernel density estimation (KDE) has been used.

KDEs are similar to histograms [132]. In a histogram, events are grouped into bins and the number in the bin is counted. Another interpretation is, that for every bin a square shaped function with a width equal the bin width and a height of one is added to the overall histogram with its center aligned to the bin center. In a KDE, the center of the function is aligned to the event itself. The used function for the event is called the *kernel*. It can be a any function that can be normalized. The kernel density estimator is then

$$\hat{f}(\mathbf{x}) = \frac{1}{nh} \sum_{i=1}^{n} k\left(\frac{\mathbf{x} - \mathbf{x_i}}{h}\right) \quad . \tag{5.1}$$

Here n is the number of events used for the KDE, $\mathbf{x_i}$ represents the events location in the parameter space and $\mathbf{x}$ is the evaluated location in the said parameter space. In this analysis a Gaussian kernel $k(t) = \frac{1}{\sqrt{2\pi}} \exp(-0.5 \cdot t^2)$ is used, which provides the advantage, that it is differentiable over the complete parameter space of t and with this the resulting KDE is also

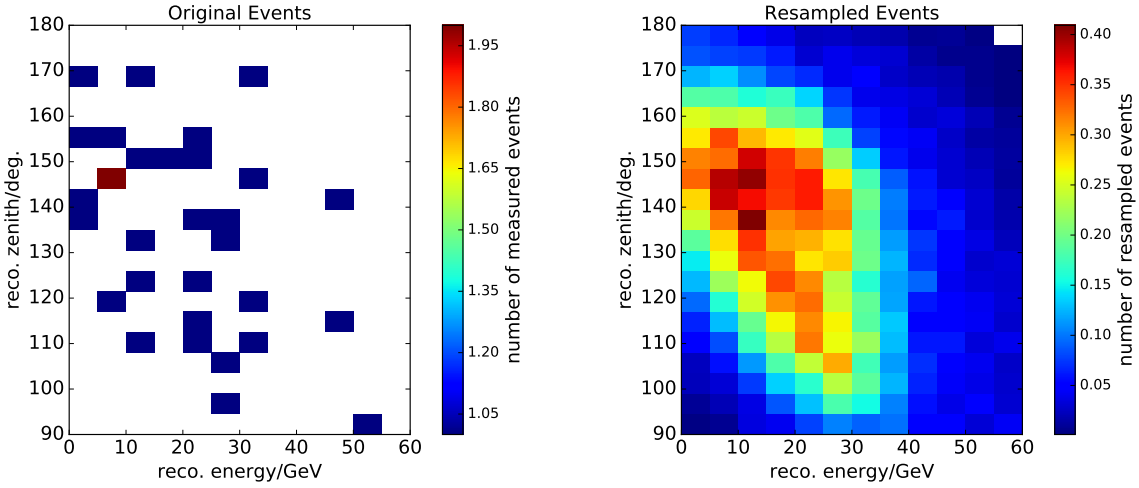

(a) (b)

Figure 5.2: Example of a resampled dataset (right) from a kernel density estimate of a very sparse background dataset (left).

differentiable. One important parameter of a KDE is the kernel width h. This is similar to the bin width in a histogram. If h is to wide, information is lost and fine details of the distribution are smeared out. If h is to slim, statistical fluctuations in the events are modeled in the KDE and can provide fake details. For a Gaussian kernel the width is identical to the standard deviation of the Gaussian. A general "rule of thumb" for the kernels width is *Silverman's rule* [132] with

$$h = \left(\frac{4\hat{\sigma}^5}{3n}\right)^{\frac{1}{5}} \approx 1.06\hat{\sigma}n^{-1/5}. \tag{5.2}$$

for a parameter space of one dimension. Here n is the number of events in the event sample and $\hat{\sigma}$ is the standard deviation of the event sample.

Now the KDE can be used as a PDF. The KDE can be evaluated at the middle of the histogram bins to generate a "binned" KDE. This method has the flaw, that only one point is sampled, which can lead to aliasing artifacts, depending on the complexity of the KDE. An anti-aliasing can be achieved by sampling finer than needed. For the final value an average of the sample points inside the bin is used. This is called "oversampling". Also, new events can be drawn from the KDE to generate single events that can be used in analysis frameworks that rely on histograms and cannot be altered easily to directly use the KDE. An example of this resampling is shown in figure 5.2.

5.4 Background Estimation

One major background for the oscillation analysis are atmospheric muons. Muons are produced in the atmosphere and are absorbed in the Earth's crust and the glacial ice of South Pole. In

a perfect detector all of them should appear as a down going track. However, due to light scattering and other detector effects some events are mis-reconstructed as up-going. The muon background is greatly reduced in the event selection (see section 4.5) by around six orders of magnitude. In this selection, events that are reconstructed as downward going are removed from the sample. Still, at the final selection level there are atmospheric muons left in the sample. The remaining events are dim events that appear like low-energy neutrino events.

To model the background of atmospheric muons, Monte Carlo simulations utilizing CORSIKA have been produced (see section 5.2). Due to the strong suppression of this kind of background, only few events survive the event selection and can be used in the analysis. After the BDT selection the dataset only consists of ∼60 events in the relevant energy range, which is too sparse to be used in the analysis. One method to smooth out the distribution so these few events can be used is the kernel density estimation as described in section 5.3. However, if also a selection on direct photons as described in section 4.2.5 is performed, the number of surviving events from the background simulation is only 3-5, to sparse even for KDEs. Furthermore, the background simulation has other limitations as it was produced 2011. Up to today the simulation framework underwent significant changes for the photon propagation, as well as for the simulation of detector noise. This is considered in the signal simulation, but not in the background simulations. Furthermore, systematic datasets for atmospheric muon background only possess 10 % of the baseline datasets statistic. This means they cannot be used in this analysis. Hence, these systematics can not be correctly reconsidered for the atmospheric muon background.

To circumvent the limitations of the simulation, the atmospheric muon background is estimated from data itself. This raises the amount of events, as well as considers the systematics. To obtain a sample of background events, the CRT-Veto and CorridorCut algorithms described in section 4.2.3 are used. Instead of discarding all the events that do not follow the signal event definition, a part of these events is used as identified background events. Events used for the background sample, if they have at least three hits in the CTR-Veto, but a maximum of six hits. Also a minimum of 5 hits inside DeepCore is still required. This criterea were chosen in such a way to not distort the energy spectrum of the muon template by requiring too many hits inside the veto. On the other hand, very few hits in the veto yield a higher relative amount of neutrinos in the template. This also would not result in a good template.

To reduce the amount of neutrinos in the template the CorridorCut was used. Instead of requiring less then two hits as for the neutrino signal selection, only events with two or three hits were selected, which reduces the amount of mis-identified neutrinos in the background sample. The resulting background template is shown in figure 5.3.

5.5 Systematics

Different systematics have to be considered in the analysis. In the analysis the global histogram of the expectation is a sum of the neutrino components and the atmospheric muon background. As described above, the atmospheric muon template is estimated from data. This means the overall normalization of the atmospheric muon background is not known, but only the shape.

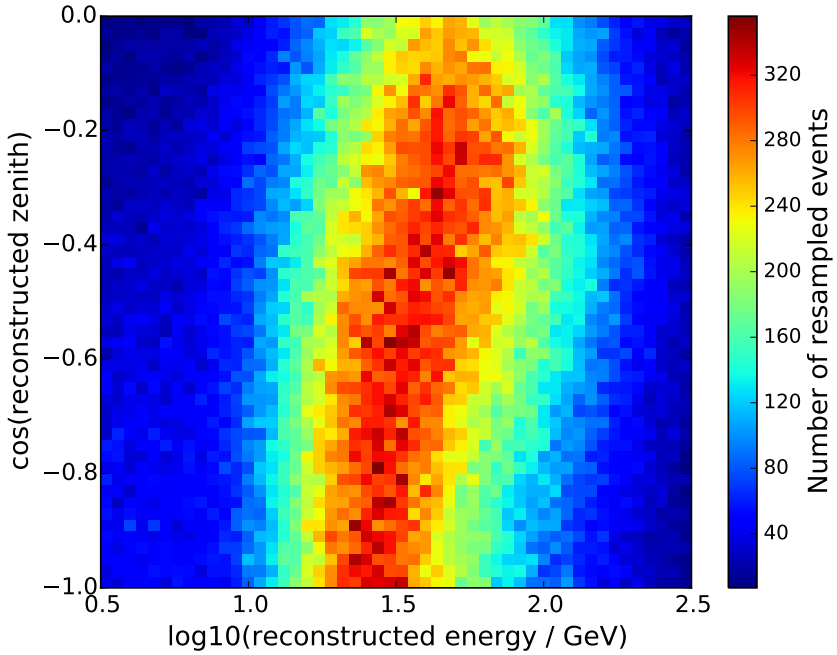

Figure 5.3: Used atm. mu template from KDE resampling.

The relative amount of atmospheric muons has to be a free parameter in the analysis.

As the ν_τ production in the atmosphere can be neglected and ν_τs from ocillation are fixed to the ν_μ flux, only the ν_e and ν_μ normalization is relevant. The three different neutrino flavors at the time of detection are then dependent on these two normalization constants. In this analysis the South Pole neutrino flux model from Honda et. al [27] is used. The uncertainty on this flux model is discussed in [133]. For this work the same values as for the three year result from [75] are used, even if the assumed uncertainties from [133] are smaller. The total neutrino normalization is a free parameter in the analysis. To account for a difference between the individual normalization of ν_e and ν_μ, a second normalization factor is included in the analysis. This parameter represents the deviation of the ν_e normalization N_e^ν from the global neutrino normalization N_global^ν with

$$f_e^\nu = N_e^\nu / N_\mathrm{global}^\nu \tag{5.3}$$

and has an expected uncertainty of 20 %.

The impact of a variation of the ν_e deviation is shown in figure 5.4. Apart from a total raise in events that is degenerated with other parameters, a variation of the ν_e deviation causes a tilt in the spectrum of reconstructed energy and zenith of the total event histogram. For the expected uncertainty of f_e^ν the total tilt of the mentioned spectra is only ± 2 %.

As the neutrino flux is also dependent on the flux of the cosmic ray primary and with this the cosmic ray index γ, uncertainties on this parameter have to be considered. As a baseline a cosmic ray index of $\gamma = 2.65 \pm 0.05$ is used [115, 133]. The variation of this systematic is shown

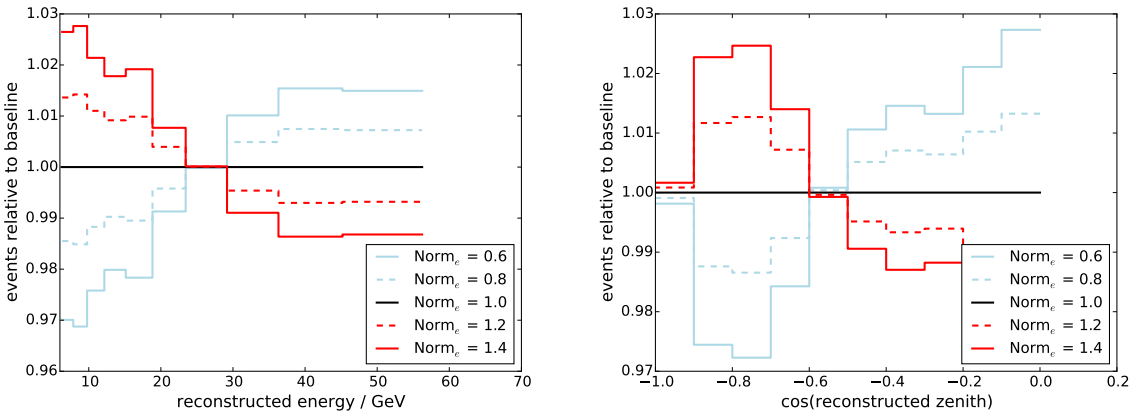

(a) (b)

Figure 5.4: Impact of changing ν_e deviation from the global neutrino normalization. All curves were normalized before they were divided by the normalized curve of the baseline dataset (1.0).

in figure 5.5. The flux-weights are multiplied by a factor of $E^{\Delta}\gamma$ where E is the energy of the simulated individual neutrinos. Since this change is based on the true energy of the neutrino, the effect is visible as a tilt in spectrum of reconstructed energy. Here the total shape variation is around 10 % for the assumed uncertainty. In the zenith spectrum a variance of around 5 % exists for more vertical zenith angles with $\cos(\theta) < -0.6$. This is due to events very low in energy that produce only hits on few strings and are more prone to be reconstructed as vertical up-going. This induces an energy dependence to the zenith reconstruction. In the fit the difference to the baseline value of γ_{Baseline} with

$$\Delta\gamma = \gamma_{\text{Baseline}} - \gamma \tag{5.4}$$

is used as a parameter.

Two very important detector systematics are the optical efficiency of the sensors and the modification of the angular sensitivity of the sensors due to the refrozen boreholes.

The optical efficiency e_{opt} accounts for all the effects that can uniformly raise or lower the perceived optical efficiency of the DOMs in respect to the baseline. Examples are a systematic shifts in the PMT efficiency, the light absorption in the ice, light transmission of the optical gel and coupling between ice and glass-sphere. To account for a different global optical efficiency than expected, datasets with differing optical efficiencies were simulated. A parameter value of 1.0 represents the optical efficiency of a plain vanilla simulation. The parameter is expected to be $0.99 \pm 10\%$. The uncertainty of 10 % was seen in other analyses and was also used in [74, 113, 115, 75]. Apart from an uniform raised or lowered event rate, the change of this parameter causes a complex shape modification of the energy and zenith spectrum. A change in detected light affects the reconstruction quality of low-energy events. The total effect of the shape modification is about $< 4\,\%$ for a 10 % variation of the optical efficiency.

To deploy the strings into the ice, holes were drilled with a hot water drill. After deployment these holes refroze, but the resulting hole-ice has a different structure than the natural grown

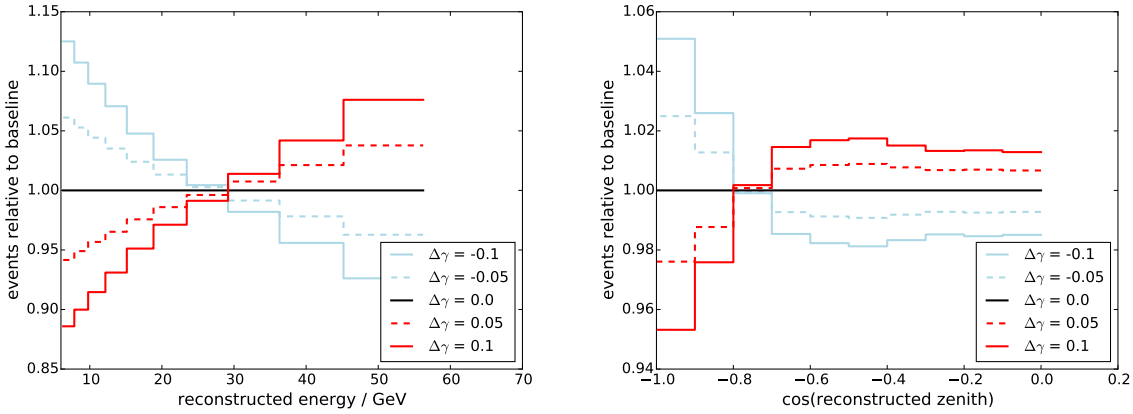

(a) (b)

Figure 5.5: Impact of changing cosmic ray index difference ($\Delta\gamma = \gamma_{\text{Baseline}} - \gamma$) from the baseline value of $\gamma_{\text{Baseline}} = 2.65$. All curves were normalized before they were divided by the normalized baseline.

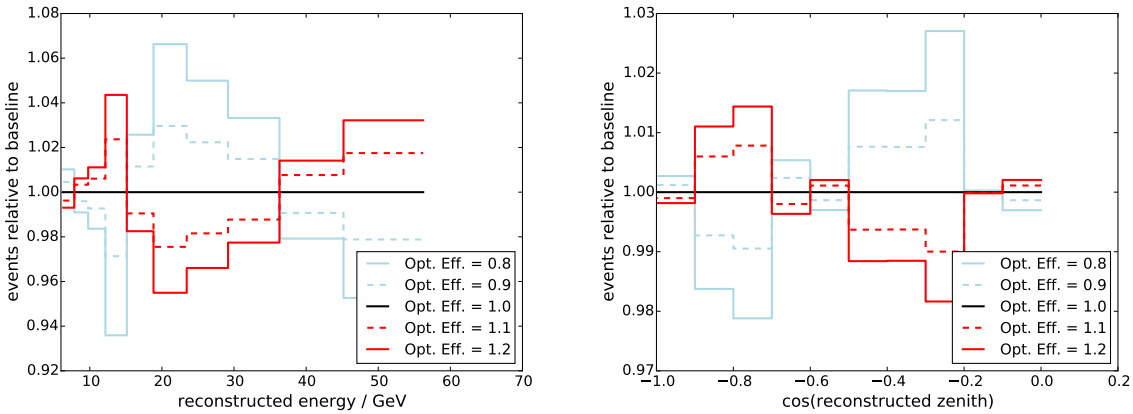

(a) (b)

Figure 5.6: Impact of changing optical efficiency of the detector. All curves were normalized before they were divided by the normalized baseline.

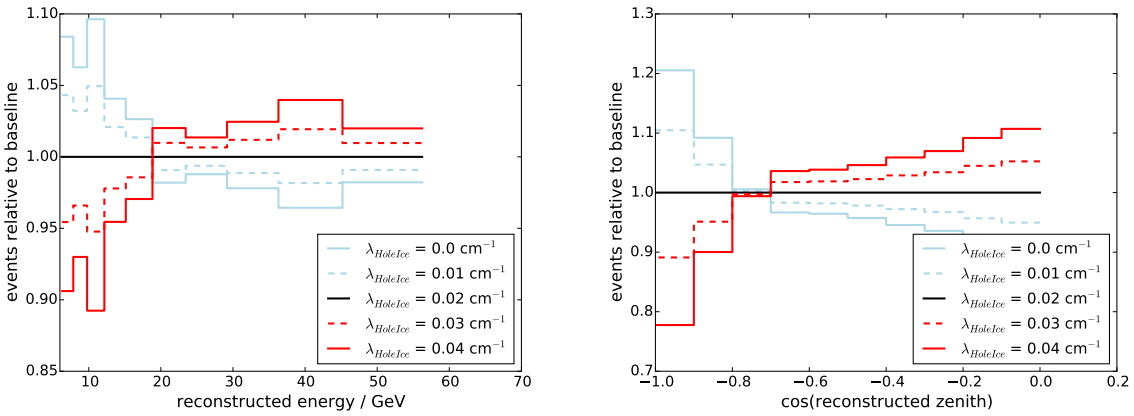

(a) (b)

Figure 5.7: Impact of changing photon scattering length in the refrozen ice columns around the strings. All curves were normalized before they were divided by the normalized baseline.

Table 5.2: Systematics that are used in the analysis with their baseline value and uncertainty region for the Gaussian prior (see section 5.6)

Systematic	**Baseline value**	**Uncertainty (±)**
Atm. ν-Flux Normalization	1.0	free
Relative ν_e-Normalization	1.0	0.2
Atm. μ Fraction	10 %	free
Cosmic Ray Spectral Index	2.65	0.05
Optical Efficiency	0.99	10 %
Hole Ice Scattering Parameter	0.02 cm^{-1}	0.01 cm^{-1}
$\sin^2(2\theta_{13})$	0.093	0.008

ice of the glacier. This results in a different scattering inside this hole-ice column and thus a modified angular acceptance of the DOM. To account for this effect, the discrete angular acceptance datasets with differing hole-ice scattering lengths s_{HoleIce} were simulated according to [134, 131] (see section 5.2). The hole-ice scattering is expected to be $\lambda_{\text{HoleIce}} = 1/s = (0.02 \pm 0.01)\,\text{cm}^{-1}$. The effect of the variation of this systematics is shown in figure 5.7. Like one would expect, the difference in scattering strongly impacts the zenith spectrum for vertical events of very low energy.

The analysis is based on a three flavor oscillation. This means that more than the two wanted oscillation parameters exist. The mass-splitting $\Delta m^2_{21} = 7.51 \cdot 10^{-5}\,\text{eV}$ which is two orders of magnitude lower than the Δm^2_{32} can be neglected in this analysis. This is also true for the mixing angle θ_{12} and δ_{CP} for which this analysis is not sensitive. The mixing angle θ_{13}, however, may have a small impact and is treated as another systematics.

All systematics and their uncertainty region are displayed in table 5.2.

5.6 Fitting Procedure

Neutrino oscillations produce a deficit of measured ν_μ compared to the case without neutrino oscillations. This deficit is apparent in the parameter space of neutrino energy and its length of propagation as described in section 2.4.1. For this analysis the length of propagation is represented by the cosine of the reconstructed zenith angle and the neutrino energy is approximated with an energy reconstruction.

The used fit is a 2D maximum likelihood fit between measured data and expectation. A sketch of the fitting principle is shown in figure 5.8. For every dataset (measurements and simulations), the events are placed into an individual 2D-histogram H with bins x_{ij}. The simulated neutrino dataset is split into four different components. Three for the CC channels and one NC channel. NC interactions are thrown into a single sample, since these events cannot be distinguished between the different flavors. No oscillation probabilities are calculated for events from NC interactions. The resulting neutrino histograms are then $H^{\mathrm{CC,e}}$, $H^{\mathrm{CC},\mu}$, $H^{\mathrm{CC},\tau}$ and H^{NC}. The count of each bin is the sum of the weights of each individual event. These consist of the aforementioned flux weights of each neutrino. A change in the spectral index from the baseline is accounted for by multiplying $E^{\Delta\gamma}$ to every single weight, where E is the energy of the simulated neutrino and $\Delta\Gamma$ is the shift of the spectral index. For CC events the weights also include the calculated neutrino oscillation probability. The optical efficiency and hole-ice variations are evaluated for every bin individually, before the fit is performed. The histograms are then modified bin-wise in the fit, to account for these systematics. This is explained in section 5.7.1.

The histogram parameter are the decadic logarithm of the reconstructed energy for index i and the cosine of the reconstructed zenith for index j. Each axis has eight bins, resulting in histograms with 64 bins. The used ranges for the parameters are $\log_{10}(E_{\mathrm{reco}}) \in [0.8, 1.75)$ and $\cos(Z_{\mathrm{reco}}) \in [-1, 0)$. As described in section 5.4 the atmospheric μ background is sampled from a KDE into a matrix $B_{\mathrm{Atm.}}$. This is done for the same 8×8 bin raster. The histograms of the individual components of the expectancy (neutrinos and atmospheric muon background) can be varied. The normalizations are scaling factors that are multiplied to the whole sub-histograms.

In the end, the individual expectancy contributions are summed up to a final expectancy histogram. Expectation and measurement are then compared bin-wise to each other with the Poisson probability function

$$P(x, \lambda) = \frac{\lambda^x e^{-\lambda}}{x!} \quad . \tag{5.5}$$

P is the probability to measure a number of x events given the expected value of λ events, assuming the events follow a Poissonian distribution. Now the likelihood

$$L = \prod_{i,j} P(x_{\mathrm{ij}}, \lambda_{ij}) \tag{5.6}$$

to get the measured histogram giving the histogram from the expectation is the product of the probabilities of each individual bin ij. For the actual fit the negative logarithm of the

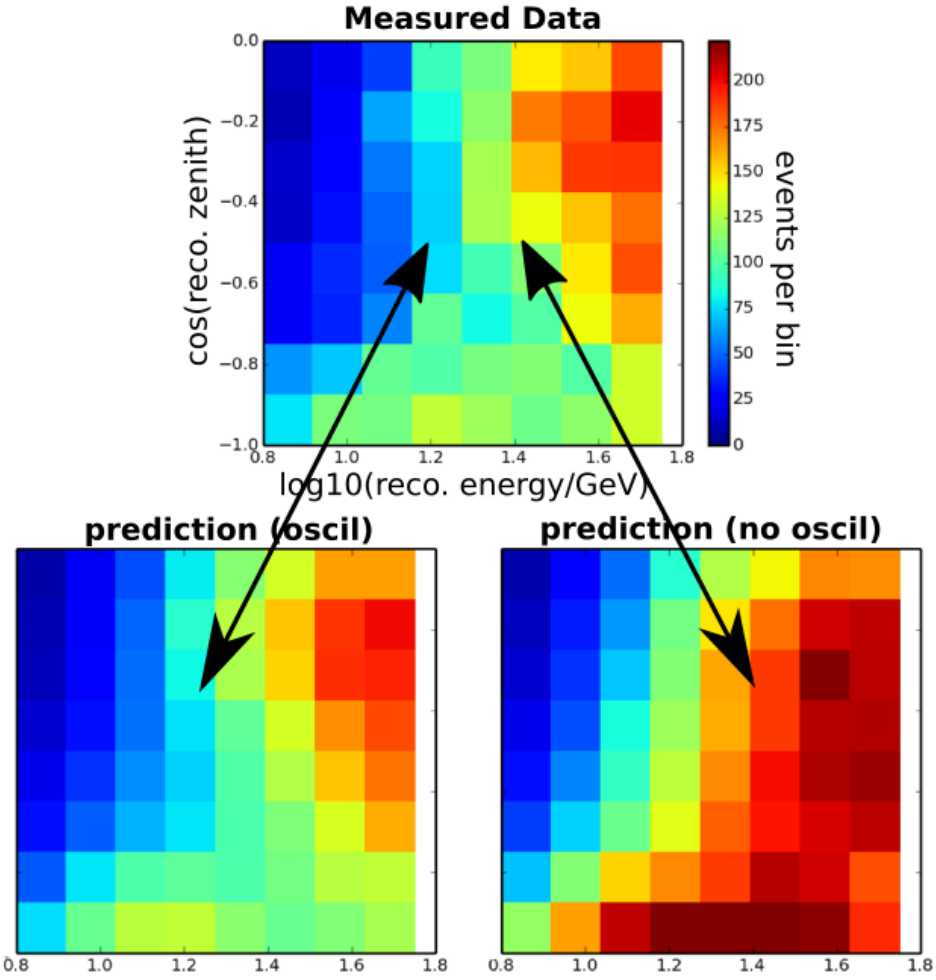

Figure 5.8: Example how the fit is performed. The measured data is histogrammed in reconstructed energy and cosine zenith. The histogram is the compared to different expectations from simulations. The colorbar is valid for all three histograms.

likelihood (nLLH) with

$$\text{nLLH} = \sum_{i,j} \lambda_{ij} + \ln(\Gamma(x_{ij}+1)) - x_{ij}\ln(\lambda_{ij}) \tag{5.7}$$

is used, which circumvents numeric issues and enables the usage of minimizers. The lowest nLLH value describes the best match between the measured histogram and the expectation. Since the measurement does not change in the fit, the additive term $\ln(\Gamma(x_{ij}+1))$ that depends only on the number of measured events can be omitted from the nLLH calculation.

To account for the systematics that were described in section 5.5, Gaussian priors are added to the likelihood description to penalize the fit if a systematic is used with an improbable value. The final nLLH description is

$$\text{nLLH} = \sum_{i,j} \lambda_{ij} - x_{ij}\ln(\lambda_{ij}) + \frac{1}{2}\sum_{k}\left(\frac{S_{k,l}-S_{k,0}}{\sigma_k}\right)^2 . \tag{5.8}$$

Here k is the number of the systematic. $S_{k,0}$ is the baseline value of the individual systematic and $S_{k,l}$ the value that is used in the fit. σ_k is the uncertainty on the used baseline value.

The lowest nLLH indicates the expectation that fits best to the data. To get this value, a minimizing algorithm is used. For this analysis the MINUIT2 [135, 136] minimizer code is used. If all parameters (oscillation and nuisance) are free the fit will return the most probable oscillation parameters for the given set of measurements, based on the expectation.

5.6.1 Contours

To get the confidence contours for the parameter space of mass-splitting and mixing angle, the nLLH values for fixed points in this parameter space are calculated. For this, the oscillation parameters are fixed, so that the fit can only vary the nuisance parameters. This gives a likelihood landscape of oscillation parameter space. Following Wilks' theorem [137], the double of the logarithmic likelihood difference between best-fit with N degrees of freedom and the scan points with N-2 degrees of freedom should follow a χ^2 distribution with two degrees of freedom

$$2\Delta_{\text{LLH}} = 2\cdot(\text{nLLH}(N-2)_{\text{ScanPoint}} - \text{nLLH}(N)_{\text{BestFit}}) = \chi^2(2) \quad . \tag{5.9}$$

From this one can calculate contours for a given confidence region.

5.6.2 Best Fit Value of Oscillation Parameters

To get the best fit value for the oscillation parameters, the best result from the parameter scan is used as a first guess. This first guess is then refined in a parameter fit where the oscillation parameters are treated as free parameters.

5.7 Dataset Combination

The analysis is based on data taken in four different years with two different detector configurations and thus event selections. Thus, the data cannot be simply added together. The data

consists of one year taken in the IC79 detector configuration and three years taken in the IC86 detector configuration. There are independent simulation sets for each detector configuration and also independent background templates (see section 5.2 and 5.4). The global normalization for each year is kept independent to each other in the fit. Every background template has an individual parameter for the amount of background. Thus, there are two separate normalization factors, one for IC79 and one for IC86, coupled to the atmospheric muon background that are modified simultaneously in the fit.

5.7.1 Parametrization of Discrete Parameters

The optical efficiency and the scattering of the hole-ice is only available as discrete datasets. Thus, these are discrete parameters. To consider the parameters in the fit, these have been "continuized". An example of this is shown in figure 5.9. For each of the systematics the available datasets are histogrammed into a 2D-histogram as described in 5.6. This gives a number of histograms for different values of the systematic parameter. For every bin the effect of the different systematic values is then parametrized with a polynomial fit. The result of this fit can now be used in the analysis to continuously modify the histograms for different values of the systematics. This treatment of the discrete nuisance parameters is done for the CC interactions of each of the three ν-flavors and the single NC histogram.

5.8 Tests

The fit framework was already successfully used in the three year oscillation analysis [75]. The IC79 data had to be prepared to be used with this framework. Also, the framework itself was extended to be usable for a fit covering different detector configurations. To see if the fit framework and data preparation are working as expected, several tests have been performed together with a sensitivity study with simulated data.

5.8.1 Blindness

To not bias the analysis it was developed and tested in "blindness" without the usage of the actual data. The fit framework was tested against "mock data" drawn from simulation. The results of this tests were validated before the analysis was performed with the actual data.

The same is true in a reduced degree for the event selection, which was developed by only using 10 % of the measured data, to prevent a tuning to specific features of the complete data. The data was used to check the event selection steps and the BDT performance.

The results from the "blind" tests of the analysis and the event selection with only the 10% was then validated by the collaboration and a permission was granted to look at the complete data. This is called an "unblinding".

5.8.2 Sensitivity

Before the analysis was performed on actual data from the IceCube detector, sensitivity studies have been performed. The studies were done for the single year of IC79 as well as for

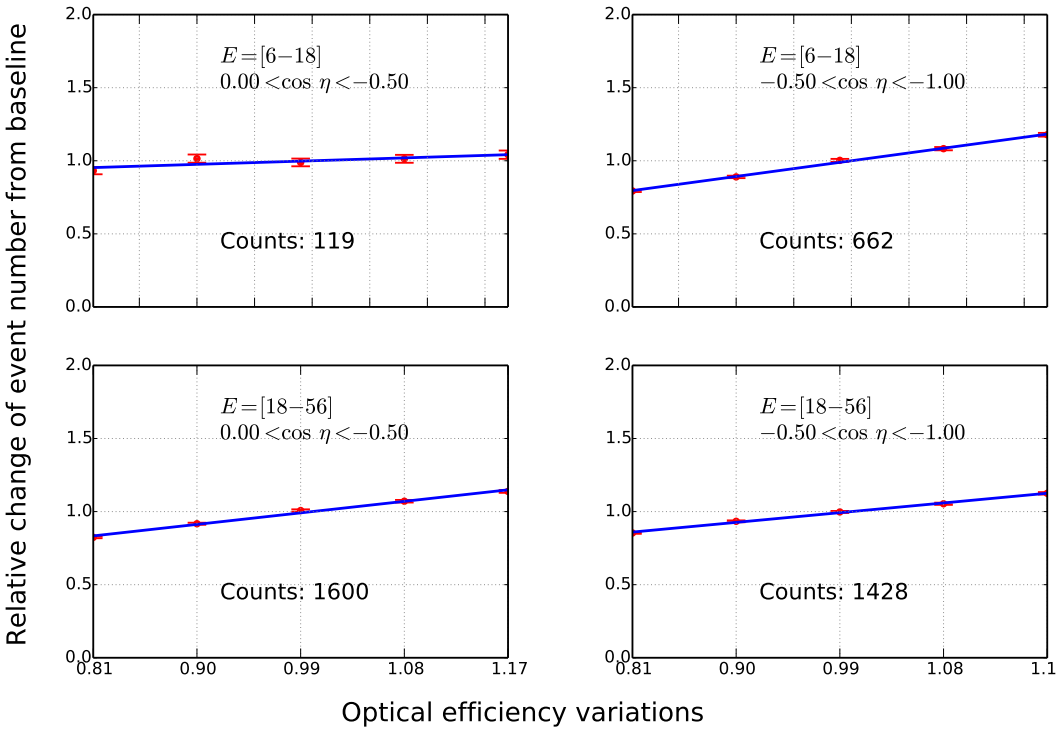

Figure 5.9: Example how the parametrization of the detector systematics of optical efficiency and hole-ice scattering is performed. The example shows a parametrization for the optical efficiency in energy and zenith bins. The used dataset consists of charged-current muon neutrino events.

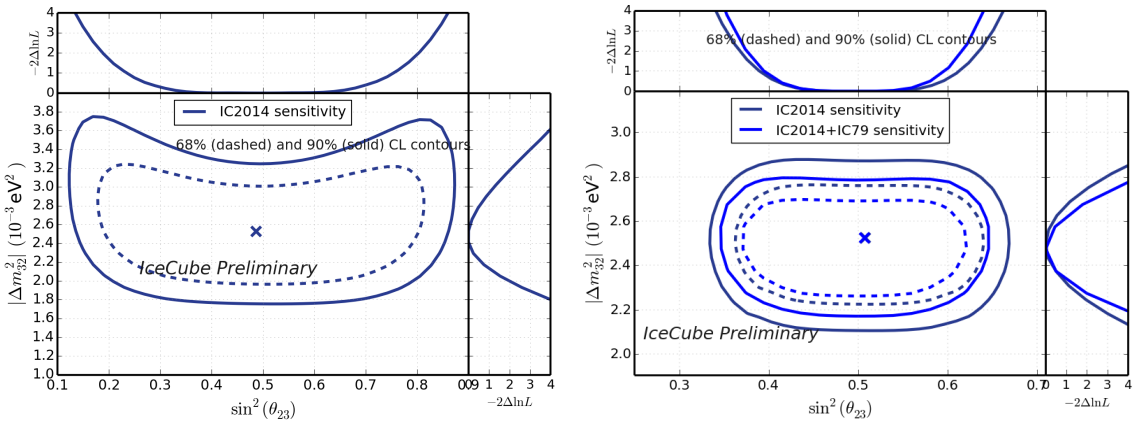

(a) One year of IC79

(b) Three years of IC86 [IC2014] and four years (one year IC79 and three years IC86 combined) [IC2014+IC79 sensitivity]

Figure 5.10: First sensitivity estimate from an Asimov approach.

the combined four year analysis. Since the contours of the final analysis will be produced with a likelihood-ratio test, the sensitivity was analyzed by the usage of an "Asimov approach" as explained in the following section, as well as with a full ensemble test. The different approaches are then compared to each other.

Asimov Test

To get an estimate of the fits sensitivity, a likelihood based statistics test has been performed for the single year of IC79 and the combined four year dataset. In this test an expectation dataset was produced from the available simulations and the atmospheric muon template. This dataset is called an "Asimov dataset" [138] named after Isaac Asimov as it strikes resemblance to one of his short stories. The dataset is produced with a given set of oscillation parameters and nuisance parameters. For the optical efficiency and the hole-ice column scattering, the baseline datasets are used. Now for this generated test dataset a 2D parameter scan with the two oscillation parameters is performed like described in 5.6. The resulting contours represent the estimate of the mean sensitivity for the analysis. A first test has been done as a "proof of concept" for the whole analysis. The result is shown in figure 5.10. Including a fourth year of data yields a significant gain in sensitivity, reducing the 90 % confidence level (C.L.) contour to about the size of the previous 68 % C.L. contour.

The above sensitivity estimate was performed with an event selection that did not include all the final level selection steps and is thus stronger than for the final selection. A sensitivity estimated with the selection as stated in section 4.5 is shown in figure 5.11. The gain for the completed event selection is a little bit lower, since more events had to be removed from the sample. The exclusion of these events was a requirement for the unblinding procedure. The resulting gain in sensitivity is strongest for the mass-splitting. The results of the Asimov

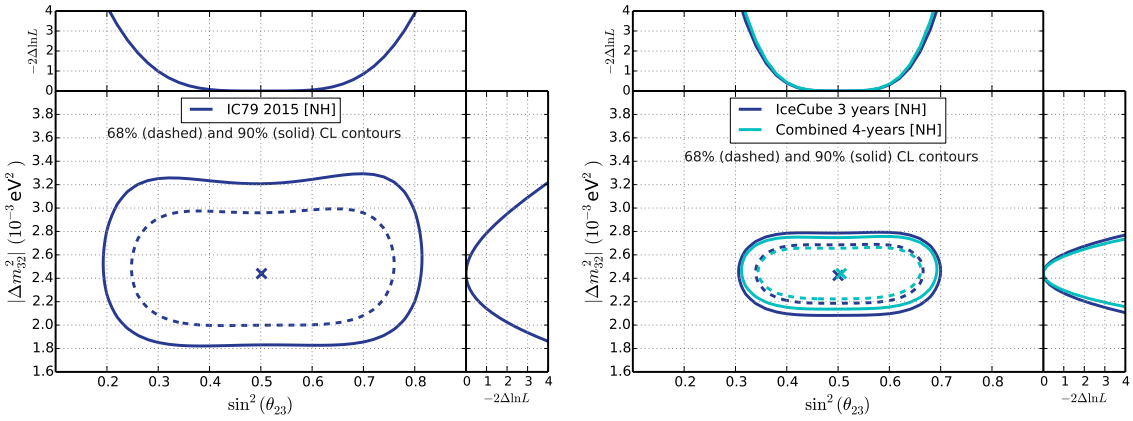

(a) One year of IC79

(b) Three years of IC86 and the combined four years (one year IC79 and three years IC86 combined)

Figure 5.11: Sensitivity estimates for a fit using the Asimov approach.

experiment for three years of IC86 are

$$\sin^2(\theta_{23}) = 0.50^{+0.14}_{-0.13} \quad \text{and} \quad \Delta m^2_{32} = 2.43^{+0.18}_{-0.14} \cdot 10^{-3}\mathrm{eV}^2 \quad . \tag{5.10}$$

If the one year of data in the IC79 configuration is added to the three years, the result changes to

$$\sin^2(\theta_{23}) = 0.51^{+0.12}_{-0.13} \quad \text{and} \quad \Delta m^2_{32} = 2.44^{+0.15}_{-0.14} \cdot 10^{-3}\mathrm{eV}^2 \quad . \tag{5.11}$$

Ensemble Test

To see if the fit is stable, an ensemble test has been performed. For this, the test Asimov dataset from before (section 5.8.2) is used as an expectancy to generate 1000 different test datasets. Each bin inside the new 2D histograms is randomly drawn from a Poissonian distribution where its mean value λ is given by the count of the equivalent bin of the Asimov dataset. The values gained by the fit for the different histograms should produce a cluster around the injection point in the parameter space. Figure 5.12a shows this test for four years of data and the two flavor oscillation case together with the expected sensitivity for a likelihood-ratio test. The test was performed for the two flavor case to test if the fit is drawn to the unphysical values of $\sin^2(2\Theta) > 1$. A contour that is strongly shifted to values greater than one would indicate problems in the fitting routine.

Figure 5.12b shows the result of an ensemble test with three flavors and matter effects. Due to the degeneracy of the parameter space of the mixing angle projection the contour stretches over a wide range of $\sin^2(\theta)$. The fit has nearly identical probability to fall to values lower or higher 0.5, since the likelihood landscape always has two minima.

The clustering around $\sin^2(\theta)$ is also an effect of this projection. If the tested dataset shows a stronger deficit than possible with the simulation datasets, the fit will stop at maximal mixing. With injected values near the maximal mixing and only few events in the final sample, this

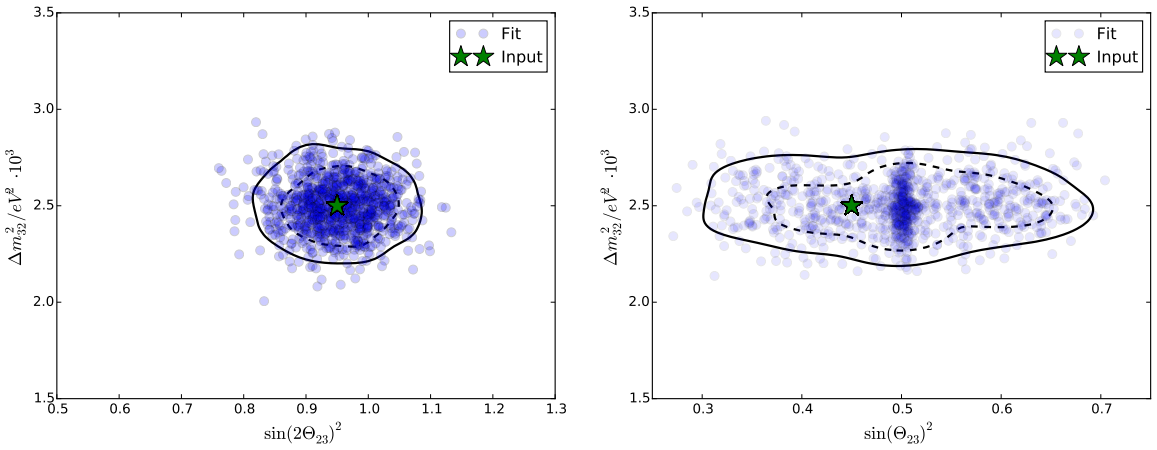

(a) two flavor approximation

(b) three flavors and matter effects

Figure 5.12: Ensemble test with 1000 single fits for four years of data (IC79, IC86-1, IC86-2, IC86-3) and two different oscillation cases and presentations. The injected oscillation parameters are marked with a green star. The black lines mark the area that includes 68 % (dashed) and 90 % (solid) C.L. obtained from a KDE of the individual fits (blue circles). A KDE was used to gain a smooth probability density estimate from the 1000 fits. An atmospheric muon background of 5 % was assumed in the single fits.

deficit can easily be produced by statistical variations. If the fit is drawn to maximal mixing, the minimizer still has the possibility to change the mass-splitting. This can induce a stronger muon neutrino deficit due to the shift in energy, since the event spectrum is not flat.

If a stronger deficit than possible from simulation is fitted with the two flavor approximation, the fit will shift into the unphysical region above $\sin^2(2\theta)$. This means if the three flavor fit returns a best-fit near maximal mixing, one can easily test with an extra two flavor fit if this measurement is valid or not. That is, if the fit wanders deep into the unphysical region. If the best-fit in the three flavor case is not at maximal mixing, both fits will return valid results in the beginning.

Figure 5.13 and 5.14 both show the double logarithmic likelihood differences ($2\Delta_{\mathrm{LLH}}$) between the best-fit of the 1000 test datasets and a fit with fixed oscillation parameters. The values of the parameters were set to the injected values of the dataset. The histograms show the relative fraction of $2\Delta_{\mathrm{LLH}}$. For a fit with two parameters, the distribution should follow a χ^2 distribution with two parameters if Wilks' theorem is valid (see section 5.6.1).

In both figures the fit of the two flavor approximation follows the χ^2 distribution with two free parameters, as expected. For the full tree flavor fit, however, a difference exists. If maximal mixing is assumed, the distribution of the fit is shifted to a χ^2 distribution with only one free parameter. This is shown in figure 5.13b. In 5.14b the mixing is weaker and the fits distribution more closely follows a χ^2 distribution with two free parameters. As stated above, the three flavor fit cannot account for an underfluctuation that is higher than expected. Thus, the fit is limited in this regard. The two flavor fit, however, can wander into the unphysical

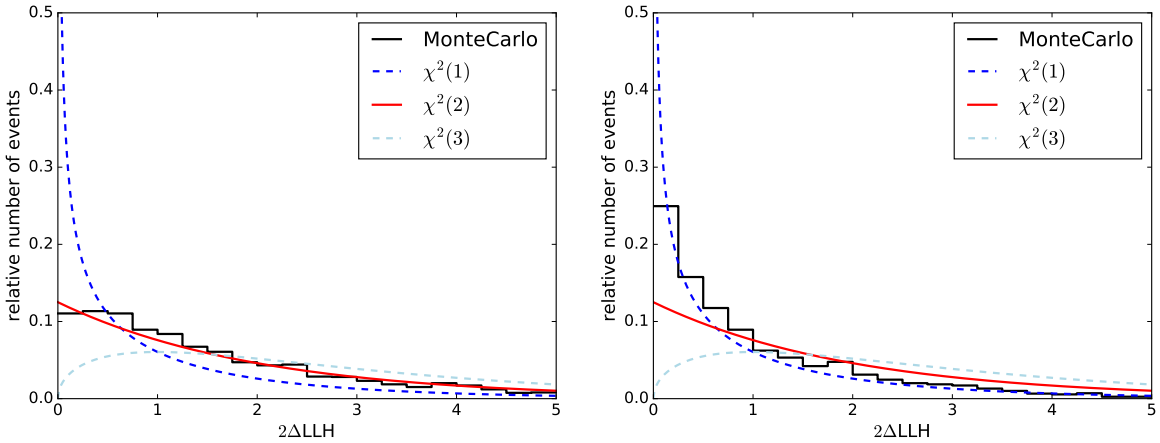

(a) two flavor approximation

(b) three flavors and matter effects

Figure 5.13: Test of validity of Wilks' theorem for full mixing. The two flavor approximation follows the χ^2 distribution with two free parameters. The three flavor fit follows a mixture of a distribution of one and two free parameters with a prevalence to one free parameter. The injected oscillation parameters are $\Theta_{23} = 0.74\,\text{rad}$ and $\Delta m^2_{32} = 2.5 \cdot 10^{-3}\,\text{eV}^2$.

region to account for the underfluctuation. This results in a difference in free parameters of the fit. Thus, Wilks' theorem is not valid and contours produced with the usage of $2\Delta_{\text{LLH}}$ are smaller for a result near maximal mixing. A correct way to obtain the contours of this analysis would be a full Feldman Cousins (FC) approach [139]. Since the FC approach is very computational intensive, it is not performed in this work. Another reason is the comparability to other experiments, since the Wilks' approach is wildly used.

5.8.3 Impact of Background from Atmospheric Muons

Due to the extraction of the atmospheric muon template from data, only the shape of the atmospheric muon distribution is known, but not the actual fraction of atmospheric muons in regard to the dataset. An estimate of the atmospheric muon content is 5-10 %. This value was derived from CORSIKA based Monte Carlo simulations at higher levels then the analysis level. To test the impact of the muon background, sensitivity tests with a differing background fraction have been performed.

Figure 5.15a shows 90 % C.L. contours for differing amounts of background in the test data. The used atmospheric muon template for the fit was the same as for the generation of the test data. Up to 10-20 % the amount of background only has a mild impact on the contour. This means, that if the template is correct, the actual amount of background only has a sub-dominant effect.

Figure 5.15b shows the same test, but the background templates between test data and the fit differ. Here the atmospheric muon template obtained from IC86 data was used for the generation of the test data. In the fit the used template is the one from IC79 data. Since for the IC86 configuration two DeepCore strings were added in regard to IC79, the energy threshold

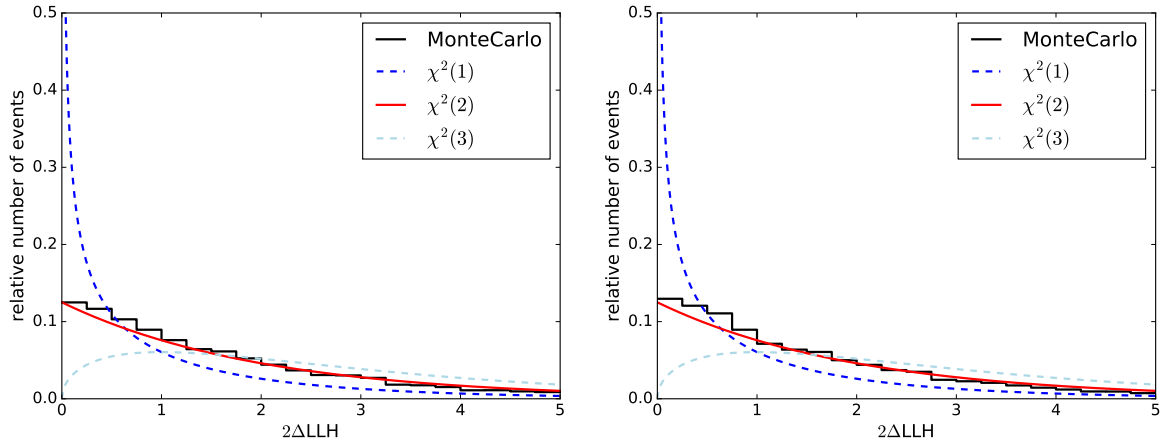

(a) two flavor approximation (b) three flavors and matter effects

Figure 5.14: Test of validity of Wilks' theorem for reduced mixing. The two flavor approximation fit the three flavor fit both follow the χ^2 distribution with two free parameters. The injected oscillation parameters are $\Theta_{23} = 0.32\,\text{rad}$ and $\Delta m^2_{32} = 2.5 \cdot 10^{-3}\,\text{eV}^2$.

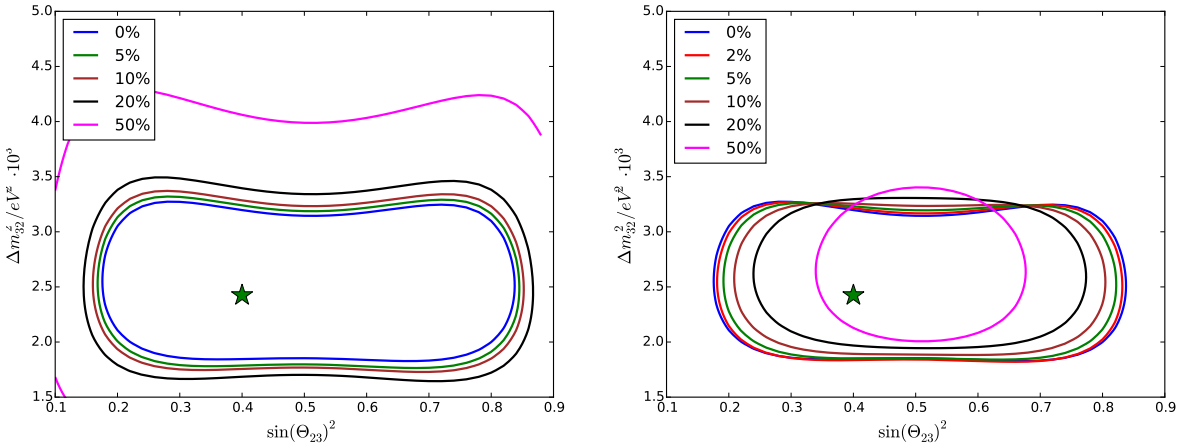

(a) Correct template (b) Wrong template

Figure 5.15: Impact of different injected fractions of atmospheric muon background on contours obtained by a Asimov driven likelihood ratio test. The injected oscillation parameters are marked by a green star. The relative amount of atmospheric muons is stated in the legend. With the correct template (left) a raising amount of muons will increase the size of the contours. Up to 20 % the growth is very mild. With a strongly incorrect template (right) the contours shrink due to a pull into the unphysical sector in a two flavor fit. Up to 10 % the contour distortion is relatively mild.

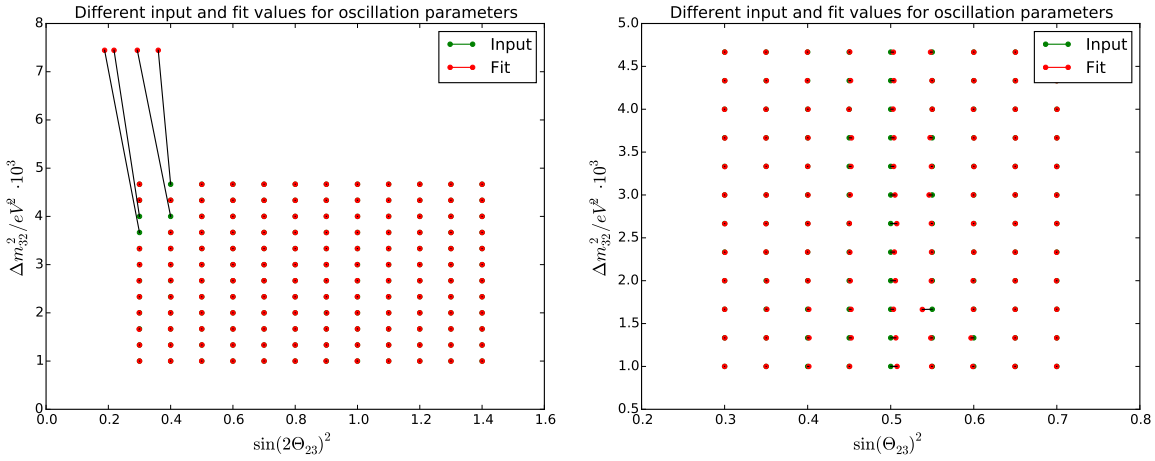

(a) Two flavor case with unphysical area

(b) Three flavor case with matter effects

Figure 5.16: Fit stability test for four years of data (IC79 and IC86). For the test an atmospheric background contamination of 5 % was assumed. Green dots are the input values of the oscillation parameters. Red dots are the best-fit values for an Asimov fit. Input and best-fit values from one single test are connected through black lines.

is shifted to lower energies. Also, the standard processing of the data changed significantly between the different years. The different event selection between IC86 and IC79 also will produce a different template. Together these factors generate a strongly different atmospheric muon template. Up to 10 % muon contamination the contour is more or less stable as shown in figure 5.15. With higher amounts of background the contour is distorted. The contour gets smaller with a higher amount of background. This is a projection artifact. If the fit is performed with only two flavors and allowed to shift into the unphysical region, the contour will shift into the unphysical area with raising amount of background.

The result of the test is, that for a realistic template the background has only a minor impact if its fraction is around or below 10 %. As stated before, for this analysis this is the case. A wrong template together with a higher background fraction will be visible in a two flavor fit as a shift into the unphysical region.

5.8.4 Fit Stability

To test the stability of the fitting framework several Asimov fits have been performed with different input parameters. If the framework is stable, the fit returns the input values. The result of this test for the combined dataset with one year of IC79 and three years of IC86 are shown in figure 5.16. The input (green) and output (red) oscillation parameters that correspond to one single test are connected by a black line. The assumed contamination with atmospheric muons is assumed to be 5 % of the full dataset.

The left plot shows the test for the two flavor case. The mixing angle is plotted as $\sin^2(2\Theta)$ and extended to the unphysical area. For four tests the fit ends at the configured limit for

the mass-splitting of $\Delta m^2_{32,max} = 7.5 \cdot 10^3\,\mathrm{eV}^2$. These tests all have input parameters without strong oscillation effects. Furthermore, the mass-splitting is high and thus the disappearance maximum is shifted to higher energies out of the used energy window. Apart from the four tests, the rest correctly recovers the input values of the oscillation parameters.

In the right plot the mixing angle is plotted as $\sin^2(\Theta)$ and the neutrino oscillation is calculated in the full three flavor case with matter effects. For the most values of $\sin^2(\Theta)$ the input values are recovered to a high degree of precision. For values near maximal mixing, the fit result is slightly shifted. The fit is done on the actual mixing angle and not $\sin^2(\Theta)$. At maximal mixing, differences in the angle lead to stronger differences in $\sin^2(\Theta)$ than for more weaker mixing. Furthermore, the parameter space of the mixing angle is degenerated, leading to a larger area of very similar likelihood values around the input parameters at maximal mixing. Apart from minor deviations, the fit is stable.

In the next chapter the results of fits against real data are presented.

Chapter 6

Results

In this chapter the final oscillation analysis result for four years of data from the IceCube detector is presented. Apart from the combined result, fits of the individual years are shown. The variation of the fitted nuisance parameters for the combined and the single fits is discussed in separate sections. Furthermore, improvements to the analysis are presented. In the last section a comparison between the single year of IC79 and a previous, published measurement using the same year is shown.

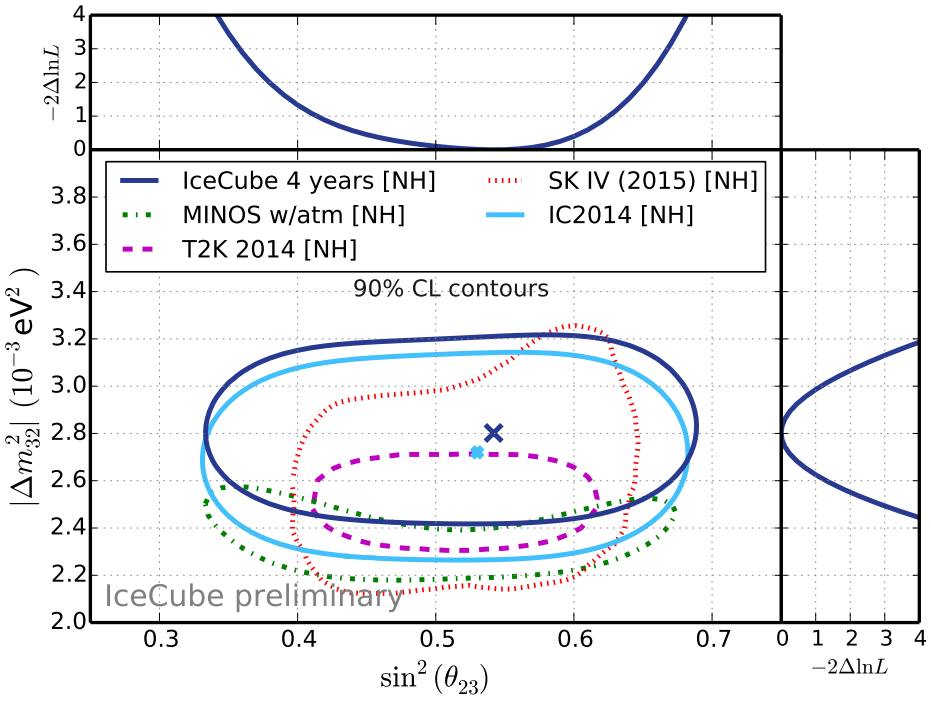

Figure 6.1: Final analysis result. Shown is the 90% C.L. contour of a parameter scan in $\sin^2(\theta_{23})$ and Δm^2_{32}. The four year result (solid, dark blue) is shown together with the previous result with three years of data [75] (solid, light blue) and results from different experiments: MINOS [88] (dashed, green), Super Kamiokande IV [141] (dashed, red), T2K [142] (dashed, pink). Plot from [140].

6.1 Introduction

The oscillation analysis described in the previous chapter was performed for data that was taken between the years 2010 and 2014. The goal was an improvement over a previous oscillation analysis that was performed by J. P. Yáñez [115] utilizing three years of IC86 based data and published in PRD in 2015 [75].

The main result is a 2D scan of the oscillation parameters for four years of data. The result was presented at the EPS-HEP2015 conference [140]. This result is discussed followed by single year fits. In the end improvements to this result and comparisons to an older oscillation analysis based on IC79 data are presented.

6.2 Combined Fit

Figure 6.1 shows a parameter scan for the two oscillation parameters and the combined four years of data. The result is plotted together with results from the IceCube three year result (solid, light blue), MINOS (dashed, green), Super Kamiokande IV (dashed, red) and T2K (dashed, pink). The dark blue curve shows the 90 % C.L. contour for the measurement. The

Table 6.1: Fitted nuisance parameters

ν-Normalization (IC79 / IC86-1 / IC86-2 / IC86-3):	0.57 / 0.75 / 0.71 / 0.61
Relative ν_e-Normalization:	0.997
Atm. μ Fraction (IC79):	3.65 %
Atm. μ Fraction (IC86):	0.73 %
Optical Efficiency:	0.978 from baseline (nominal 0.968)
Hole Ice Scattering Parameter :	$0.0216\,\mathrm{cm}^{-1}$
$\Delta\gamma$:	0.014
θ_{13}:	0.15519

best-fit is indicated with the dark blue cross. The values for the oscillation parameters from the four year fit are

$$\sin^2(\theta_{23}) = 0.54^{+0.08}_{-0.13} \quad \text{and} \quad \Delta m^2_{32} = 2.80^{+0.20}_{-0.16} \cdot 10^{-3}\mathrm{eV}^2 \quad . \tag{6.1}$$

The three year result without IC79 yields $\sin^2(\theta_{23}) = 0.53^{+0.08}_{-0.13}$ and $\Delta m^2_{32} = 2.72^{+0.20}_{-0.19} \cdot 10^{-3}\mathrm{eV}^2$.

The four year analysis result is an improvement over the three year analysis, especially for the mass splitting. Due to the lower string density and differing reconstruction, the systematic error for the IC79 sample is a bit higher than for a single year of IC86. The lower string density also results in a lower statistics for this single year. The result is consistent with the improvement expected from the sensitivity study depicted in section 5.8.2.

The fitted values for the nuisance parameters are near the expected value with deviances below one sigma. The ν normalization factors of IC79 and the third year of IC86 are lower than for the other two years of IC86. This is expected since both IC79 and IC86-3 have a reduced live time. The relative atmospheric muon background is a free parameter in the fit and the spectrum is different between IC79 and IC86. The relative amount obtained by the fit is below 5 % for both datasets. The values for all nuisance parameters are listed in table 6.1.

The goodness of fit is estimated with a χ^2 test. At the best-fit it is $\chi^2 = 238.1$. The fit uses four histograms with a total of 256 bins. Since the number of degrees of freedom is reduced due to the number of fitted parameters[1] this results in

$$\frac{\chi^2}{\mathrm{ndof}} = 238.1/243 = 0.98 \tag{6.2}$$

indicating a good fit to the data. The individual pulls

$$P = \frac{N_{\mathrm{Data}} - N_{\mathrm{BestFit}}}{\sqrt{N_{\mathrm{BestFit}}}} \tag{6.3}$$

of every bin of the four years of data are shown in figure 6.2. A perfect match between the measured data and the fit gives a pull of 0. An absolute value of one gives a deviation of one standard deviation given the expectation of the fit. A clustering of strong pulls in one direction

[1] including θ_{13}

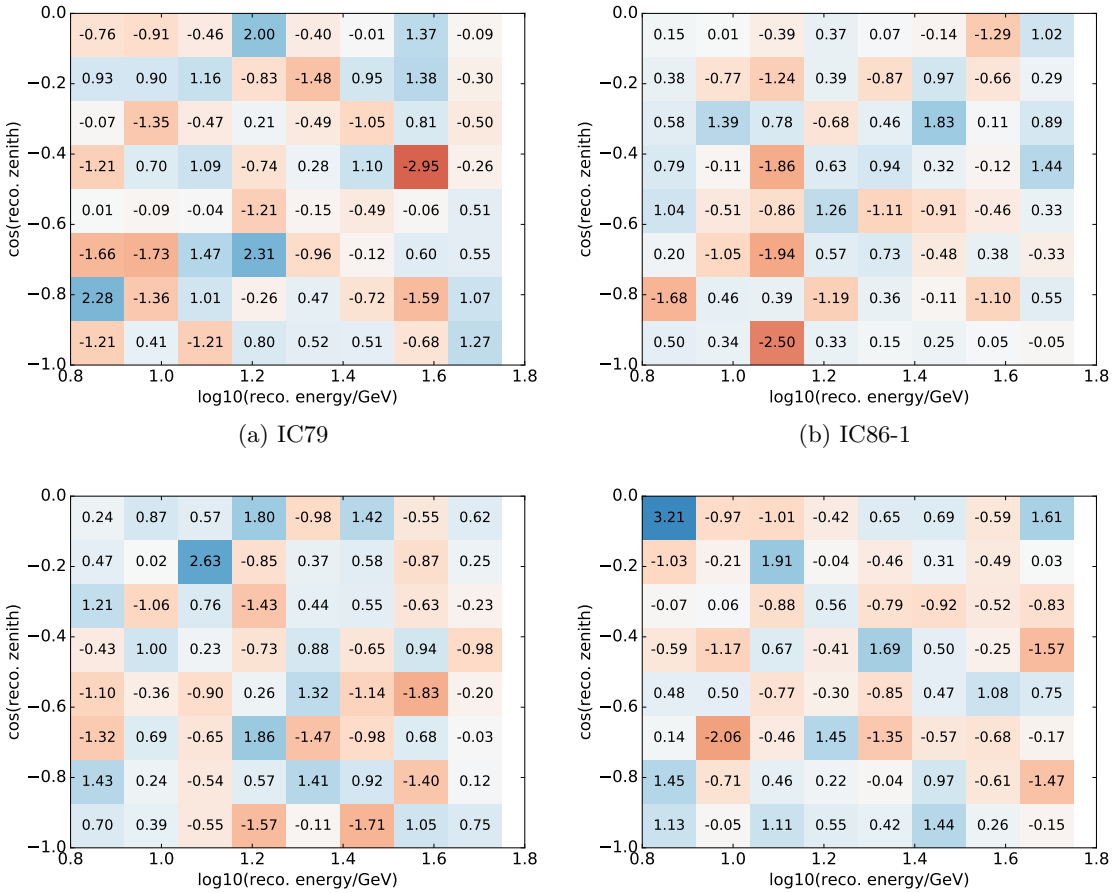

(a) IC79 (b) IC86-1

(c) IC86-2 (d) IC86-3

Figure 6.2: Pulls for the individual years of data of the combined fit.

would indicate a bad fit to the data. All four years show a homogeneous distribution of pulls with most values between -1 and 1. Some few stronger pulls with $|P| \geqq 2$ are present in every year of data. These stronger pulls do not form obvious clusters.

Figure 6.3 shows a L/E projection for four years of data and the best-fit parameters. The data follows the best-fit expectation over the whole parameter space and the non-oscillation hypothesis (dashed red) is clearly disfavored. The deviation of the data from the best-fit of the Monte Carlo is within the expected limits.

The analysis was also tested in a two flavor fit to see if it drifts deep into the unphysical region. This gives a best-fit at $\sin^2(2\theta_{23}) = 1.02^{+0.88}_{-0.96}$ being compatible with maximal mixing. The drift into the unphysical region is well within the statistical uncertainty of the fit. The full contour is shown in the appendix in figure C.20.

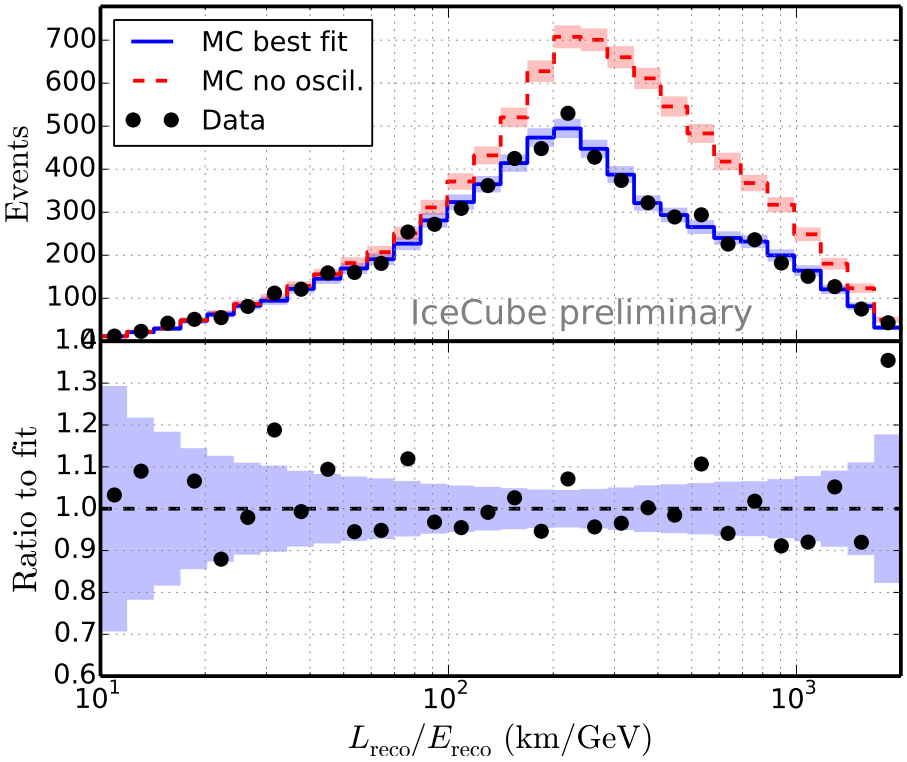

Figure 6.3: L/E projection histogram of the events from data and expectation with the reconstructed propagation length divided by the reconstructed energy on the x-axis. The data follows the best-fit of the oscillation hypothesis (blue, solid). The non-oscillation hypothesis (red, dashed) is disfavored. The light blue band reflects the statistical uncertainty for the expected number of events.

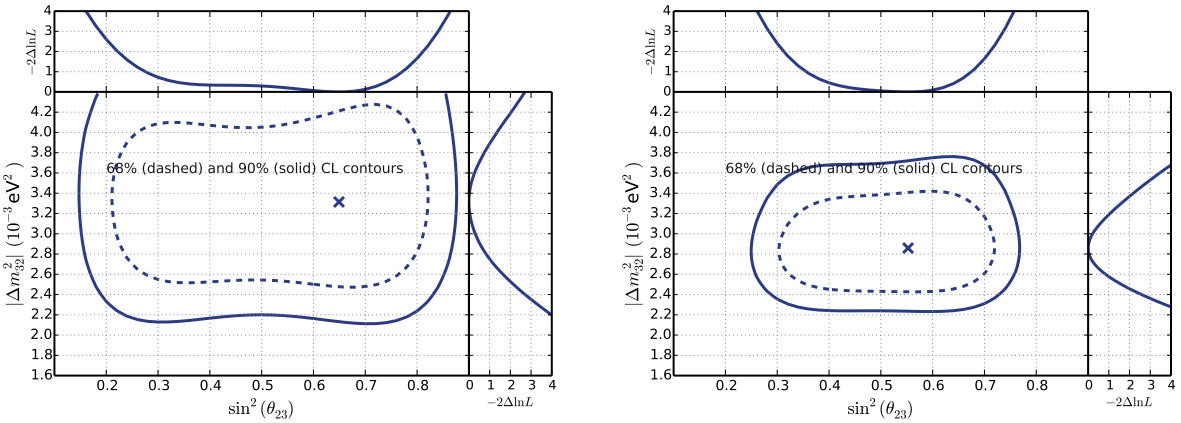

(a) IC79 (b) IC86-3

Figure 6.4: Single year contours from parameter scans for three flavor oscillation, matter effects and normal hierarchy. Shown is the single year of IC79 (left plot) and the third year of IC86 (right plot).

6.3 Single Year Fit

The fit was also performed for every year individually. This reduces the number of fit parameters, as the atmospheric muon background consists only of one template and the ν normalization is fitted only for one dataset.

Figure 6.4 depicts the resulting contours for the single years of data. Due to the higher event count and the better energy reconstruction the contours for the single year of IC86 are smaller than for the one year of IC79. Overall the contours are compatible to each other. The other years of IC86 are comparable to the third year, albeit the first year is shifted to smaller mass splittings (see figure C.19 in the appendix).

Figure 6.5 shows the resulting L/E projections for the single year fits for IC79 and the third year of IC86. The separation between oscillation and no oscillation hypothesis is stronger for the one year of IC86. The data follows the oscillation hypothesis for both datasets. Also for both datasets there is a small systematic shift at low L/E. This is not present for the other years of IC86. The event count in this area is very low and errors are very high, so the impact of this systematic shift is contained.

6.4 Systematics

To analyze the impact of the different systematic parameters, their values for the whole parameter space are presented in the following.

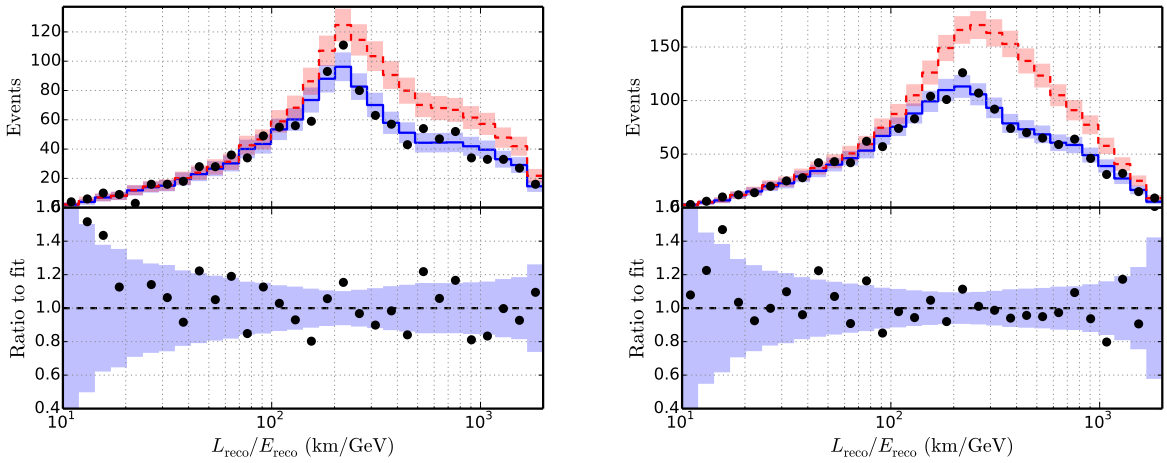

(a) IC79 (b) IC86-3

Figure 6.5: L/E projection histogram of the events from data and expectation with the reconstructed neutrino propagation length divided by the reconstructed energy on the x-axis. The light blue band reflects the statistical uncertainty for the expected number of events. Shown are the projections for single year fits of IC79 data (left plot) and the third year of IC86 (right).

6.4.1 Combined Fit

The nuisance parameters that are varied for the combined fit are listed in table 6.1. At each scan point in the parameter space of the oscillation parameters, different values for the nuisance parameters are obtained as a best-fit for this specific pair of oscillation parameters.

The fits of individual scan-points of the oscillation parameter-space are independent of each other. At the beginning of every fit a global dataset normalization between data and Monte Carlo is performed for each year of data. The Monte Carlo has to have the same amount of events than the dataset from the measurement. In the fit, the neutrino normalization is varied as a free parameter. The parameter is shown for each year in figure 6.6 as a color-map in the parameter space of the oscillation parameters. The 68 % (dashed) and 90 % C.L. contours of the combined analysis is also shown together with the global best fit value (black cross). In the 68 % area the parameter only varies slightly. The strong global differences between the single years of data are caused by differing life-time of the data. For the IC79 data a detector down-time in preparation of the first IC86 run reduced the overall life-time, as did several tests of the detector in the last half of the year of the configuration. For the third year of IC86 the used dataset was not yet complete and is missing some data. These two years are comparable in detector life-time.

The neutrino normalization and the optical efficiency both impact the number of neutrinos in the sample and are thus degenerated parameters. Also, since the number of events in the dataset is fixed, the parameter is also degenerated with respect to the relative atmospheric muon content.

The relative atmospheric muon content for each scanned point is shown separate in figure

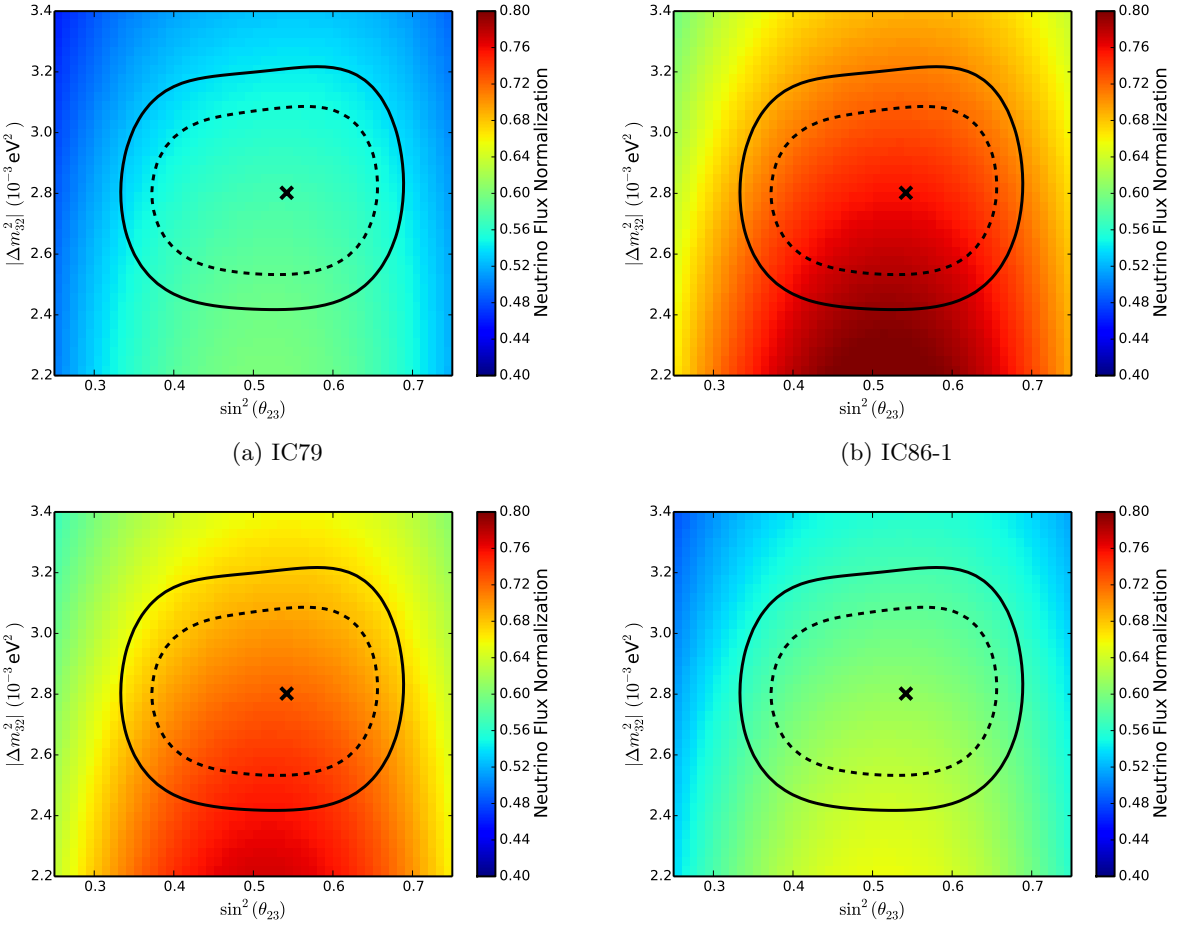

(a) IC79 (b) IC86-1

(c) IC86-2 (d) IC86-3

Figure 6.6: The deviation from the initial neutrino normalization factor for a scan in $\sin^2(\theta_{23})$ and Δm^2_{32}. The global neutrino normalization is done for every year individual, due to differing live-time. The best-fit is indicated by the black cross. Also depicted are the 68% (dashed black) and the 90% (solid black) C.L. contours for the combined four year fit.

6.7 for the one year of IC79 and the three years of IC86. For the year of IC79 the background is fitted to 3-4 % in the scanned parameter space. This is close to the predicted amount of background from the event selection, which is assumed to be 5 %.

The relative amount of background for the IC86 dataset is fitted to 0-2 % which is very low. Overall, the atmospheric background does not have a relevant impact for this analysis.

Figure 6.8 shows the parameters of systematic uncertainties that are shared between the different datasets. The combined best-fit resides close to the baseline values of the fit. For the combined analysis the cosmic-ray index and the optical efficiency have the strongest impact on the shape of the energy spectrum and thus these parameters are susceptible to the value of the mass splitting, which impacts the energy dependence of the oscillation. The hole-ice scattering coefficient has a strong impact on the amplitude of the oscillation. The relative

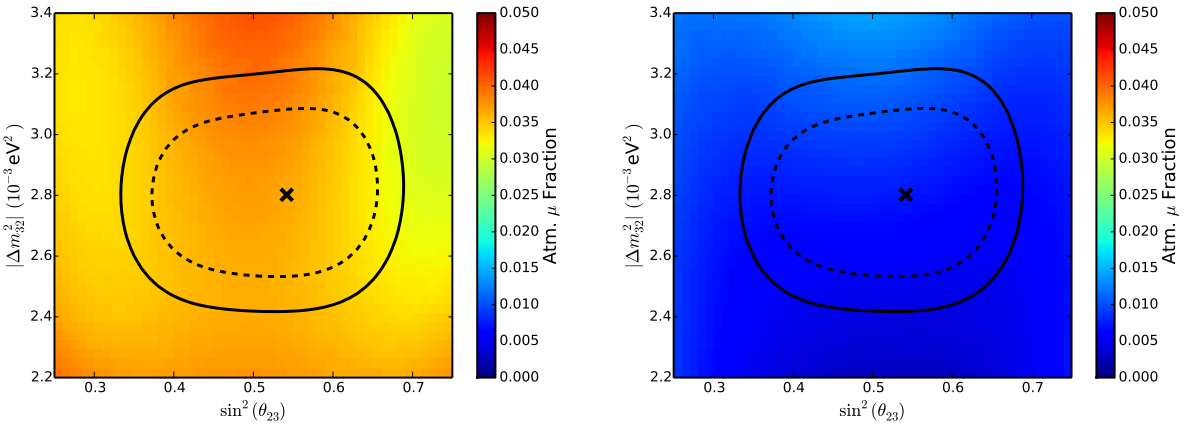

(a) IC79 (b) IC86

Figure 6.7: The atmospheric muon fraction of the IC79 dataset (left) and the three years of IC86 (right) for a scan in $\sin^2(\theta_{23})$ and Δm^2_{32}. Both parameters are fitted at the same time for the two different detector configurations. The best-fit is indicated by the black cross. Also depicted are the 68% (dashed) and the 90% (solid) C.L. contours for the combined four year fit.

ν_e deviation has a similar effect on both oscillation parameters. In the 68 % contours of the fit these parameters only vary by a small amount, being mostly in the expected uncertainty interval around the base values.

6.4.2 Single Year Fit

For single year fits the amount of systematic parameters and with this the degrees of freedom are lower than for the combined fit. Only one global neutrino normalization parameter and only one atmospheric muon template are used. The systematic values for the single year parameter scans are shown in figure 6.9, 6.10, 6.11, 6.12 and 6.13 with the respective 68 % (dashed) and 90 % C.L. (solid) contours. The best fit value for the single years of data is shown as a black cross. If no significant other deviations exist, the plots are shown as a comparison between the one year of IC79 and the third year of IC86 due to the similarity of best-fit and contour. The other years of IC86 are shown in appendix C.

In figure 6.9 the deviation from the initial global neutrino normalization is shown. The overall deviation is below 4 % for all years of data, like expected. The highest deviations are for maximal mixing. This is a compensation by the fit for the disappearing events due to the oscillation effect, to keep the total number of events constant.

Figure 6.10 shows the relative ν_e normalization in respect to the global neutrino normalization. The one year of IC79 as well as the years IC86-1 and IC86-3 result in fitted deviations around zero. The second year of IC86 deviates with a higher best-fit value around 0.2 ± 0.2. This is still in the expected uncertainty of the value.

The fitted atmospheric muon fraction for IC79 and IC86-3 as shown in 6.11 is below 5 %

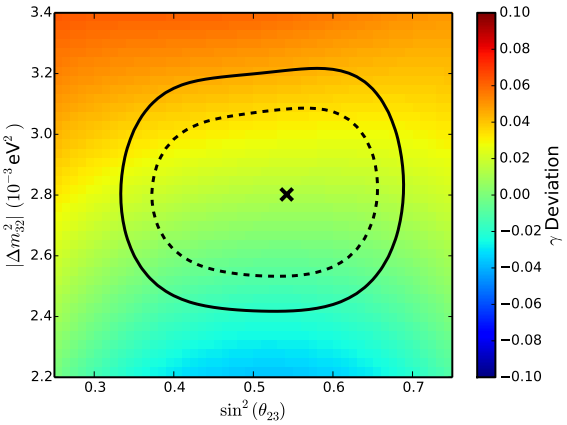

(a) Deviation from the initial cosmic ray index

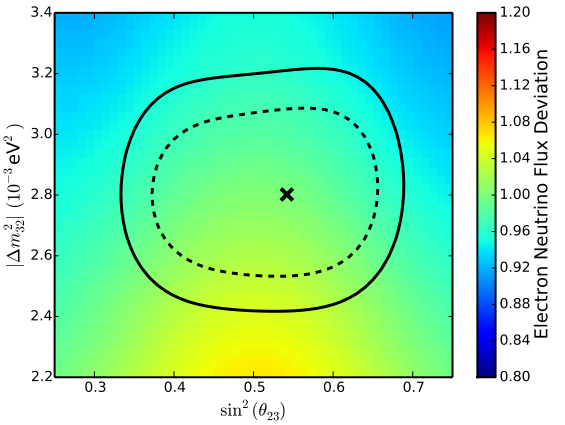

(b) Electron neutrino normalization relative to the total ν normalization

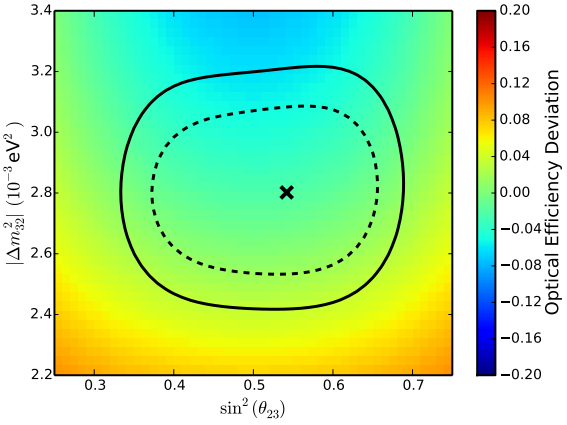

(c) Deviation of the optical efficiency from the baseline value

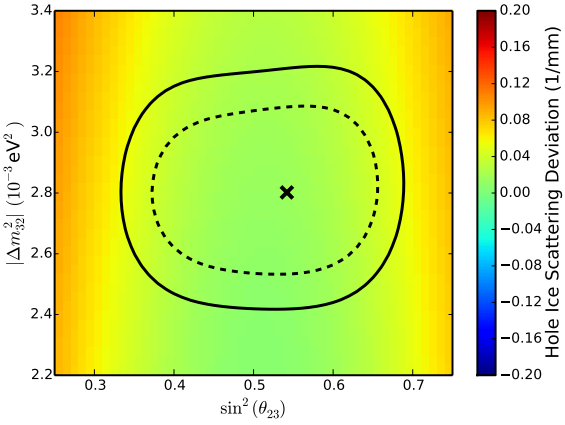

(d) Deviation of the scattering parameter inside the hole ice columns from the baseline value

Figure 6.8: Different systematic parameters for the combined four year scan in $\sin^2(\theta_{23})$ and Δm^2_{32}. Also depicted are the 68% (dashed black) and the 90% (solid black) C.L. contours for the combined four year fit.

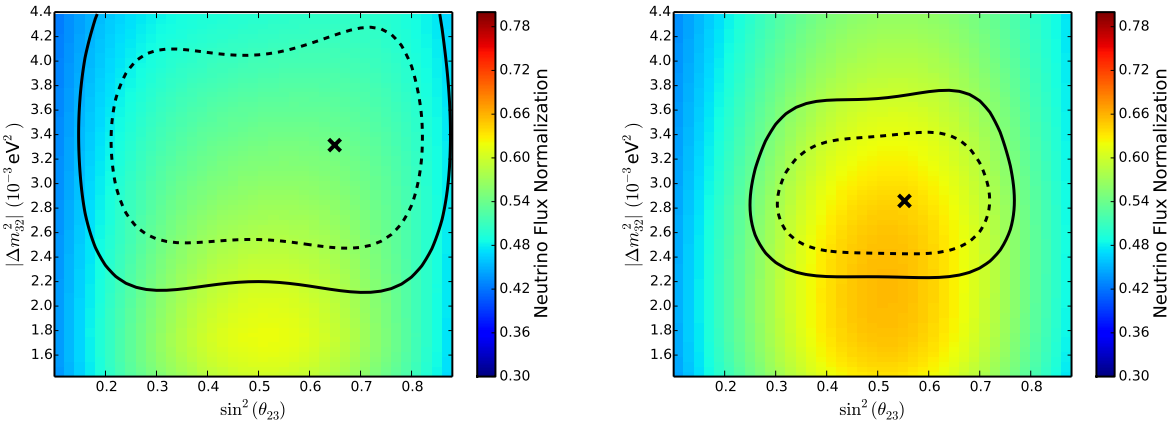

(a) IC79 (b) IC86-3

Figure 6.9: The neutrino normalization factor for a scan in $\sin^2(\theta_{23})$ and Δm^2_{32} for single years of data. The left plot shows the result for the single year of IC79, whereas the right plot shows the result for the single year of IC86-3 data. The best-fit is indicated by the black cross. Also depicted are the 68% (dashed black) and the 90% (solid black) C.L. contours for every year.

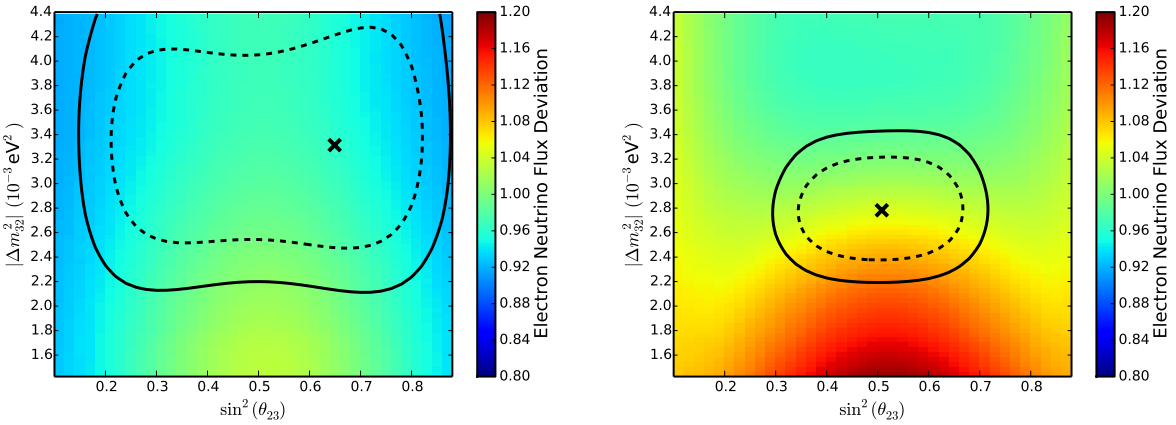

(a) IC79 (b) IC86-2

Figure 6.10: The relative ν_e-normalization in respect to the global neutrino normalization factor for a scan in $\sin^2(\theta_{23})$ and Δm^2_{32} for single years of data. The left plot shows the result for the single year of IC79, whereas the right plot shows the result for the single year of IC86-2 data. The best-fit is indicated by the black cross. Also depicted are the 68% (dashed black) and the 90% (solid black) C.L. contours for every year.

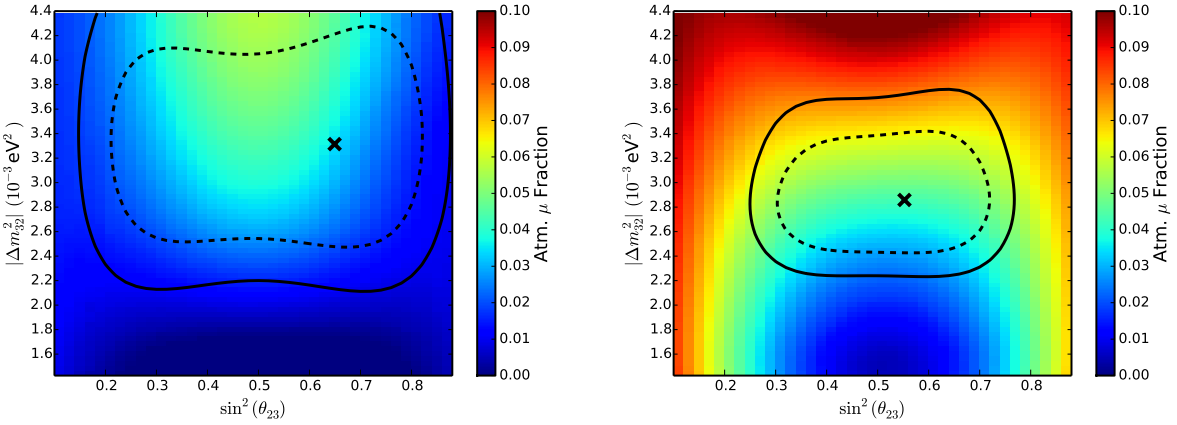

(a) IC79 (b) IC86-3

Figure 6.11: The atmospheric muon fraction of the dataset for a scan in $\sin^2(\theta_{23})$ and Δm^2_{32} for single years of data. The left plot shows the result for the single year of IC79, whereas the right plot shows the result for the single year of IC86-3 data. The best-fit is indicated by the black cross. Also depicted are the 68% (dashed black) and the 90% (solid black) C.L. contours for every year.

as expected from the combined fit and the event selection. For the years of IC86 the first and second year fit to ∼0 % atmospheric background, which is very low. Since the impact of the atmospheric muon background can partly be absorbed by the variation of other parameters this is plausible. Due to the general low amount the atmospheric background does not limit this analysis.

The cosmic-ray index has a strong impact on the shape of the energy distribution of the dataset. A variation can shift the maximum of the distribution to lower or higher energies. For IC79 and IC86-3 this parameter is shown in figure 6.12. For the IC79 dataset the fit returns a slightly higher value of the cosmic-ray index. This is in tune with the first year of IC86 (shown in the appendix). The second and the third year of IC86 return values near the baseline. The deviation inside the 68 % C.L. area is small and well within the expected limits.

Figure 6.13 shows the relative deviation from the optical efficiency of the baseline. For the IC79 dataset this parameter varies only slightly over the full parameter space. For the IC86 datasets the parameter shows a larger variation. A change of the parameter causes a variation in the total number of neutrino events and a modification of the measured energy-zenith spectrum. The changed number of neutrino events is absorbed by the free neutrino normalization parameter. Thus, the remaining impact is a modification of the energy-zenith spectrum. The impact of this modification is dependent on the resolution of the energy and zenith reconstruction. Since the resolution of the energy reconstruction for IC79 is poorer, this results in a weaker parameter for the optical efficiency.

The deviation from the baseline of the hole-ice scattering coefficient is shown in figure 6.14 for the single year of IC79 and the third year of IC86. A stronger scattering in the refrozen ice columns around the DOMs results in a stronger deficit efficiency of horizontal and down-

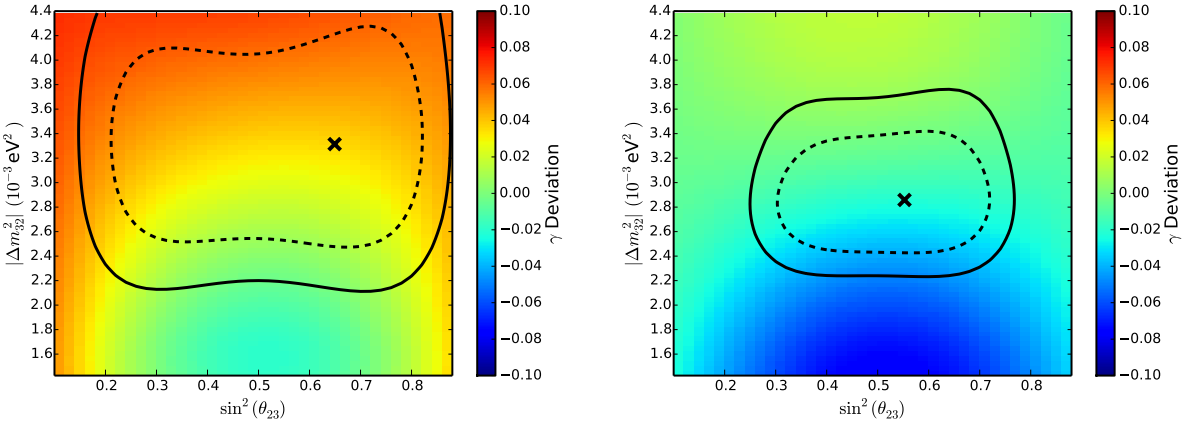

(a) IC79 (b) IC86-3

Figure 6.12: The deviation from the initial value of the cosmic ray index ($\Delta\gamma = \gamma - 2.65$) for a scan in $\sin^2(\theta_{23})$ and Δm^2_{32} for single years of data. The left plot shows the result for the single year of IC79, whereas the right plot shows the result for the single year of IC86-3 data. The best-fit is indicated by the black cross. Also depicted are the 68% (dashed black) and the 90% (solid black) C.L. contours for every year.

going tracks. For the single years a slightly higher scattering parameter between 0.023 $\frac{1}{\text{cm}}$ and 0.026 $\frac{1}{\text{cm}}$ is preferred. The exception is the third year of IC86 with a value of 0.014 $\frac{1}{\text{cm}}$. All fitted values are within the uncertainty range for the hole-ice.

The last fitted parameter is the mixing angle θ_{13}. Since the fit is not sensitive to this parameter, it has no real impact and its variation is negligible. The plots for θ_{13} are shown in figure C.29 in the appendix.

6.5 Improvements to the Analysis

In the following sections some improvements to the analysis are explored. Since new simulation datasets with the SpiceLea ice model were produced, the impact of these on the result of the fit is looked at. Also a the normalization is fixed to a region without oscillation effects.

6.5.1 Fixing the Horizon

As stated in section 5.5, the neutrino normalization is a free parameter in the fit. No prior information about the total flux or the shape of neutrino oscillations is exploited. This leads to a robust analysis but also causes a loss in sensitivity.

Muon neutrinos with a small baseline below some ten km will not show oscillation effects in the energy range used for this analysis. This baseline is typical for very horizontal events. Thus, horizontal events show no oscillation effects and can be used for normalization purposes.

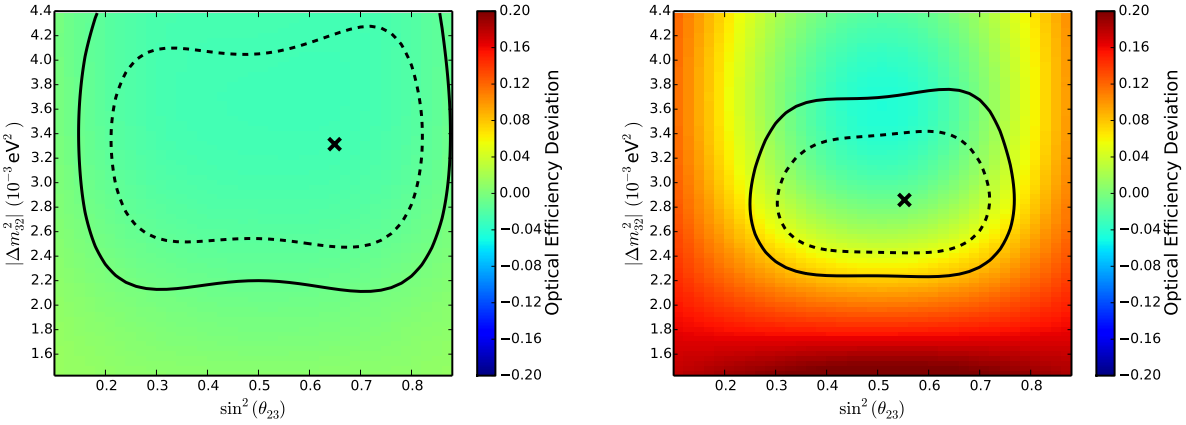

(a) IC79 (b) IC86-3

Figure 6.13: The deviation from the initial optical efficiency factor (0.99) for a scan in $\sin^2(\theta_{23})$ and Δm^2_{32} for single years of data. The left plot shows the result for the single year of IC79, whereas the right plot shows the result for the single year of IC86-3 data. The best-fit is indicated by the black cross. Also depicted are the 68% (dashed black) and the 90% (solid black) C.L. contours for every year.

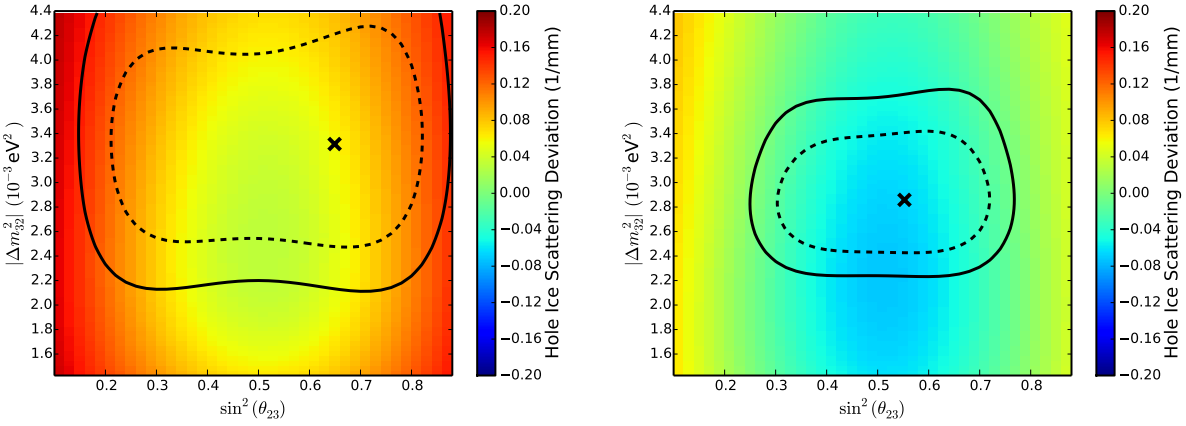

(a) IC79 (b) IC86-3

Figure 6.14: The deviation to the initial photon scattering length in the refrozen ice columns for a scan in $\sin^2(\theta_{23})$ and Δm^2_{32} for single years of data. The left plot shows the result for the single year of IC79, whereas the right plot shows the result for the single year of IC86-3 data. The best-fit is indicated by the black cross. Also depicted are the 68% (dashed black) and the 90% (solid black) C.L. contours for every year.

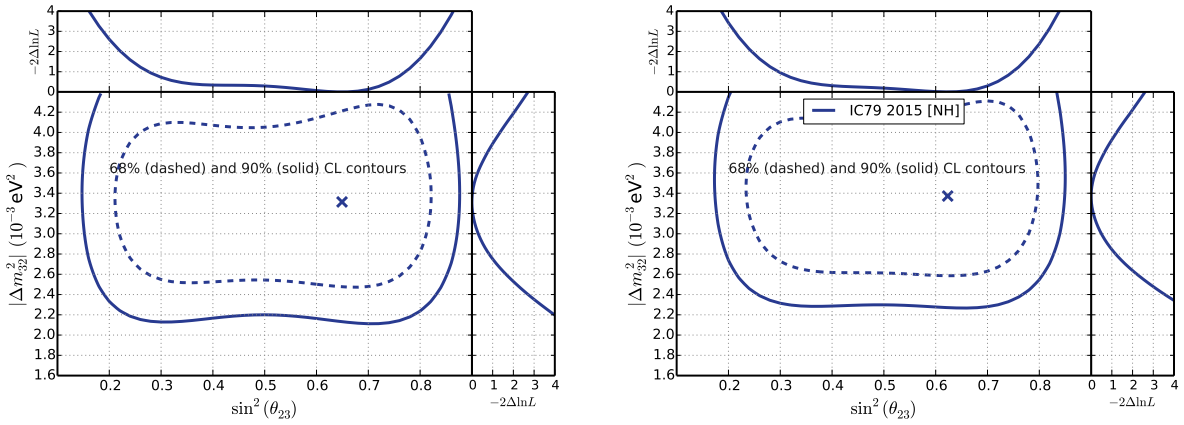

(a) no prior (b) with prior

Figure 6.15: 90 % (solid) and 68 % (dashed) C.L. contours for parameter scans in Δm^2_{32} and $\sin^2(\theta)$ with three flavors and matter effects. The left plot shows the result without a prior on the number of horizontal events and is the same as in 6.4a. The right plot shows the result if a prior is used.

A Gaussian prior

$$P = \frac{1}{2}\sum_k \frac{\left(N^{\text{hor.}}_{\text{sim}} - N^{\text{hor.}}_{\text{data}}\right)^2}{N^{\text{hor.}}_{\text{data}}} \tag{6.4}$$

has been added to the fit to exploit the horizontal events for normalization. If the number of horizontal events of the expectation from simulation $N^{\text{hor.}}_{\text{sim}}$ is different to the number of horizontal events in data $N^{\text{hor.}}_{\text{data}}$ the prior will penalize the fit. A poissonian error on these numbers is assumed. For the selection of horizontal events every event with a reconstructed zenith angle between 90.0° and 97.4° is used. Figure 6.15 shows the difference for the 68 % and 90 % C.L. contours for the usage of the prior for normalization in the IC79 single year fit. The best-fit point is only shifted very slightly. However, the contours shrink due to the rise in sensitivity.

6.5.2 High Energy GENIE Datasets

Due to historic reasons, the main simulation datasets used in the fit only cover neutrino energies up to 190 GeV. The high energy tail of events is then patched into the dataset by using existing high energy neutrino datasets (see section 5.2.1). Since no high-energy datasets for detector systematics were available for IC79, the event variations due to different scattering in the hole-ice or different optical efficiencies were generated solely from the low-energy GENIE datasets. In the course of the analysis new high-statistics GENIE datasets that include the low- and high-energy region became available. These also cover detector systematics. For these newer datasets an updated version of the SpiceMie ice model called “SpiceLea” was used (see 3.4.4). The parameters of the new datasets are shown in table 6.2.

If solely the high-energy GENIE datasets are used in the analysis, no high-energy tail has

Table 6.2: High-energy neutrino datasets for IC79 used in an improved version of the analysis

Particle:	ν_e, ν_μ, ν_τ
Numbers:	12050, 14050, 16050
Generator:	GENIE
Noise Model:	Poissonian and coincident photons
Ice Model:	SpiceLea
Energy Range [GeV]:	$3 - 1000\,\mathrm{GeV}$
Optical Efficiencies:	0.81, 0.90, 0.99, 1.08, 1.17
Hole-Ice scattering length [cm]:	30, 50, 100, inf

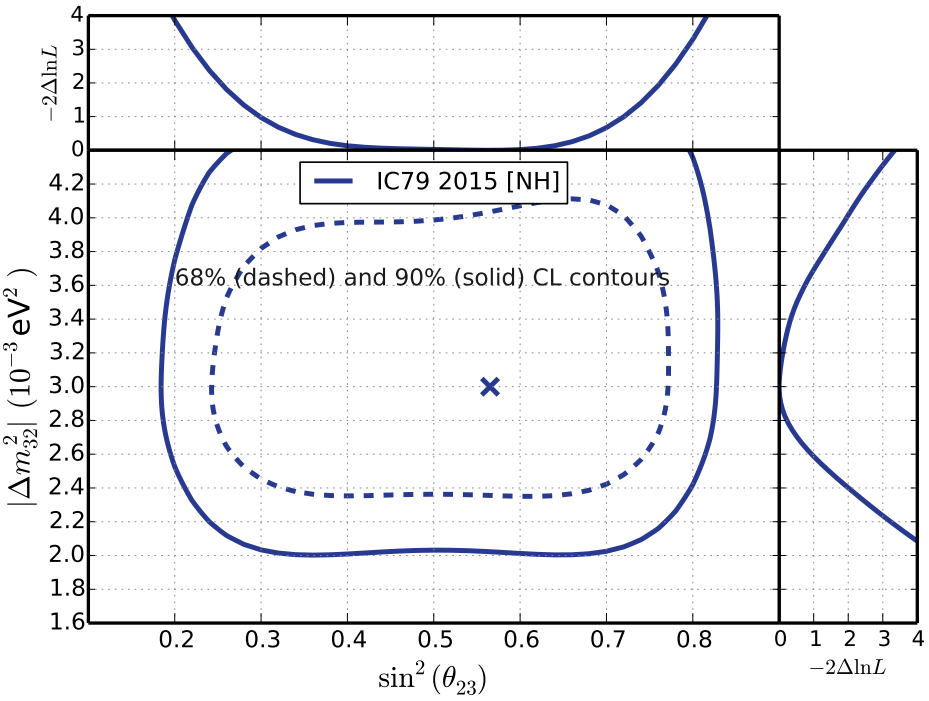

Figure 6.16: Impact of the usage of high energy GENIE datasets. Shown are 90 % (solid) and 68 % (dashed) C.L. contours for parameter scans in Δm^2_{32} and $\sin^2(\theta)$ with three flavors and matter effects.

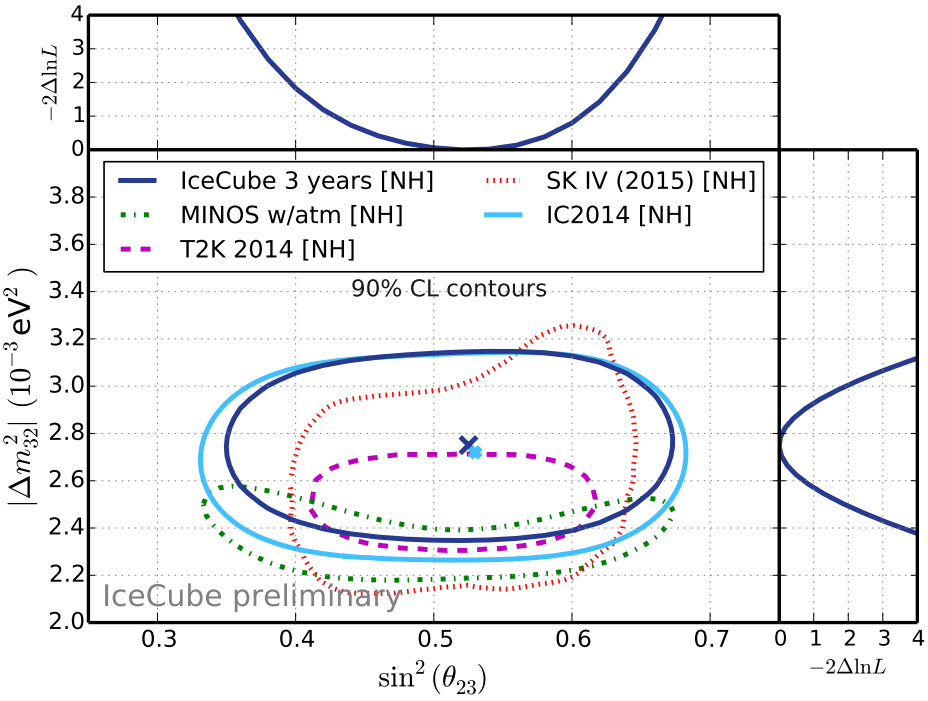

Figure 6.17: 90% C.L. contour of a parameter scan in $\sin^2(\theta_{23})$ and Δm^2_{32} with matter effects and three neutrino flavors. For the IC79 dataset the high energy GENIE simulation and a prior on the number of horizontal events is used. The improved four year result (solid, dark blue) is shown together with the previous result with three years of data [75] (solid, light blue) and results from different experiments: MINOS [88] (dashed, green), Super Kamiokande IV [141] (dashed, red), T2K [142] (dashed, pink).

to be added to the simulation data. The result for a the single year IC79 fit is shown in figure 6.16. Additionally the fit uses a prior on the number of horizontal events. The new datasets cause a shift in the best-fit to lower mass splittings and a slightly higher oscillation amplitude. This shift reduces the contour size in $\sin^2(\theta_{23})$.

6.5.3 Combined Fit with Improvements

Figure 6.17 shows a fit with for years of data if the new simulations and the prior on horizontal events are used. In comparison to the published three year result the best-fit remains the same while the contour shrinks in both oscillation parameters. The gain is mostly due to the shifted best-fit for the year of IC79. This shows, that a significant improvement can be achieved with the new simulation datasets and a normalization in the horizontal zenith region

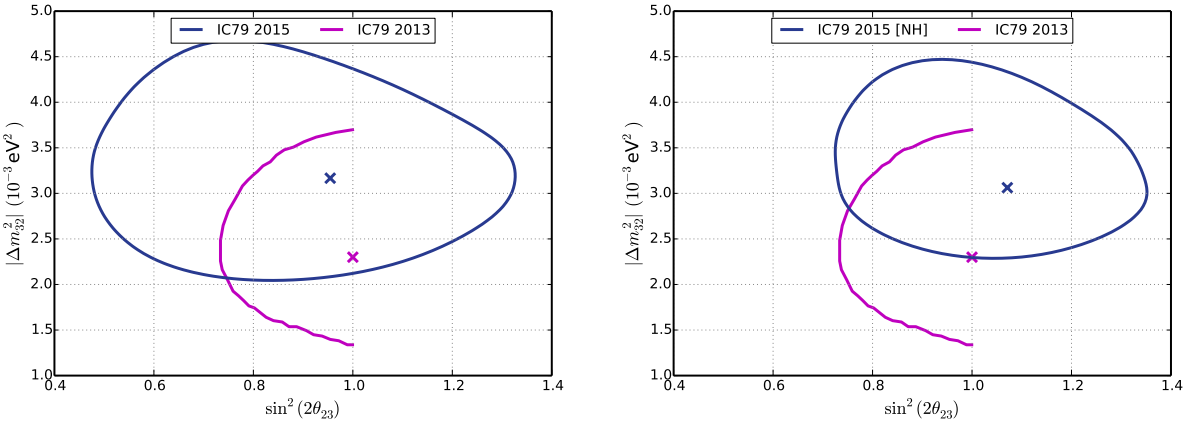

(a) free normalization

(b) fixed normalization

Figure 6.18: 90 % contours from parameter scans for the two flavor approximation in Δm^2_{32} and $\sin^2(2\theta)$. Shown are the PRL result from 2013 [74] and the result from this work (2015). Both analyses give comparable results if the normalization in the 2015 analysis is fixed for horizontal events. The region $\sin^2(2\theta) > 1$ marks the unphysical sector.

6.6 Two Flavor Fit Comparison

A measurement of neutrino oscillations with data of the IC79 detector configuration has been published in Physical Review Letters (PRL) [74]. The result of this measurement was presented in $\sin^2(2\theta)$ and done using the two flavor approximation. Figure 6.18a shows the result from [74] (2013) together with the single IC79 contour of this work (2015) both for the two flavor approximation. The fit has been allowed to also cover the unphysical area of $\sin^2(2\theta) > 1$.

The best-fit for the 2015 contour is much higher than for the 2013 result, even if the number disappearing events is similar and slightly higher for the 2015 analysis. Also the contour in the physical area of $\sin^2(2\theta) < 1$ is much bigger, especially in oscillation amplitude. This is caused by two effects. It is obvious from the contour of the 2013 result that, if allowed to, the best-fit would be in the unphysical region. This is indicated by the shape of the contour and the best-fit being at $\sin^2(2\theta) = 1$. A small shift into the unphysical region drags the contour with it. If not allowed by the fit, the contour is affected by this. The second reason is the free neutrino normalization factor in the 2015 fit. As explained above, this reduces the sensitivity, especially in the mixing amplitude. The 2013 analysis uses a high energy region of 0.1-10 TeV with ∼40.000 events [74] for normalization. In this energy region no oscillation effects are visible for the possible baselines. The high number of high energy events fixes the normalization.

Figure 6.18b shows both contours, if for the 2015 fit the number of horizontal events in the expectation is fixed to the number of horizontal events in data. This causes a slight shift of the best-fit into the unphysical region. This shift is not very strong and still explainable with statistical variations in the datasets. The fixed horizontal region also causes a shrink in contour size, especially in $\sin^2(2\theta)$. Both contours are comparable in size. The fixed 2015

contour is a bit smaller in mass splitting, which is most likely caused by the slightly higher number of low-energy events.

Chapter 7

Summary and Outlook

In the first section of this chapter a brief summary of the thesis is given. In the second section an outlook for future oscillation analyses is presented.

7.1 Summary

In this thesis a measurement of the oscillation parameters $\sin^2(\theta_{23})$ and Δm^2_{32} with data taken with the IceCube-DeepCore detector was presented. Atmospheric muon neutrinos (ν_μ) produced in the Earth's atmosphere cross the Earth and reach the IceCube detector. In the course of their propagation the probability to measure these initial ν_μ in a different neutrino flavor changes. For ν_μ with energies of $\sim$25 GeV that travel a distance equal Earth's diameter the probability of oscillation into ν_τ is maximal. This oscillation is visible as a deficit of measured ν_μ with respect to the hypothesis without oscillations.

The data for this analysis was measured with the IceCube detector. IceCube is a neutrino detector at the geographic South Pole instrumenting around one cubic kilometer of clear glacial ice with 5160 light detectors. The light detectors are used to detect the faint Čerenkov light of fast charged particles like muons in the ice. Some of which are created in charged-current neutrino interactions of atmospheric ν_μ. The overwhelming part of measured muons, however, is produced directly by meson decays in the atmosphere and reaches the detector. This background of events has to be reduced to measure the deficit of atmospheric muon neutrinos due to oscillations.

An event selection was presented that reduces the background of atmospheric muons by about six orders of magnitude. The remaining muon background rate is below that of neutrino interactions of other flavors than ν_μ. For this event selection a machine learning algorithm was used as an integral part. The final dataset used for the fit consists of 1172 events for IC79 and 5174 events for IC86 and thus 6346 events in total.

The analysis itself is an extension of a three year (IC86) result and includes one additional year of data from a previous year (IC79). The complete dataset covers a timespan of four years from 2010 to 2014. The data measured with the IceCube detector is compared to simulations with different oscillation hypothesis. The hypothesis that matches the data best then gives the measured oscillation parameters. The different oscillation hypothesis are created with full three flavor oscillations in mind, which means that every neutrino flavor can oscillate into the other two flavors. Furthermore a distortion of the oscillation pattern due to interactions between electron neutrinos with the matter of Earth is reconsidered in the analysis.

Due to the low statistics of the remaining atmospheric muon simulation, this background is estimated from data. The obtained events are processed in a kernel density estimation (KDE) to extract the maximum of information and generate a smooth template for the background that can be used in the fit.

The result of the fit with

$$\sin^2(\theta_{23}) = 0.54^{+0.08}_{-0.13} \quad \text{and} \quad \Delta m^2_{32} = 2.80^{+0.20}_{-0.16} \cdot 10^{-3}\text{eV}^2 \tag{7.1}$$

with a reduced χ^2 of 0.98 is an improvement over the published three year result and shows the possible gain if more statistics is incorporated into the analysis. Furthermore the single years have been compared to each other in individual fits. The single year of IC79 has larger contours due to a reduced statistics and resolution for the zenith and energy reconstruction. This is impacted by the lower number of strings in the center of DeepCore with respect to

IC86. If these strings are included, the low-energy performance of IceCube improves and with it statistics and reconstructional resolution.

Enhancements to the IC79 part of the analysis are presented. A Gaussian prior on the difference of horizontal events that do not take place in neutrino oscillations improves the sensitivity of the analysis. Furthermore, an updated neutrino simulation is used in the analysis. This shifts the best-fit of the IC79 part of the analysis to be more compatible with the three years of IC86.

The IC79 result for the two flavor approximation is compared to and older result of the IceCube collaboration. Differences in the contours are mostly due to the huge number of high energy events in the old analysis that were used for normalization purposes.

7.2 Outlook

Neutrino oscillation analyses with IceCube data are limited by systematics. A major effort in the collaboration is aims to raise the resolution of reconstructions and improve the understanding of the detector systematics. Furthermore, since the detector is stable in its configuration and taking data, several years of data can be processed with the same event selection. New years can be easily included to analyses. An improvement in resolution and statistics may permit a handle on the neutrino mass hierarchy [143]. Also, the feasibility to measure neutrino oscillations with IceCube through ν_τ appearance is explored [144].

The PINGU detector as described in section 2.4.3 will increase the event statistic and simultaneously lower the detection threshold. This will enable the determination of the neutrino mass ordering. Furthermore this also permits a higher precision in the measurement of the neutrino oscillation parameters being competitive with todays best neutrino oscillation experiments for the atmospheric mixing parameters. With this enhanced sensitivity PINGU may be able to solve if the atmospheric mixing is maximal or not.

Apart from three flavor neutrino oscillations IceCube data is used to determine the existence of sterile neutrinos [145].

Appendices

Appendix A

Calculations

Neutrino Oscillations

In section 2.3.1 the oscillation probability for the vacuum case was derived (equation 2.21). This expression can be written in a more convenient way by using the unitarity relation from equation 2.7 as follows:

$$
\begin{aligned}
P_{\nu_\alpha \to \nu_\beta}(L,E) &= \sum_{k,j} U^*_{\alpha k} U_{\beta k} U_{\alpha j} U^*_{\beta j} \exp\left(-i\frac{\Delta m^2_{kj} L}{2E}\right) \\
&= \sum_{k=j} U^*_{\alpha k} U_{\beta k} U_{\alpha k} U^*_{\beta k} \\
&+ \sum_{k>j} U^*_{\alpha k} U_{\beta k} U_{\alpha j} U^*_{\beta j} \exp\left(-i\frac{\Delta m^2_{kj} L}{2E}\right) \\
&+ \sum_{k<j} U^*_{\alpha k} U_{\beta k} U_{\alpha j} U^*_{\beta j} \exp\left(-i\frac{\Delta m^2_{kj} L}{2E}\right) \\
&= \sum_{k} |U_{\alpha k}|^2 |U_{\beta k}|^2 \\
&+ \sum_{k>j} U^*_{\alpha k} U_{\beta k} U_{\alpha j} U^*_{\beta j} \exp\left(-i\frac{\Delta m^2_{kj} L}{2E}\right) \\
&+ \sum_{j<k} U^*_{\alpha j} U_{\beta j} U_{\alpha k} U^*_{\beta k} \exp\left(-i\frac{\Delta m^2_{jk} L}{2E}\right) \\
&= \sum_{k} |U_{\alpha k}|^2 |U_{\beta k}|^2 \\
&+ \sum_{k>j} U^*_{\alpha k} U_{\beta k} U_{\alpha j} U^*_{\beta j} \exp\left(-i\frac{\Delta m^2_{kj} L}{2E}\right) \\
&+ \sum_{k>j} [U_{\alpha j} U^*_{\beta j} U^*_{\alpha k} U_{\beta k}]^* \exp\left(-i\frac{(-\Delta m^2_{kj}) L}{2E}\right)
\end{aligned}
$$

$$
\begin{aligned}
P_{\nu_\alpha \to \nu_\beta}(L,E) =& \sum_k |U_{\alpha k}|^2 |U_{\beta k}|^2 \\
&+ \sum_{k>j} \left(\Re[U^*_{\alpha k} U_{\beta k} U_{\alpha j} U^*_{\beta j}] + i \Im[U^*_{\alpha k} U_{\beta k} U_{\alpha j} U^*_{\beta j}] \right) \exp\left(-i \frac{\Delta m^2_{kj} L}{2E} \right) \\
&+ \sum_{k>j} \left(\Re[U^*_{\alpha k} U_{\beta k} U_{\alpha j} U^*_{\beta j}] - i \Im[U^*_{\alpha k} U_{\beta k} U_{\alpha j} U^*_{\beta j}] \right) \exp\left(i \frac{\Delta m^2_{kj} L}{2E} \right) \\
=& \sum_k |U_{\alpha k}|^2 |U_{\beta k}|^2 \\
&+ \sum_{k>j} \Re[U^*_{\alpha k} U_{\beta k} U_{\alpha j} U^*_{\beta j}] \left[\exp\left(-i \frac{\Delta m^2_{kj} L}{2E} \right) + \exp\left(i \frac{\Delta m^2_{kj} L}{2E} \right) \right] \\
&+ i \sum_{k>j} \Im[U^*_{\alpha k} U_{\beta k} U_{\alpha j} U^*_{\beta j}] \left[\exp\left(-i \frac{\Delta m^2_{kj} L}{2E} \right) - \exp\left(i \frac{\Delta m^2_{kj} L}{2E} \right) \right] \\
=& \sum_k |U_{\alpha k}|^2 |U_{\beta k}|^2 \\
&+ 2 \sum_{k>j} \Re[U^*_{\alpha k} U_{\beta k} U_{\alpha j} U^*_{\beta j}] \cos\left(\frac{\Delta m^2_{kj} L}{2E} \right) \\
&+ 2 \sum_{k>j} \Im[U^*_{\alpha k} U_{\beta k} U_{\alpha j} U^*_{\beta j}] \sin\left(\frac{\Delta m^2_{kj} L}{2E} \right)
\end{aligned}
$$

We see that

$$
P_{\nu_\alpha \to \nu_\beta}(0\,\mathrm{eV}^{-1}, E) = \delta_{\alpha\beta} = \sum_k |U_{\alpha k}|^2 |U_{\beta k}|^2 + 2 \sum_{k>j} \Re[U^*_{\alpha k} U_{\beta k} U_{\alpha j} U^*_{\beta j}] \quad . \tag{A.1}
$$

This means that

$$
\sum_k |U_{\alpha k}|^2 |U_{\beta k}|^2 = \delta_{\alpha\beta} - 2 \sum_{k>j} \Re[U^*_{\alpha k} U_{\beta k} U_{\alpha j} U^*_{\beta j}] \quad . \tag{A.2}
$$

Appendix B

Tables and Listings

Event Selection

In the event selection several different definitions for hits are used. These are listed here for clarification.

hit: A triggered single DOM.

hit map: All hits of one event.

waveform: The waveform is the digitized readout of the PMT.

pulse: A pulse is extracted from the recorded waveform or a hit DOM. It represents a reconstructed single photon.

pulse series: A series of pulses ectracted from the waveform of one hit.

pulse map: The extracted pulses of a complete event.

Table B.1: Event rates at different levels of the event selection. Two flavor neutrino oscillation is assumed with $\Delta m^2_{32} = 2.39 \cdot 10^{-3}$ and $\sin^2(2\theta_{23}) = 0.948$.

Level	$\frac{\nu_e^{\text{no osc.}}}{\text{mHz}}$	$\frac{\nu_\mu^{\text{no osc.}}}{\text{mHz}}$	$\frac{\nu_\mu^{\text{osc.}}}{\text{mHz}}$	$\frac{\nu_\tau^{\text{osc.}}}{\text{mHz}}$	$\frac{\mu_{\text{atm.}}^{\text{CORSIKA}}}{\text{mHz}}$	$\frac{\text{Data}}{\text{mHz}}$
DC filter	1.116	6.084	5.139	0.198	12343.786	17449.759
3	0.627	2.993	2.532	0.115	268.475	478.217
4	0.463	2.133	1.820	0.085	124.551	143.754
5	0.442	2.060	1.761	0.081	116.839	79.318
pre BDT	0.229	1.017	0.824	0.047	6.701	5.289
after BDT	0.113	0.534	0.409	0.028	0.063 (from 63 events)	0.647
final	0.009	0.073	0.057	0.002	0.009 (from 9 events)	0.067
final (hist)	0.006	0.051	0.037	0.002	0.005 (from 5 events)	0.043

Appendix C

Supplementary Figures

Event Selection

Figure C.1 shows the optimization process of the CRT cleaning which is explained in section 4.2.2. The cylindrical cleaning with six parameters only has a minimal advantage over the cleaning with four parameters.

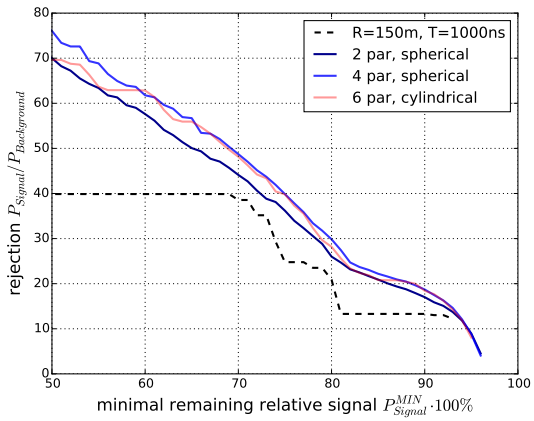

(a) Minimal remaining relative amount of signal events against possible rejection. Shown are three configurations with a different number of parameters and the standard configuration of IceCube (R = 150 m, T = 150 m). The parameters of the three configurations under test were left free. The curves show the best possible rejection for a given minimal amounbt of remaining signal events. The standard configuration is allways suboptimal.

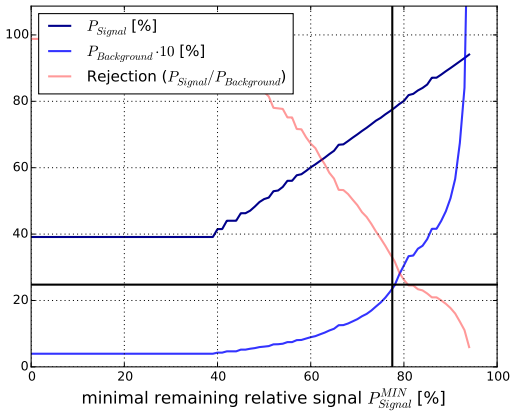

(b) Remaining relative amount of signal and background events and resulting rejection for a given minimal remaining relative amount of signal events. Used was a spherical cleaning configuration with four parameters ($R_{\mathrm{IC}}, T_{\mathrm{IC}}, R_{\mathrm{DC}}, T_{\mathrm{DC}}$). The rejection achived by the IceCube standard configuration and its amount of remaining relative signal is marked with the black lines.

Figure C.1: CRT Cleaning optimization for the usage with the CRT-Veto.

Rates

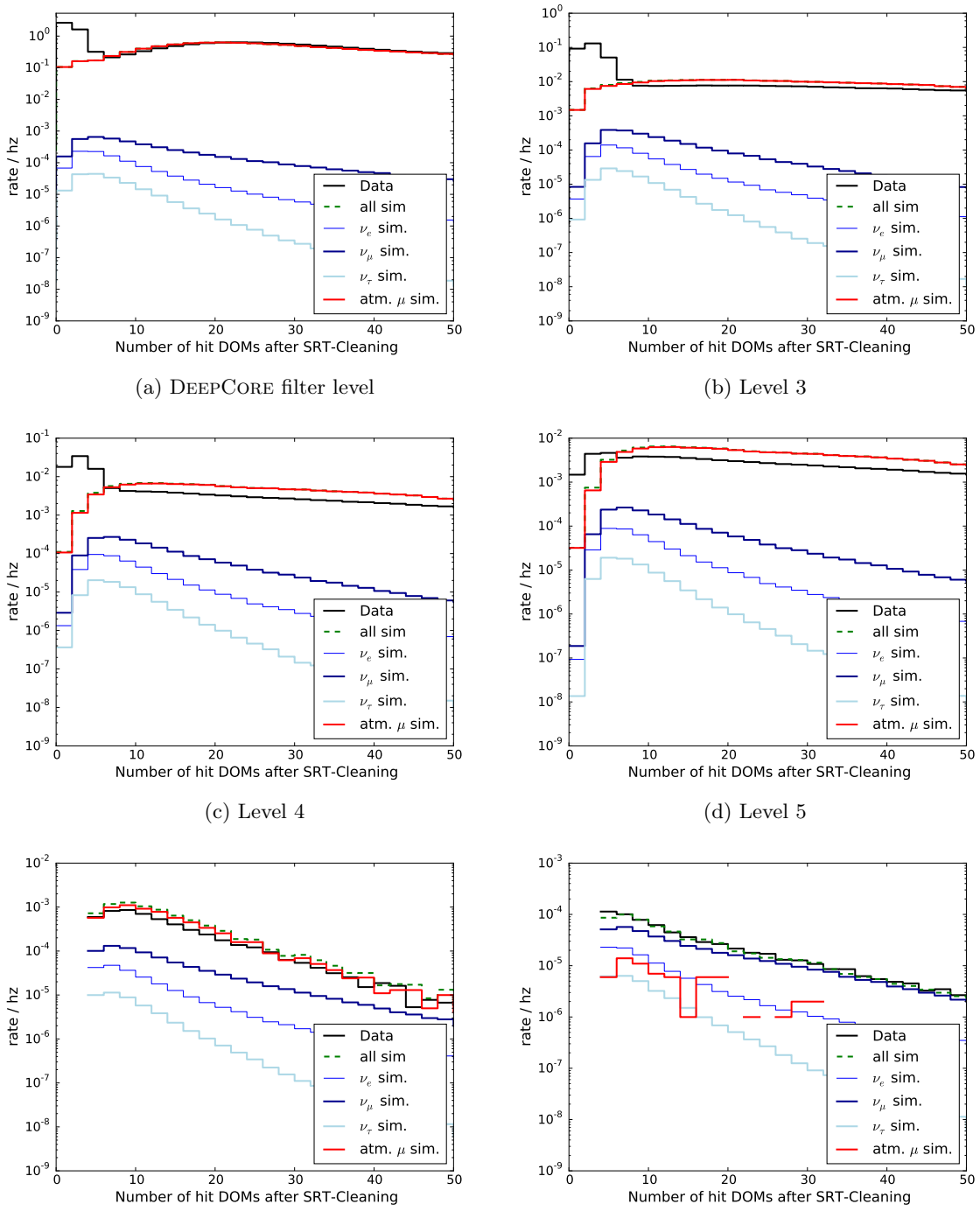

(a) DeepCore filter level

(b) Level 3

(c) Level 4

(d) Level 5

(e) PreBDT level

(f) after BDT

Figure C.2: Rates of data and simulation datasets against the number of hits per event at the different levels of the event selection. The pulse-map was processed with the SeededRT cleaning to remove pulses by detector noise. Two flavor neutrino oscillation is assumed with $\Delta m^2_{32} = 2.39 \cdot 10^{-3}$ and $\sin^2(2\theta_{23}) = 0.948$. The low energy GENIE simulations of ν_e and ν_μ are extended with high energy simulations generated with NuGen.

BDT Performance

The figures in this section show the distributions of variables used in the BDT of the event selection as described in section 4.5. The variable distributions are presented before and after the BDT selection was performed on the dataset. In the end of this section the overtraining check of the BDT is shown.

Variable distributions before BDT selection

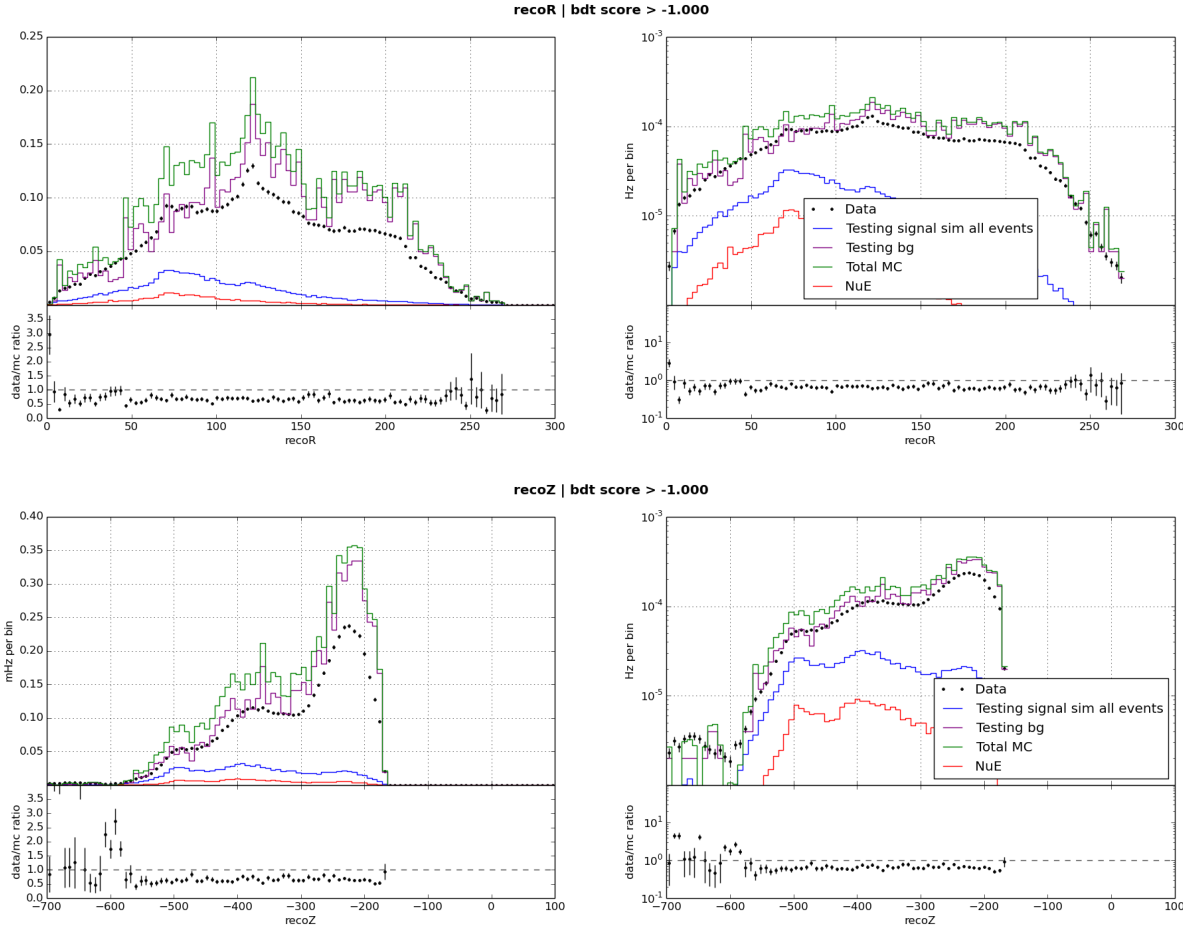

Figure C.3: Distributions of different variables before the BDT selection - Part 1

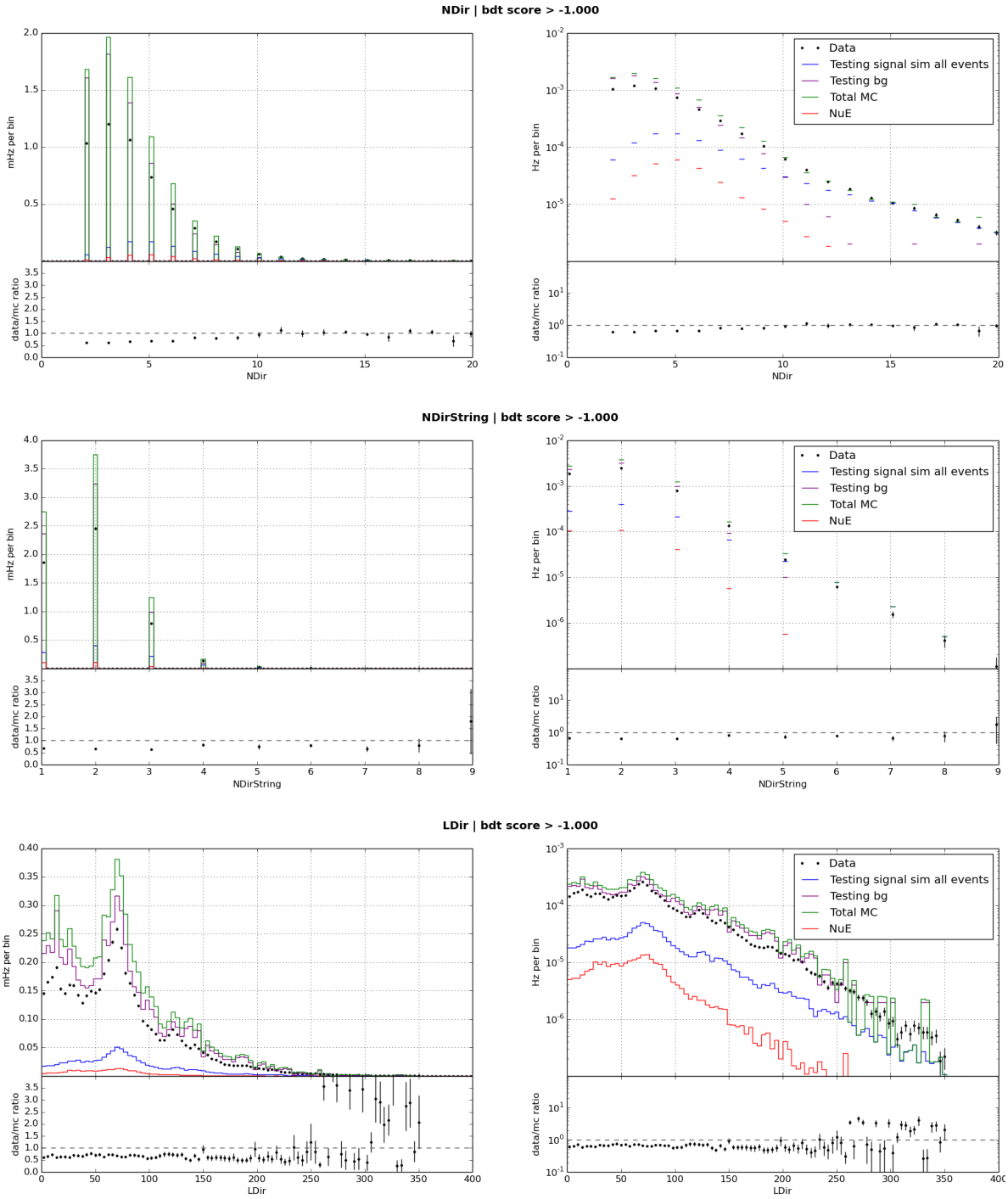

Figure C.4: Distributions of different variables before the BDT selection - Part 2

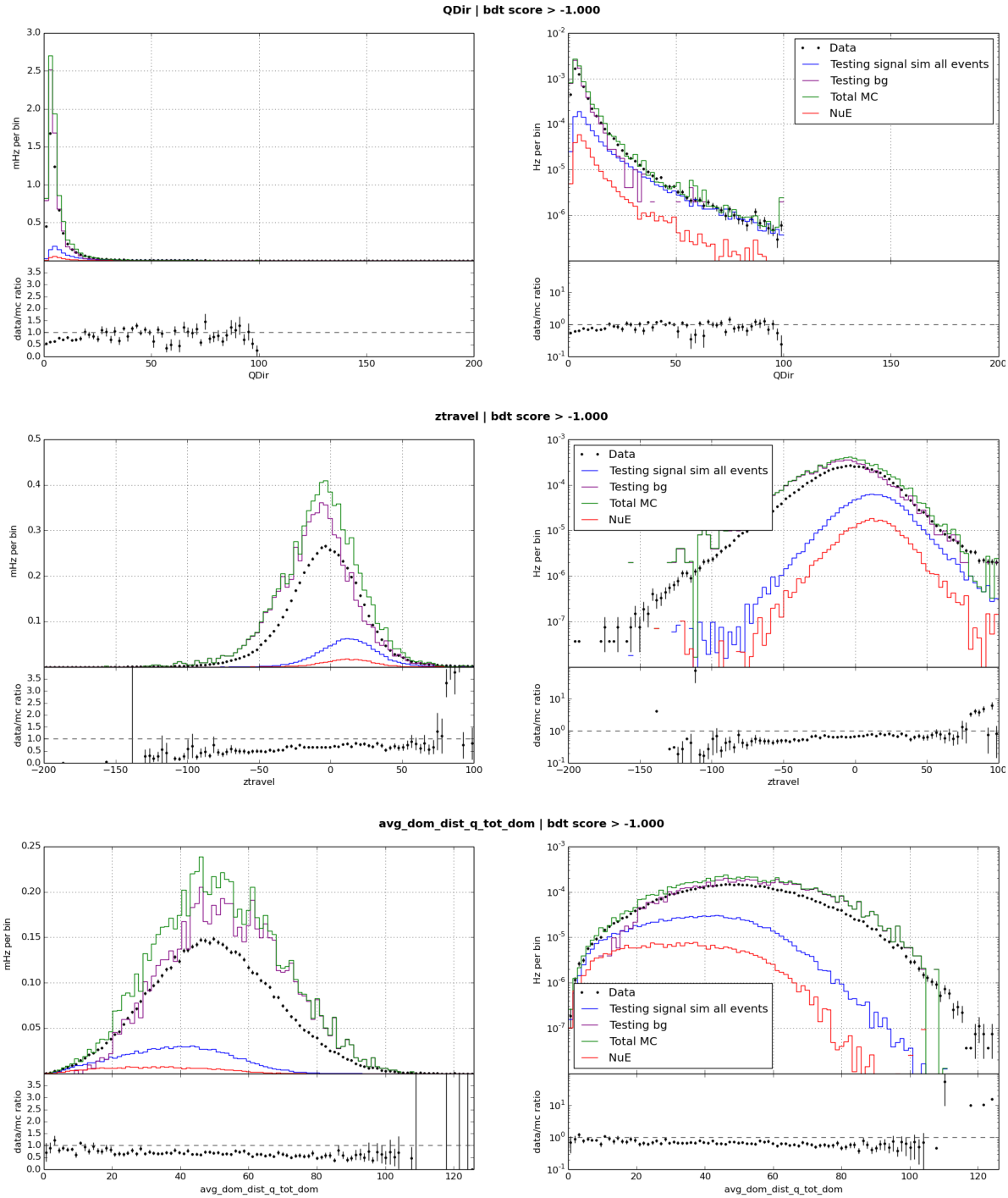

Figure C.5: Distributions of different variables before the BDT selection - Part 3

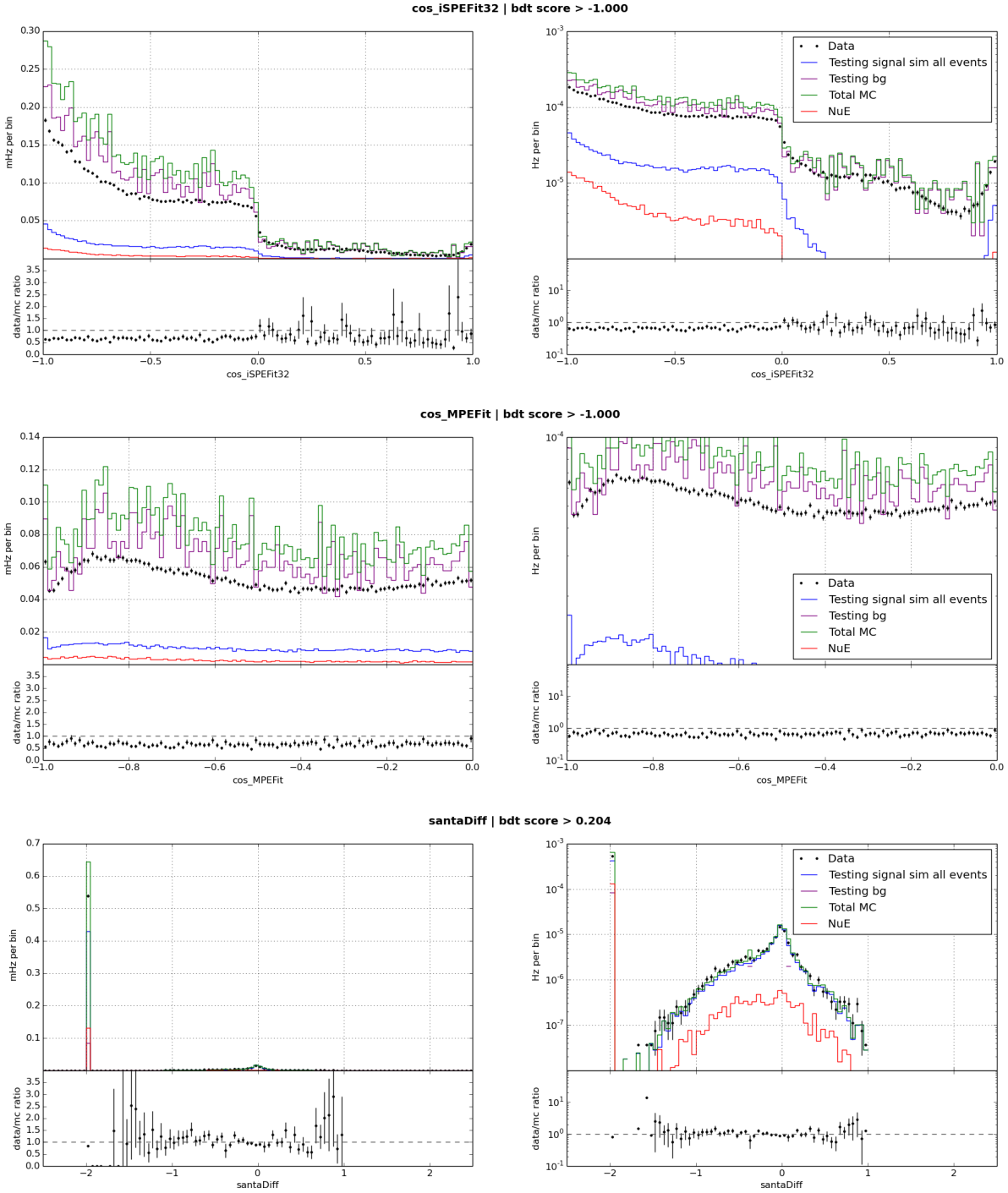

Figure C.6: Distributions of different variables before the BDT selection - Part 4

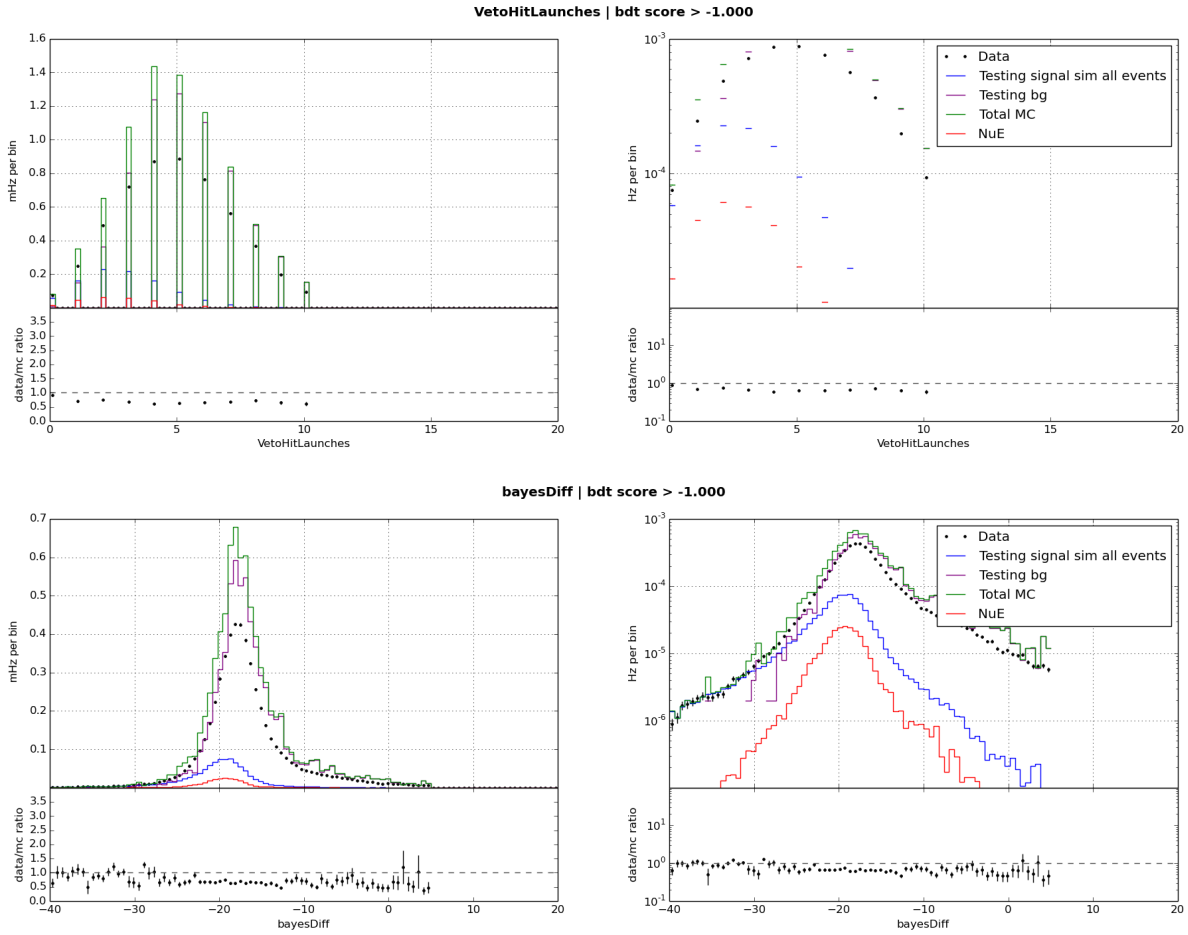

Figure C.7: Distributions of different variables before the BDT selection - Part 5

Variable Distributions After BDT Selection

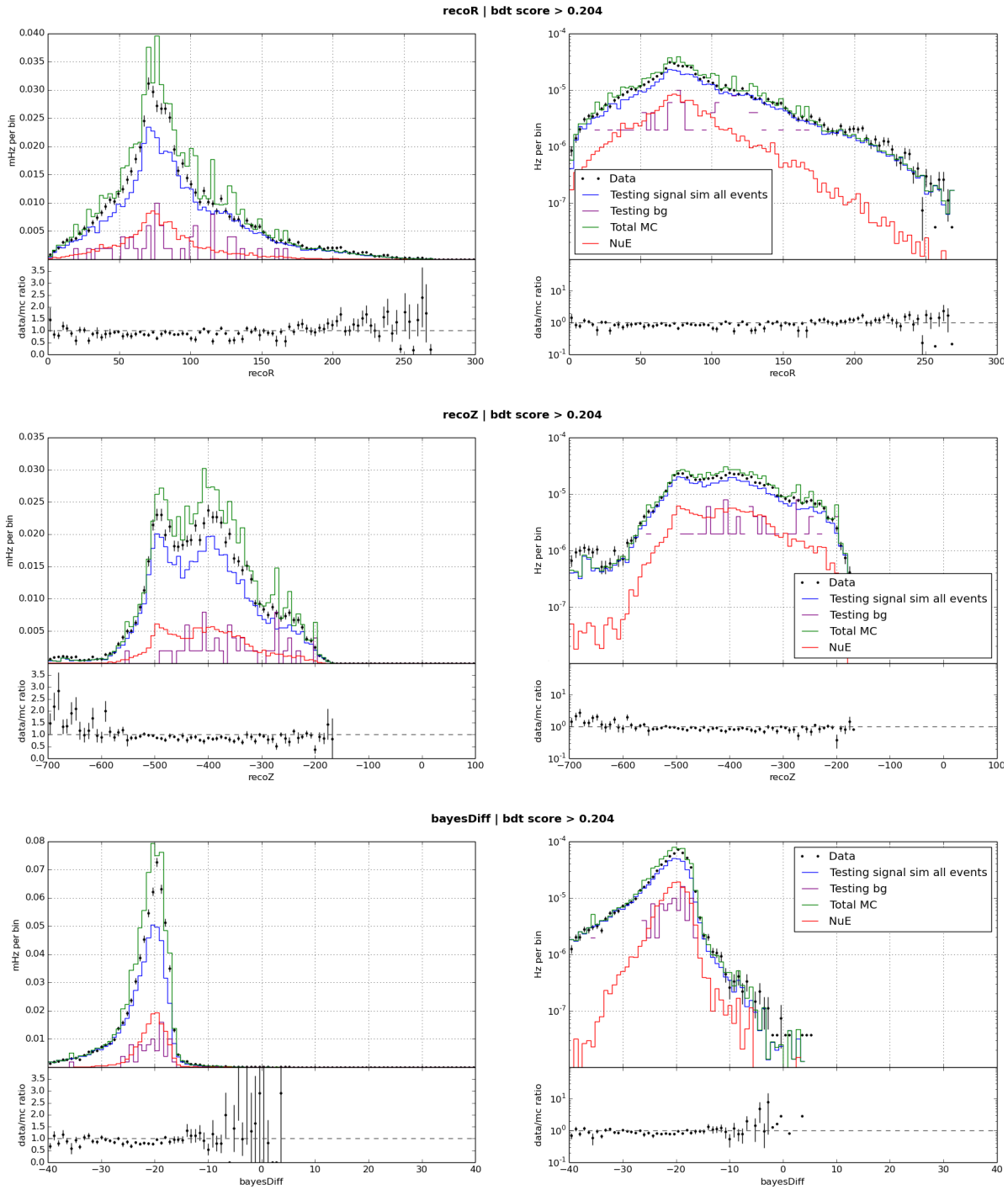

Figure C.8: Distributions of different variables after the BDT selection - Part 1

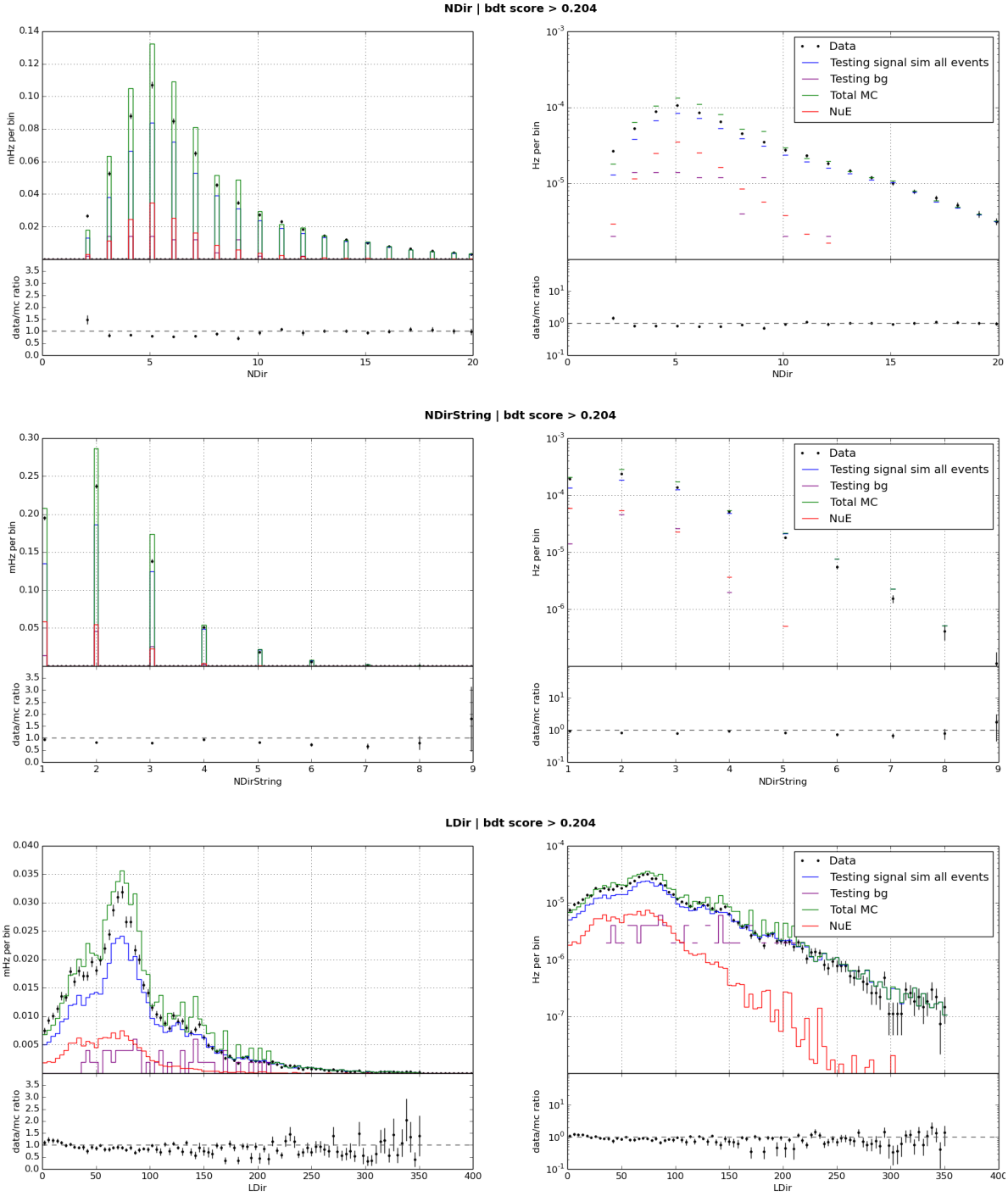

Figure C.9: Distributions of different variables after the BDT selection - Part 2

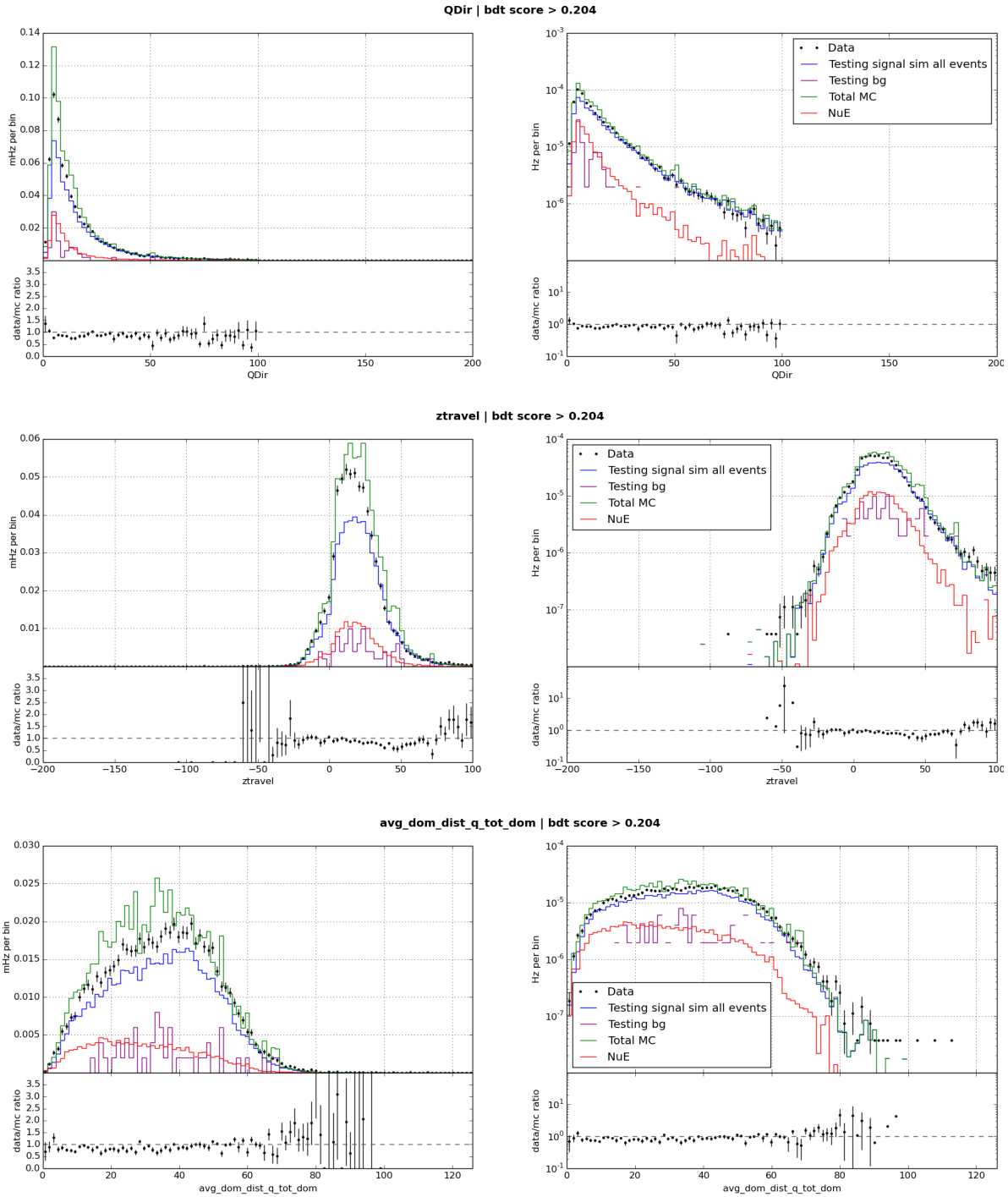

Figure C.10: Distributions of different variables after the BDT selection - Part 3

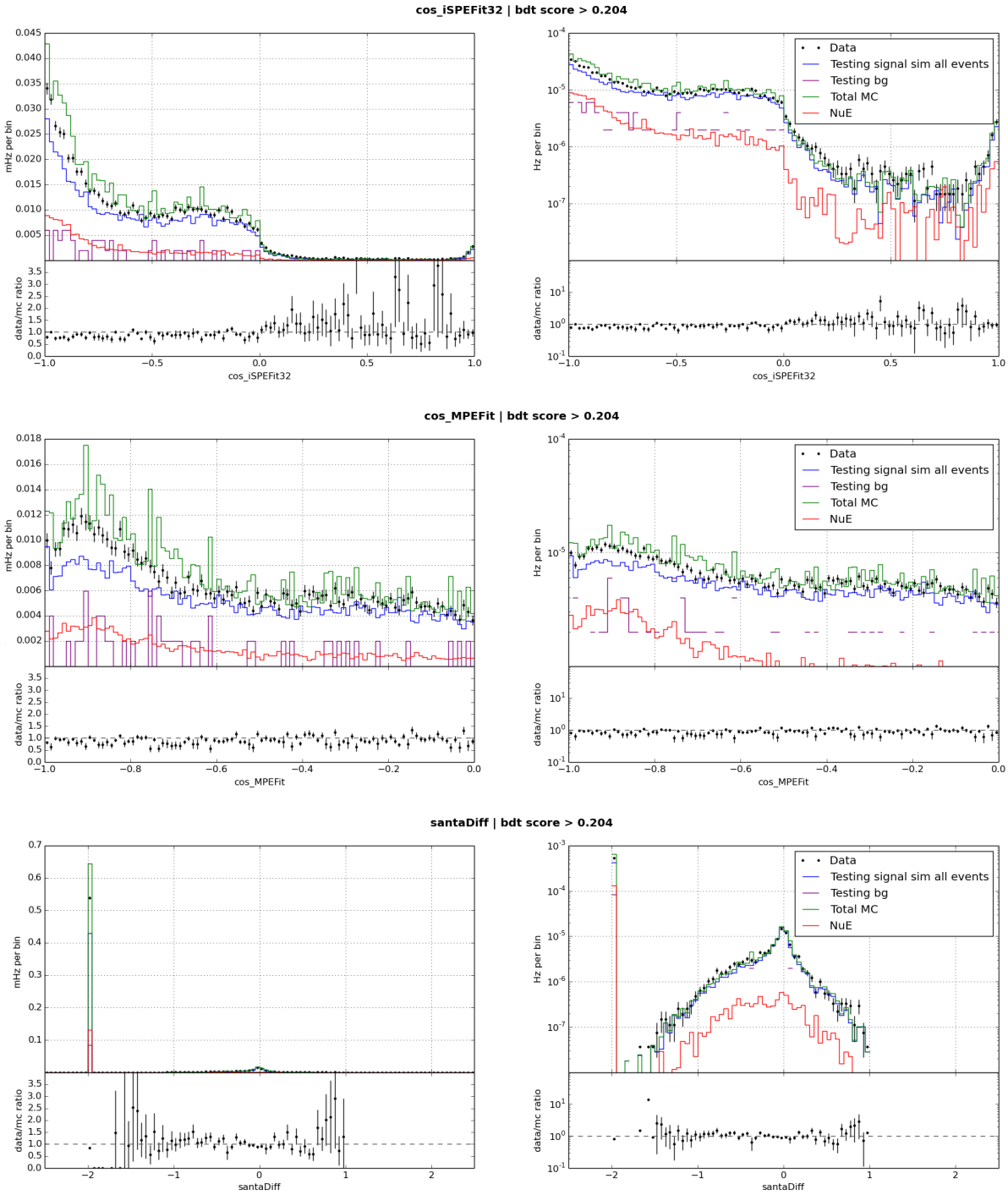

Figure C.11: Distributions of different variables after the BDT selection - Part 4

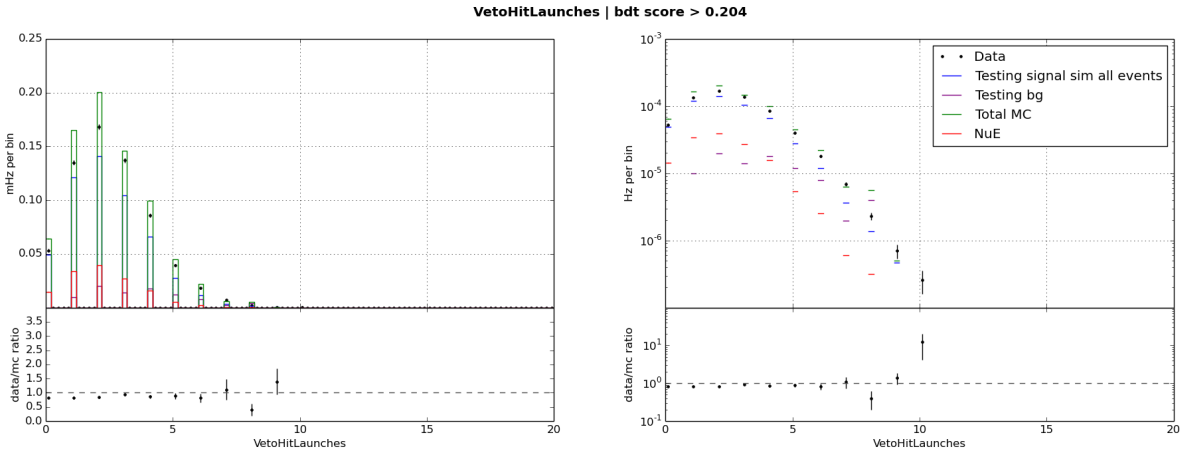

Figure C.12: Distributions of different variables after the BDT selection - Part 5

BDT Checks

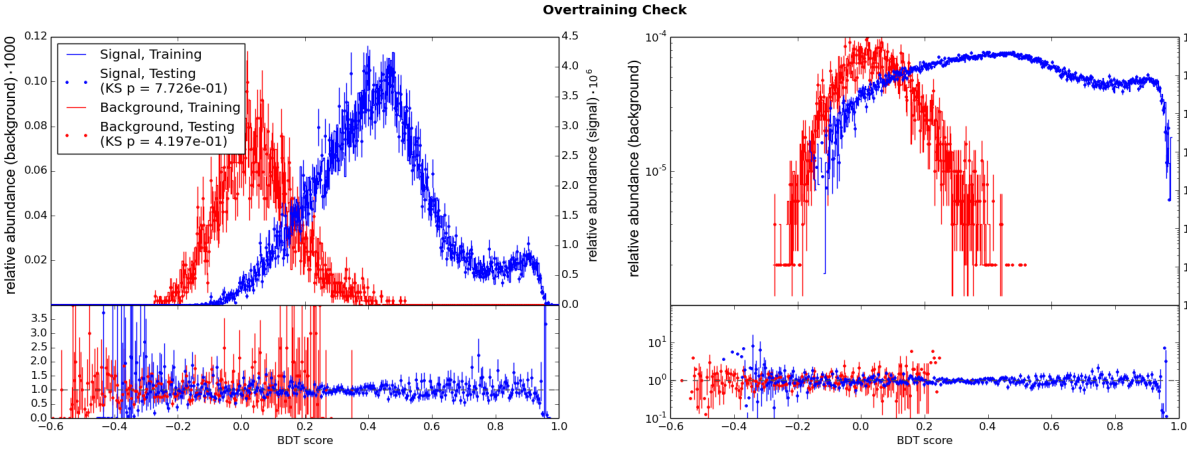

Figure C.13: Relative abundance against BDT score for training and testing datasets of signal and background. Left the linear scale and right the logarithmic scale is shown. The p value from the Kolmogorov-Smirnov (KS) test is good for both background and signal.

Reconstructions

This section presents supplemental figures for the zenith and energy reconstruction performance.

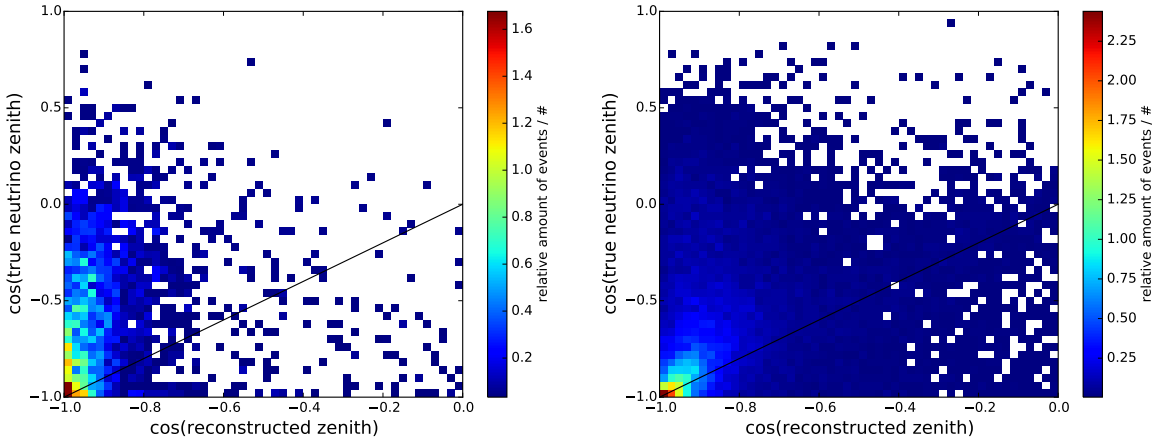

(a) $0.3 \leqq \log_{10}(E/\mathrm{GeV}) < 0.8$

(b) $0.8 \leqq \log_{10}(E/\mathrm{GeV}) < 1.3$

(c) $1.3 \leqq \log_{10}(E/\mathrm{GeV}) < 1.8$

(d) $1.8 \leqq \log_{10}(E/\mathrm{GeV}) < 2.3$

Figure C.14: Scatter plot of the cosine of the true zenith angle against the cosine of the zenith reconstructed with MPEFit for for different slices in simulated neutrino energy. The sample consists of muon neutrino events from a GENIE simulation at the final level of the event selection described in section 4.5. Events with $\cos(\theta_{\mathrm{MPEFit}}) > 0$ were removed from the sample.

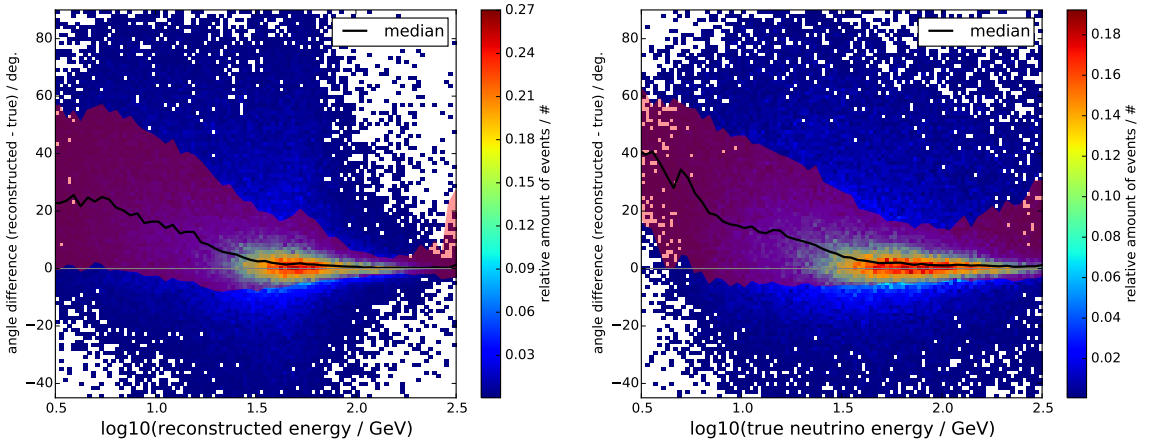

(a) agains reconstructed neutrino energy (b) agains true simulated neutrino energy

Figure C.15: Performance of the likelihood based reconstruction using the multi-photon PDF (MPEFit) for muon neutrino events from a GENIE simulation at the final level of the event selection described in section 4.5. Events with $\cos(\theta_{\mathrm{MPEFit}}) > 0$ were removed from the sample. The black line marks the median of the events, while the lower and upper edge of the red band mark 16 % and 84 % quantile.

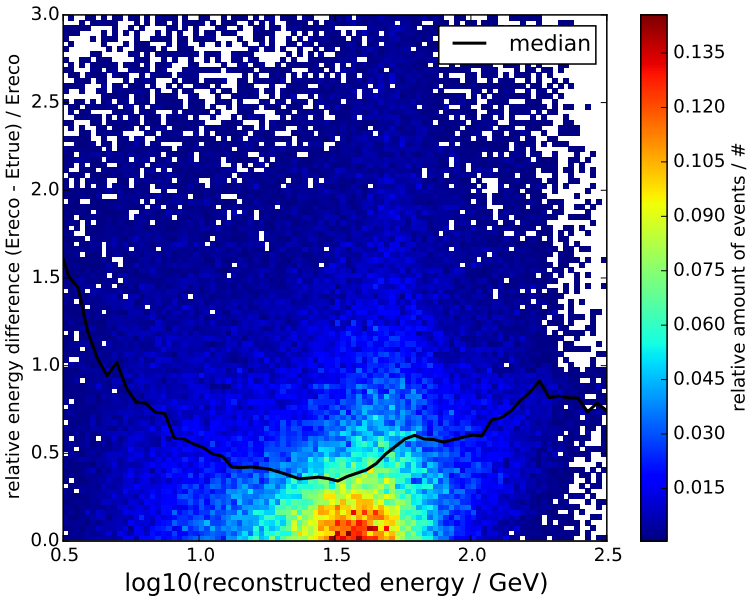

Figure C.16: Absolute relative difference between reconstructed and true energy against the reconstructed energy. The black line marks the median of the events, while the lower and upper edge of the red band mark 16 % and 84 % quantile. The events are from a muon neutrino dataset simulated with GENIE at the final level of the event selection described in section 4.5.

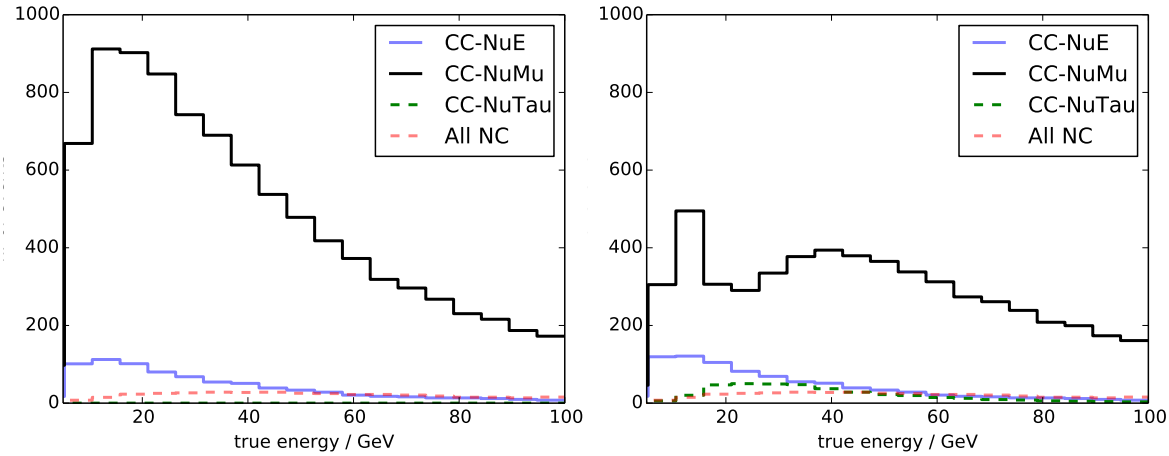

(a) no oscillation (b) oscillation

Figure C.17: The effect of ν_μ disappearance due to oscillation on the spectrum of true neutrino energy from simulations. NC events cannot be seperated in flavor and thus no oscillation effect is visible for these events.

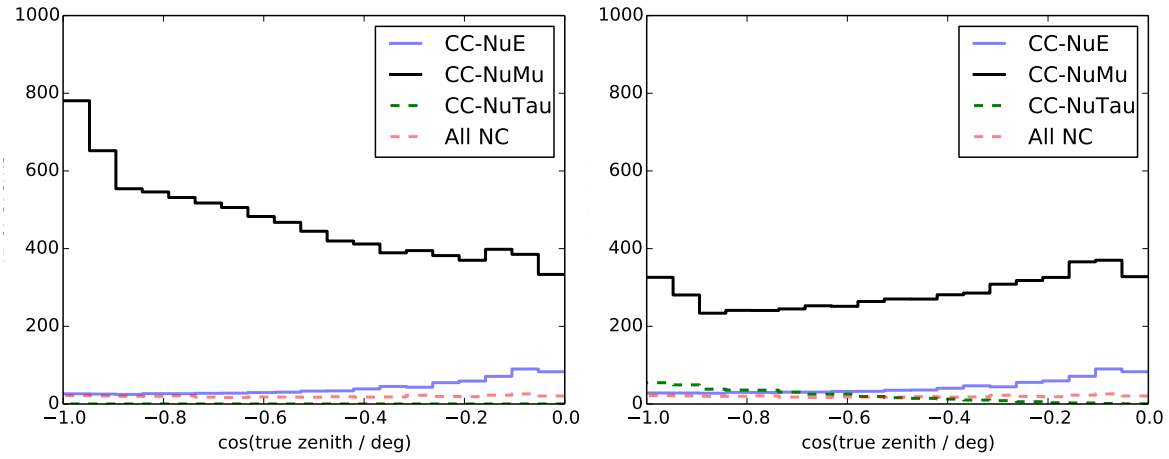

(a) no oscillation (b) oscillation

Figure C.18: The effect of ν_μ disappearance due to oscillation on the cosine of the true zenith direction from simulations. NC events cannot be seperated in flavor and thus no oscillation effect is visible for these events.

Results

Contours

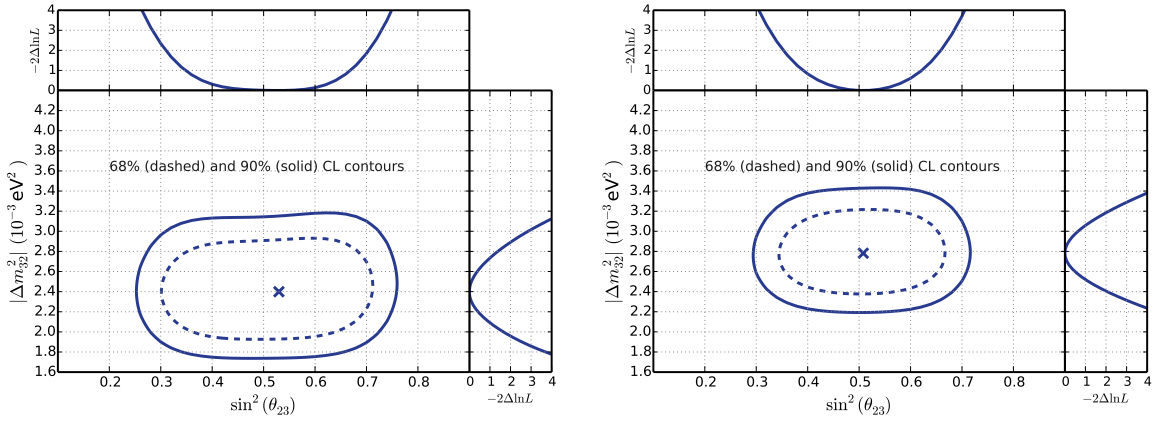

(a) first year of IC86 (b) second year of IC86

Figure C.19: Single year contours from parameter scans for three flavor oscillation, matter effects and normal hierarchy.

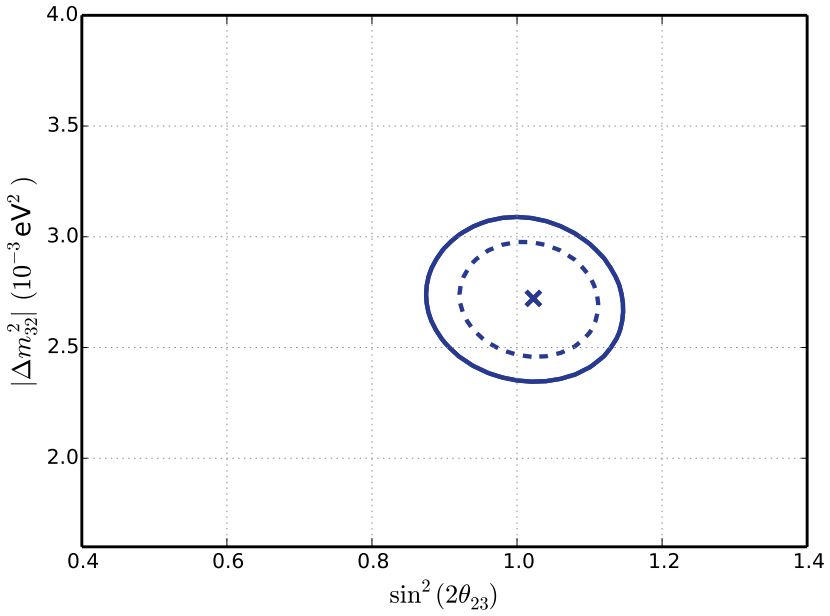

Figure C.20: Contour for a two flavor fit of the combined four years.

LE-Plots

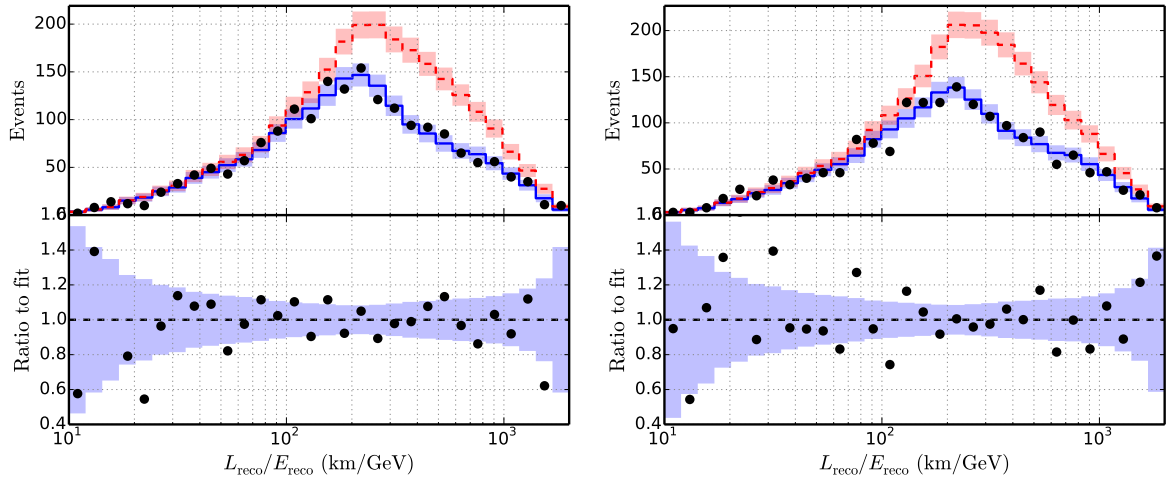

(a) first year of IC86

(b) second year of IC86

Figure C.21: L/E projection histogram of the events from data and expectation with the reconstructed propagation length divided by the reconstructed energy on the x-axis. The light blue band reflects the statistical uncertainty for the expected number of events. Shown are plots for fits on single years of data.

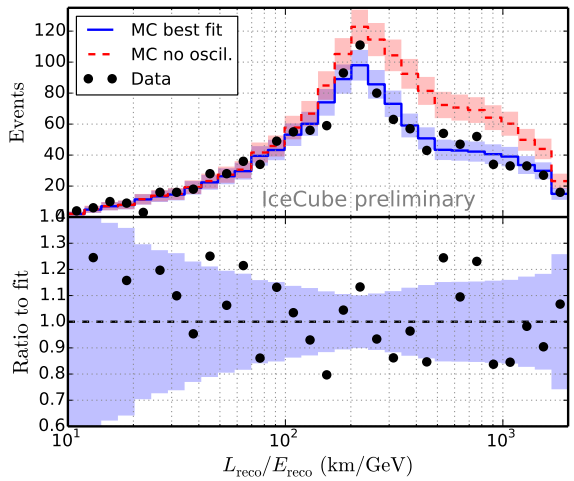

(a) IC79

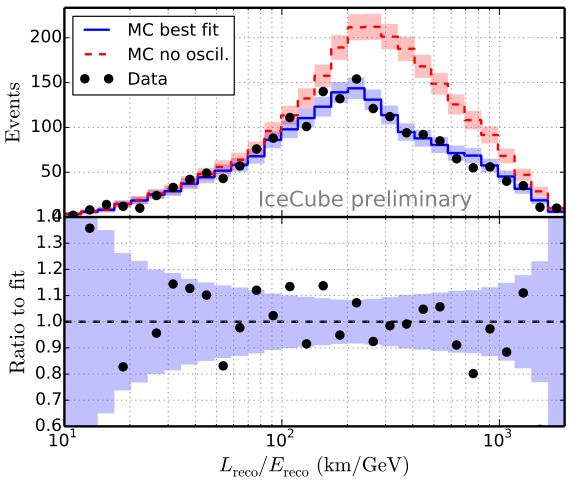

(b) first year of IC86

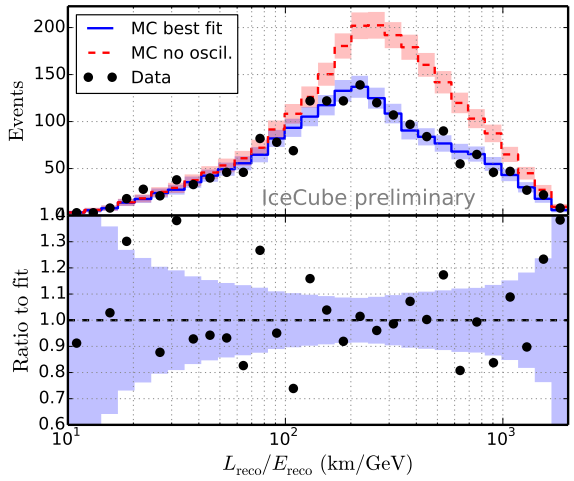

(c) second year of IC86

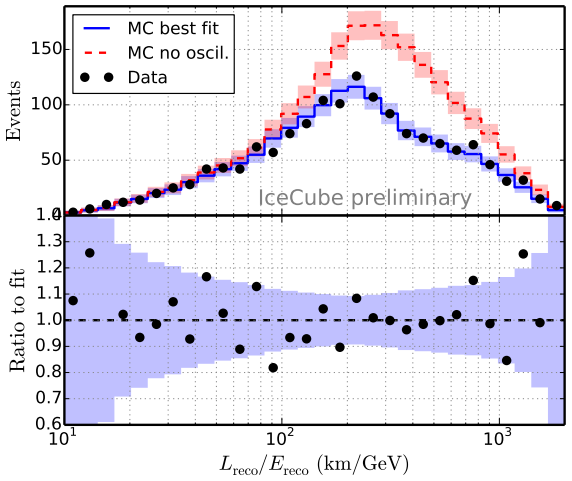

(d) third year of IC86

Figure C.22: L/E projection histograms of the events from data and expectation with the reconstructed propagation length divided by the reconstructed energy on the x-axis. The light blue band reflects the statistical uncertainty for the expected number of events. Shown are single years of data of the combined four year fit.

Systematic Impact of Parameters in the Fit

In the main part of this thesis the figures of the systematic impact of fit parameters is shown for only one year of the three IC86 datasets. The additional two years are presented in this appendix.

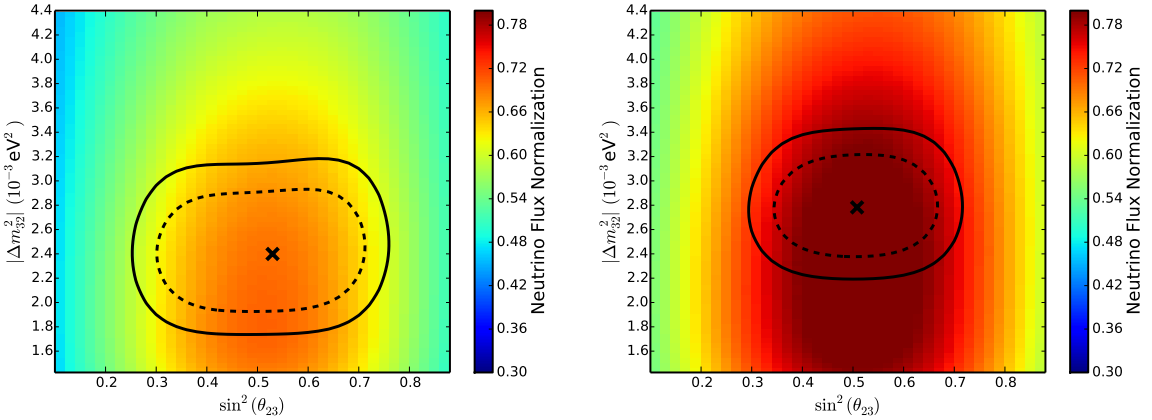

Figure C.23: The deviation from the initial neutrino normalization factor for a scan in $\sin^2(\theta_{23})$ and Δm^2_{32} for single years of data. The left plot shows the result for the single year of IC86-1, whereas the right plot shows the result for the single year of IC86-2 data. The best-fit is indicated by the black cross. Also depicted are the 68% C.L. (dashed black) and the 90% (solid black) contours for every year.

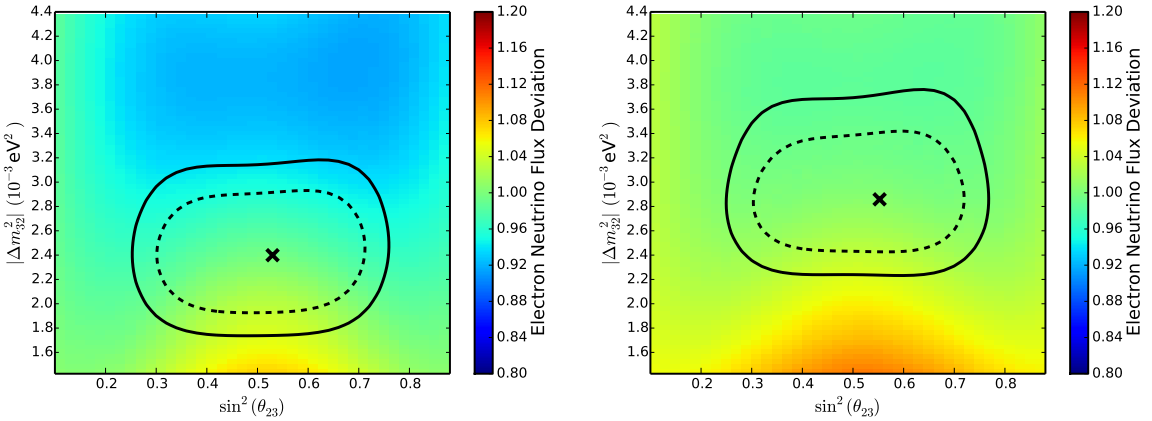

Figure C.24: The deviation of the ν_e-normalization factor from the total ν-normalization factor for a scan in $\sin^2(\theta_{23})$ and Δm^2_{32} for single years of data. The left plot shows the result for the single year of IC86-1, whereas the right plot shows the result for the single year of IC86-3 data. The best-fit is indicated by the black cross. Also depicted are the 68% C.L. (dashed black) and the 90% (solid black) contours for every year.

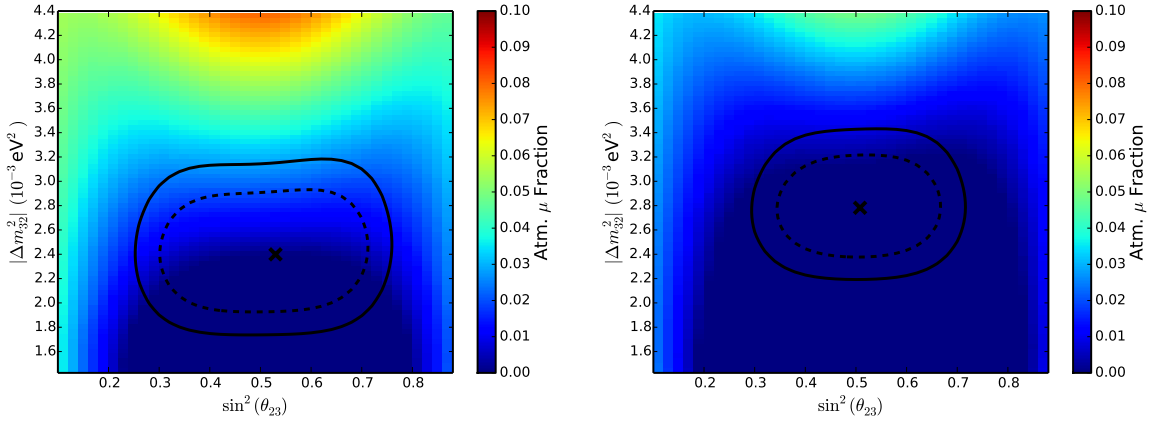

Figure C.25: The atmospheric muon fraction of the dataset for a scan in $\sin^2(\theta_{23})$ and Δm^2_{32} for single years of data. The left plot shows the result for the single year of IC86-1, whereas the right plot shows the result for the single year of IC86-2 data. The best-fit is indicated by the black cross. Also depicted are the 68% C.L. (dashed black) and the 90% (solid black) contours for every year.

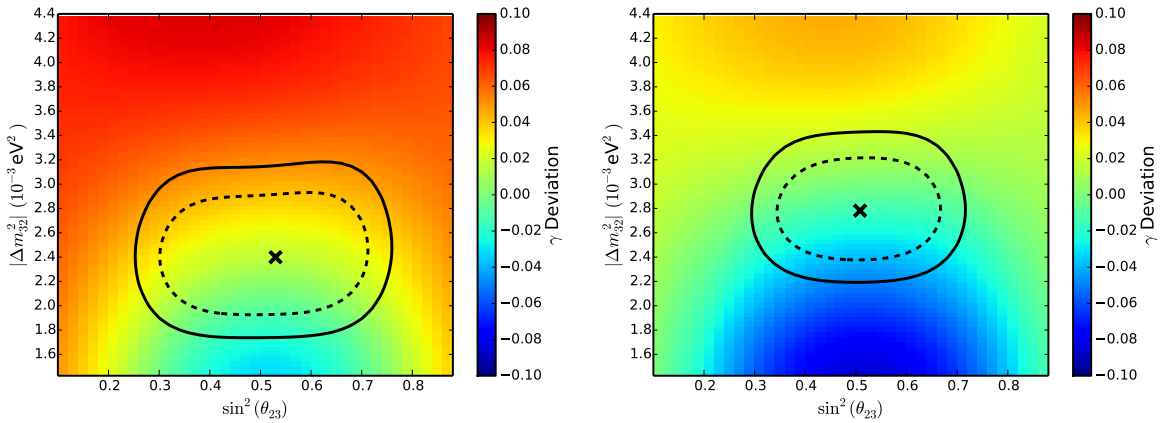

Figure C.26: The deviation from the initial value of the cosmic ray index (2.65) for a scan in $\sin^2(\theta_{23})$ and Δm^2_{32} for single years of data. The left plot shows the result for the single year of IC86-1, whereas the right plot shows the result for the single year of IC86-2 data. The best-fit is indicated by the black cross. Also depicted are the 68% C.L. (dashed black) and the 90% (solid black) contours for every year.

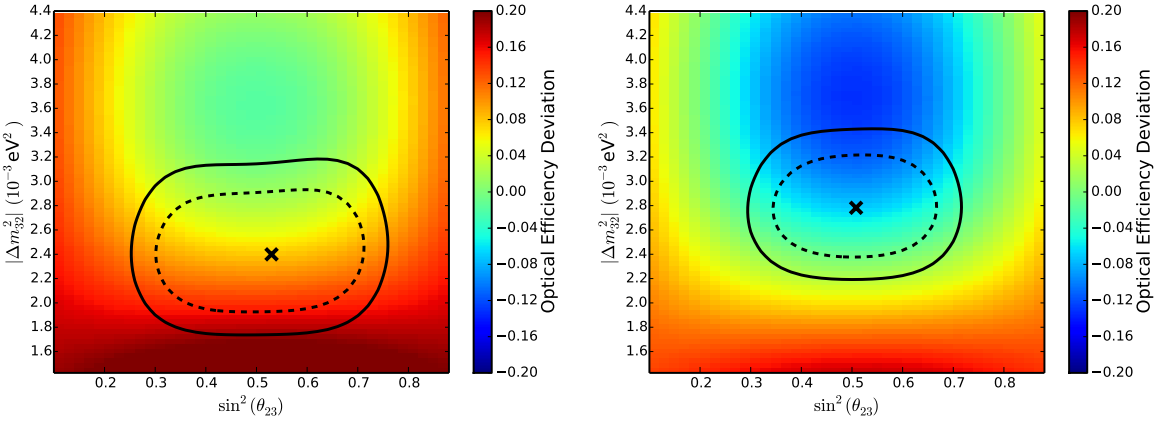

Figure C.27: The deviation from the initial optical efficiency factor (0.99) for a scan in $\sin^2(\theta_{23})$ and Δm^2_{32} for single years of data. The left plot shows the result for the single year of IC86-1, whereas the right plot shows the result for the single year of IC86-2 data. The best-fit is indicated by the black cross. Also depicted are the 68% C.L. (dashed black) and the 90% (solid black) contours for every year.

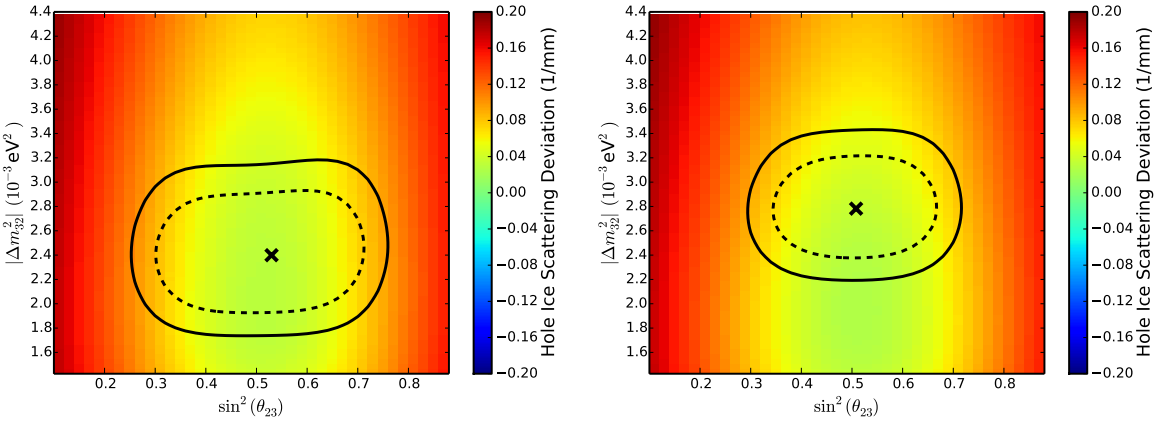

Figure C.28: The deviation to the initial photon scattering length in the refrozen ice columns for a scan in $\sin^2(\theta_{23})$ and Δm^2_{32} for single years of data. The left plot shows the result for the single year of IC86-1, whereas the right plot shows the result for the single year of IC86-2 data. The best-fit is indicated by the black cross. Also depicted are the 68% C.L. (dashed black) and the 90% (solid black) contours for every year.

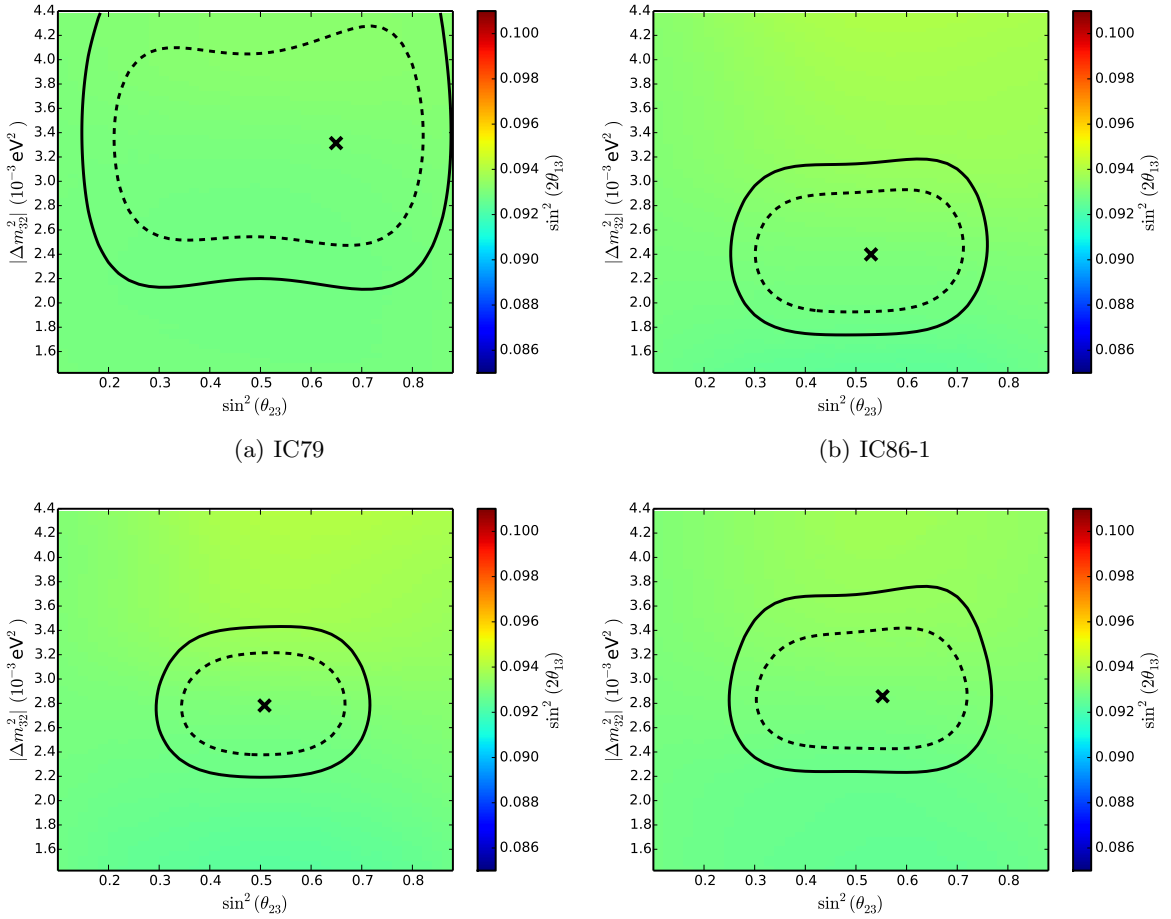

(a) IC79

(b) IC86-1

(c) IC86-2

(d) IC86-3

Figure C.29: The deviation from the initial value for θ_{13} for a scan in $\sin^2(\theta_{23})$ and Δm^2_{32} for single years of data. The plots show single years of data. The best-fit is indicated by the black cross. Also depicted are the 68% C.L. (dashed black) and the 90% (solid black) contours for every year.

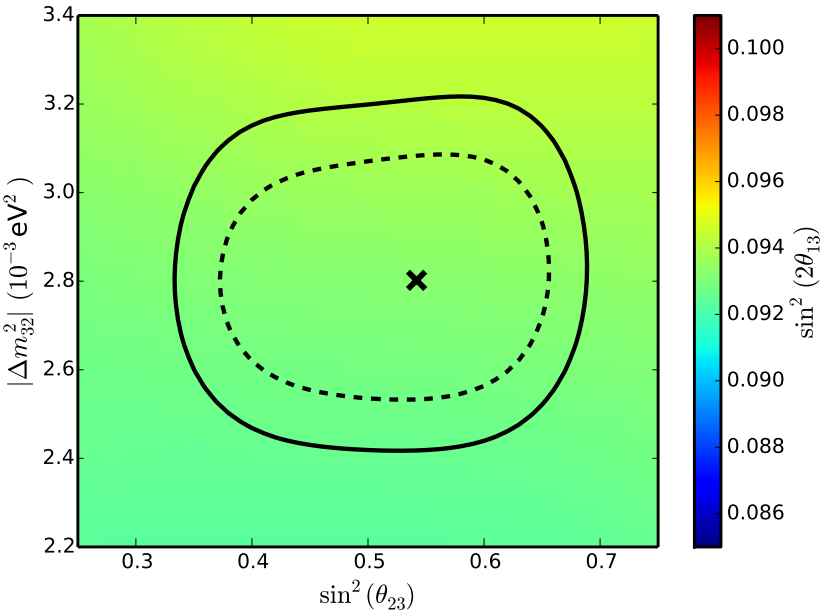

Figure C.30: The deviation from the initial value for θ_{13} for a scan in $\sin^2(\theta_{23})$ and Δm^2_{32} for the combined fit with four years of data. The best-fit is indicated by the black cross. Also depicted are the 68% C.L. (dashed black) and the 90% (solid black) of the fit.

Bibliography

[1] Wolfgang Pauli. *Wissenschaftlicher Briefwechsel mit Bohr, Einstein, Heisenberg u.a. Band II: 1930-1939*. Springer-Verlag, 2008.

[2] C. L. Cowan, F. Reines, F. B. Harrison, H. W. Kruse, and A. D. McGuire. Detection of the free neutrino: a confirmation. *Science*, 124(3212):103–104, 1956.

[3] G. Danby, J. M. Gaillard, Konstantin A. Goulianos, L. M. Lederman, Nari B. Mistry, M. Schwartz, and J. Steinberger. Observation of High-Energy Neutrino Reactions and the Existence of Two Kinds of Neutrinos. *Phys. Rev. Lett.*, 9:36–44, 1962.

[4] K. Kodama et al. Observation of tau neutrino interactions. *Phys. Lett.*, B504:218–224, 2001.

[5] Donato Di Ferdinando. Nuclear emulsions in the OPERA experiment. *Radiat. Meas.*, 44:840–845, 2009.

[6] K. Zuber. *Neutrino Physics*. Series in High Energy Physics, Cosmology and Gravitation. CRC Press, 2003.

[7] MissMJ. Standard Model of Elementary Particles. `https://upload.wikimedia.org/wikipedia/commons/0/00/Standard_Model_of_Elementary_Particles.svg`, 2006.

[8] S. Schael et al. Precision electroweak measurements on the Z resonance. *Phys. Rept.*, 427:257–454, 2006.

[9] J. Angrik et al. KATRIN design report 2004. 2005.

[10] J. A. Formaggio and G. P. Zeller. From eV to EeV: Neutrino-Cross Sections Across Energy Scales. *Rev. Mod. Phys.*, 84:1307, 2012.

[11] K. A. Olive et al. Review of Particle Physics. *Chin. Phys.*, C38:090001, 2014.

[12] D. Casper. The Nuance neutrino physics simulation, and the future. *Nucl. Phys. Proc. Suppl.*, 112:161–170, 2002. [,161(2002)].

[13] James Bjorken. Current algebra at small distances. *SLAC-PUB*, 0338, 1967.

[14] Sheldon L. Glashow. Resonant scattering of antineutrinos. *Phys. Rev.*, 118:316–317, Apr 1960.

[15] Rabindra N. Mohapatra and Palash B. Pal. *Massive Neutrinos in Physics and Astrophysics, Third Edition (World Scientific Lecture Notes in Physics, Vol. 72)*. World Scientific Publishing Company, 2004.

[16] Norbert Schmitz. *Neutrinophysik (Teubner Studienbücher Physik) (German Edition)*. Vieweg+Teubner Verlag, 1997.

[17] Ettore Majorana and Luciano Maiani. *Ettore Majorana Scientific Papers: On occasion of the centenary of his birth*, chapter A symmetric theory of electrons and positrons, pages 201–233. Springer Berlin Heidelberg, Berlin, Heidelberg, 2006.

[18] C. Giunti and C.W. Kim. *Fundamentals of Neutrino Physics and Astrophysics*. OUP Oxford, 2007.

[19] K. Daum et al. Determination of the atmospheric neutrino spectra with the fréjus detector. *Zeitschrift für Physik C Particles and Fields*, 66(3):417–428, 1995.

[20] J. W. Cronin, T. K. Gaisser, and S. P. Swordy. Cosmic Rays at the Energy Frontier. *Scientific American*, 276:44–49, January 1997.

[21] Claus Grupen. *Astroparticle Physics*. Springer Berlin Heidelberg, 2005.

[22] E. Fermi. On the Origin of the Cosmic Radiation. *Phys. Rev.*, 75:1169–1174, Apr 1949.

[23] T. Gaisser. *Cosmic Rays and Particle Physics*. Cambridge University Press, Cambridge, 1999.

[24] T. Stanev. *High Energy Cosmic Rays*. Springer Verlag, second edition, 2010.

[25] Peter K. F. Grieder. *Extensive Air Showers: High Energy Phenomena and Astrophysical Aspects - A Tutorial, Reference Manual and Data Book (Astrophysics and Space Science Library)*. Springer, 2011.

[26] Atmospheric Neutrino Flux Tables for One-Year-Average (HAKKM, 2014). `http://www.icrr.u-tokyo.ac.jp/~mhonda/nflx2014/index.html`, 2014. [Online; accessed 29-June-2016].

[27] M. Honda, M. Sajjad Athar, T. Kajita, K. Kasahara, and S. Midorikawa. Atmospheric neutrino flux calculation using the nrlmsise-00 atmospheric model. *Phys. Rev. D*, 92:023004, Jul 2015.

[28] B. Pontecorvo. Neutrino Experiments and the Problem of Conservation of Leptonic Charge. *Sov. Phys. JETP*, 26:984–988, 1968. [Zh. Eksp. Teor. Fiz.53,1717(1967)].

[29] Serguei Chatrchyan et al. Observation of a new boson at a mass of 125 GeV with the CMS experiment at the LHC. *Phys. Lett.*, B716:30–61, 2012.

[30] Georges Aad et al. Observation of a new particle in the search for the Standard Model Higgs boson with the ATLAS detector at the LHC. *Phys. Lett.*, B716:1–29, 2012.

[31] Y. Fukuda et al. Evidence for oscillation of atmospheric neutrinos. *Phys. Rev. Lett.*, 81:1562–1567, 1998.

[32] Q. R. Ahmad et al. Measurement of the rate of $\nu_e + d \rightarrow p + p + e^-$ interactions produced by ^8B solar neutrinos at the Sudbury Neutrino Observatory. *Phys. Rev. Lett.*, 87:071301, 2001.

[33] The Royal Swedish Academy Of Sciences. Scientific Background on the Nobel Prize in Physics 2015 - Neutrino Oscillations. `https://www.nobelprize.org/nobel_prizes/physics/laureates/2015/advanced-physicsprize2015.pdf`, 2015.

[34] John N. Bahcall, Aldo M. Serenelli, and Sarbani Basu. New solar opacities, abundances, helioseismology, and neutrino fluxes. *Astrophys. J.*, 621:L85–L88, 2005.

[35] Bruce T. Cleveland, Timothy Daily, Jr. Raymond Davis, James R. Distel, Kenneth Lande, C. K. Lee, Paul S. Wildenhain, and Jack Ullman. Measurement of the solar electron neutrino flux with the homestake chlorine detector. *The Astrophysical Journal*, 496(1):505, 1998.

[36] Raymond Davis. Solar neutrinos. ii. experimental. *Phys. Rev. Lett.*, 12:303–305, Mar 1964.

[37] P. Anselmann et al. Solar neutrinos observed by GALLEX at Gran Sasso. *Phys. Lett.*, B285:376–389, 1992.

[38] M. Cribier. Results of the whole GALLEX experiment. *Nucl. Phys. Proc. Suppl.*, 70:284–291, 1999.

[39] N. Ferrari. GNO and its performances. *Nucl. Phys. Proc. Suppl.*, 100:48–50, 2001.

[40] A. I. Abazov et al. Search for neutrinos from the sun using the reaction $^{71}\mathrm{Ga}(\nu_e,e^-)^{71}\mathrm{ge}$. *Phys. Rev. Lett.*, 67:3332–3335, Dec 1991.

[41] S. Fukuda et al. The Super-Kamiokande Detector. *Nuclear Instruments and Methods in Physics Research Section A: Accelerators, Spectrometers, Detectors and Associated Equipment*, 501(23):418 – 462, 2003.

[42] J. Hosaka et al. Solar neutrino measurements in super-kamiokande-i. *Phys. Rev. D*, 73:112001, Jun 2006.

[43] J. P. Cravens et al. Solar neutrino measurements in super-kamiokande-ii. *Phys. Rev. D*, 78:032002, Aug 2008.

[44] K. Abe et al. Solar neutrino results in super-kamiokande-iii. *Phys. Rev. D*, 83:052010, Mar 2011.

[45] J. Boger et al. The Sudbury neutrino observatory. *Nucl. Instrum. Meth.*, A449:172–207, 2000.

[46] C. Athanassopoulos et al. The Liquid scintillator neutrino detector and LAMPF neutrino source. *Nucl. Instrum. Meth.*, A388:149–172, 1997.

[47] A. Aguilar et al. Evidence for neutrino oscillations from the observation of $\overline{\nu}_e$ appearance in a $\overline{\nu}_\mu$ beam. *Phys. Rev. D*, 64:112007, Nov 2001.

[48] C. Athanassopoulos et al. Candidate events in a search for $\overline{\nu}_\mu \to \overline{\nu}_e$ oscillations. *Phys. Rev. Lett.*, 75:2650–2653, Oct 1995.

[49] C. Athanassopoulos et al. Evidence for $\overline{\nu}_\mu \to \overline{\nu}_e$ oscillations from the lsnd experiment at the los alamos meson physics facility. *Phys. Rev. Lett.*, 77:3082–3085, Oct 1996.

[50] C. Athanassopoulos et al. Results on $\nu_\mu \to \nu_e$ neutrino oscillations from the lsnd experiment. *Phys. Rev. Lett.*, 81:1774–1777, Aug 1998.

[51] C. Athanassopoulos et al. Results on $\nu_\mu \to \nu_e$ oscillations from pion decay in flight neutrinos. *Phys. Rev. C*, 58:2489–2511, Oct 1998.

[52] K. Eitel. The KARMEN search for appearance of anti-nu/e's. *Prog. Part. Nucl. Phys.*, 48:89–98, 2002. [,89(2002)].

[53] A. A. Aguilar-Arevalo et al. Improved Search for $\bar{\nu}_\mu \to \bar{\nu}_e$ Oscillations in the MiniBooNE Experiment. *Phys. Rev. Lett.*, 110:161801, 2013.

[54] Shalom Eliezer and Arthur R. Swift. Experimental consequences of e mixing in neutrino beams. *Nuclear Physics B*, 105(1):45 – 51, 1976.

[55] Harald Fritzsch and Peter Minkowski. Vector-Like Weak Currents, Massive Neutrinos, and Neutrino Beam Oscillations. *Phys. Lett.*, B62:72, 1976.

[56] S.M. Bilenky and B. Pontecorvo. Lepton mixing and neutrino oscillations. *Physics Reports*, 41(4):225 – 261, 1978.

[57] S. Nussinov. Solar Neutrinos and Neutrino Mixing. *Phys. Lett.*, B63:201–203, 1976.

[58] Boris Kayser. On the quantum mechanics of neutrino oscillation. *Phys. Rev. D*, 24:110–116, Jul 1981.

[59] J. Rich. The Quantum mechanics of neutrino oscillations. *Phys. Rev.*, D48:4318–4325, 1993.

[60] L. Wolfenstein. Neutrino Oscillations in Matter. *Phys. Rev.*, D17:2369–2374, 1978.

[61] Samoil Bilenky. *Introduction to the Physics of Massive and Mixed Neutrinos (Lecture Notes in Physics)*. Springer, 2010.

[62] Marius Wallraff and Christopher Wiebusch. Calculation of oscillation probabilities of atmospheric neutrinos using nuCraft. *Comput. Phys. Commun.*, 197:185–189, 2015.

[63] Adam M. Dziewonski and Don L. Anderson. Preliminary reference earth model. *Physics of the Earth and Planetary Interiors*, 25(4):297 – 356, 1981.

[64] S. P. Mikheev and A. Yu. Smirnov. Resonance Amplification of Oscillations in Matter and Spectroscopy of Solar Neutrinos. *Sov. J. Nucl. Phys.*, 42:913–917, 1985. [Yad. Fiz.42,1441(1985)].

[65] S. P. Mikheev and A. Yu. Smirnov. Resonant amplification of neutrino oscillations in matter and solar neutrino spectroscopy. *Nuovo Cim.*, C9:17–26, 1986.

[66] T. K. Kuo and James Pantaleone. Neutrino oscillations in matter. *Rev. Mod. Phys.*, 61:937–979, Oct 1989.

[67] Frank D. Stacey and Paul M. Davis. *Physics of the Earth*. Cambridge University Press, 2008.

[68] B. L. N. Kennett and E. R. Engdahl. Traveltimes for global earthquake location and phase identification. *Geophysical Journal International*, 105(2):429–465, 1991.

[69] Evgeny K. Akhmedov and M. Yu. Khlopov. Resonant Enhancement of Neutrino Oscillations in Longitudinal Magnetic Field. *Sov. J. Nucl. Phys.*, 47:689–691, 1988. [Yad. Fiz.47,1079(1988)].

[70] Evgeny K. Akhmedov. Parametric resonance in neutrino oscillations in matter. *Pramana*, 54:47–63, 2000.

[71] Evgeny K. Akhmedov. Parametric resonance of neutrino oscillations and passage of solar and atmospheric neutrinos through the earth. *Nucl. Phys.*, B538:25–51, 1999.

[72] R. B. Patterson. Prospects for Measurement of the Neutrino Mass Hierarchy. *Ann. Rev. Nucl. Part. Sci.*, 65:177–192, 2015.

[73] Francis Halzen and Spencer R. Klein. IceCube: An Instrument for Neutrino Astronomy. *Rev. Sci. Instrum.*, 81:081101, 2010.

[74] M. G. Aartsen et al. Measurement of Atmospheric Neutrino Oscillations with IceCube. *Phys. Rev. Lett.*, 111(8):081801, 2013.

[75] M.G. Aartsen et al. Determining neutrino oscillation parameters from atmospheric muon neutrino disappearance with three years of IceCube DeepCore data. *Phys. Rev.*, D91(7):072004, 2015.

[76] M. Ageron et al. ANTARES: The First Undersea Neutrino Telescope. *Nucl.Instrum.Meth.*, A656:11–38, 2011.

[77] S. Adrin-Martnez and other. Measurement of atmospheric neutrino oscillations with the {ANTARES} neutrino telescope. *Physics Letters B*, 714(25):224 – 230, 2012.

[78] K. Abe et al. The T2K Experiment. *Nucl. Instrum. Meth.*, A659:106–135, 2011.

[79] M. G. Aartsen et al. Letter of Intent: The Precision IceCube Next Generation Upgrade (PINGU). 2014.

[80] S. Adrian-Martinez et al. Letter of Intent for KM3NeT2.0. 2016.

[81] Xinheng Guo et al. A Precision measurement of the neutrino mixing angle θ_{13} using reactor antineutrinos at Daya-Bay. 2007.

[82] F. Ardellier et al. Double Chooz: A Search for the neutrino mixing angle theta(13). 2006.

[83] J. K. Ahn et al. RENO: An Experiment for Neutrino Oscillation Parameter θ_{13} Using Reactor Neutrinos at Yonggwang. 2010.

[84] S. Abe et al. Precision Measurement of Neutrino Oscillation Parameters with KamLAND. *Phys. Rev. Lett.*, 100:221803, 2008.

[85] M. He et al. Jiangmen Underground Neutrino Observatory. 2014.

[86] Zelimir Djurcic et al. JUNO Conceptual Design Report. 2015.

[87] P. Adamson et al. The NuMI Neutrino Beam. *Nucl. Instrum. Meth.*, A806:279–306, 2016.

[88] P. Adamson et al. Combined analysis of ν_μ disappearance and $\nu_\mu \rightarrow \nu_e$ appearance in MINOS using accelerator and atmospheric neutrinos. *Phys. Rev. Lett.*, 112:191801, 2014.

[89] D. S. Ayres et al. NOvA: Proposal to build a 30 kiloton off-axis detector to study nu(mu) —¿ nu(e) oscillations in the NuMI beamline. 2004.

[90] IceCube Gallery. internal document.

[91] Particle Data Group - Atomic and nuclear properties of water (ice) (H2O). `http://pdg.lbl.gov/2015/AtomicNuclearProperties/HTML/water_ice.html`, 2015. [Online; accessed 29-June-2016].

[92] L. Rdel. Simulation Studies of the Cherenkov Light Yield from Relativistic Particles in High-Energy Neutrino Telescopes with Geant4, 2012.

[93] P. B. Price and K. Woschnagg. Role of Group and Phase Velocity in High-Energy Neutrino Observatories. *Astropart. Phys.*, 15:97–100, 2001.

[94] Hamamatsu Photonics K.K. *Photomultiplier Tube R7081-02 for IceCube Experiment*, 2003.

[95] R. Abbasi et al. The IceCube Data Acquisition System: Signal Capture, Digitization, and Timestamping. *Nuclear Instruments and Methods in Physics Research A*, 601:294–316, April 2009.

[96] Gerald T. Przybylski. *Analog Transient Waveform Digitizer R1.1 (V2)*, 1999.

[97] R. Abbasi et al. The design and performance of IceCube DeepCore. *Astroparticle Physics*, 35:615–624, May 2012.

[98] M. Ackermann et al. Optical Properties of Deep Glacial Ice at the South Pole. *Journal of Geophysical Research: Atmospheres*, 111(D13):n/a–n/a, 2006.

[99] P. B. Price, K. Woschnagg, and D. Chirkin. Age vs depth of glacial ice at south pole. *Geophysical Research Letters*, 27(14):2129–2132, 2000.

[100] M. G. Aartsen et al. Measurement of South Pole Ice Transparency with the IceCube LED Calibration System. *Nucl.Instrum.Meth.*, A711:73–89, 2013.

[101] The IceCube Collaboration. The IceCube Neutrino Observatory VI: Neutrino Oscillations, Supernova Searches, Ice Properties. *ArXiv e-prints*, November 2011.

[102] Costas Andreopoulos, Christopher Barry, Steve Dytman, Hugh Gallagher, Tomasz Golan, Robert Hatcher, Gabriel Perdue, and Julia Yarba. The GENIE Neutrino Monte Carlo Generator: Physics and User Manual. 2015.

[103] Torbjorn Sjostrand, Stephen Mrenna, and Peter Z. Skands. PYTHIA 6.4 Physics and Manual. *JHEP*, 05:026, 2006.

[104] A. Gazizov and M. P. Kowalski. ANIS: High Energy Neutrino Generator for Neutrino Telescopes. *Comput.Phys.Commun.*, 172:203–213, 2005.

[105] D. Heck, J. Knapp, J. N. Capdevielle, G. Schatz, and T. Thouw. *CORSIKA: a Monte Carlo code to simulate extensive air showers.* February 1998.

[106] D. Chirkin and W. Rhode. Muon Monte Carlo: A High-Precision Tool for Muon Propagation through Matter. 2004.

[107] C. Kopper. clsim. `https://github.com/claudiok/clsim`. [Online; accessed 20-June-2016].

[108] *Geant4 Physics Reference Manual*, 2013. [Online; accessed 29-June-2016].

[109] *The OpenCL Specification*, 2012. [Online; accessed 29-June-2016].

[110] D. Chirkin. Photon Propagation Code. `http://icecube.wisc.edu/~dima/work/WISC/ppc/`, 2010. [Online; accessed 29-June-2016].

[111] M. G. Aartsen et al. The IceCube Neutrino Observatory Part VI: Ice Properties, Reconstruction and Future Developments. In *Proceedings, 33rd International Cosmic Ray Conference (ICRC2013)*, 2013.

[112] M. Larson. Vuvuzela - doxygen page. http://software.icecube.wisc.edu/simulation_trunk/doxygen/vuvuzela/index.html. [Online; accessed 28-June-2016].

[113] S. Euler. *Observation of oscillations of atmospheric neutrinos with the IceCube Neutrino Observatory*. PhD thesis, RWTH Aachen University, 2013.

[114] M. Larson. NoiseEngine - Algorithm. http://software.icecube.wisc.edu/icerec_trunk/projects/NoiseEngine/index.html. [Online; accessed 29-June-2016].

[115] J. P. Yáñez Garza. *Measurement of neutrino oscillations in atmospheric neutrinos with the IceCube DeepCore detector*. PhD thesis, Humboldt-Universität zu Berlin, 2014.

[116] D. Chirkin. Neutrino search with IceCube. internal report - https://internal.icecube.wisc.edu/reports/data/icecube/2008/07/006/icecube_200807006_v1.pdf, 2008.

[117] J. Ahrens et al. Muon Track Reconstruction and Data Selection Techniques in AMANDA. *Nuclear Instruments and Methods in Physics Research A*, 524:169–194, May 2004.

[118] M.G. Aartsen, R. Abbasi, Y. Abdou, M. Ackermann, J. Adams, et al. Improvement in Fast Particle Track Reconstruction with Robust Statistics. 2013.

[119] D. Pandel. Bestimmung von Wasser- und Detektorparametern und Rekonstruktion von Myonen bis 100 TeV mit dem Baikal-Neutrinoteleskop NT-72. ftp://ftp.desy.de/pub/preprints/desy/thesis/desy-thesis-01-023.ps.gz, February 1996.

[120] S. Euler. FiniteReco. http://software.icecube.wisc.edu/icerec_trunk/projects/finiteReco/index.html. [Online; accessed 29-June-2016].

[121] J. A. Aguilar et al. A fast algorithm for muon track reconstruction and its application to the ANTARES neutrino telescope. *Astroparticle Physics*, 34:652–662, April 2011.

[122] M. Wolf. CommonVariables. http://software.icecube.wisc.edu/icerec_trunk/projects/CommonVariables/index.html. [Online; accessed 29-June-2016].

[123] A. Terliuk. Energy reconstruction of ν_μ events in DeepCore. internal report - https://internal.icecube.wisc.edu/reports/data/icecube/2013/04/001/icecube_201304001_v2.pdf, 2013.

[124] M.G. Aartsen et al. Energy Reconstruction Methods in the IceCube Neutrino Telescope. *JINST*, 9:P03009, 2014.

[125] Kevin P. Murphy. *Machine learning : a probabilistic perspective*. Adaptive computation and machine learning series. MIT Press, Cambridge (Mass.), 2012.

[126] M. Richman. pybdt. http://software.icecube.wisc.edu/icerec_trunk/projects/pybdt/index.html. [Online; accessed 29-June-2016].

[127] RobertE. Schapire. The strength of weak learnability. *Machine Learning*, 5(2):197–227, 1990.

[128] Yoav Freund and Robert E Schapire. A decision-theoretic generalization of on-line learning and an application to boosting. *Journal of Computer and System Sciences*, 55(1):119 – 139, 1997.

[129] H.-J. Yang, B. P. Roe, and J. Zhu. Studies of boosted decision trees for MiniBooNE particle identification. *Nuclear Instruments and Methods in Physics Research A*, 555:370–385, December 2005.

[130] Trevor Hastie, Saharon Rosset, Ji Zhu, and Hui Zou. Multi-class AdaBoost. *Statistics and Its Interface*, 2(3):349–360, 2009.

[131] Photonics - Codebase. `https://sourceforge.net/projects/photonics/`. [Online; accessed 29-June-2016].

[132] B. W. Silverman. *Density Estimation for Statistics and Data Analysis*. Chapman and Hall, 1986.

[133] Morihiro Honda, T. Kajita, K. Kasahara, S. Midorikawa, and T. Sanuki. Calculation of atmospheric neutrino flux using the interaction model calibrated with atmospheric muon data. *Phys. Rev.*, D75:043006, 2007.

[134] J. Lundberg, P. Miocinovic, T. Burgess, J. Adams, S. Hundertmark, et al. Light Tracking for Glaciers and Oceans: Scattering and Absorption in Heterogeneous Media with Photonics. *Nucl.Instrum.Meth.*, A581:619–631, 2007.

[135] F. James and M. Roos. Minuit: A System for Function Minimization and Analysis of the Parameter Errors and Correlations. *Comput. Phys. Commun.*, 10:343–367, 1975.

[136] ROOT Mathematical Libraries: Minuit2 Minuit2 Minimization Package. `http://seal.web.cern.ch/seal/MathLibs/Minuit2/html/`. [Online; accessed 29-June-2016].

[137] S. S. Wilks. The Large-Sample Distribution of the Likelihood Ratio for Testing Composite Hypotheses. *Annals Math. Statist.*, 9(1):60–62, 1938.

[138] Glen Cowan, Kyle Cranmer, Eilam Gross, and Ofer Vitells. Asymptotic formulae for likelihood-based tests of new physics. *Eur. Phys. J.*, C71:1554, 2011. [Erratum: Eur. Phys. J.C73,2501(2013)].

[139] G. J. Feldman and R. D. Cousins. Unified Approach to the Classical Statistical Analysis of Small Signals. Phys. Rev. D, 57:3873–3889, April 1998.

[140] M. Vehring. Measurement of Atmospheric Neutrino Oscillations with the IceCube/DeepCore Detector. *Proceedings of Science (EPS-HEP2015)*, 419, 2015.

[141] Roger Wendell. Atmospheric Results from Super-Kamiokande. *AIP Conf. Proc.*, 1666:100001, 2015.

[142] K. Abe et al. Measurements of neutrino oscillation in appearance and disappearance channels by the T2K experiment with 6.610^{20} protons on target. *Phys. Rev.*, D91(7):072010, 2015.

[143] M. Leuermann. *Ph.D. Thesis*. PhD thesis, RWTH Aachen University, in preparation.

[144] M. Larson. *Ph.D. Thesis*. PhD thesis, Københavns Universitet, in preparation.

[145] M. Wallraff. *Ph.D. Thesis*. PhD thesis, RWTH Aachen University, in preparation.

Acknowledgements

I dreaded to write this page, since there are so many people that were involved with this work or helped me in the course of the last few years. So, I most probably will forget to thank people.

First of all I want to thank my advisor Prof. Dr. Christopher Wiebusch. The work in his group and with him was a vital part of my life. He gave me the opportunity to work in an international collaboration of scientists on a very interesting, ongoing topic that gives one of the indications that the SM has to be extended. He supported me in the stressing unblinding phase and always had an open ear if questions arose.

Second, I want to give my thank to Prof. Dr. Thomas Hebbeker for being the second reviewer of this thesis, even though he has a full schedule.

Third, I want to thank all people in the IceCube Aachen group. They are the best colleagues one could hope for. Especially I thank my old office colleagues Dirk Heinen, Martin Bissok and Larissa Paul. It was fun to work in one office with them and playing pranks on each other. Furthermore, Martin Bissok together with Jan Blumenthal were not only colleagues but close friends. These two I also want to thank for the introduction of foam arrow warfare to the working place. Furthermore I want to thank Martin Leuermann, Rene Reimann and Lisa Schumacher for the countless walks to the coffee machine. Lets not forget Sebastian Euler and Marius Wallraff who supported me in the first phase of this work and gave me invaluable tips.

From outside the Aachen group I want to thank Juan Pablo Yáñez and Andrii Terliuk who helped me a lot in the course of this analysis and especially in a stay at DESY Zeuthen.

Gratitude goes to all the people in the IceCube collaboration, especially the oscillation group. It was very interesting to work in an international collaboration and discuss with other "oscillators" at the collaboration meetings.

A special thank goes to my family. I could not have done this work without them. The supported me while being on this bumpy ride.

At last, I want to thank my lovely wife Irene who did not see me very often in the last weeks before finishing this work. Thank you for your support, your understanding, your care and your love.